Innovative configurations of thermochemical energy storage devices by topology optimization

by

Gabriele Humbert

Main Supervisor: Dr. Adriano Sciacovelli

Secondary supervisor: Prof. Yulong Ding

A thesis submitted to the University of Birmingham for the degree of

DOCTOR OF PHILOSOPHY

Birmingham Centre for Energy Storage

School of Chemical Engineering

College of Engineering and Physical Science

University of Birmingham, UK

October 2022

Un passo alla volta.

“Insistisci.”
Lello Humbert

Abstract

One of the main challenges to increasing the share of renewable energy sources in future energy scenarios is the mismatch between energy supply and demand. Thermal energy storage technologies have been identified as one possible solution to this challenge. Among the different thermal energy storage technologies, thermochemical energy storage devices are envisioned to have a large impact due to large theoretical energy density, negligible heat losses and possible heat-upgradation. Such devices rely on reversible chemical reactions where the energy is first stored in the form of chemical compounds generated by means of an endothermic reaction and recovered later on by recombining the compounds to drive an exothermic reaction.

However, several technical limitations still hamper the successful introduction of thermochemical energy storage technologies in the market. In particular, the effective configuring of these devices is a complex engineering challenge due to the intrinsic dynamic operation, the complex multi-physics problems involved and the vast range of system requirements. Furthermore, standard design approaches are often driven by the analysts' insight and experience, constraining the assessed configurations to a limited number of conceived solutions and precluding the full exploitation of the potential storage material.

To break these barriers, this dissertation explores the use of topology optimization as a systematic design tool for the effective configuration of thermochemical energy storage devices Topology optimization is a form-finding methodology able to identify optimal designs without the need for any guess regarding the initial layout. Compared to

conventional design approaches, the key advantage of topology optimization is thus its matchless design freedom. Novel enhancement pathways are identified by the analysis of the emerging design trends, and design solutions that outperform the current state-of-the-art are obtained.

Specifically, this dissertation studies the heat transfer enhancement of reactive beds through the insertion of extended surfaces made of highly conductive material. Design guidelines for practitioners are derived from the analysis of the generated designs for variable bed properties, desired discharge time and bed size. Thus, the mass transfer enhancement of reactive beds is achieved through the generation of non-intuitive flow channel geometries aiming to effectively distribute gas reactants to reactive sites. Finally, the two approaches are combined to generate reactive beds employing optimized flow channel and extended surface geometries, ultimately leading to the concurrent enhancement of heat and mass transfer.

Acknowledgements

This thesis is the result of a long journey far away from home. This journey has not always been easy. Actually, the journey has often been complicated and tough, making me doubt my choices and the direction to take.

First, I would like to thank myself. I believed in myself and I had been brave enough to take this long step away from my comfort place. It is amazing today to think how far I got and how much closer I got to the person I want to become.

Nonetheless, this journey would have been a failure if it wasn't for the many people I met during these years, to whom I would like to express my deepest gratitude. They all become part of me and have a special place in my heart.

I want to thank my Italian mentors: Eliodoro Chiavazzo, Pietro Asinari and Vito Cerone. They were the first to spot (some sort of) potential in me and made me believe that I could give my contribution to science. Then, I want to thank my supervisors: Yulong Ding and Adriano Sciacovelli. To Yulong, thank you for showing me how to pursue great purposes without getting lost in the details. And especially thank you for creating a positive and supportive environment all over the BCES group. To Adriano, a huge thanks for your support, time and help during these three years. I really admire your passion and enthusiasm for science, which have often been of inspiration to me. Thanks for helping me face my weaknesses, it was not always an easy process, but I am sure it made me a better researcher.

I am extremely grateful to all the office mates and friends I met during my time at BCES: Luca, Adina, Marisa, Helena, Robin, Pouriya, Giovanni, Shivangi, Gan, Marco, Jonas, Andrea

and Anabel. Each of you helped me by creating a friendly and positive environment; I will miss our lunch breaks and our hunting for free food in the M&M building.

Thanks to Birmingham. I probably did not like you at first; you were different from what I was used to. But you became a better place with time, and I started to like you. Thanks to the green of the meadow during summer, thanks to the yellow of the trees in Autumn and thanks to the pale red of the bricks during the golden hour. Thanks to the pubs and the pints. Thanks to Alicia's pizza. Thanks to brutalist buildings and thanks to Canon Hill park. But most importantly, thanks to the people I met in Birmingham.

To Birmingham Futsal Club, thanks for the great matches and life experiences. Thanks to Mark, your immense passion for futsal is contagious, and your dedication made me often feel like a real professional player: this is a feeling I won't forget.

To Dynamo Keynes, thanks for the countless matches at Bournbrook or Pebble Mill fields. These have always been a great distraction from the PhD burden, and they often made my day. A special thanks go to the Italian chaps: Martello, Loco, Marco Piadina, Marco Arancina, Marco Filosofo Statale, Marco Bassista, Giulio, Stefano, Fabio, Omar & Rocco. Mi ritengo davvero fortunato ad avervi incontrato, siete riusciti a rendere Birmingham un po' più casa. Mi mancheranno le nostre pinte insieme e il perdere partite di poker a casa Pantuso.

Grazie ai miei amici di sempre: Umbi, Pippo, Cipi, Arianna, Enrico, Marco, Bianca, Gaia, Bri, Matteo, Fra, Luca and Aide. Grazie per il senso di famiglia e di pace che mi regalate ogni volta che passiamo del tempo insieme. A Jacopone, grazie per la tua genuinità, per tutte le risate insieme e per i tuoi apprezzamenti sulle mie camicie. Grazie a Marco Di Natale, sei stato davvero importante in questi tre anni di dottorato. Grazie per le lunghe chiacchierate e le

birre insieme. Grazie per le ospitate. Grazie per avermi ascoltato e consigliato. Grazie per avermi capito. Ti auguro ti trovare sempre la tua strada, dritta o tortuosa che sia.

To Patricia and Gilmore (P&G), thanks for welcoming me to the British world and for all the good times we had together. Thanks for being funny and *wow*, we created great memories together. To Andrea and Silvia, only with time I fully understood how important you have been and still are to me. You have always been there, helping me find my place in Birmingham. I always felt I could rely on you, and this is something priceless. I wish you the very best, and I admire how strong you are as a team.

Grazie a Gianlu, Stefi, Eli and Lori per i tanti bei momenti vissuti insieme. Lori e Eli, non cambiate mai e siate sempre sereni e leggeri. Alla mia famiglia, Valina, Mami e Papo, sapete già quanto io vi voglia bene e quanto siate importanti per me. Grazie per avermi permesso di crescere nel modo che volevo io, supportandomi con amore in ogni mia decisione. Crescendo capisco sempre di più quanto io sia fortunato ad avere voi. Valina, grazie per essere la mia migliore amica. Per la tua leggerezza, la tua dolcezza e per la tua saggezza. Sei stata la mia guida più volte di quante credi.

To Bella, you are the most important part of this PhD. I feel incredibly lucky I met you and that you let me be part of your life, of our lives. If I feel a better person today, it is mostly because of you. All this would not have been possible without your gigantic support and encouragement; the biggest thanks go to you. I feel really, really lucky to have you as my Cocoon and to be yours. Thanks for being you.

Ai nonni, grazie per avermi insegnato il valore dell'amore per la famiglia. A nonno Giulio, mi manchi, ma ti sento sempre vicino durante i nostri aperitivi con vino e salame.

Publications and awards

The following scientific contributions constitute part of this dissertation.

J refers to journal publications, ***C*** refers to conference papers, ***P*** refers to posters, ***A*** refers to awards, and ***BC*** refers to book chapters.

J1 – *Humbert G, Ding Y, Sciacovelli A. Combined enhancement of thermal and chemical performance of closed thermochemical energy storage system by optimized tree-like heat exchanger structures. Applied Energy 2022; 311:118633.*

J2 – *Humbert G, Ding Y, Sciacovelli A. High-performance thermochemical energy storage systems: discovery of innovative fins designs through topology optimization. Submitted to Applied Energy.*

J3 – *Humbert G, Ding Y, Sciacovelli A. Topology optimization for mass transfer enhancement in open thermochemical energy storage reactors. Submitted to Journal of Energy Storage.*

C1 – *Humbert G, Ding Y, Sciacovelli A. Performance maximization of closed system thermochemical energy storage through reactor design and dynamic operating condition formulation. In: 34th international conference on Efficiency, Cost, Optimization, Simulation and Environmental Impact of Energy Systems (ECOS) 2021 proceedings. p. 916–27.*

C2 – *Humbert G, Ding Y, Sciacovelli A. Performance maximization of thermochemical energy storage reactors through topology optimization. In: 35th international conference on Efficiency, Cost, Optimization, Simulation and Environmental Impact of Energy Systems (ECOS) 2022 proceedings.*

C3 – *Humbert G, Ding Y, Sciacovelli A. topology optimization for heat and mass transfer intensification in thermochemical energy storage reactive beds. In: 15th International Conference on Heat Transfer, Fluid Mechanics and Thermodynamics (HEFAT) 2022 proceedings.*

P1 – *Humbert G, Ding Y, Sciacovelli A. Design optimization of closed system Thermochemical Energy Storage reactors. Energy Research Accelerator Early Career Researcher (ERA ERC) conference 2020.*

P2 – *Humbert G, Ding Y, Sciacovelli A. Design optimization of closed system thermochemical reactors through surrogate models. 15th International Conference on Energy Storage (ENERSTOCK) 2021.*

The following scientific contributions were published during the Ph.D studies period but do not constitute part of this dissertation:

J4 – *Humbert G, Roosendaal C, Swanepoel J K, Navarro H M, Le Roux W G, Sciacovelli A. Development of a latent heat thermal energy storage unit for the exhaust of a recuperated solar-dish Brayton cycle. Applied thermal engineering 2022*:118994*.*

J5 – *Ge R, Humbert G, Martinez R, Attallah M M, Sciacovelli A. Additive manufacturing of a topology-optimised multi-tube energy storage device: Experimental tests and numerical analysis. Applied Thermal Engineering 2020; 180:115878.*

BC1 – *Sciacovelli A, Li Y, Vecchi A, Humbert G, Fisher R. Chapter 14: Modelling and Optimisation of Thermal Energy Storage Systems. Therm. Energy Storage Mater. Devices, Syst. Appl., 2021, p. 480–523.*

C4 – *Humbert G, Madani SH, Izadi A, Hosseini SV, Swanepoel JK, Roosendaal C, et al. Selection and performance of TES options for decentralized generation of electricity and heat by small-scale solar air Brayton cycle. In: 12th International conference on Applied Energy (ICAE) 2020 proceedings.*

C5 – *Humbert G, Roosendaal C, Swanepoel J K, Navarro H M, Le Roux W G, Sciacovelli A. Design and performance assessment of a high-temperature latent heat thermal energy storage for small scale solar-air Brayton cycle. In: 14th International Conference on Heat Transfer, Fluid Mechanics and Thermodynamics (HEFAT) 2021 proceedings, p. 596-601.*

C6 – *Humbert G, Ding Y, Sciacovelli A. Thermochemical energy storage fluids – investigation of wetting behaviour on commercial heat exchangers substrates. In: 15th International Conference on Heat Transfer, Fluid Mechanics and Thermodynamics (HEFAT) 2022 proceedings.*

C7 – *Ge R, Pizzolato A, Humbert G, Maute K, Verda V, Attallah M, Sciacovelli A. 3D printing manufacturability of a topology-optimized multi-tube latent heat storage system. In: 16th UK Heat Transfer conference (UKHTC) 2019 proceedings.*

C8 – *Niknam P, Humbert G, Sciacovelli A. Initial CFD assessment of compact latent heat thermal energy storage system for mobile application in the maritime sector. In: 15th International Conference on Heat Transfer, Fluid Mechanics and Thermodynamics (HEFAT) 2022 proceedings.*

The following awards were conferred during the Ph.D. studies period:

A1 – *Best poster awarded to "Design optimization of closed system Thermochemical Energy Storage reactors" at the Energy Research Accelerator Early Career Researcher (ERA ERC) conference 2020.*

A2 – *Best paper in renewable energy 2 awarded to "Design and performance assessment of an high-temperature latent heat thermal energy storage for small scale solar-air Brayton cycle" at the 15th international conference on heat transfer, fluid mechanics and thermodynamics (HEFAT) and the editorial board of applied thermal engineering (ATE).*

Table of contents

List of figures

xxx

List of tables

List of abbreviations

ADS	*Axial Distribution System*
AM	*Additive Manufacturing*
BDF	*Backward Differentiation Formula*
BF	*Branched Fins*
CAD	*Computer Aided Design*
CFD	*Computational Fluid-Dynamics*
EOM	*Energy Output Maximization*
FC	*Flow Channels*
FE	*Finite Element*
FEM	*Finite Element Method*
GA	*Genetic Algorithm*
GCMMA	*Globally Convergent Method of Moving Asymptotes*
HCM	*Highly conductive Material*
HE	*Heat Exchanger*
HT	*Heat Transfer*
HTF	*Heat Transfer Fluid*
HVAC	*Heating, Ventilation and Air Conditioning*
IP	*Interior Point*
LG	*Large Grain*
LHTES	*Latent Heat Thermal Energy Storage*

LP	*Linear Programming*
MBB	*Messerschmitt-Bolkow-Blohm*
MMA	*Method of Moving Asymptotes*
MT	*Mass Transfer*
MUM	*Material Utilization Maximization*
NS	*Navier Stokes*
PA	*Performance Assessment*
PCM	*Phase Change Material*
PDE	*Partial Differential Equation*
PF	*Packing Factor*
PM	*Performance Metric*
PV	*Photovoltaic*
RAMP	*Rational Approximation of Material Properties*
RDS	*Radial distribution system*
SG	*Small Grain*
SHS	*Sensible Heat Storage*
SIMP	*Solid Isotropic Material with Penalization*
SLM	*Selective laser melting*
SLP	*Sequential linear programming*
TCM	*Thermochemical material*
TCS	*Thermochemical Storage*
TES	*Thermal Energy Storage*
TO	*Topology Optimization*

List of symbols

Symbols

b_i	*Polynomial coefficient [-]*
$\dot{c}$	*Molar sink term [mol/ m^3/s]*
c	*Molar concentration [mol/m^3]*
C	*Heat capacity [J/kg]*
c_p	*Specific heat [J/kg/K]*
D	*Diffusion coefficient [m^2/s]*
d_g	*Grains diameter [m]*
E	*Energy density [kWh/m^3]*
f	*Objective function [-]*
H	*Reactive bed height [m]*
$h(p)$	*Pressure term [-]*
h_{HTF}	*Convective heat transfer coefficient [W/m^2/K]*
$\boldsymbol{J}$	*Jacobian [-]*

K	*Permeability [m^2]*
k_{cin}	*Kinetic coefficient [1/s]*
$l_{1,..,3}$	*Fins' length parameters [m]*
m	*Mass [kg]*
M	*Molar mass [kg/mol]*
N_t	*Number of time steps [-]*
N	*Order of the multivariate polynomial [-]*
N_s	*Size of the optimization problem [-]*
P	*Specific thermal power [W/kg]*
p	*Pressure [Pa]*
P_{avg}	*Specific thermal power averaged in time [W/kg]*
p_{SIMP}	*Interpolation exponent for the SIMP scheme [-]*
p_{TANH}	*Interpolation coefficient for the TANH scheme [-]*
$\dot{q}$	*Volumetric heat generation [$W/m^3/s$]*
q	*Convexity factor [-]*
q_j	*Generic optimization criteria [-]*

$\boldsymbol{R}$	Generic system of algebraic equation [-]
r_0	*Pipe radius [m]*
R_{gas}	*Ideal gas constant [J/mol/K]*
r_{min}	*Filter radius [-]*
R_{out}	*Outer radius [m]*
$\tilde{\boldsymbol{s}}$	*Filtered design variable [-]*
$\boldsymbol{s}$	*Design variable for the density-based design model [-]*
s^*	*Cut-off parameter [-]*
T	*Temperature [K]*
t	*Time [s]*
t^*	*Desired discharge time [s]*
u	*Velocity [m/s]*
$\boldsymbol{U}$	Generic PDE solution [-]
V^*	*Maximum volume fraction [-]*
W	*Reactive bed size [m]*
$\boldsymbol{x}$	*Coordinate vector [-]*

x_j	*Generic design variable [-]*
ΔH	*Standard enthalpy of reaction [J/mol]*
ΔS	*Standard entropy of reaction [J/mol/K]*

Greek symbols

α_b	*Brinkman term*
α	*Reaction advancement [-]*
β	*Projection steepness parameter [-]*
$\beta_{1,\dots,3}$	*Fins' angles parameter [°]*
γ	*Stoichiometric coefficient [-]*
Γ_{in}	*Inner boundary [m^2]*
Γ_{int}	*Interface boundary [m^2]*
Γ_{HTF}	*HTF boundary [m^2]*
δ_{dif}	*Vapour diffuser channels size [m]*
δ_{HCM}	*Fins thickness [m]*
$\boldsymbol{\Lambda}$	*Vector of adjoint variables [-]*

ε	*Porosity [-]*
η	*Projection threshold [-]*
λ	*Thermal conductivity [W/m·K]*
ρ	*Density [kg/m^2]*
μ	*Dynamic viscosity [Pa·s]*
Ω_D	*Ground domain volume [m^3]*

Subscripts

0	*Dehydrated state*
1	*Hydrated state*
b	*Bed*
charg	*Charge*
disch	*Discharge*
eff	*Effective*
eq	*Equilibrium*
max	*Maximum*

$peak$	*Peak in time*
r	*Reactor*
v	*Vapour*

Superscript

~	*Normalized function*

Chapter 1

Introduction

The heating sector represents a significant share of the total final energy consumption in the UK and worldwide. In 2018, thermal energy accounted for ≈44% of the final energy demand and was responsible for more than one-third of the overall CO_2 emissions, mainly derived from space heating (43%) and process heat in the industry (18%) [1]. The deep decarbonisation of the heating sector by 2050 is one of the priorities of the current energy policies, as highlighted by the net zero target imposed by the UK government [2]. Furthermore, approximately 90% of the world's energy use involves the generation or manipulation of heat, and the targeted deep decarbonisation seems inconceivable without breakthroughs in thermal science and engineering [3].

The decarbonisation of the energy sector builds upon a rapid uptake of Renewable Energy Sources (RES), such as solar and wind energy, throughout all kinds of energy uses. However, as a consequence of daily and seasonal fluctuations in energy generation, the use of RES-based systems suffers from the mismatch between energy supply and demand, as depicted in Figure 1.1 in the instance of solar energy generated during a single day. In the context of the decarbonisation of thermal energy, one of the ways to mitigate the intermittency of RES and better match supply-demand is to store the heat by means of thermal energy storage (TES) devices [4]. The main goal of TES devices is to accumulate heat when the production

exceeds the demand and to deliver thermal energy to the users when requested. By doing so, TES devices guarantee the energy systems increased flexibility and enable sector integration. TES devices are currently tested in various applications, such as utility-scale power generation, industry, district heating, district cooling, and buildings [5].

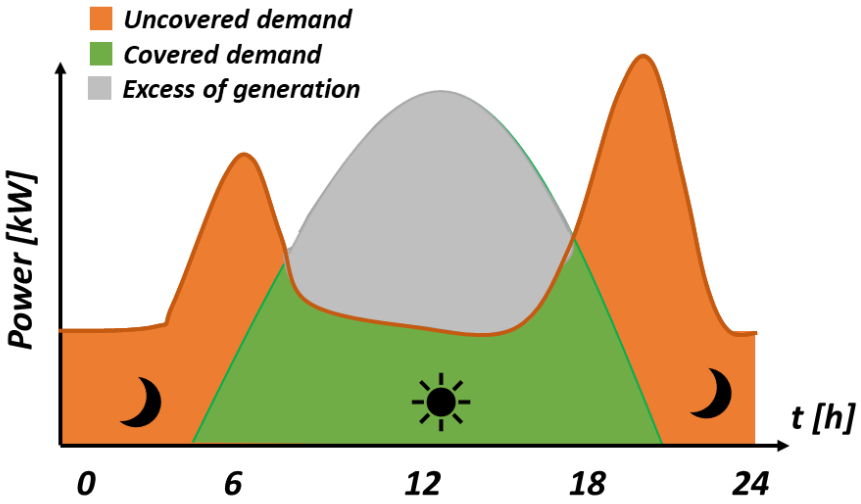

Figure 1.1 Solar energy generation and energy demand during a typical day.

As summarized in Figure 1.2, TES devices can be grouped into three main categories: sensible heat storage (SHS), latent heat thermal energy storage (LHTES), and thermochemical energy storage (TCS) [6]. Each TES device category differs in the way thermal energy is stored. In SHS devices, the heating or cooling of a storage medium is used to retrieve or deliver heat. In the framework of low-temperature applications ($T < 120$ °C), water is typically adopted as a storage medium given its wide availability and low cost combined with a relatively high heat capacity. When larger operational temperatures are required, the interest is shifted towards solid storage mediums, such as concrete and castable ceramics. Overall, given its low technological complexity and limited investment cost, the TES market is dominated by SHS solutions, with a share of 46.2% in the instance of United States market [7].

Nonetheless, LHTES devices, which rely on the phase change of a storage medium, are rapidly catching up (31.2%). Typically, the solid-liquid transition of the phase change materials (PCMs) is considered to limit the storage medium's volume variation. The melting of the storage material, i.e. LHTES device charging, takes place during the off-peak periods, while the PCM solidification occurs during the LHTES device discharge to supply heat to the users. Compared to SHS, LHTES devices provide the advantages of larger energy density at quasi-isothermal charging/discharging temperatures [8], but at the expense of larger investment costs and higher device complexity. Concerning low-temperature applications, numerous studies have demonstrated the technical feasibility and benefits of LHTES devices' integration into the existing energy system, which ultimately makes their TLR level close to commercial use. However, when higher temperature levels are requested (T > 120 °C), the existing literature on the effective integration of LHTES devices is still poor, and research efforts are still necessary to overcome a series of technical barriers, such as device life-span [9,10] and limited heat transfer rates [11].

Finally, in TCS devices, reversible chemical reactions are used to store and deliver thermal energy [12]. An endothermic chemical reaction is performed during the charging period by utilizing excess heat. Thus, the chemical compounds are kept in separate containers during storage until periods of high demand. At this point, the stored heat is released by the initiation of the exothermic reaction. Among the different TES options, TCS devices present the advantages of the highest theoretical energy density, nearly negligible heat losses during the storage period and possible heat up-gradation between charging and discharging steps. The existing reactors mainly adopt gas-solid reactions based on several solid thermochemical materials, such as salt hydrates, metal hydrides and metal oxides [13].

Nonetheless, despite the great interest in TCS systems, the technological maturity level is still lower than the other TES categories, with only a few prototype demonstrations in the operation environment (TRL 7) [14]. In fact, research suggests that the performance attained by the existing TCS devices is far from their theoretical potential [15].

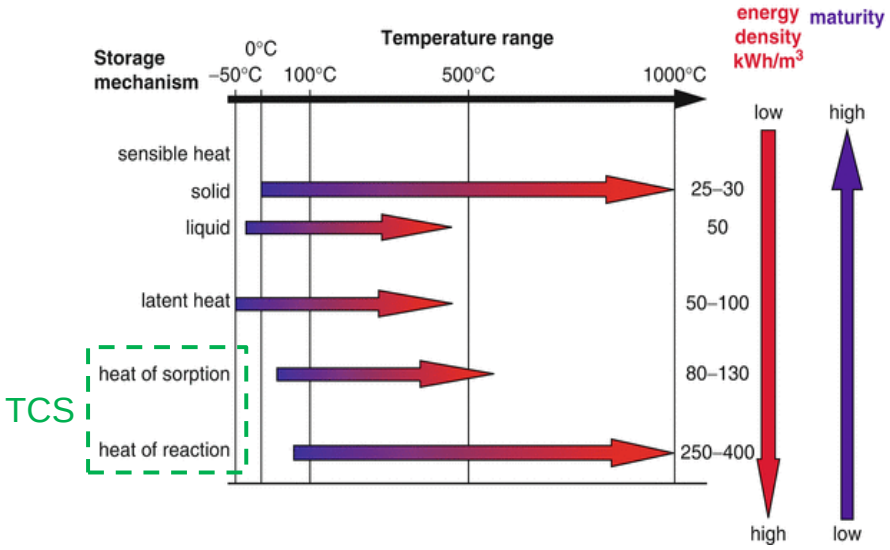

Figure 1.2. Energy density versus temperature for the different TES technologies [16].

The full exploitation of the thermochemical energy storage potential highly relies on effectively transferring heat and reactants from or to the reaction sites. As a consequence, the architecture of TCS devices needs to be functionally configured so that performance is maximized. However, the physical phenomena involved in TCS devices are based on heat transfer, fluid flow, species transport and reaction kinetics, making their analysis challenging. Besides, time-dependent studies are required to capture their behaviour fully. To this extent, advanced numerical tools must be built to accurately predict the device's performance and to describe the intertwined physical phenomena listed above.

On the other hand, the design choices and configuration modification can be ineffective if purely led by the analysts' insights. Conventional design approaches are based on the

sensitivity analysis of heuristically selected geometrical parameters. That is, a series of a priori selected configurations are analyzed, and the most performing solution is adopted as the 'optimal' design. However, the optimal global solutions might not belong to the range of configurations initially conceived by the designers, ultimately precluding the full exploitation of the storage material potential. To overcome this limitation, this thesis combines advanced numerical models and topology optimization to derive the best performing configuration of TCS devices. In such a way, besides the generation of TCS device configurations which outperform the current state-of-the-art, the emerging design trends are analysed, and practical design guidelines for the performance enhancement of TCS devices are derived.

1.1 Research questions

The numerical approach adopted in this work aims to provide fundamental insights into the effective configuration of TCS devices integrated into energy systems. Low- to medium-temperature TCS devices are considered. In such a framework, the existing literature mainly considered heuristic approaches for the configuration of the device architecture, with the deriving performance limited by the initial design choices. The overarching goal of this dissertation is thus achieved through the fulfilment of the following research questions:

- **Q_1**: How does the interplay between heat transfer and mass transfer in TCS reactive beds influence the correct positioning of extended surfaces?
- **Q_2**: How and how much can the thermal performance of closed system TCS reactors be enhanced by the design of optimized extended surface geometries?

- **Q_3**: How and how much can the thermal performance of open system TCS reactors be enhanced by the design of optimized flow channel geometries?
- **Q_4**: How and how much can we concurrently enhance heat and mass transfer in closed system TCS reactors through the design of optimized flow channels and extended surface geometries?

1.2 Contributions from the dissertation

Despite the considerable interest in TCS technologies, only a few studies have focused so far on TCS devices' configurations. Besides, these attempts suffered from limited design freedoms, as only a small number of configuration candidates were studied and assessed. This work differs significantly from these previous efforts, as it adopts optimization algorithms able to investigate vast design domains, i.e. a large number of possible geometrical solutions, and generate optimal configurations for specific design constraints and desiderata. The main contributions to knowledge derived from this dissertation can be summarized as follows:

(i) Application of the topology optimization algorithm to the design of TCS devices to guide the discovery of non-intuitive geometrical features enhancing the performance.

(ii) Design of fit-for-purpose TCS reactor designs with superior performance compared to literature benchmarks.

(iii) Definition of practical guidelines for the correct positioning of extended surfaces in closed system TCS reactors.

(iv) Generation and assessment of new enhancement pathways for the mass transfer intensification of TCS reactors by means of flow channel designs.

(v) Definition of practical guidelines for the effective configuring of flow channels distributing gas reactants in both open and closed system TCS reactors.

1.3 Outline of the dissertation

The outline of the dissertation is summarized in Figure 1.3.

Chapter 2 describes the working principles and key design challenges of TCS devices. Thus, the state-of-the-art for geometrical configurations of TCS devices is reviewed, along with the attempts to enhance their performance through the variation of geometrical features. The discussion defines the knowledge gaps for the effective configuration of TCS devices which are then addressed in the different thesis chapters.

Chapter 3 introduces the topology optimization algorithm and discusses how this can be coupled with advanced numerical tools to constitute a practical design tool. Common terminology and notations used throughout the whole dissertation are introduced. The application of the topology optimization algorithm as a design tool is illustrated through numerical examples. Finally, the state-of-the-art for topology optimization of energy devices is reviewed to highlight the methodology's potential and current limitations.

Chapter 4 addresses the research question $\boldsymbol{Q_1}$. A conventional optimization tool is adopted to investigate how the correct positioning of radial fins in TCS reactive beds is influenced by the interplay between heat and mass transfer. The key idea is to establish if and for which design cases the well-established design guidelines for the performance maximization of heat transfer problems can be applied to TCS devices. Besides, the influence of the material

properties evolution with the hydration level on the optimal fins configuration is investigated.

In ***Chapter 5***, topology optimization is adopted for configuring extended surfaces in TCS reactive beds to address research question $\boldsymbol{Q_2}$. A novel optimization problem is formulated to simultaneously identify the optimal extended surface geometry and the optimal amount of heat exchanger material. The performance of the generated designs is compared to the one of a literature benchmark to quantify the benefits led by the adopted methodology. Besides, the influence of relevant design parameters, such as desired discharge time, bed porosity and bed size, on the optimal design is elucidated.

Chapter 6 addresses research question $\boldsymbol{Q_3}$. The mass transfer in reactive beds is intensified by means of a topology optimization approach. Non-heuristic flow channel designs are derived with the intent to distribute the gas reactants to the reactive sites effectively. Two reactor configurations are explored, and the performance benefits are quantified against state-of-the-art solutions.

Chapter 7 combines and extends the methodologies presented in chapters 5 and 6 to concurrently enhance heat and mass transfer in TCS reactors. The chapter addresses research question $\boldsymbol{Q_4}$. A multi-step topology optimization approach is introduced, in which first the optimal flow channel design is derived, followed by the optimization of the extended surface geometry. The multi-step topology optimization approach is compared to the pure heat transfer and mass transfer optimization pathways. Recommendations are thus provided about which optimization pathway is the most indicated depending on specific design constraints.

Finally, ***Chapter 8*** discusses the key results and contributions of this dissertation as well as the potential areas for future studies.

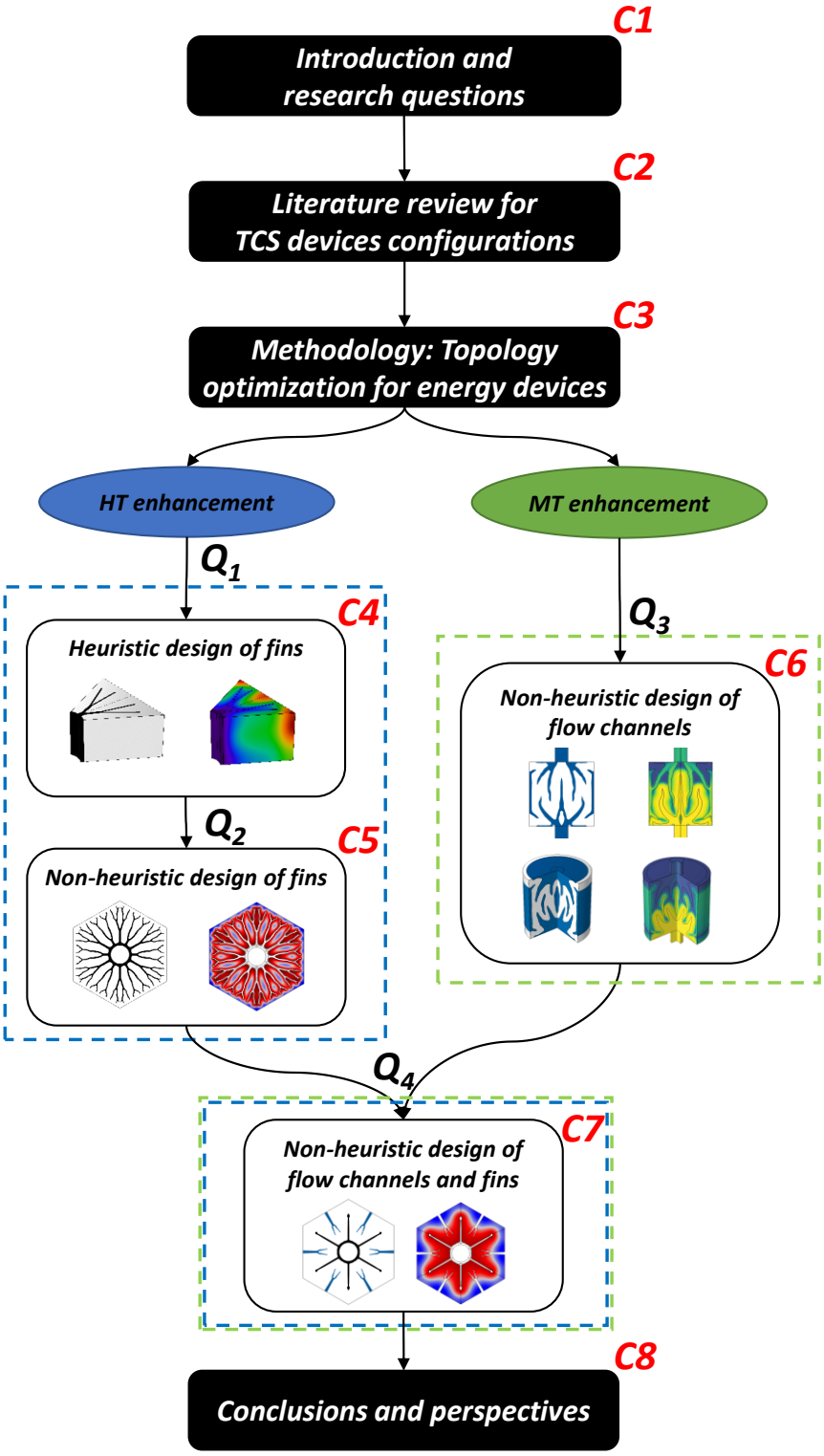

Figure 1.3 Mind map of the dissertation.

Chapter 2

Geometrical configurations of thermochemical energy storage reactors

Thermochemical energy storage technologies are based on reversible chemical reactions, which are exothermic in one direction and endothermic in the reverse direction. As summarized in Figure 2.1, the endothermic process is used to retrieve thermal energy when there is an excess of heat, e.g. during sunny days in summer, while the exothermic process generates thermal energy, which can be transferred to the users to satisfy the energy demand, e.g. domestic heating in winter. Between these two processes, the two compounds can be kept separate so that thermal energy can be stored as long as desired, making TCS systems particularly attractive for long-term thermal energy storage.

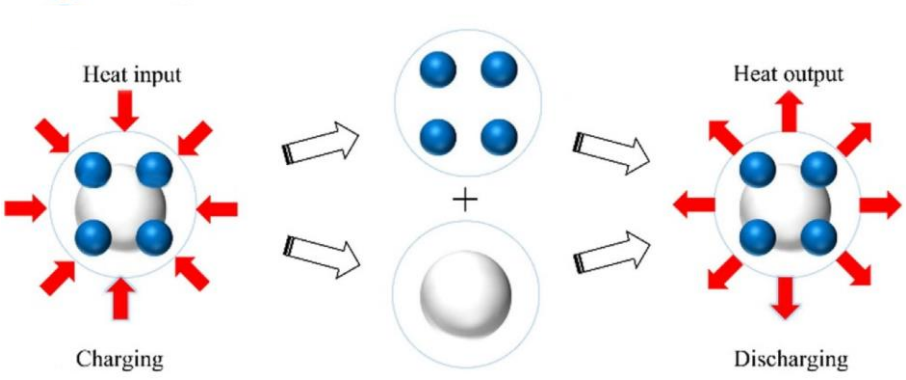

Figure 2.1 The process of a thermochemical energy storage cycle: charging, storing, discharging [17].

The thermochemical reversible reactions adopted in TCS devices are grouped into four categories based on the state of materials involved: (i) gas-gas reversible reactions, (ii) liquid-gas reversible reactions, (iii) liquid-liquid reversible reactions and (iv) solid-gas reversible reactions [18]. Solid-gas reactions have attracted more interest because of their wide range of turning temperatures and self-separation of reactants [19]. For these reasons, this dissertation solely focuses on gas-solid reactions.

The solid material involved in the thermochemical process is called thermochemical material (TCM). Compared to sensible and phase change materials, TCMs present larger energy densities, ultimately leading to more compact storage solutions, as shown in Figure 2.2 (a). For example, the required volume of storage material to satisfy a passive house's annual thermal energy need, 1900 kWh [17], reduces from 82 m^3 for an SHS adopting water to only 4 m^3 for a TCS system employing $MgCl_2 \cdot 6H_2$.

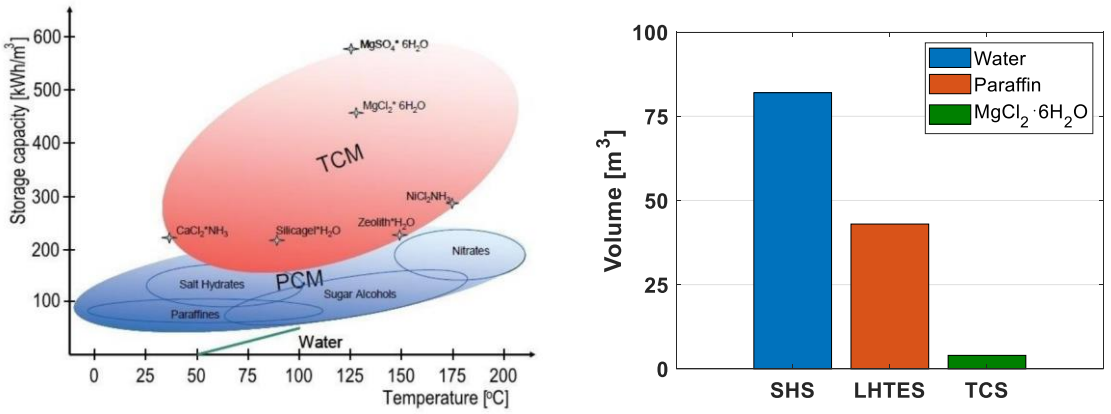

(a) *(b)*

Figure 2.2 (a) Energy density of typical storage materials versus temperature of operation [6]; (b) storage material volume needed to cover the annual thermal energy demand of a passive house (1900 kWh) [17].

A further advantage of TCS systems, which is often overlooked in the literature, is their ability to provide heat upgrade between charging and discharging processes [20]. Low-

temperature levels can indeed be adopted to drive the endothermic reactions at low-pressure values. Hence, low-grade heat sources can be used to drive the TCS charging process. Later, waste heat can provide the gas reactants evaporation enthalpy and drive the exothermic chemical reaction at relatively high-pressure. The available waste heat temperature level defines the gas reactants' pressure and determines the thermal upgrade between the discharging and charging processes.

Finally, evidence has been reported about the techno-economic benefits that could be achieved by using TCS systems. For example, Scapino et al. [21] considered various energy systems operating in the UK market. The integration of TCS systems into organic ranking cycles was proven to lead to profitability increases of up to 41%, ultimately demonstrating how TCS solutions could become an asset under specific market conditions.

This dissertation deals with low- to medium-temperature TCS devices, which is a strategic temperature range, given that more than 70% of the total energy consumption in the European residential sector is supplied in this temperature range [22]. Therefore, there is great interest in the decarbonisation of residential and commercial heating between 50-200 °C. In this framework, this chapter is organised as follows: firstly, the working principle of TCS systems, the different reactor types and operational modes are introduced. Secondly, the state-of-the-art for geometrical configurations of thermochemical energy storage devices is reviewed. A strong focus is placed on the attempts to enhance the device's performance through the reconfiguration of its geometry. Finally, the identified knowledge gaps in the effective configuration of TCS devices are discussed.

2.1 Working principle of TCS devices

This section illustrates the working principle of TCS devices considering gas-solid reactions. Although various gas reactants are available, a relevant fraction of TCS studies focus on water and the correspondingly available TCMs. Ammonia is also considered as an alternative candidate, although its toxicity and incompatibility with commercial containment materials make it a less attractive solution [23]. During the charging process, heat is delivered to the TCM, resulting in the formation of a dehydrated TCM, $MX \cdot m\ H_2O$, according to the forward reaction 2.1:

$$MX \cdot nH_2O + heat \leftrightarrow MX \cdot m\ H_2O + (n-m)H_2O \qquad 2.1$$

Wherein *MX* generically represents the TCM, *n* represents the number of water moles in the hydrated TCM, and *m* is the number of water moles in the dehydrated TCM. The enthalpy of this formation reaction is thus:

$$\Delta_r H_{m\rightarrow n} = \sum_{ractants}\Delta H_i - \sum_{products}\Delta H_i < 0 \qquad 2.2$$

Equation 2.2 indicates the energy generated during the forward reaction. This energy is used to deliver heat during the discharge process. On the other hand, the reverse decomposition reaction costs energy and can thus occur in the presence of an excess of the supplied energy. The storage process consists instead of keeping separated TCM and water.

Thermochemical processes based on solid-gas reactions are classified into adsorption, absorption and chemical reactions [12]. Adsorption is a surface phenomenon at the interface between two phases, where cohesive forces, e.g. van der Walls forces, act between the sorbate and sorbent molecules [24]. Absorption processes involve instead substances being incorporated into the bulk volume of the second substance in a different phase [25]. In both cases of adsorption and absorption processes, no change in the molecular configuration

occurs. Contrarily, the molecular configurations vary when chemical reactions are considered. Compared to physical bonds, stronger forces characterize chemical bonds, leading to larger energy density when chemical reactions are considered.

In the framework of low-temperature applications, the term sorption heat storage is often adopted to refer to TCS systems. According to Scapino et al. [26], sorption heat storage implies using both physical and chemical bonds. The two compounds needed for the gas-solid reaction to occur are thus referred to as the sorbent, i.e. solid TCM, and the sorbate, e.g. water vapour. The classification of gas-solid sorption heat storage systems is reported in Figure 2.3, where the predominant type of reaction that occurs during the process is emphasized.

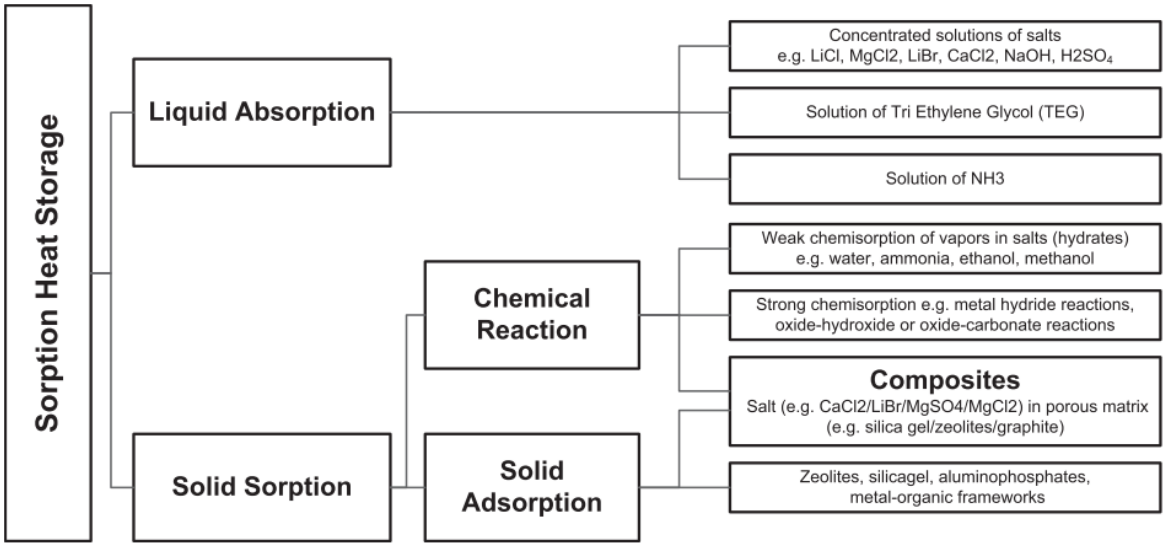

Figure 2.3 Classification of sorption heat storage [26].

Solid adsorption includes purely adsorbent materials, such as zeolites, silica gel and aluminophosphates [27]. Since weak bonding forces are present, relatively low energy densities characterize these materials. Besides, the water uptake is typically low due to structural limitations [26]. The chemical reaction category includes instead materials

undergoing solid/gas reactions in which an absorption process is predominant, but, in principle, adsorption may also take place. In this category, the use of hygroscopic salts such as magnesium chloride ($MgCl_2$), sodium sulphide (Na_2S), strontium bromide ($SrBr_2$) and magnesium sulphate ($MgSO_4$) [28] is researched. While few studies demonstrated the applicability of pure salts in large-scale TCS devices [29–31], many studies have investigated host matrices to support the TCM and enhance heat and mass transport in the reactive bed. In particular, host matrices are recommended to prevent the formation of compact blocks hindering vapour transport and to improve cyclability [32]. The host matrices can be either inert, such as cellulose, expanded graphite and vermiculate, or adsorber materials [19].

Several reviews have been published in recent years on the high potential of pure and composite TCMs for temperature storage below 100°C [28,33,34], with a clear focus on seeking large energy density. However, selecting the most suitable TCM is a more complex challenge. Besides the large energy density, the key properties requested for a TCM are high sorbate uptake, low charging temperature, good heat and mass transfer properties, compatibility with commercial containment materials and limited investment cost [5,35].

Furthermore, the proper TCM selection strongly depends on the operating conditions. Such operating conditions need to be compared with the TCM phase diagram, which indicates under which conditions the TCM undergoes hydration or dehydration [19], as depicted in Figure 2.4. Applying conditions, intended as a combination of water vapour pressure and temperature, below the solid line results in a dehydrated TCM, i.e. $MX \cdot mH_2O$ according to the reaction 2.1. For the TCM hydration to occur, conditions above the solid line should, hence, be applied. Such conditions can be achieved by utilizing a heat exchanger or varying

the vapour pressure. The latter is assumed here to be dictated by the temperature of a water compartment in agreement with the liquid/vapour line.

In the instance of a discharge process, the initial TCM phase is $MX \cdot mH_2O$. The temperature T_{w1} is applied in the water compartment, leading to a vapour pressure equal to p_h. Being these conditions above the equilibrium line, the TCM hydrates into $MX \cdot nH_2O$. During the reaction, the temperature of the TCM increases due to the exothermic reaction. Nevertheless, as long as the TCM temperature remains below T_h, i.e. equilibrium temperature for the imposed vapour pressure, a hydration process occurs. During the TCS charging, the initial TCM phase is $MX \cdot nH_2O$, and a fixed temperature, T_d, is applied. The targeted energy application dictates such a temperature. The vapour pressure applied to the system, p_d, is derived from the temperature T_{w2} imposed in the water compartment. As long as the vapour content in the TCM is below p_d, the TCM dehydrates.

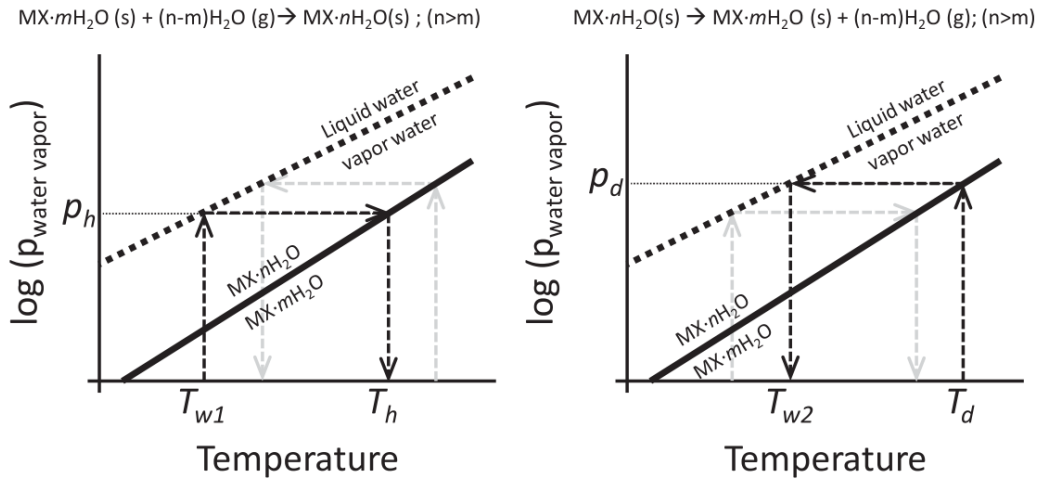

Figure 2.4 Phase change diagram and operating conditions from [19]: left for the TCS discharging process and right for the TCS charging process.

2.2 Operational modes

Systems for solid-gas reactors can be designed as either open or closed systems [18], as depicted in Figure 2.5. An open system exchanges mass and energy with the environment and consists of a single vessel containing the solid TCM crossed by moist air at atmospheric pressure. During the charging process, the airflow is heated up from a heat source, e.g. solar collectors, and circulated in the reactive bed in such a way that salt dehydration occurs. On the other hand, cold and humid air from the ambient flows through the reactor during discharge and is heated up by the exothermic process. The hot airflow exiting the reactor is thus circulated to the user. As the heat transfer fluid and the reactive gas carrier are the same, no additional heat exchanger is needed in open systems. However, significant drops in the system coefficient of performance have been measured [36,37] due to variations in the inlet airflow humidity. Hence, a humidifier is often recommended as an additional component to control humidity [38].

In contrast, closed systems exchange only energy with the environment and two vessels are required [39]. A first vessel containing the solid TCM and a second for the evaporation and condensation of the reactive gas. The system is evacuated to satisfactorily achieve sorbate transport between the reactor and the sorbate reservoir. During the charging process, the heat supplied is transferred to the reactor by means of an HTF, such as water [40] or diathermic oil [31]. Concurrently, a gas-liquid phase change reaction occurs in the condenser, where heat is released. Thus, the discharge process requires a low-grade heat source to generate vapour to hydrate the TCM, while the thermal energy provided by the exothermic reaction is retrieved by an HTF connected to the targeted energy application.

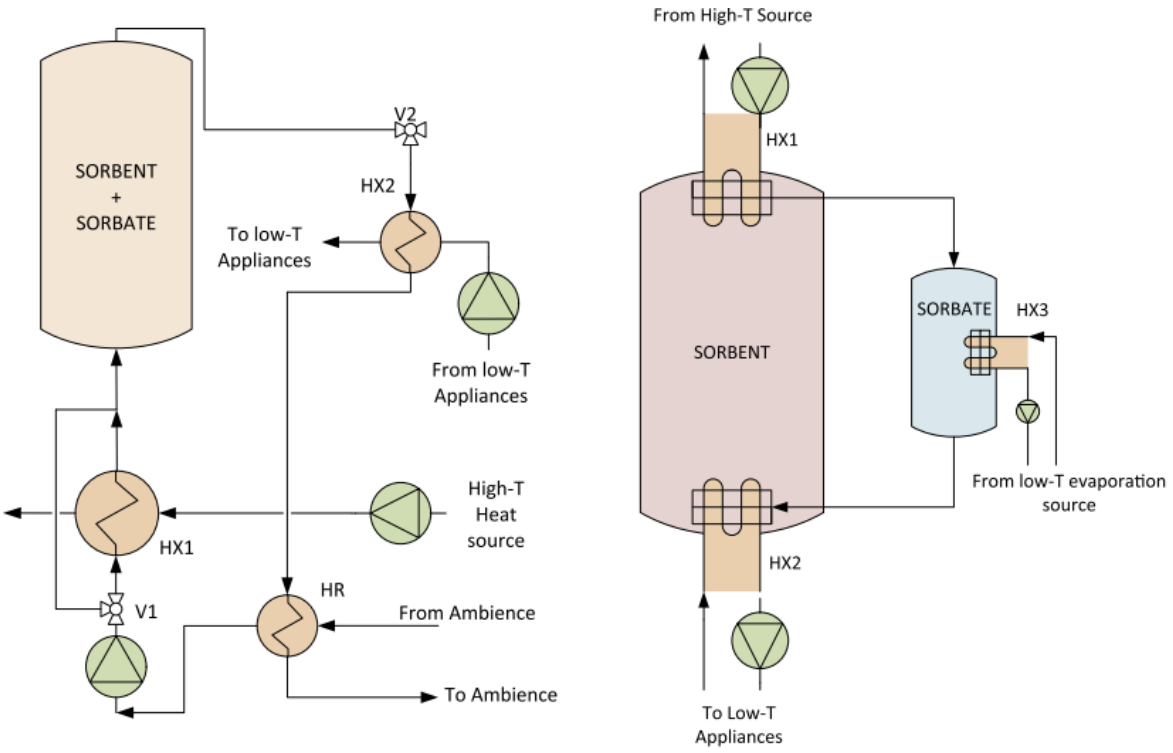

Figure 2.5 Basic schematics for the TCS system operational modes from Scapino et al. [26]. Left: open systems. During dehydration/desorption, valve V1 directs the airflow to HX1 to be heated up by a high-temperature heat source, e.g. solar collector. During hydration/sorption, HX1 is bypassed, while HX2 is used to transfer heat to the user. A heat recovery unit, HR, is often adopted to increase the system coefficient of performance. Right: closed systems. During the desorption/dehydration process, high-temperature heat is provided to the storage module through HX1, while the sorbate is condensed in the E/C unit, where a low-temperature sink removes heat. Thus, during the sorption process, the sorbate evaporates thanks to a low-temperature source and is transported to the storage module, where heat is retrieved and delivered to a low-temperature appliance.

A comparison of the advantages and disadvantages of open and closed modes is reported in Table 2.1. Overall, closed systems have a higher thermal power density due to the absence of inert gases passing through the reactors [41]. Fumey et al. [42] concluded that closed systems are more suitable than open systems in heating applications as these can achieve higher output temperatures. However, the need to ensure evacuated systems makes design and manufacturing challenging.

Recent studies demonstrated that open systems lead to superior efficiencies compared to closed systems. Bertsch et al. [43] modelled solid sorption storage concepts and compared open and closed systems. Significant heat losses were predicted for closed reactors, while negligible losses were obtained for open systems. This result is also supported by Michel et al. [37]. Here, open and closed systems were compared for a reactive bed employing $SrBr_2 \cdot 6H_2O$, and the predictions indicated average specific powers of 1.13 and 0.96 W/kg, respectively, for open and closed systems.

Table 2.1 Advantages and disadvantages of open and closed systems [15,18,26,44].

	Open system	*Closed system*
Advantages	• Simpler design • Operates under atmospheric conditions • Fewer components • Heat output controlled by air mass flow rate	• Higher discharge temperature for similar vapour pressure conditions • No mass exchange with the environment • Suitable for both cooling and heating • Higher power density (no inert gas) • Heat output controlled by the reactants flow rate
Drawbacks	• Humidifier and fan are required to increase humidity content and circulate air • Large pressure drops deriving from poor TCM permeability	• More complicated system design and operation • Requires a condenser/evaporator unit • TCM properties limit the heat transfer rate • Evaporation energy must be constantly supplied • Evacuation is needed to avoid the accumulation of non-condensable gases

2.2.1 Implications at reactor level

The flow patterns characterizing TCS reactors operated in the open and closed modes are presented in Figure 2.6 in the instance of a simplified 2D rectangular configuration. Concerning open systems during the discharge process, the airflow crossing the reactive bed

concurrently provides the gas reactants to the reactive site and collects the heat generated by the exothermic reaction. Michel et al. [31] demonstrated mass transfer as the main limiting factor for this type of reactor, with such a result obtained through the second law of thermodynamics. Consequently, the reactive bed permeability was reported to influence the reaction rate strongly. For this reason, open system reactors need to be configured with the primary aim of maximizing mass transfer in the reactive bed.

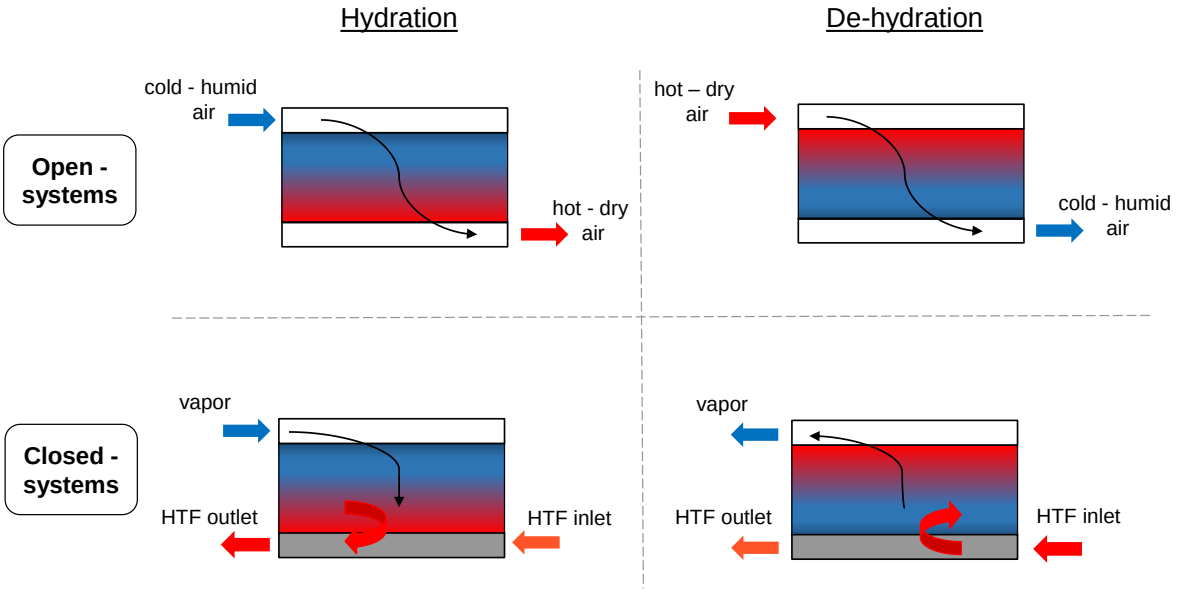

Figure 2.6 Simplified schematics for open and closed system reactors in the instances of both hydration and dehydration processes, partially adapted from Michel et al. [37].

Concerning TCS reactors operated in the closed mode, two distinct flow patterns are present. A first flow pattern for the gas reactants, driven by the pressure difference between the vacuum chamber pressure and the local vapour pressure in the reactive bed, and a second flow pattern for the heat transfer. The latter is instead driven by the temperature difference between the reactive bed temperature and the HTF temperature. Michel et al. [37] concluded that heat transfer is the key limiting factor in closed reactors. The reaction front for this type of reactor was predicted indeed to move from the heat exchanger surface

towards the vacuum chamber walls. Consequently, the poor reactive bed thermal conductivity strongly influenced the reaction rate. Heat transfer can be enhanced by adding conductive binders, e.g. ENG [40], or by inserting extended surfaces made of highly conductive materials [31], as reviewed in section 2.7.

2.3 Performance metrics

Performance metrics (PMs) are defined in this section to fairly assess TCS devices' performance. Such PMs are used in this chapter to compare the performance of existing TCS devices and throughout the whole thesis to quantify the performance improvements deriving from the proposed optimization approaches. According to [45], PMs need to be defined in order to be unique, measurable, applicable to more cases and relevant. Table 2.2 presents and discusses the adopted PMs.

Table 2.2 Key performance metrics (PMs) related to TCS devices, partially adapted from [4,45,46].

PM	Definition	Unit
Material energy density	$E_{TCM} = \frac{\Delta H_R^0 \, (n-m)}{M_n} \, \rho_{min}$ Where ΔH_R^0 is the reaction enthalpy, M_n is the molar weight in the n-hydration state and ρ_{min} is the minimum bulk density between the two TCM hydration states.	*[J/m³]*
Bed energy density	$E_{bed} = \frac{V_{TCM}}{V_{bed}} \, \alpha \, E_{TCM}$ Where V_{TCM} is the volume dedicated to the porous TCM and V_{bed} is the volume dedicated to the reactive bed, while α is the reaction advancement.	*[J/m³]*
Reactor energy density	$E_r = \frac{V_{bed}}{V_{reactor}} \, E_{bed}$ Where $V_{reactor}$ is the volume devoted to the porous TCM bed, the reactants diffuser and the HTF pipes.	*[J/m³]*
Charge and Discharge time	t_c and t_d The time needed to charge/discharge 90% of reactor energy density E_r.	*[s]/[h]/[d]*
Temperature lift	$\Delta T = T_{HTF,\ out} - T_{HTF,\ in}$ HTF temperature difference between the outlet and inlet interfaces of the reactor component.	*[K]*
Specific power	$P = \frac{\dot{m}_{HTF} c_{p.HTF} \, \Delta T}{m_{TCM}}$ Thermal power exchanged between the reactor component and the system over the mass of storage material, m_{TCM}. It is measured by two different parameters: - P_{avg}: average specific power in time; - P_{peak}: peak of specific power in time.	*[W/kg]*

Packing factor	$PF = \frac{V_{enhancer}}{V_{bed}}$ Where $V_{enhancer}$ is the volume of enhancer material in the device.	*[-]*

2.3.1 Definition of reference volumes

The definition of TCM, enhancer material, bed and reactor volumes adopted in this dissertation is reported in Figure 2.7 in the instance of a TCS reactor operated in closed mode and employing extended surfaces. The bed volume is defined in this work as the sum of the volume devoted to the porous TCM, V_{TCM}, and the volume devoted to the enhancer material, represented in Figure 2.7 as V_{HCM}. The reactor volume is instead defined by the sum of the bed volume, V_{bed}, the volume devoted to the vapour distribution channels, V_{FC}, and the volume devoted to the HTF pipes, V_{HTF}.

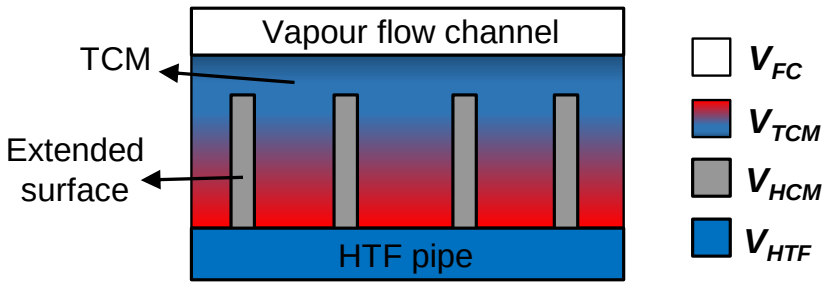

Figure 2.7 Definition of reference volumes in a TCS reactor operated in the closed mode and employing extended surfaces.

The reactor energy density thus significantly differs from the theoretical value calculated from the reaction enthalpy, E_{th}. Table 2.3 illustrates the steps leading to the energy density value reduction from its theoretical value to its final value at the reactor scale in the instance of $SrBr_2 \cdot 6H_2O$. The considered E_{th} refers to the bulk density of the hydrated $SrBr_2 \cdot 6H_2O$ [37] and is around 9 times higher than liquid water over a 60°C temperature range [29]. In a fixed bed reactor, this value reduces due to the storage medium porosity. A factor of 0.7 is

considered in the example, as typically observed in the literature [29,30,47]. An additional reduction factor needs to be considered for the presence of enhancer materials, which ultimately reduces the volume devoted to the storage material in the reactor configuration. Besides, only a fraction of the stored energy is retrieved by the user in the desired discharge time. We assume this fraction to be represented by the final reaction advancement, for which a 0.9 factor is considered. Finally, the discharged energy is referred to the reactor volume through the ratio V_{bed}/V_r, for which a value 0.53 is considerd in the example [40].

Table 2.3 Comparison between TCM and reactor energy density in the instance of $SrBr_2 \cdot 6H_2O$.

PM	*Units*	*Reduction factor*	*Value*
E_{th}	**[kWh/m^3]**	-	629.0
E_{TCM}	**[kWh/m^3]**	$(1-\varepsilon_1)$	440.3
E_{bed}	**[kWh/m$^3_{bed}$]**	$(1-\varepsilon_1)\cdot(1-PF)\cdot\alpha(t_f)$	356.6
E_r	**[kWh/m^3_r]**	$(1-\varepsilon_1)\cdot PF\cdot\alpha(t_f)\cdot\frac{V_{bed}}{V_r}$	189.0

2.4 Reactor types

Three main gas-solid reactor types are studied in the literature: fixed bed, moving bed and fluidized bed [12]. In fixed bed reactors, also referred to as packed bed reactors in the literature, the solid particles are located in a container and crossed by a flux of reactants. The reactive bed is thus a porous medium that allows for the gas reactants' transport but needs to be sufficiently packed to ensure satisfactory energy density. Besides, the void fraction of these porous mediums penalizes the effective thermal conductivity of the reactive bed, as air presents poorer thermal conductivity values than typical TCMs [19]. As a result, heat and mass transfer enhancement techniques are often required to attain

satisfactory thermal performance [48]. Concerning moving beds, part of the beds can be entirely or partially removed during the continuous operation, with the reactants circulation similar to fixed bed type. Once steady-state conditions are reached, homogenous bed temperatures are also achieved [49,50]. However, the required automation for the process entails a large investment cost, making this reactor type unattractive. Finally, the solid particles are suspended in a fluid flow in fluidised beds. Fluidized beds present a larger heat transfer rate and improved thermal stability, deriving from the reduction of possible thermal hotspots [51]. However, the reactor complexity is further increased, and corrosion of internal components is more likely to occur.

Fixed bed reactors are the most popular choice in TCS devices due to their ease of manufacturing and simple operation. For this reason, the literature review conducted in the next sections solely focuses on fixed bed reactors.

2.5 Existing prototypes

This section reviews the PM from the existing prototypes employing a TCM weight above 20 kg. As reported in Table 2.4, the vast majority of the tested prototypes employ physisorption materials such as zeolites and silica gels [52–60]. Nevertheless, recent projects also demonstrated the functioning of TCS reactors based on salt hydrates [29,40,61], for which larger reactor energy densities were measured. Besides, a significant reduction of the required charging temperature was also achieved, ultimately unlocking the integration of TCS devices in a larger number of energy systems.

Regarding the type of systems tested, open system TCS reactors are preferred. As discussed in section 0, this choice is due to the lower technological complexity and reduced number of

required components compared to closed systems. However, a larger peak of thermal power output was measured in the instances of TCS reactors operated in the closed mode, indicating that this operational mode was favourable for energy systems targeting high power-density devices, as can be appreciated in Figure 2.8 (a). For example, in the framework of the SOLUX project, Mauran et al. [40] measured peaks up to 64.0 W/kg. For the same thermochemical material ($SrBr_2$), but for a TCS reactor operated in open mode, Michel et al. [29] measured thermal power output peaks of only 2.0 W/kg [29].

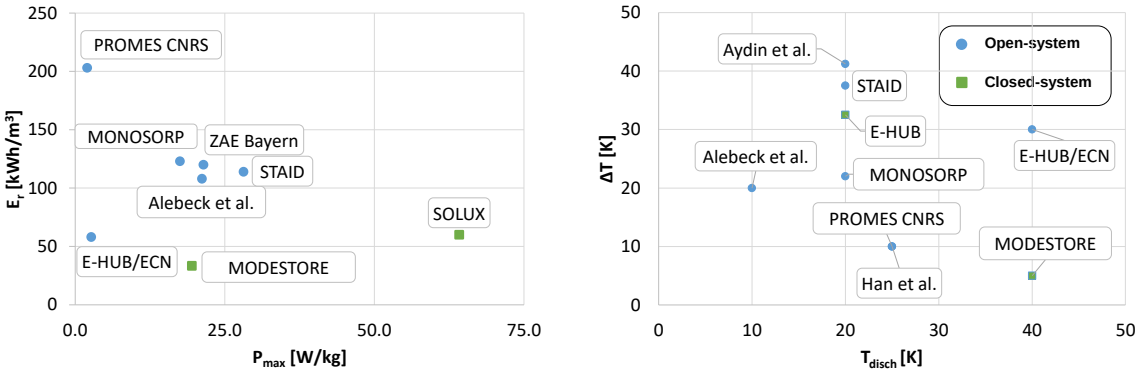

(a) *(b)*

Figure 2.8 Performance metrics comparison for the reviewed prototypes: (a) reactor energy density versus maximum power output; (b) temperature lift versus discharging temperature. The reviewed prototypes are labelled according to Table 2.4.

Differently from other TES technologies, the temperature lift provided by TCS reactors is not known a priori. The temperature lift is indeed determined by the reaction mechanisms in the reactive bed. Faster kinetics can lead to a rapid release of heat, thus enhancing the temperature lift from the reactor, as well as the thermal power output [62,63]. The effective reactivity of the TCM highly relies on the ability to transfer heat and reactants from or to the reaction sites, depending on whether the charging or discharging process is considered. Consequently, besides selecting a proper TCM, the achieved temperature lift is influenced

by the operating conditions and the TCS device configuration. Concerning the reviewed prototypes, the maximum temperature lift is depicted in Figure 2.8 (b) as a function of the discharging temperature. Overall, the maximum temperature lift reduces with the discharge temperature, although a clear trend is hard to establish from the reported results due to the vast range of tested operating conditions and selected materials.

Despite the promising results reported above, a consistent gap exists between the measured performance and the theoretical maximum values. As also reported by Liu et al. [64], a 50% reduction between the material energy density, E_{TCM}, and the measured reactor energy density, $E_{r,}$ was observed in the literature. Such a discrepancy can also be observed in Figure 2.9 for the prototypes reviewed. Furthermore, such a performance gap was measured regardless of the prototype size. For example, for a laboratory-scale reactor employing 0.2 kg of MgSO4-zeolite composite, Hongois et al. [53] measured a 55% reduction. That is, fundamental insights into TCS reactors' operation and performance enhancements are still required.

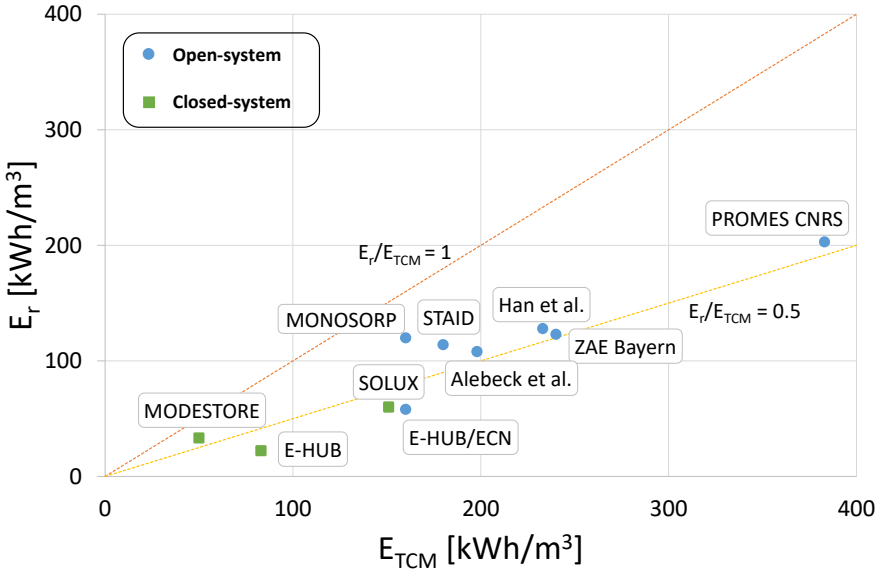

Figure 2.9 Reactor energy density versus material energy density for the main TCS reactor prototypes reported in the literature. The reviewed prototypes are labelled according to Table 2.4.

Table 2.4 Performance metrics for the main prototypes (m_{TCM} > 20 kg) reported in the literature.

Project /authors	TCM	System type	m_{TCM} [kg]	E_{TCM} [kWh/m³]	E_r [kWh/m³]	P_{max} [W/kg]	P_{avg} [W/kg]	T_{charg} [K]	T_{disch} [K]	Max ΔT [K]	Ref.
ZAE Bayern	Zeolite 13X	Open	14000	240	123	17.5	11.1	130	60	-	[52]
PROMES CNRS	$SrBr_2$	Open	400	383	203	2.0	0.75 - 2	80	25	10.0	[29]
MODESTORE	Silica gel	Closed	200	50	33.3	19.5	5.0	88	40	5.0	[53]
SOLUX	EG-$SrBr_2$	Closed	187	151	60	64.2	13.4 - 21.4	80	35	-	[40]
Alebeck et al.	Zeolite 13X	Open	170	198	108	21.2	4.7	190	10	20.0	[54,55]
E-HUB/ECN	Zeolite 13X	Open	150	160	58	2.7	-	185	40	30.0	[56]
STAID	Zeolite 13X	Open	80	180	114	28.1	27.5	180	20	37.5	[57]
MONOSORP	Zeolite 4A	Open	70	160	120	21.4	21.0	170	20	22.0	[58]
Aydin et al.	Vermiculite-$CaCl_2$	Open	70	-	39 - 123	13.6	9.6	80	20	41.2	[61]
E-HUB	Zeolite 5A	Closed	41	83	22.2	24.0	20.0	103	20	32.5	[59]
Han et al.	Zeolite 13X	Open	20	233	128	-	64.0	180	25	10.0	[60]

2.5.1 Key design challenges

Several practical issues must be addressed before successfully commercialising TCS devices [15]. The lack of satisfactory performance observed in the previous section was attributed in the literature to several technical design challenges, as summarized in Table 2.5. These design challenges are grouped in this section into cost, cycling stability, corrosion, power output control, and heat and mass transfer enhancement.

Table 2.5 Design challenges and specific solutions adopted in the literature.

Design challenge	***Solutions***
Cost	• Cheaper materials and production processes • Optimization of operation and configuration
Cycling stability	• Use of composite TCMs • Selection of suitable operating conditions
Corrosion	• Use of composite TCMs • Selection of suitable containment materials • Coating techniques
Control of power output	• Modular reactor configuration • Dynamic operating conditions
Heat transfer enhancement	• Composite TCMs with enhanced properties • Effective configuration of the reactor • Extended surfaces
Mass transfer enhancement	• Composite TCMs with enhanced properties • Effective configuration of the reactor • Gas reactant diffusers

The high investment cost still hampers the commercialization of TCS technologies. Despite its improved performance indeed, Scapino et al. [26] calculated an energy production cost from TCS systems up to 10 times larger than for sensible heat storage systems. This cost increase is mainly due to the TCMs costs, which can vary from 80 €/t ($MgSO_4$) to 2400 €/t ($SrBr_2$), as reported by Palacios et al. [65]. Nonetheless, Stengler et al. [66] stated that the current production process of TCMs on a large industrial scale is not yet optimized and costs may reduce drastically with increasing usage. For example, Gilles et al. [67] investigated an alternative and cost-efficient synthesis pathway to reduce the production cost of Strontium Bromide, and also discussed the carbon footprint of strontium bromide when used for low-temperature energy storage (<100 °C).

The thermal outputs of TCS reactors were reported to degrade along the charging/discharging cycles [29]. Examples of stability problems are material coagulation and pulverization [68]. In particular, the material coagulation is induced by the undesired contact with liquid water or the TCM melting at local hot spots. Therefore, it is crucial to ensure local temperatures in the reactive bed are below critical values. This can be achieved through the effective configuration of the device, for example ensuring optimal cooling of the reactive bed [31], as well as by selecting suitable operating conditions. In particular, dynamic operating conditions strategies can be implemented to mitigate the thermal effect of faster reaction rates during the initial stages of the hydration process so that more stable and controlled temperatures can be obtained [69].

Side reactions can produce by-products that cause the containment materials' corrosion [26]. As an example, for TCS systems employing sodium sulphide, H_2S can be produced [68]. The dissolution of H_2S into liquid water causes the corrosion of typical commercial

containment metals and the formation of H_2. To prevent this effect, corrosion-resistant coatings are adopted [68]. Besides, Solé et al. [70] tested the corrosion rates for copper, aluminium, stainless steel 316L and carbon steel with four salt hydrates: $CaCl_2$, Na_2S, $MgSO_4$ and $MgCl_2$. The immersion tests were performed at conditions aimed at replicating the operation of open systems: batch temperature of 60 °C and humidity at 99%. The results indicated stainless steel 316L as suitable containment material for each selected TCMs.

In the instance of constant operating conditions, TCS devices present a thermal power output decreasing in time due to the reduced reaction rate [61]. This undesired trend was mitigated in the literature by the use of modular configurations [71]. In modular configurations, the storage material is located in several smaller reactors with volume and shape optimized according to the system requirements. One main advantage is that an increase/reduction of the number of modules to match larger-scale demands requires low technical efforts. Similarly, the size of the modules can be modified to match different thermal power output needs.

Control strategies for the gas reactant flow have been presented with the same finality of controlling the thermal power output. Bürger and Linder [72] developed analytical expressions to describe the operational regimes of a plate-type reactor. Thus, numerical simulations were adopted to predict the behaviour of the TCS device for variable gas flow rates. These variable gas flow rates cause significantly different temperature profiles in the reactive bed and, thus, variable power output from the reactor. Similarly, in one of our previous studies, Humbert et al. [69] presented a numerical strategy to identify dynamic gas flow rates to ensure constant thermal power output from a TCS device. The results demonstrated the targeted constant thermal power output to be maintained for +20% of

the discharge time compared to operations at a constant gas flow rate. This result was achieved by incrementing the gas reactant flow in time from a minimum value to a maximum one, dictated by the deliquescence conditions for the investigated TCM. Besides, the targeted power output could be obtained for larger fraction of the discharge time in the instances of optimized reactor designs compared to non-optimized geometries.

Concerning the heat and mass transfer enhancement in the reactive beds instead, several routes have been explored in the literature to improve the reactor performance and reduce the gap with the expected theoretical values. A large fraction of this literature has been devoted to tailoring the material properties through the realization of composite TCMs [28,73,74]. However, while these materials can successfully reduce hydrothermal instabilities and achieve acceptable energy densities [26], their enhanced thermos-physical properties are often inadequate to achieve satisfactory performance for the reactor operation. In this regard, Stengler et al. [75] performed a numerical sensitivity analysis for a TCS device utilizing extended surface geometries. The results showed the extended surface geometry to effectively mitigate the low thermal conductivity of the reactive bed and that a further increase of the bulk thermal conductivity would have a negligible impact on the device's overall performance.

This dissertation explores the reconfiguration of the TCS reactor as an effective and straightforward way to enhance system performance. Overall, there is a large consensus in the literature about the need to effectively configure a TCS device to exploit the storage material fully [13,47,76]. The primary goal of the reactor geometry is the optimal transfer of heat and reactants from/to the reactive sites. However, only limited and partial attempts have been reported in the literature to define guidelines on the effective reactor

configuration [77]. Besides, the intertwined multi-physical phenomena that govern a TCS system's overall performance make the optimal design of these devices challenging [78,79]. The following sections review the state-of-the-art TCS reactors' geometrical configurations and the existing attempts to identify the geometrical features that maximize performance.

2.6 Geometrical configurations of open system TCS reactors

An overview of the main geometrical configurations adopted in the literature for open system TCS reactors is reported in Figure 2.10. Each configuration is modular, thus only a single module is shown to represent the whole reactor concept. Besides ease of implementation and scalability, modular configurations can also ensure reduced pressure drops in the reactive beds. In fact, shorter gas reactant paths in the porous medium can be achieved, with a consequent reduction in the energy consumed by the auxiliary components. The following sections review the experimental and numerical findings regarding cylindrical, radial, rectangular and sieve reactors. Furthermore, additional and unique configurations that do not belong to the types listed before are discussed.

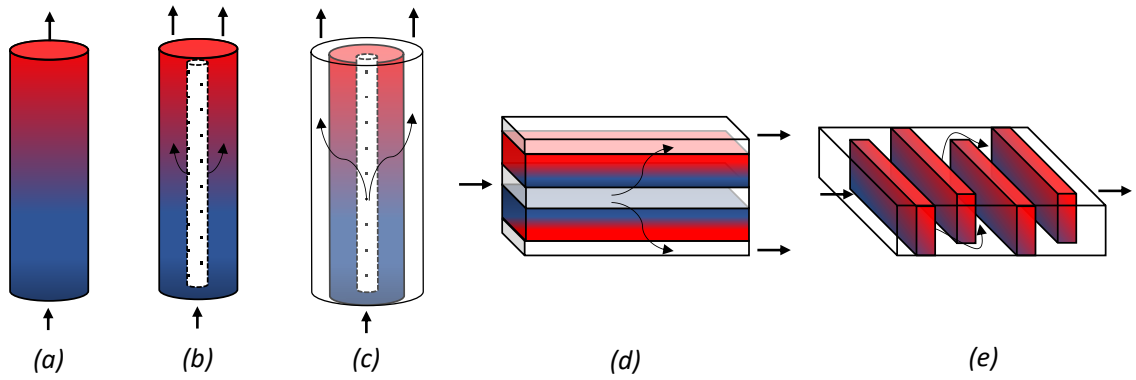

Figure 2.10 Simplified schematics for the open system TCS reactor configurations adopted in the literature: (a) cylindrical reactor, (b) cylindrical rector employing a diffuser, (c) radial reactor, (d) rectangular reactor, (e) sieve reactor.

2.6.1 Cylindrical reactors

Due to their ease of manufacturability, cylindrical reactors are the most investigated configurations, especially for laboratory-scale testing [80–82]. For example, Clark et al. [83] tested the performance of a cylindrical reactor filled with $SrCl_2$. The goal was to demonstrate the feasibility of the proposed TCM in the context of heating for building applications. The results demonstrated that $SrCl_2$ impregnated in a cement matrix led to satisfactory densities at a suitable regeneration temperature of 90°C. A cylindrical reactor was also tested by Gaeini et al. [84]. In this study, a series of experimental tests for a 62.5 L unit using zeolite 13X were conducted with the aim of validating a 2D axisymmetric numerical model. Radial effects due to flow maldistribution and heat losses were studied. Besides, the optimal aspect ratio, defined as the ratio between diameter over height, was found as 1.5. In a similar fashion, Li et al. [85] numerically studied the effect of non-uniform porosity. Different TCMs were considered in cascading storage sub-units. The non-uniform porosity facilitates the conversion near the reactor walls, and the proposed cascade concept was proven as an effective solution in the context of low-temperature TCS systems.

However, for scaled-up designs entailing longer units, the required large pressure drops make cylindrical reactors unattractive [86]. Nevertheless, mass transfer limitations can be attenuated by air diffusers [61]. Michel et al. [87] measured the use of a gas diffuser to lead to an effective permeability increase of up to +70% compared to a reactive bed without diffusers. Benefits were also reported in terms of specific power, +12.5%. Similarly, Aydin et al. [61] tested the geometrical configuration depicted in Figure 2.11. The concept entails a perforated diffuser pipe with a 0.05 m diameter in a cylindrical reactor with an outer diameter equal to 0.2 m. Vermiculite-$CaCl_2$ composites were considered under different inlet

air humidity levels. A fourfold increase in absolute humidity was tested to lead to a 2.3 times increase in the average power output. Higher exergy and energy efficiencies were measured for the operation of the proposed composite TCM compared to zeolite 13X due to the reduced required charging temperature. However, no comparisons were made with other reactor configurations, making it hard to quantify the benefits led by the selected geometry.

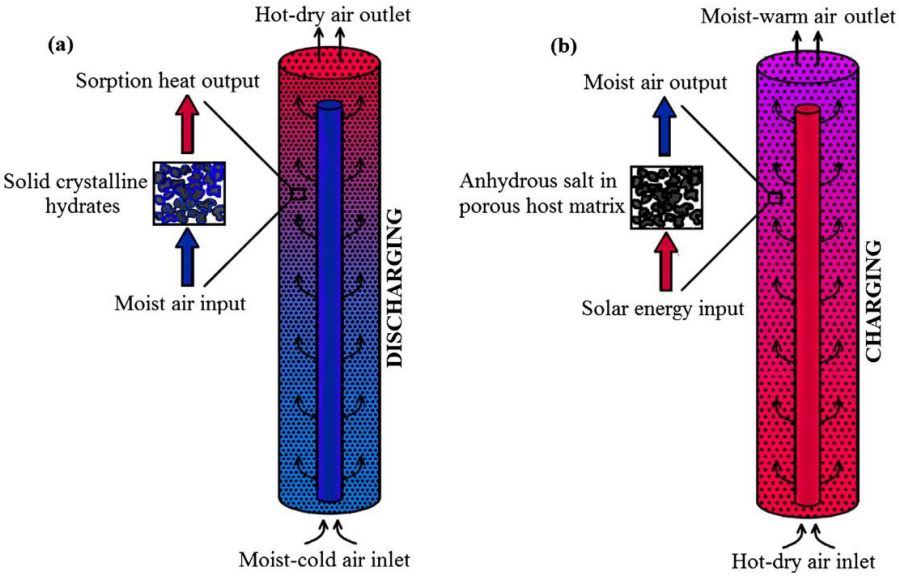

Figure 2.11 Operating principle of the TCS device proposed by Aydin et al. [61]: (a) discharging process and (b) charging process.

Hawwash et al. [88] compared the performance of cylindrical reactors and truncated cones with variable aspect ratios, defined as the ratio between outlet and inlet areas, as depicted in Figure 2.12. Magnesium chloride hexahydrate, $MgCl_2 \cdot 6H_2O$, was selected as reference TCM, with the amount of storage material fixed for all the investigated designs. Shorter charging times were encountered for small aspect ratios at the expense of an increased pressure drop. The minimum desorption time was predicted for conical reactors with a 0.17 aspect ratio, and the reported results indicated the power output peak to be flattened by

the selected geometrical parameters. This aspect is overlooked by the authors but might lead to interesting insights for generating reactors with constant power outputs in time.

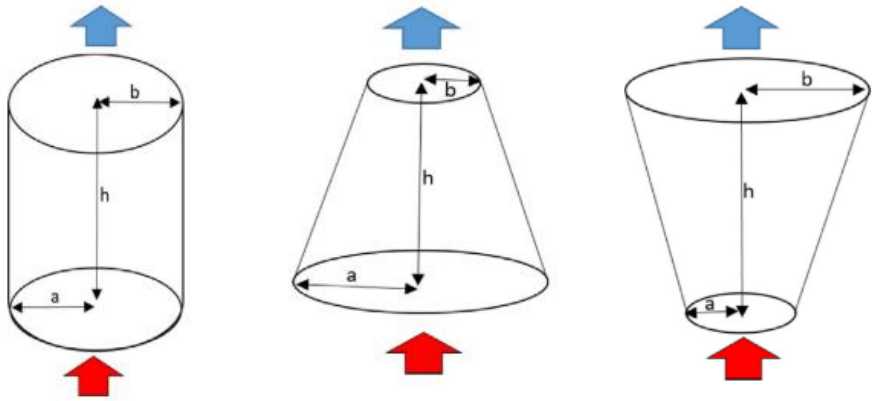

Figure 2.12 Geometrical configurations investigated by Hawwash et al. [88]**.**

2.6.2 Radial reactors

With the aim of mitigating the mass transfer resistance effects, radial reactors have been proposed and investigated by Krönauera et al. [89] for a 14 tons storage adopting zeolite 13X. The reactor, depicted in Figure 2.13, was charged using industrial waste heat at 130°C, and the stored energy was delivered 7 km away from the charging station. A storage capacity of 2.3 MWh was reached, leading to 616 kg of saved carbon dioxide per cycle. However, the flow misdistribution through the reactive bed precluded the desired power output, indicating the need for a more in-depth analysis of the effective configuration of radial TCS reactors, similarly to what was already done in the context of sensible heat storage devices by McTigue et al. [90].

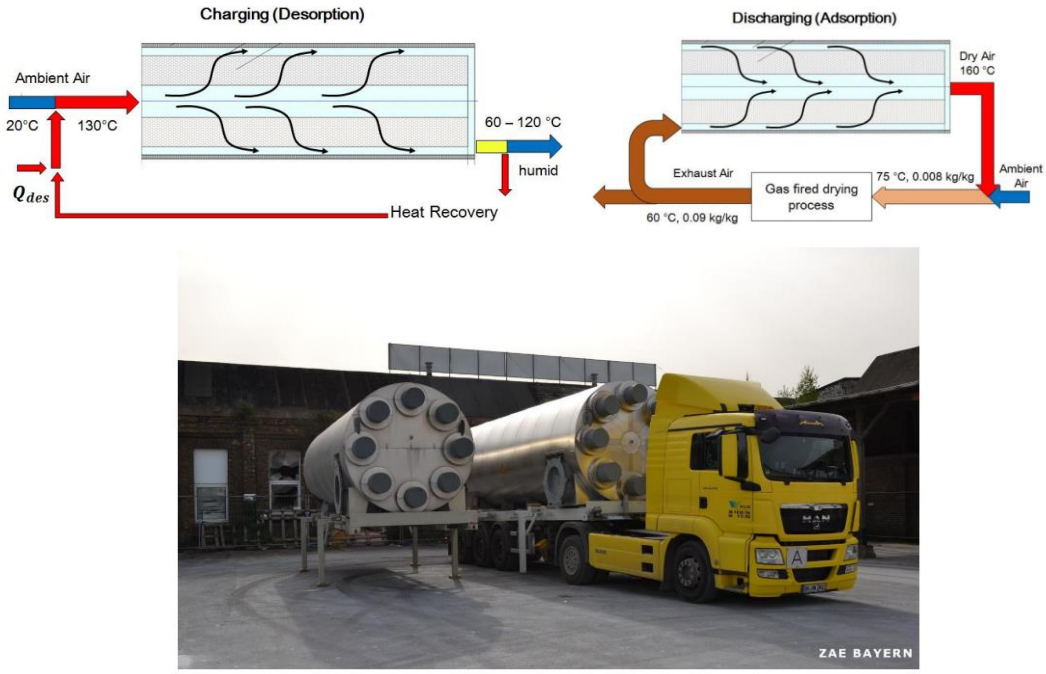

Figure 2.13 Radial reactor concept tested by Krönauera et al. [89]***: top for the schematics of the charging and discharging processes, bottom for the mobile TCS at the discharging station.***

2.6.3 Rectangular reactors

According to Aydin et al. [38], rectangular configurations present a series of advantages: (i) limited pressure drop in the reactor, (ii) ease of scalability by increasing the number of segments and (iii) simple manufacturing. In fact, rectangular reactors are a popular choice for large-scale testing reactors. For example, Michel et al. [29] tested a 105 kWh storage unit employing $SrBr_2 \cdot 6H_2O$ in the context of long-term storage for domestic applications. The adopted geometry is depicted in Figure 2.14. The rectangular configuration was adopted to ensure a simple and cheap storage unit, with the mass transfer limitations mitigated by selecting a small reactive bed height. Promising results with rectangular reactors were also obtained by Alebeek et al. [54]. Here, a 0.5 m^3 reactor employing Zeolite 13X was tested in the context of domestic heating applications. The intent was to design a high-power density device. The reactor segments were configured to reduce the pressure drop in the system

and the response time, i.e. charging and discharging times. A maximum delivered power of 4.4 kW was measured, with a thermal efficiency of 76%. However, the authors noticed a non-uniform flow in the reactive bed leading to a heterogeneous temperature outlet profile. Overall, such a result negatively impacted the system's thermal performance; thus, further studies were recommended to maximize performance.

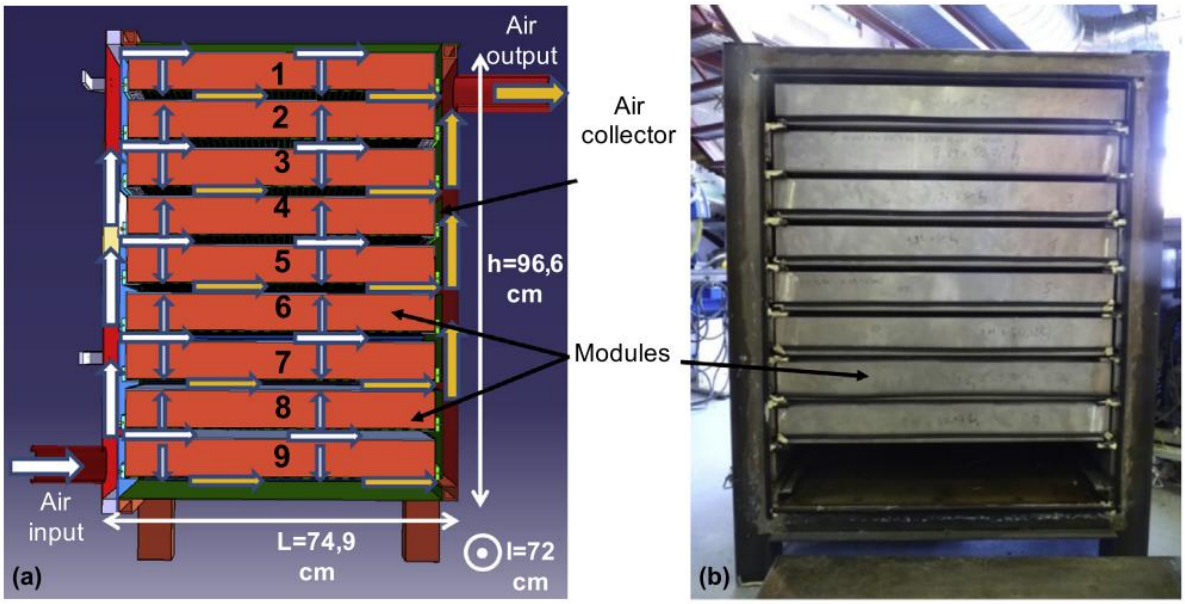

Figure 2.14 Rectangular reactor prototype from Michel et al. [29]: (a) schematic of the vertical section; (b) picture of the prototype without insulation.

Numerical studies are reported in the literature aimed at improving reactor performance through the variation of geometrical variables. Malley-Ernewein et al. [91] studied a rectangular reactor using constructal theory [92]. The results exhibited an increase in the number of salt layers to benefit the overall system performance. Besides, a height-over-width ratio of 1.6 was identified as optimal. Mukherjee et al. [93] studied the influence of the bed porosity and geometrical variables on the ratio between extracted thermal power and power consumption instead. A 19% porosity reduction decreased such a ratio by 64%,

while a height-over-length value of 0.5 was predicted to increase the performance metric by 6.2 times.

A variation of the conventional rectangular configuration depicted in Figure 2.10 was proposed by Weber et al. [71] in the framework of the SolSpace project. The proposed storage concept consisted of several segments that provided constant power output in time. A total of four quadrants were considered, with each quadrant subdivided into six segments, as depicted in Figure 2.15. The airflow entered a central duct and exited the device from one of the four vertical edges. The reactive layers were tilted to favour a homogeneous air mass transfer. However, as shown in Figure 2.15, the velocity field was predicted to be slightly higher in the regions with reduced bed height. Nevertheless, despite the slightly inhomogeneous fluid flow, a satisfactory average outlet temperature was maintained over the entire discharge process.

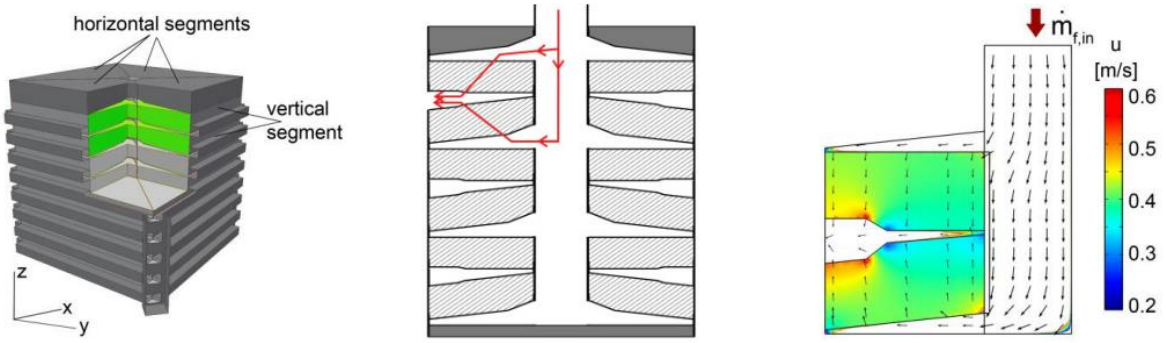

Figure 2.15 Schematic views of the segmented TCS device proposed by Weber et al. [71,94]***: left for isometric view, centre for vertical cross-section, right for the predicted velocity field in the vertical cross-section.***

In contrast with the studies reported above, Han et al. [60] investigated an open system configuration where thermal energy was transferred to water transported in pipes crossing the reactive bed. The conventional rectangular configuration was modified in trapezoidal containers with gaps on both sides, as depicted in Figure 2.16. The adopted trapezoidal

geometry was selected to provide airflow paths sideways to the reactive bed and represent a unique solution in the context of open system TCS reactors. However, no studies are reported in the literature to assess the eventual benefits of this geometrical solution. Zeolite 13X was used as TCM, with 5 kg of material employed in each container. Copper fins enhanced the heat transfer from the reactive bed to the HTF, i.e. water inside the pipes. The results showed a charging time reduction of 0.75 h compared to a configuration without copper fins. Besides, a higher discharge temperature of +2 °C was achieved.

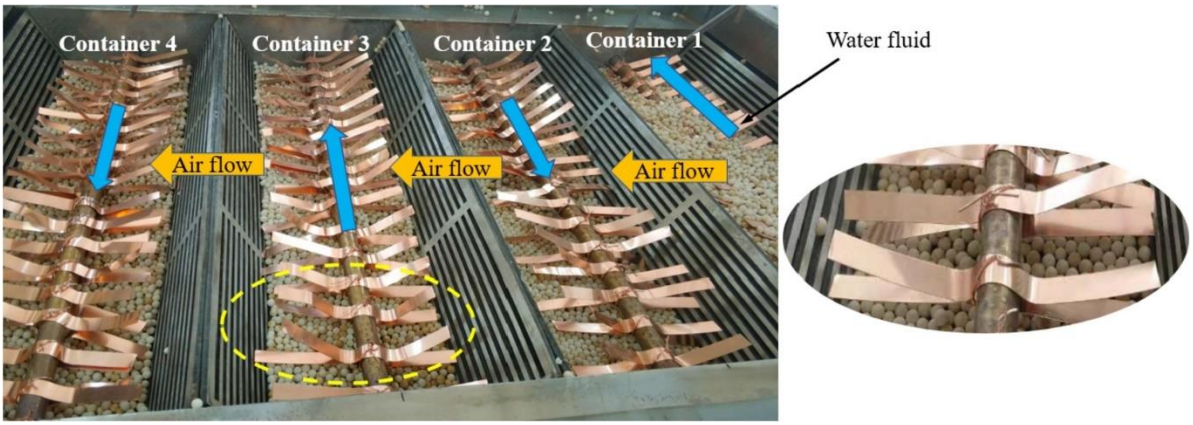

Figure 2.16 Picture of the reactor configuration tested by Han et al. [60].

2.6.4 Sieve reactors

In the context of TCS devices, sieve reactors were first proposed by Chen et al. [95]. Blocks of TCM are located in the reactor, with the TCM contained in a perforated grid to allow the airflow to permeate. The space between these blocks allows the airflow circulation at a negligible pressure drop and was referred to as flow channels. As an additional advantage, using separate TCM regions mitigate deliquescence issues. The geometrical configuration proposed in [95] is reported in Figure 2.17, with a spiral flow channel connecting inlet and outlet interfaces. The reactive porous bed was made of $MgCl_2 \cdot 6H_2O$, and the effects of several geometric parameters on the thermal performance were studied. The increase in

the plate numbers and length led to a reduction in the charging time, and a final configuration adopting six sieve plates and a ratio between plate length and thickness of 30 was selected. The authors concluded that the proposed geometry facilitates the mass transfer in the reactor, although no quantitative comparison with other geometrical configurations was reported.

Sieve reactors were also investigated by Li et al. [96], with strontium bromide hexahydrate as thermochemical material. From a reference case considering uniform TCM blocks dimension, the upper blocks, i.e. away from the airflow inlet, were under-utilized due to the flow maldistribution. Non-uniform TCM block dimensions were thus analysed. Considering fixed distance between blocks, a 2.4% charging time reduction was achieved for increased bed lengths from the top to the bottom of the reactor. Besides, the distance between each reactive bed was shortened from 2 cm to 1 cm, and a further reduction in the charging time of 11.4% was obtained. However, despite the promising results reported above, to the best of the author's knowledge, no experimental studies of sieve reactors are reported in the literature.

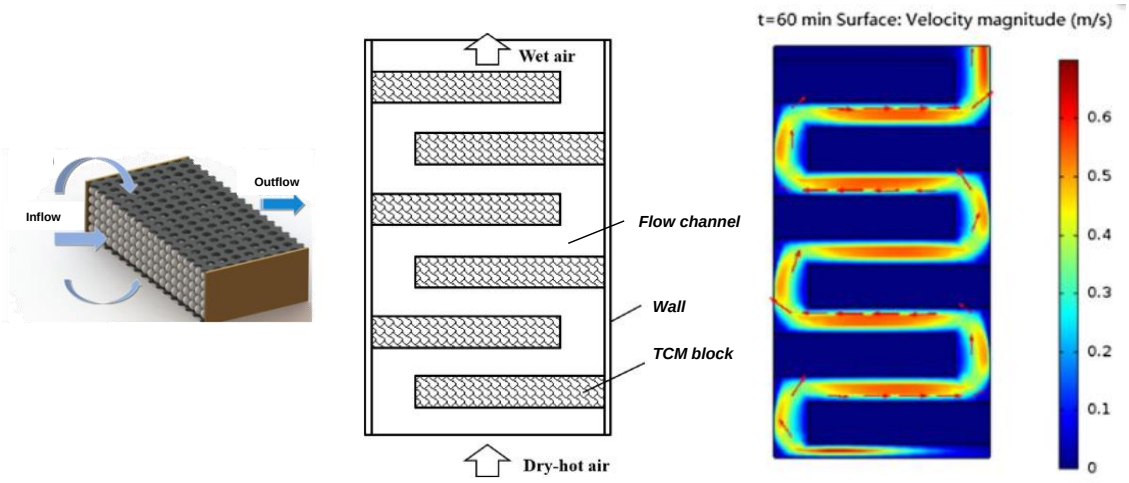

(a) *(b)* *(c)*

Figure 2.17 (a) sieve reactor concept [96]***; (b) geometrical configuration proposed by Chen et al.*** [95]***; (c) flow field*** [95]***.***

2.6.5 Additional configurations

In addition to the main geometrical configurations examined above, recent studies focused on manufacturing the TCM structure to promote mass transfer. In the framework of the MonoSorp project, Bales et al. [58] developed a modular reactor concept employing 70 kg of 4A zeolite. An innovative geometry was proposed consisting of honeycomb structures called 'monoliths', as depicted in Figure 2.18. A series of small straight diffuser channels were thus used to distribute the sorbate in the TCM. The main advantage of this configuration was the limited pressure loss, and better adsorption properties were measured compared to conventional reactors employing fills. An additional advantage of this geometrical configuration is its simple and flexible design. The block-shaped monoliths can indeed be configured in any shape, depending on the available volume. In a similar fashion, Liu et al. [97] tested a honeycomb reactor with a mesoporous Wakkanai Siliceous Shale (WSS)-22.4 $_{wt.}$% $CaCl_2$. A relatively high heat extraction, 65%, was measured for a 926

g of storage material. The monolith cross-section measured 0.01 m^2, with a wall thickness for each cubic cell of 0.28 mm.

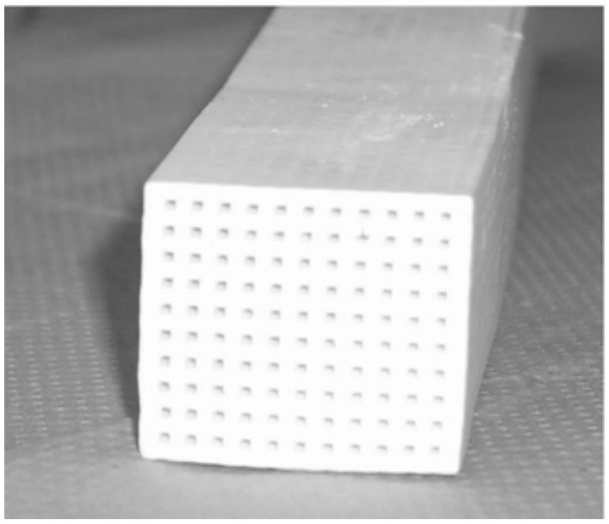

Figure 2.18 Monolith structures tested in the MonoSorp project [58].

2.7 Geometrical configurations of closed system TCS reactors

In closed-system TCS reactors, three key areas can be distinguished dedicated to HTF, gas diffuser and TCM. A straightforward configuration for TCS reactors in closed mode is the use of rectangular modules. An example of this configuration is the storage unit proposed by Mauran et al. [35]. Here, the stacking of several modules was considered, and each module consisted of a plate exchanger inserted between two layers of TCM and two diffusers, as depicted in Figure 2.19. The design had the advantages of large exchange and diffuser surfaces and simple extrapolation of thermal performance for a scaled-up unit. However, a small bed over reactor volumes ratio was obtained, around 0.53, which was dictated by the small reactive bed height adopted in the unit. The storage unit led to thermal power outputs in the range of 2.5 – 4 kW, although the system was designed to react from a heat-transfer point of view to react at a peak power of 10 kW. Further analysis elucidated that although

graphite inserts were used, the expected heat transfer coefficient was not reached due to interfacial thermal resistance between TCM and the heat exchanger.

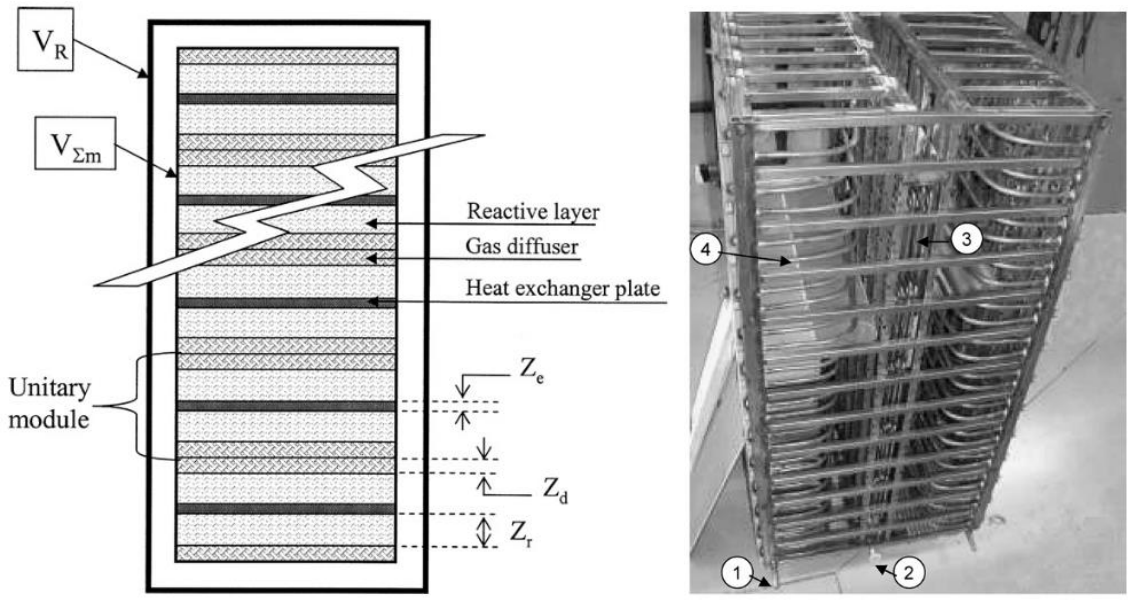

Figure 2.19 Rectangular reactor proposed by Mauran et al. [40]: (a) Vertical cross-section; (b) Photograph of the prototype with focus on (1) Inlet collector of the coolant, (2) outlet of the pouring water at (3) the bottom of the evaporator/condenser and (4) tube connection to a plate exchanger.

In fact, research suggests that heat transfer is the dominant limiting factor for TCS devices in closed mode [31]. Consequently, extended surfaces made of highly conductive materials (HCM), such as aluminium, steel, or copper [98], are often considered to enhance the heat transfer in the reactive bed. Extended surfaces have been extensively applied in technologies such as adsorption chillers and heat pumps [99], from which relevant insight can be transferred to the design of TCS devices.

The heat transfer enhancement effect led by extended surfaces increases with the surface area and thus with the amount of HCM employed. However, using a larger amount of HCM entails a reduced volume devoted to the storage material. Consequently, significant focus is

placed in the literature on identifying optimized extended surface geometries that can guarantee satisfactory performance with a limited amount of HCM [100].

The extended surface configuration becomes increasingly important in case of poor heat transfer coefficient at the bulk/heat exchanger interface [101,102]. This interfacial heat transfer coefficient depends on the TCM particle size [103] and is subject to change during the hydration and dehydration processes. Besides, it might also vary across the storage lifetime due to undesired phenomena such as agglomeration and shrinking [75]. However, no standardized correlations are reported in the literature for quantifying such a coefficient, and the data reported appear inconsistent. For example, Lahmidi et al. [47] analysed an $SrBr_2 \cdot 6H_2O$ reactive bed and assumed a 1000 $W/m^2/K$ value. The analysis highlighted that the TCM/heat exchanger wall resistance was negligible for the overall reactor performance. Contrarily, through the comparison of numerical and experimental results for an $SrBr_2 \cdot 1H_2O$ reactive bed, Stengler et al. [31] reported an interfacial heat transfer coefficient in the range from 30 to 45 $W/m^2/K$. Such thermal resistance was also identified as the most significant limitation to the storage maximum thermal power output. Overall, it remains unclear from the literature to what extent the heat transfer coefficient at the TCM/heat exchanger interface influences the overall system performance.

For low-pressure regimes, the gas reactants transfer in the reactive bed can penalize the reactor performance. In the instance of a sorption heat pump employing $MnCl_2$, Stitou et al. [104] reported mass transfer as the key limiting factor for the desorption process, operated at a vacuum pressure below 70 mbar. In this regard, only marginal attempts have been made to overcome coupled heat and mass transfer limitations in reactive beds, such as the one proposed by Neveu et al. [105]. Here, the authors employed a second-law based design

method to show how conductive fins and networks of gas diffusers could comprehensively enhance the performance of the thermochemical storage system.

The main geometrical configurations of extended surfaces adopted in TCS reactors are summarized in Figure 2.20. The numerical and experimental studies carried out for each of the depicted configurations are reviewed in the following sections.

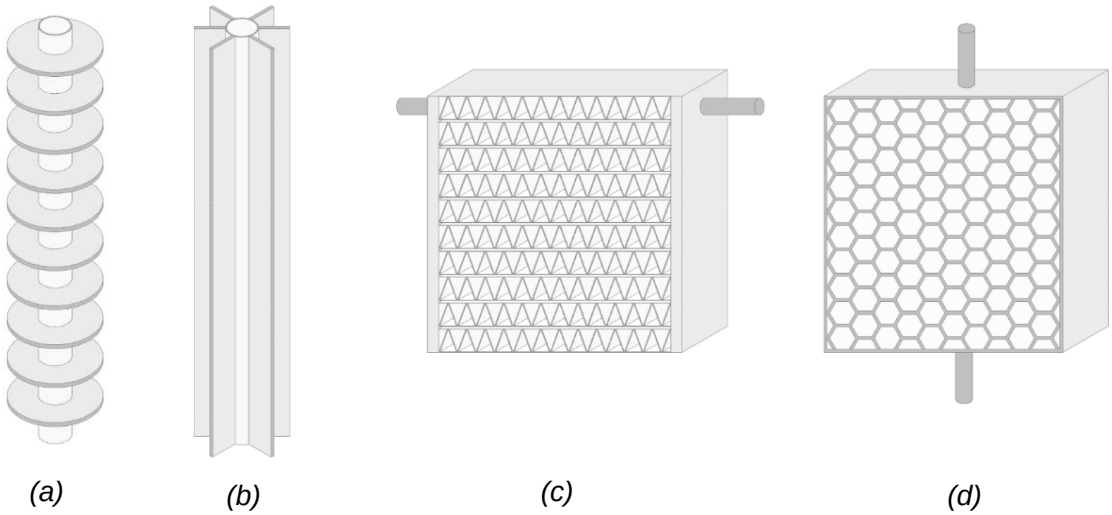

Figure 2.20 Main geometrical configurations for extended surfaces in closed system TCS reactors [98]***: (a) annular fins; (b) longitudinal fins; (c) plate-fin; (d) honeycomb structure.***

2.7.1 Annular fins

Due to their ease of manufacturability, annular fins are one of the most adopted configurations. In the instance of a silica gel reactive bed, Mitra et al. [106] studied the performance of an annular fin reactor for variable fin pitch and height and considered two different particle sizes. Shorter fins with a larger spacing were observed to lead to maximum performance in the case of low particle size, 30 μm, while longer fins with a smaller pitch were favourable in the case of large particle size, 70 μm. The effect of the particle size on the optimal annular fins size was also analysed by Niazmand et al. [107]. Here, different fins

spacing and operating conditions were considered and maximized performance was obtained for the particle size range of 20-30 μm.

In a similar fashion, Niazmand et al. [108] developed a three-dimensional numerical model considering inter-particle and intra-particle mass transfer resistance in a silica gel reactive bed. A parametric study was performed to identify the appropriate fins geometry. For the range of geometrical parameters explored, a $3 \cdot 10^{-3}\ m$ fins spacing was predicted to maximize the specific cooling power. Besides, the neglection of the TCM/HCM interfacial thermal resistance led to significant errors in the predicted performance.

Furthermore, as shown in Figure 2.21, Golparvar et al. [109] developed a detailed three-dimensional model to predict the dynamic response of a reactive bed filled with zeolite 13X in the context of adsorption cooling systems. Annular and longitudinal fins were considered in the study, and the fins' height and spacing were varied to identify the optimal configurations. Overall, reducing the fins spacing decreased the coefficient of performance while increasing the specific cooling power. Besides, as a side-effect, the fins spacing reduction also caused undesirable re-sorption of material particles located in the regions of the system with lower temperatures. The results showed that annular finned tubes outperformed longitudinal ones for similar dimensions and operating conditions. A 10% higher total cooling power was indeed predicted. In addition, the authors estimated using optimized configurations to save about 370 L of fuel per annum, with a consequent decrease in greenhouse emissions of 738 kg_{CO_2}.

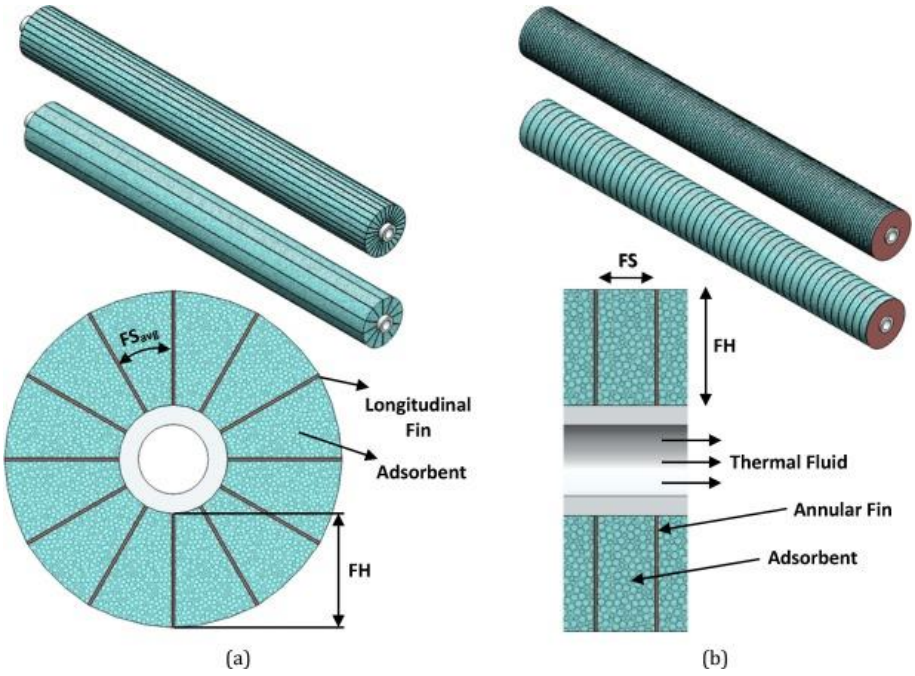

Figure 2.21 Finned tubes investigated by Golparvar et al. [109] ***: (a) longitudinal fins, (b) annular fins.***

2.7.2 Longitudinal fins

The potential of straight longitudinal fin insertions in TCS reactive beds was studied by Ranjha et al. [110]. A total of six radial fins elongating from the HTF pipe wall were used. Two reactor configurations were analysed: a first configuration where the HTF flows through the outer annular shell and a second configuration where the HTF flows in a central pipe. The results demonstrated the first configuration, i.e. HTF on the outer shell, as the best performing solution. A more complex fins architecture was proposed and tested by Stengler et al. [31], as shown in Figure 2.22. The adopted geometry was inspired by the design guidelines for pure heat conduction problems from constructal theory [92] and topology optimization [111], from which tree-shaped fin structures are advised to boost heat transfer. A relatively large packing factor, 17%, was adopted to pursue a high power density device. The reactive bed was filled with monohydrate strontium bromide, and the device functioning as a heat transformer was investigated. The reported results demonstrated the

temperature lift to be adjustable through the steam pressure variation and thus demonstrated the proposed device as a suitable solution for various industrial applications. For instance, the storage was charged at 180°C and 1 kPa steam pressure and discharged at 280°C and 560 kPa.

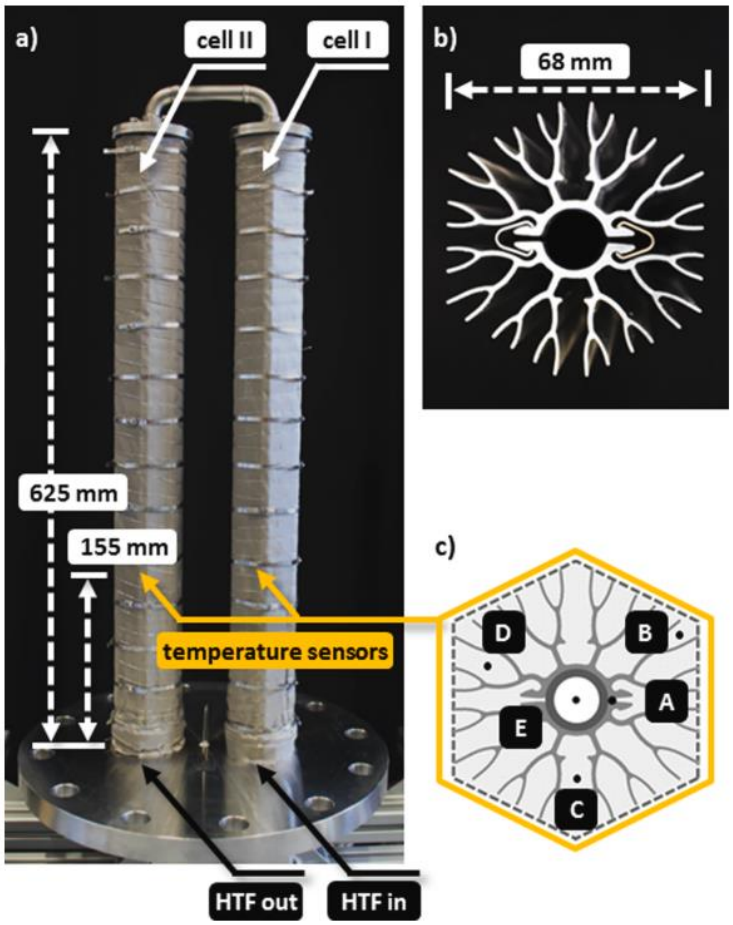

Figure 2.22 TCS device prototype tested by Stengler et al. [31]: (a) laboratory-scale module containing 4.7 kg of storage material; (b) cross-section of the aluminium branched fins, and (c) positions of the temperature sensors.

In a follow-up study, Stengler et al. [75] combined numerical and experimental analysis to demonstrate their proposed branched fins design to effectively mitigate the low bulk thermal conductivity. In fact, poor performance enhancement (+3%) /was predicted for a further 100% increase in the bulk thermal conductivity. However, the analysis also showed

the importance of the interfacial resistances at the TCM-fins boundary due to mass-transfer induced swelling of the TCM material, which in turn became the primary performance limitation factor for the whole system.

Branched fins were also considered in the study presented by Kant et al. [112]. The fins length and bifurcation angles were used as design variables, as well as the packing factor, the HTF pipe size and the bed size. Optimal values were obtained so that the levelized cost of storage was minimized. Besides, a feasible design window was derived comparing the obtained performance maps with the techno-economic targets expressed by the U.S. Department of Energy Buildings Technologies Office, specifically energy storage density > 80kWh/m^3 and a storage cost below 15$/kWh.

Fernandes et al. [113] developed a dynamic model to accurately predict the thermal response of a heat storage absorber immersed in a hot water tank. A simplified schematic of the investigated system is reported in Figure 2.23. The investigated system was proposed to increase the thermal inertia and storage density of conventional hot water tank systems and thus reduce the need for thermal energy backup during operation. Silica gel was considered as TCM, and the use of fins made of copper was also considered to enhance heat transfer both for the HTF side and the reactive bed side, as summarized in Figure 2.23. A final configuration utilizing 27 internal fins and 120 external annular fins was predicted to produce a heat output 2.3 times larger than a finless adsorber. In a follow-up study [114], the proposed heat storage concept, along with evaporator and condenser units, was modelled in TRNSYS and optimized by means of the GenOpt software. The results indicated long and slender units adopting a larger number of thin fins to enhance the system performance. Similarly, thick and long condenser and evaporator units were also found to

improve the system's performance. The optimized system presented a 16% savings in the annual backup of thermal energy compared to a conventional storage system.

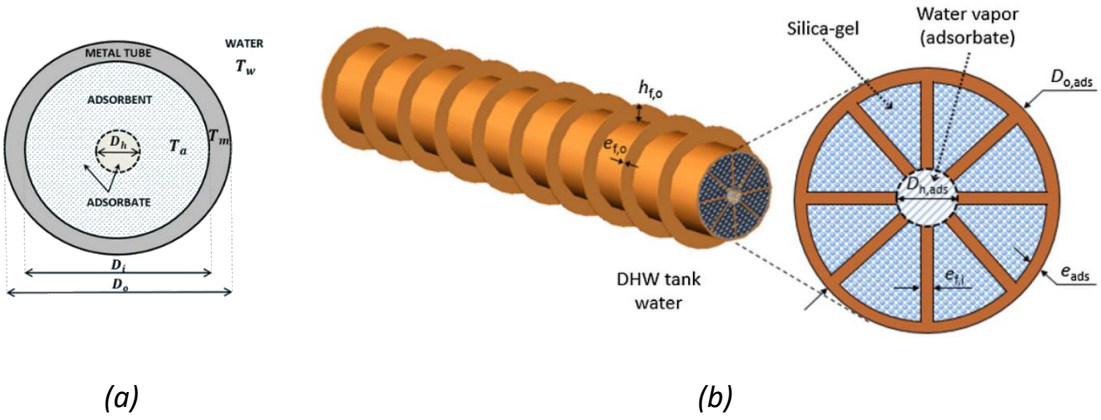

(a) *(b)*

Figure 2.23 (a) Storage device concept proposed by Fernandes et al. [113]***, (b) optimized heat storage configuration employing internal longitudinal fins and external annular fins*** [114]***.***

2.7.3 Plate-fins

In TCS devices adopting plate-fin heat exchangers, the heat is transferred between the reactive bed and the HTF through baffles so that metal plates with vast surface areas separate the two mediums. The HTF spreads over the metallic plate on one side, while fins are connected to the plate on the reactive bed side to facilitate heat transfer. In the context of adsorption cooling systems, Chang et al. [115] investigated plate-fin heat exchangers with corrugated fins to enhance the heat transfer in a silica gel bed. The tested design is reported in Figure 2.24. Under standard conditions test of 80°C hot water temperature and 30°C cooling water temperature, a specific cooling power of 176 W/kg was achieved. A further example of a plate-fin adsorption chiller is depicted in Figure 2.25 [116]. Straight fins elongating in the reactive bed from the HTF interface were adopted here. Silica gel-water was considered as working pair. The experimental results demonstrated the proposed configuration to provide a specific cooling power ranging from 75 to 276 W/kg.

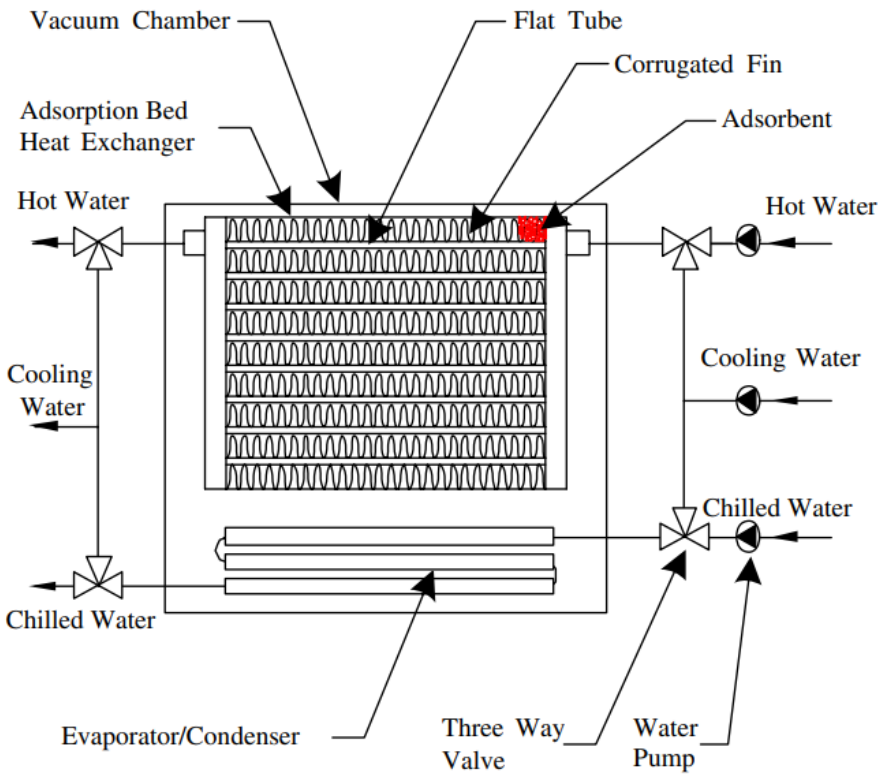

Figure 2.24 Schematic of the plate-fin adsorption chiller employing corrugated fins investigated by Chang et al. [115]***.***

Kowasari et al. [77] addressed the effective configurations of plate-fin heat exchangers through a three-dimensional model to examine how the geometrical configurations of trapezoidal aluminium fins affected the reactive bed thermal performance. The obtained performance was also compared to straight fins to identify the best performing geometrical solution. The heat transfer resistance was found to be mainly influenced by both the fin spacing and fin height, while the mass transfer resistance in the reactive bed was independently controlled through the variation of the bed height. Overall, higher specific cooling power was achieved by means of smaller bed dimensions at the expense of a lower coefficient of performance. Nevertheless, straight fins resulted in a more appropriate

solution since slightly higher specific cooling power was obtained compared to trapezoidal configurations.

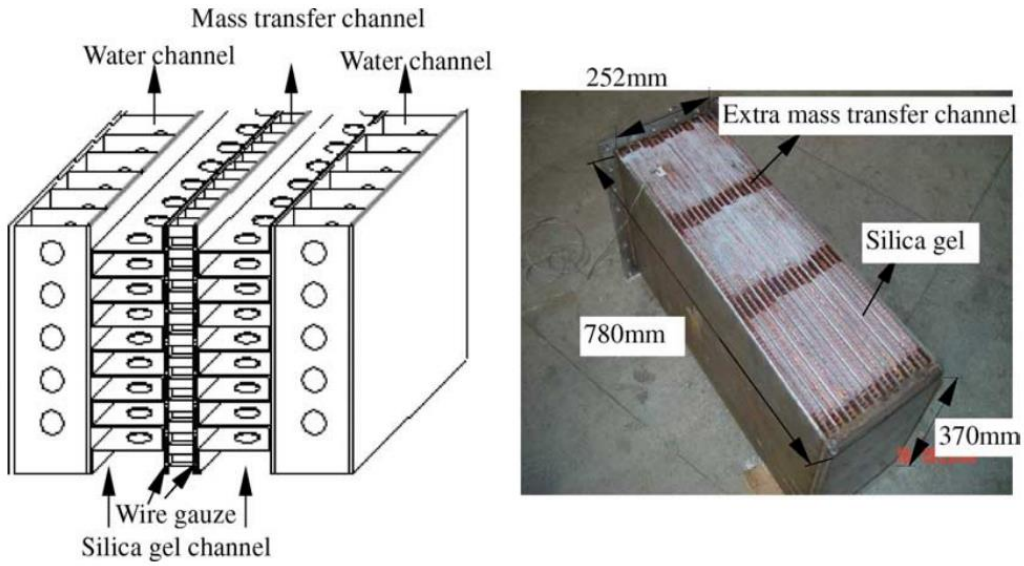

Figure 2.25 (a) Schematic of adsorber configuration employing straight fins proposed by Liu et al. [116]***; (b) picture of the adsorber.***

Similarly, Wang et al. [117] predicted and compared the thermal performance of three reactor architectures adopting extended surfaces. $Ca(OH)_2/CaO$ was considered as reference TCM, and the results exhibited plate pin fin sinks reactors to enhance the convective heat transfer in the reactive domain. In fact, a dehydration time reduction of around -33% compared to plate-fin sinks reactors was predicted. However, the hydration process was dominated by heat conduction mechanisms, and negligible performance differences were observed among the proposed reactor architectures.

2.7.4 Honeycomb structures

An example of TCS reactor employing honeycomb heat exchangers is depicted in Figure 2.26. The reported design was tested by Fopah-Lele et al. [30] and utilized 1 kg of $SrBr_2 \cdot 6H_2O$. The honeycomb structure was realized with a small wall thickness of $0.1 \cdot 10^{-3}\ m$ and a packing

factor value of only 7%. A peak for the HTF outlet temperature of 43 °C was measured, although a relatively low average outlet temperature was recorded for the tested 4 hours of discharging process. The authors attributed this limited temperature lift to the reactive bed's poor heat transfer and suggested increasing the heat exchanger surface area. An additional benefit of honeycomb configurations is the mitigation of agglomeration effects derived from separating the stored material in different compartments.

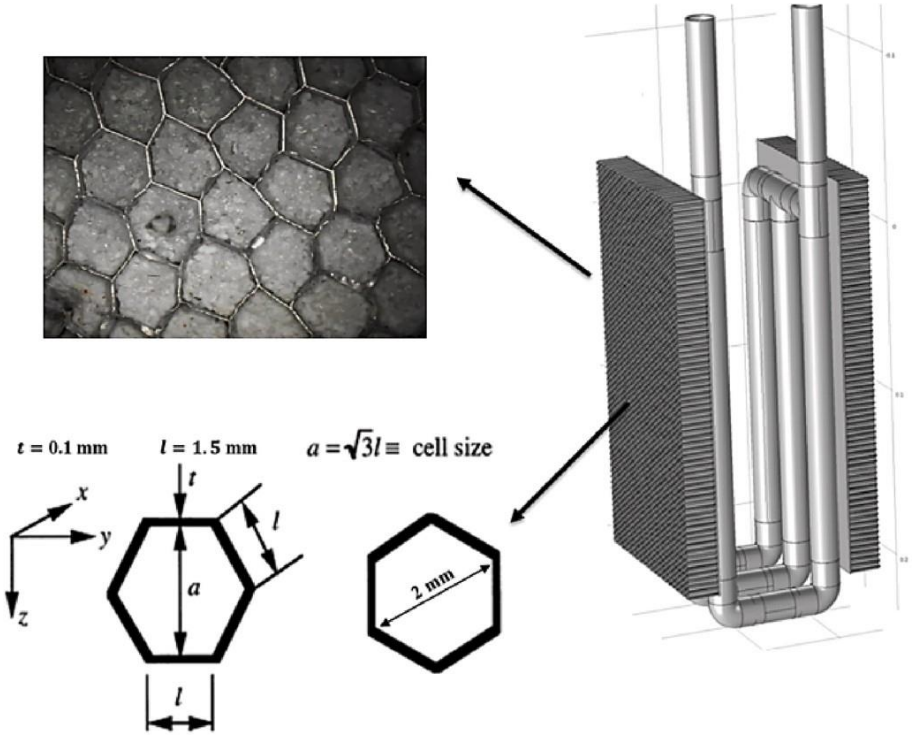

Figure 2.26 Honeycomb heat exchanger adopted by Fopah-Lele et al. [30].

In recent years, Kant et al. [118] numerically studied the performance of a honeycomb structure filled with potassium carbonate. The metallic honeycomb structure was used to connect HTF pipes located in a staggered configuration and placed in a vacuum shell. The influence of key geometrical parameters on the hydration process was analysed. The results indicated the increase in the cell height and the decrease in the wall thickness to provide

enhanced thermal transport. Besides, the maximum temperature in the reactive bed can be reduced by reducing the distance between HTF pipes.

Honeycomb structures were also included in the numerical work presented by Papakionnis et al. [98]. Here, the authors compared the thermal performance of five geometries for adsorption-packed bed reactors. For low bed porosity, i.e. highly compacted TCS material, the largest reactor power density was obtained for honeycomb structures. However, the use of radial fins was found favourable for high bed porosity.

2.8 Conclusions

This chapter introduced the working principle of TCS devices, and quantitative performance metrics were defined to assess the existing prototypes. Thus, the state-of-the-art for geometrical configurations of TCS reactors operated in open and closed modes was reviewed, along with the primary efforts to enhance the reactors' performance through device reconfiguration. The following main **knowledge gaps** were identified:

(i) Lack of use of systematic optimization tools for the performance enhancement of TCS reactors.

(ii) Lack of design guidelines for the correct positioning of extended surfaces in closed system TCS reactors.

(iii) Limited and partial attempts in the performance enhancement of open system TCS reactors.

(iv) Lack of concurrent heat and mass transfer enhancement pathways in closed system TCS reactors.

Knowledge gap (i) is addressed in the thesis through the coupling of surrogate models and topology optimization with numerical models predicting the TCS reactors' behaviours. In this way, the optimal designs generated in this thesis are tailored to specific requirements and constraints typical for TCS devices integration in energy systems. Knowledge gap (ii) led instead to the definition of the research questions **Q1** and **Q2**, reported in section 1.1. By means of the developed numerical framework, guidelines for the correct positioning of extended surfaces in closed system TCS reactors are provided in chapters 4 and 5. Knowledge gap (iii) led to the definition of research question **Q3** and is addressed in chapter 6 of this dissertation through the generation of non-intuitive flow channel designs that effectively distribute gas reactants to the reactive sites. Finally, the knowledge gap (iii) led to the definition of the research question **Q4**, which is addressed in chapter 6 through a multi-step topology optimization approach aiming at generating designs employing optimized flow channels and fins.

Chapter 3

Topology Optimization as a design tool for energy devices

Energy efficiency is considered a massive part of the solution to climate change as it can reduce carbon emissions and ensure energy security without the need for new technologies [119]. In 2018, the European Union set a target of a 32.5% improvement in energy efficiency by 2030 [120]. The challenge is clear: future energy systems must produce less and less waste. An energy system has to convert energy resources to produce a beneficial effect; along this energy chain, the energy vectors are transformed, stored, or intensified [121]. The form of these energy vectors can be different: mechanical, thermal, lighting, electric, chemical, etc., and the final form of the energy vector depends on which application the energy system is linked to.

Since 2000, the efforts to increase energy efficiency have been significant; however, the global boost of energy demand is pushing researchers to find more and more optimization strategies [119]. The Topology Optimization (TO) method originates at the end of the 1980s from the field of structural mechanics to answer the question: *"how should we place a material to maximize its mechanical performance?"* [122]. The key feature of topology optimization is that no initial guess is needed, and the solution is free to evolve towards the global maximum solution.

Hence, compared to traditional optimization methodology, the key advantage of TO is its matchless design freedom. Considering the structural mechanics problem reported in Figure 3.1, a classical approach is the use of sizing optimization to identify the thickness of each structural element. A more recent alternative is shape optimization, which consists of the free modification of the geometry of a selected number of holes [123]. The a priori selection of the number of holes might preclude, however, the identification of the global optimal layout. Topology optimization searches instead for the optimal size, shape and number of structural elements, with no a priori assumptions required to identify the optimal layout [124]. The resulting optimal design might be hard to conceive heuristically and can unlock novel enhancement pathways which can hardly be achieved in traditional ways.

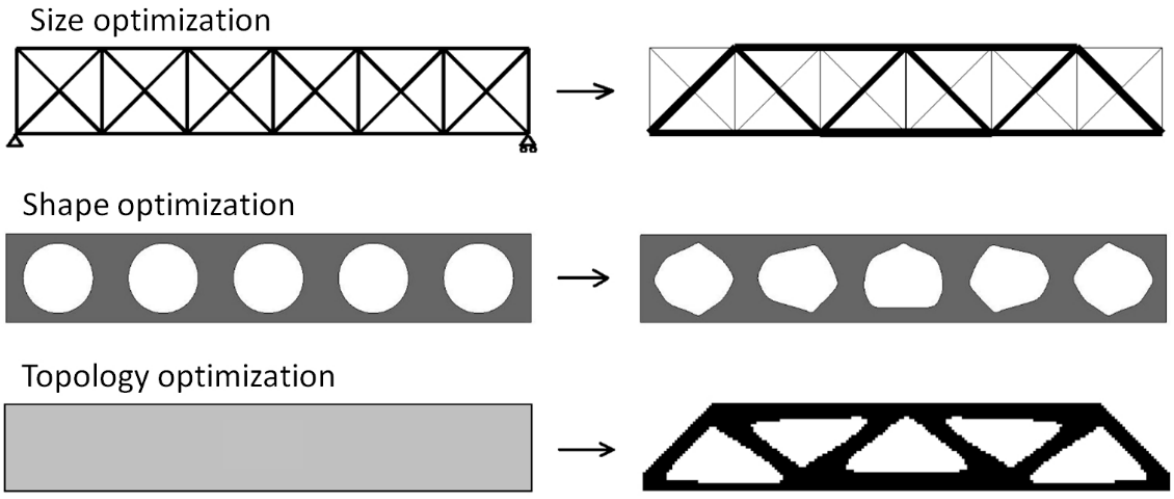

Figure 3.1 Comparison of size, shape and topology optimization for a structural mechanics problem [124]***.***

A more specific definition of topology optimization can be found in published review papers [125,126]. Nowadays, structural mechanics is considered a mature field for topology optimization, and several topology optimization-based designs can be found in the market [127]. The approach adopted for optimising mechanical structures has then been extended to other types of physics, such as heat conduction, fluid mechanics, conjugate heat transfer,

mass transfer, electromagnetism, acoustics, etc., with the aim of defining which is the optimal material distribution for specific design requirements.

The outline of this chapter is as follows: section 3.1 introduces the key concepts and terminology adopted throughout this dissertation. Thus, the key elements and parameters of the topology optimization algorithm are presented and clarified by means of two design examples in section 3.2. Specifically, the optimal distribution of highly conductive material (HCM) is derived in the instance of a steady-state and a time-dependent heat conduction problem. Section 3.3 provides an overview of topology optimization as a design tool for energy technologies, with a particular focus on energy storage devices.

3.1 Topology Optimization as a design tool

This section presents the key elements of the topology optimization algorithm and how this can be coupled with numerical models for the optimization of real-world devices. Besides, the main choices made for the implementation of the topology optimization algorithm as a design tool for TES devices and the rationale behind such choices is presented in this section. Three different tools are needed [128]: (i) a design model to define how the layout is influenced by the optimization variables, (ii) an analysis tool to predict the physics response and (iii) an optimization model to define the objective, the constraints and the search strategy. While the design and optimization models are almost insensitive to the targeted design case, the analysis model differs for each energy system and is, thus, detailed in each chapter.

3.1.1 Design model and material interpolation schemes

The design model needs to allow for the description of the material distribution in the ground domain. In this work, a density-based description is adopted [125], where a scalar indicator, $\boldsymbol{s}(\boldsymbol{x})$, is used to switch between materials:

$$\boldsymbol{s}(\boldsymbol{x}) = \begin{cases} 1 & \forall\, \boldsymbol{x} \in\ \Omega_b \\ 0 & \forall\, \boldsymbol{x} \in\ \Omega_w \end{cases} \qquad 3.1$$

Where Ω_b is the design region filled with material 1 and Ω_w is the design region filled with material 2, such that $\Omega_D = \Omega_w \cup \Omega_b$. To allow for a continuous representation of the material distribution, the binary, i.e. black and white, material description {0;1} is smoothed to a continuous representation [0;1] [124], as depicted in Figure 3.2.

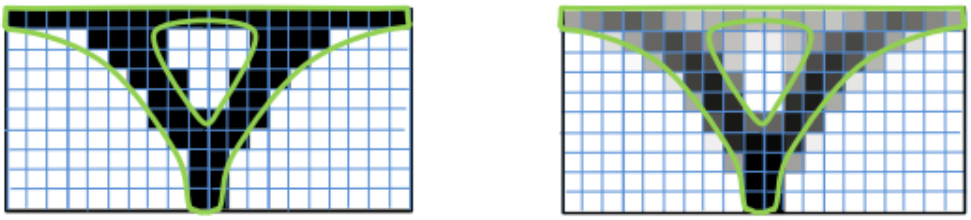

Figure 3.2 The density-based design model: left for the integer design description, right for the smoothed density description [128]***. The black colour refers to material 1 in the region Ω_b, while the white colour refers to material 2 in the region Ω_w.***

On the one hand, this allows the use of a gradient-based optimizer but raises the issue of describing non-physical material, i.e. grey regions. This issue is faced by introducing artificial laws for the material properties, chosen in a way to penalize grey areas and promote final binary designs. The most popular material interpolation scheme is the Simplified Isotropic Material with Penalization (SIMP), first introduced by Bendsoe and Sigmund [129], which, in the instance of thermal conductivity, $\lambda(\boldsymbol{s})$, can be expressed as follow:

$$\lambda(s) = \lambda_0 + (\lambda_1 - \lambda_0)\boldsymbol{s}^p \qquad 3.2$$

Where λ_0 is the thermal conductivity of material 1, and λ_1 is the thermal conductivity of material 2. The parameter *p* is the penalization exponent, which determines the concavity of the material interpolation function. Given its simplicity, SIMP interpolation is widely adopted in the literature, e.g. in structural mechanics problems [130] and heat transfer problems [131]. An alternative to SIMP penalization is the Rational Approximation of Material Properties (RAMP) model [132]:

$$\lambda(\boldsymbol{s}) = \lambda_0 + (\lambda_1 - \lambda_0)\frac{\boldsymbol{s}}{1 + q_{RAMP}(1 - \boldsymbol{s})} \tag{3.3}$$

Here, the parameter *q* is adopted to tune the concavity of the interpolation function. Previous authors demonstrated that a RAMP scheme could be preferred when dealing with large property ratios [128]. In more recent years, the TANH scheme was presented by Amigo et al. [133]:

$$\lambda(\boldsymbol{s}) = (1 - m_{TANH}(\boldsymbol{s}))\,\lambda_0 + m_{TANH}(\boldsymbol{s})\,\lambda_1 \tag{3.4}$$

Where the design-dependent parameter $m_{TANH}(\boldsymbol{s})$ is defined according to:

$$m_{TANH}(\boldsymbol{s}) = \frac{tanh\,[p_{TANH}(\boldsymbol{s} + sgn(\lambda_0 - \lambda_1)\varepsilon_{TANH} - 0.5) + 1]}{2} \tag{3.5}$$

With *sgn* denoting the signum function. A hyperbolic tangent function is adopted in the TANH scheme to describe the transition of material properties. In conflict with the SIMP and RAMP schemes, the TANH scheme allows for the tuning of the control variable value at which the material properties transition takes place by the tuning of the parameter ε_{TANH}. In this way, singular transition regions can be avoided to penalize unphysical materials further. However, the use of the TANH scheme can lead to numerical instabilities that can significantly increase the nonlinearities of the optimization process and thus is not widely adopted in the literature.

The different material interpolation strategies are presented in Figure 3.3 with different concavities. As mentioned, the concavity of the material interpolation is crucial to avoid premature convergence to sub-optimal layouts on the one hand, but it also increases the nonlinearity of the numerical problem. Consequently, the proper selection of scheme and penalization parameters must be addressed. Unfortunately, although several guidelines are provided in the literature, the effective selection of such optimization parameters strongly depends on the physical problem considered, as discussed in a numerical example in section 3.2.

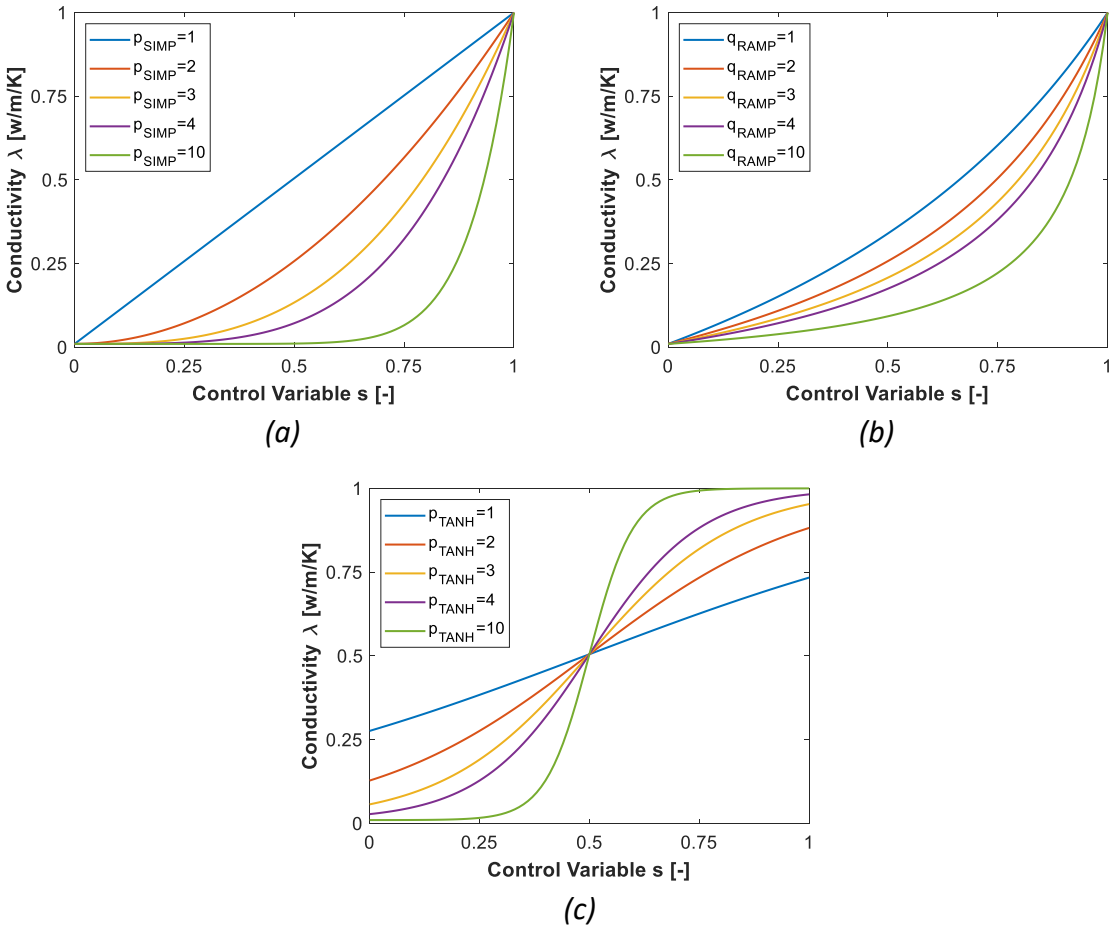

Figure 3.3. Comparison of the main artificial law for material interpolation [128] ***: (a): SIMP scheme; (b): RAMP scheme; (c) TANH scheme.***

3.1.2 Optimization model

Thanks to the density-based approach described above, the amount of material distributed in the design domain can be calculated as the integral of the scalar indicator $\boldsymbol{s}(\boldsymbol{x})$, which generally takes the name of material density [122], and can be used to constraint the maximum volume allowed in the optimal layout. The optimization model drives how this material is distributed in the ground domain. The main goal is to limit the computational effort to obtain the optimal layout. To such an extent, gradient-based routines are generally chosen [134]. These routines can solve fine-resolution problems with up to millions of design variables using only a few hundred function evaluations. A generic optimization problem with Partial Differential Equations (PDE) constraints can be formulated as follow:

$$\begin{cases} min_s\, f(\mathbf{s}, \mathbf{U}(\mathbf{s})) \\ s.t.\, \mathrm{g}_i\big(\mathbf{s}, \mathbf{U}(\mathbf{s})\big) = 0, \mathrm{i} = 1, \dots, \mathrm{N}_{eq} \\ \mathrm{h}_j\big(\mathbf{s}, \mathbf{U}(\mathbf{s})\big) \leq 0, \mathrm{j} = 1, \dots, \mathrm{N}_{ieq} \\ \boldsymbol{R}\big(\mathbf{s}, \mathbf{U}(\mathbf{s})\big) = \mathbf{0} \\ \boldsymbol{s} \in \boldsymbol{S} = \{\mathbb{R}^{N_s} \big|\, \mathrm{s}_{min} \leq \mathrm{s}_i \leq \mathrm{s}_{max}, i = 1, \dots, N_s \end{cases} \tag{3.6}$$

Where $\mathbf{U}(\mathbf{s})$ is the design-dependent PDE solution of the physical problem, *f* is the objective function, g_i and h_j are the equality and inequality constraints, respectively, and $\boldsymbol{R}\big(\mathbf{s}, \mathbf{u}(\mathbf{s})\big)$ is the system of algebraic equations representing the physical problem after discretization. In this thesis, the generic optimization problem presented in 3.6 is solved by means of two possible optimization routines: the Method of Moving Asymptotes (MMA) and its extension, namely the Globally Convergent Method of Moving Asymptotes (GCMMA) [135]. Both optimization routines rely on the idea of Sequential Linear Programming (SLP) and Sequential Quadratic Programming (SQP), for which a series of approximated subproblems replace a non-convex optimization problem. The MMA and GCMMA optimization routines

require the objective and constraints sensitivity to be computed in order to update the design variable. However, the need for a limited computational cost imposes alternative pathways to a straightforward sensitivity calculation. A widely adopted approach in the literature is the analytical differentiation of the sensitivity problem, which leads to the following formulation of a generic optimization criterion q_j [128]:

$$\frac{dq_j}{ds_i} = \frac{\partial q_j}{\partial s_i} - \left(\left(\frac{\partial \boldsymbol{R}}{\partial \boldsymbol{U}}\right)^{-T} \frac{\partial q_j}{\partial \boldsymbol{U}}\right)^T \frac{\partial \boldsymbol{R}}{\partial s_i} \tag{3.7}$$

The term in bracket is referred to as adjoint problem [136] and can be solved by introducing the following adjoint equation:

$$\left(\frac{\partial \boldsymbol{R}}{\partial \boldsymbol{U}}\right)^{-T} \boldsymbol{\Lambda} = \frac{\partial q_j}{\partial \boldsymbol{U}} \tag{3.8}$$

Where $\boldsymbol{\Lambda}$ is the vector of adjoint variables and $\frac{\partial \boldsymbol{R}}{\partial \boldsymbol{U}}$ is the Jacobian, $\boldsymbol{J}$, of the physical problem. The adjoint problem in equation 3.8 is insensitive to the size of the optimization problem, N_s, reducing significantly the computational burden with respect to a forward sensitivity calculation [137]. Given the dynamic behaviour of most of the engineering applications tackled in this dissertation, the sensitivity analysis must be solved for time-dependent studies, for which the adjoint equation assumes the following matrix form:

$$\begin{bmatrix} \boldsymbol{I} & \boldsymbol{J}_{dyn}^{(0)^T} & & & \\ \boldsymbol{J}^{(1)^T} & \boldsymbol{J}_{dyn}^{(1)^T} & & & \\ & \boldsymbol{J}^{(2)^T} & & & \\ & & \ddots & \boldsymbol{J}_{dyn}^{(N_t-1)^T} & \\ & & \ddots & & \boldsymbol{J}^{(N_t)^T} \end{bmatrix} \begin{bmatrix} \boldsymbol{\Lambda^0} \\ \boldsymbol{\Lambda^1} \\ \vdots \\ \vdots \\ \boldsymbol{\Lambda^{N_t}} \end{bmatrix} = \begin{bmatrix} (\partial q_j) \,/\, (\partial \boldsymbol{U}^{(\mathbf{0})}) \\ (\partial q_j) \,/\, (\partial \boldsymbol{U}^{(\mathbf{1})}) \\ \vdots \\ \vdots \\ (\partial q_j) \,/\, (\partial \boldsymbol{U}^{(\boldsymbol{N_t})}) \end{bmatrix} \tag{3.9}$$

Where N_t is the number of time steps. The single matrix block at the end of the diagonal allows the final adjoint field $\boldsymbol{\Lambda}^{N_t}$ to be computed, and the adjoint equation can be solved

backwards in time. In other words, calculating a time-dependent adjoint problem requires one forward (physical problem) and one backward (sensitivity problem) solution, ultimately leading to a computationally affordable optimization problem.

Numerical instabilities, such as the checkerboard effect and mesh dependence, may arise when describing the layout with the density-based approach [138]. Among the several regularization techniques proposed, filtering is one of the most adopted [139] to solve these issues. The design variable, $\boldsymbol{s}$, is mapped into the filtered field $\tilde{\boldsymbol{s}}$:

$$\tilde{\boldsymbol{s}} = \left(\Sigma_{i=1}^{\Omega_\omega} \bar{\omega}_i\right)^{-1} \Sigma_{i=1}^{\Omega_\omega} \bar{\omega}_i \boldsymbol{s}_i \qquad 3.10$$

Where Ω_ω is the circular domain with a radius r_{min} centred in x^e, while $\bar{\omega}_j$ is the filter weight calculated as a linear function:

$$\bar{\omega}_i = r_{min} - \left\| x^i - x^e \right\| \qquad 3.11$$

However, this approach creates a grey region of difficult physical interpretation which does not disappear during the optimization iterations [140]. Hence, a projection strategy is typically used to reduce the grey region and create a crisp material interface. The projected field then describes the final geometry $\bar{\boldsymbol{s}}$ following the hyperbolic tangent formulation suggested by Wang et al. [140]:

$$\bar{\boldsymbol{s}} = \frac{\tanh(\beta\eta) + \tanh(\beta(\boldsymbol{s} - \eta))}{\tanh(\beta\eta) + \tanh(\beta(1 - \eta))} \qquad 3.12$$

Where $\beta \geq 0$ is the projection factor, which dictates the steepness of the projection function, while $\eta \in (0,1)$ is the projection threshold. The deriving control variable fields can be appreciated in Figure 3.4 in the instance of an MBB beam.

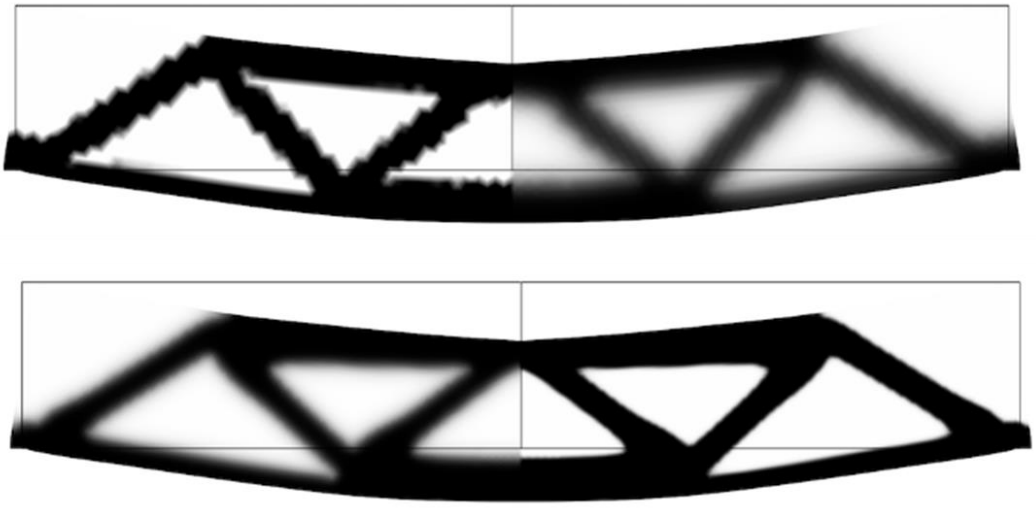

Figure 3.4. Different control variable fields for an MBB Beam [141]***. Top: raw control variable field, s, to the left and filtered field, $\tilde{s}$, on the right; Bottom: filtered field, $\tilde{s}$, to the left and projected field, $\bar{s}$, to the right.***

The flow of computation used in this work is depicted in Figure 3.5. The initial guess made is a homogeneous distribution of material 2 equal to the maximum volume fraction selected for the specific design case. The FEM analysis and the adjoint problem solution are carried out in the commercial software COMSOL Multiphysics [142], while the design variable update, i.e. optimization and regularization, and convergence check are performed in MATLAB environment [143].

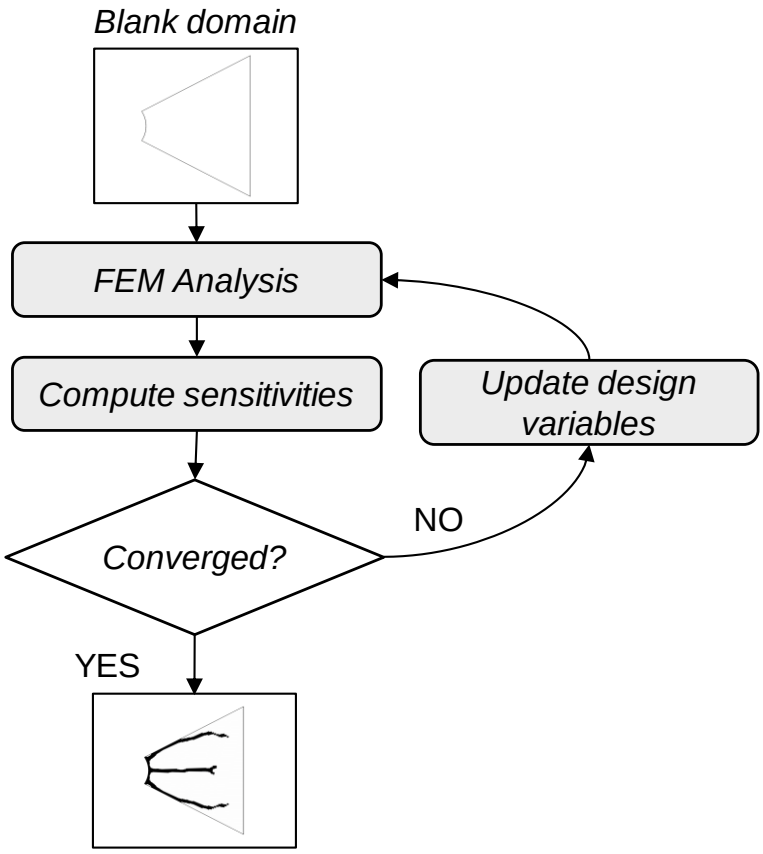

Figure 3.5. Computational flow for the systematic design tool adopted.

3.1.3 Post-processing of Topology Optimization results

The seek for optimal performance often presents material distributions characterized by complex geometrical features that challenge the final design's manufacturability. In most cases, the obtained designs must be reproduced through additive manufacturing, AM, techniques, such as selective laser melting, SLM, [144] or material extrusion [145]. Nonetheless, regardless of the manufacturing method, specific constraints must be accounted for to ensure the manufacturability of the generated designs [146]. In recent years, researchers attempted to introduce numerical strategies to account for these constraints during the topology optimization design process. Such strategies act on (i) the optimization process itself or (ii) the post-processing of the optimization results.

Regarding the inclusion of manufacturing constraints during the optimization process, relevant efforts have been made to control the length scale of geometrical elements. In particular, minimum values must be guaranteed for both distributed materials. An effective strategy to achieve this is filtering methods [124]. As already discussed in 3.1, these methods were developed to limit mesh dependency and check-board effects; nonetheless, the set of desired control radius can be directly adopted to determine the minimum length scale. Initial efforts in this direction were made by Guest et al. in [147], where a Heaviside projection method was adopted to control the minimum length scale of one of the two materials. A few years later, double projection methods were proposed to ensure a minimum length scale for both distributed materials [148]. However, using such numerical strategies further increases the complexity of the optimization process and is not recommended in the case of complex multi-physics problems [128].

In the framework of post-processing of TO designs, the initial step regards the smoothness of the surface boundaries and their parametrization. The smoothness of the surface boundaries is adopted as tessellated surfaces require many tool path turnings, resulting in increased production time and cost. The parameterization of the boundaries is important as sections or features of the optimal geometry might be unfeasible regardless of the manufacturing method, e.g. undercuts, and thus parametrization can facilitate the elimination or modification of such features. A simple strategy to parametrize a TO-based geometry is the manual reconstruction by solid geometry modelling [128]. However, despite its simple application, this process is characterized by low repeatability and can significantly increase the design time. Other than manual reconstruction, the optimal design smoothing and parametrization can be achieved through an integrated optimization algorithm [149]. In

the framework of TO with a density-based approach, several efforts have been made with image processing techniques to convert grey designs into binary structures. For example, Bremicker et al. [150] adopted a three-step design process for initiating structural optimization at the early stages. An initial optimal design was derived in a SIMP framework and then converted into a binary map. Thus, computer vision techniques were adopted to parametrize the initial design, which was then treated by size and shape optimization techniques. Similarly, Lin and Chao [151] adopted image processing to remove noisy elements and voids in the final design. Furthermore, the derived external boundaries were described through B-splines, and the holes were defined by geometric shape templates.

In alternative to image processing, the TO-results interpretation based on material density iso-lines is a more direct approach, widely adopted in the literature. In the early 90s, Maute and Ramm [152] adopted cubic or Bezier splines to interpret iso-density contours. However, the authors highlighted that such a strategy might lead to unfeasible designs in case of strong checker-board patterns, with this limitation partially overcome by the density redistribution model proposed by Young and Park [153]. Recently, Hsu et al. [150] automated the design interpretation considering 2D and 3D structures using B-spline curves and swept techniques. The influence of the threshold density value on the compliance increase was investigated to identify the optimal trade-off between performance and design complexity reduction, and trivial geometrical features were removed by using a filter. Such a filter targeted the solids containing elements connected by only one node to other groups. Similarly, trivial voids were removed if they represented less than 1% of the total number of elements. However, the use of the proposed 3D structure interpretation was limited to simple structures and was found to fail in reproducing complex geometries.

An alternative smoothing and parametrization approach for density-based TO designs was proposed by Chang and Tang [154]. Here, a set of control points were acquired from the grey design and adopted to approximate the reconstructed surfaces by means of B-splines, as shown in Figure 3.6. The solid model construction was operated in a CAD environment, and the imported control points parametrized the surfaces, which were then adopted to perform shape optimization.

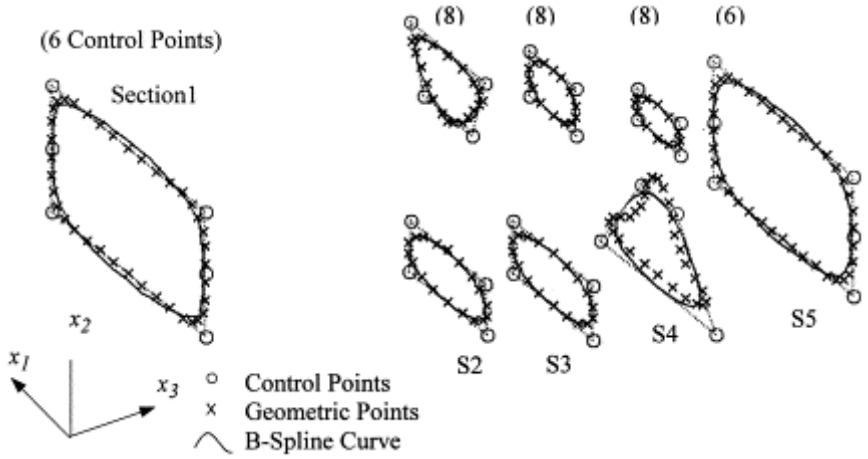

Figure 3.6 Section contours and curves for the smoothing and parametrization strategy proposed by Chang et al. [154]***.***

3.2 Numerical examples

In this section, the use of topology optimization as a design for thermal energy devices is investigated through two numerical examples. In the first example, the optimal highly conductive material (HCM) distribution is obtained for a cylindrical heat sink device. Here, particular attention is made to the influence of the penalization parameters for the adopted material interpolations scheme. In the second example, the optimal highly conductive material distribution was obtained in the instance of sensible heat storage with solid storage

material. The influence of the desired discharge time is analysed to exhibit the need for time-dependent analysis when dealing with TES devices.

3.2.1 Heat sink

A steady-state heat conduction problem was analysed, where the cooling of a hot domain was considered and HCM was distributed according to the following optimization problem:

$$\begin{cases} \min \int_{\Omega_D} \mathrm{T}\, dxdy \\ s.t. \int_{\Omega_D} \boldsymbol{s}\, d\boldsymbol{x} - V^* \leq 0 \quad where\, V^* = 0.2 \\ 0 \leq \boldsymbol{s} \leq 1 \end{cases} \tag{3.13}$$

Where T is the temperature and V^* is the maximum volume fraction for the HCM, set to 0.2 in this example. The first equation of system 3.13 constitutes the objective function of the example, while the second and third equations are the volume constraints imposed on the problem to limit the amount of HCM distributed in the ground domain. The adopted design domain considers one-quarter of a radial cross-section of a cylindrical heat sink [155], as depicted in Figure 3.7. Here, the outer radius of the circular domain, R_{out}, was set equal to 1, while the inner radius, r_0, was set at 0.1. Besides, dimensionless parameters are adopted in the numerical examples.

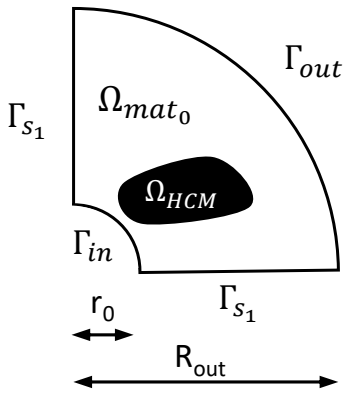

Figure 3.7. Design domain considered for the numerical example.

The heat transfer is governed by the following steady-state diffusive equation:

$$\lambda(\boldsymbol{s})\nabla^2 T = q_{vol} \qquad 3.14$$

Where $\lambda(\boldsymbol{s})$ is the design-dependent thermal conductivity interpolated with the SIMP scheme (equation 3.2) between $\lambda_0 = 1$, and $\lambda_1 = \lambda_{HCM} = 200$. Besides, a constant volumetric heat generation $q_{vol} = 1$ was used in the whole domain. Equation 3.14 constitutes the analysis model of the physical system. This was implemented first in COMSOL environment [142] and then exported in Matlab environment [143] to allow for the interface with the optimization routine and filtering and regularization techniques, as both were based on Matlab scripts adapted from previous works from Pizzolato Alberto and Behrou Reza [156].

The design-dependent term, $\lambda(\boldsymbol{s})$, of equation 3.14 expresses the influence of the design variable, *s,* on the thermal conductivity and varies between the thermal conductivity value for the two materials considered in the example, as depicted in Figure 3.3 and is referred to as material interpolation. As mentioned, material interpolation is a crucial step in topology optimization as it determines what materials are more 'appealing' to the optimizer. For the

example considered, HCM is the enhancer material, and, if no volume constraints were imposed, a ground domain filled with HCM would be obtained.

A Neumann boundary condition was adopted to impose a constant convective heat flux at the inner boundary, Γ_{in}:

$$q_{conv} = h\,(T - T_{\infty}) \tag{3.15}$$

Where $T_{\infty} = 0$ and $h = 10$. A quadrilateral mesh with 14000 elements was used for the investigation.

A homogeneous value $\boldsymbol{s} = V^{*}$ was selected as the initial guess for the material distribution, and the MMA optimizer was adopted [135]. The filter radius, projection steepness, and projection threshold parameters were set constant in the analysis, and their values are listed in Table 3.1 according to the guidelines provided in [111] and [128]. The SIMP scheme exponent, *p*, was varied in the analysis to investigate its effect on the final design. That is, the convexity of the interpolation scheme was varied (see Figure 3.8). Larger p-values penalize intermediate values for the control variable, *s,* and thus promote final binary designs, ad detailed in Section 3.1.1. On the other hand, the increase of the p-value also increases nonlinearities in the numerical problem and thus increases the possibility to encounter local minimum, i.e. final designs which are not the global optimum solution, and reduces the convergence time of the optimization problem.

Table 3.1. Default optimization parameters for the heat conduction examples.

Description	***Symbol***	***Value***
Filter radius	r_f	0.02
Projection steepness	β	2.0
Projection Threshold	η	0.5

The optimization problem set-up described above is solved through the computational flow depicted in Figure 3.5. As mentioned, the optimization routine starts for a blank domain with homogeneous material distribution $\boldsymbol{s} = V^*$. Thus, the analysis model is solved in COMSOL environment [142], i.e. the system performance with the current design is predicted, and the adjoint sensitivity is calculated, i.e. objective function sensitivity to the material distribution variation. At this point, the convergence is checked by comparing the objective function from the previous optimization iteration with the updated one. If convergence is not reached, the design variables are updated. In this step, performed in Matlab Environment [143], the MMA optimizer is used to modify the material distribution in the ground domain according to the adjoint sensitivity solution, while the filtering and regularization techniques summarized in Figure 3.4 are applied. At this point, the updated control variable field is passed into Comsol Environement [142] to start a new iteration.

Consequently, the design varies at each optimization iteration. The design evolution along the optimization iterations is shown in Sections 5.5 and 7.4.1 for the topological optimization problems of TCS reactors targeted in this thesis. This example focuses instead on the influence of the p-value on the final design.

Figure 3.8 shows the optimal design after 160 iterations for different values of p. With a unitary penalization exponent, a linear interpolation between the thermal conductivity of material 0 and material 1 was considered. In this case, the final design exhibits vast grey areas representing unphysical materials with intermediate thermo-physical properties. Nonetheless, the material density is larger in the proximity of the cooled boundary to enhance heat transfer and promote temperature reduction in the domain. With the increase of the penalization exponent value, binary designs were obtained. The grey areas nearly

disappeared in the instances of $p = 3.0$ and $p = 5.0$. A tree-shaped structure was highlighted in both binary designs, in agreement with the general guidelines for heat transfer intensification of heat sink devices [92].

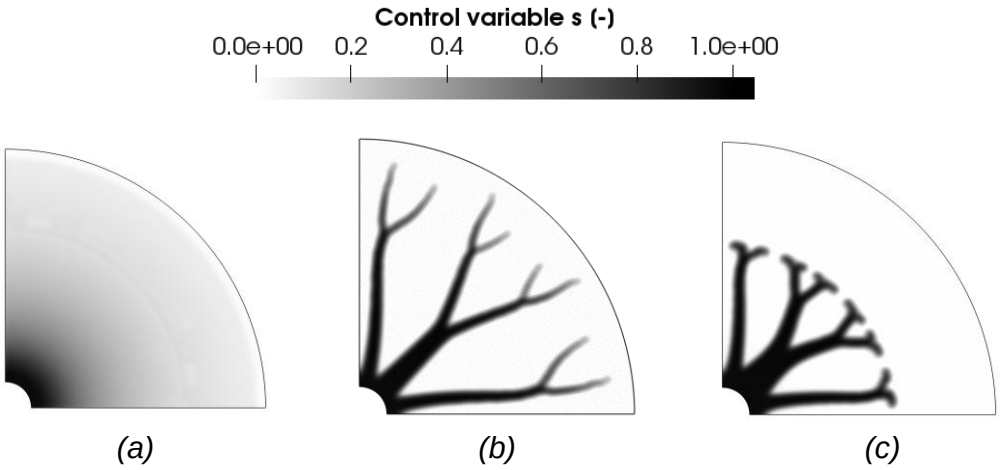

Figure 3.8. Effect of the SIMP exponent, p, on the final design. (a) p = 1.0; (b) p = 3.0; (c) p = 5.0.

However, in Figure 3.8 (c), the HCM did not spread in the regions away from the cooling interface. In fact, during the initial optimization steps, the use of large penalization exponents did not allow the material distribution to distribute in the entire ground domain. Consequently, the final design presented shorter and thicker fins than the optimization case of Figure 3.8 (b). The choice of $p = 3.0$ allowed also to obtain the best performing layout, in agreement with the rule of thumb suggested by Sigmund et al. [125] for the selection of SIMP penalization exponent values.

Nevertheless, increasing the penalization parameters can help obtain black and white designs in design cases where intermediate material properties are particularly attractive [157,158]. In these instances, using large penalization parameters might become necessary to achieve meaningful results. Using continuations schemes is an effective numerical strategy to ensure binary results and avoid sub-optimal layouts [139]. The idea for this

numerical strategy is to use a lower penalization effect at the beginning of the optimization process to allow the distributed material to spread in the entire design domain and thus gradually increase the penalization effect to sharpen the material's interface. This strategy is generally adopted in the case of complex multi-physics problems [156,159] and ensures more convex optimization problems during the initial optimization iterations, with great benefits for the convergence speed of the numerical study [124].

3.2.2 Sensible heat storage

The optimal HCM distribution was obtained in this section for a shell-and-tube Sensible Heat Storage (SHS) device employing concrete as storage material [160]. Despite the high technological maturity of SHS devices, only a single attempt for the non-heuristic optimization of SHS systems has been presented in the literature [161]. The ground domain under investigation did not vary compared to the previous numerical example and is depicted in Figure 3.7.

The governing equations describing the targeted energy device are written in the following way:

$$C(\boldsymbol{s})\frac{\partial T}{\partial t} = k(\boldsymbol{s})\nabla^2 T \qquad 3.16$$

Where $C(\boldsymbol{s})$ is the design-dependent heat capacity and t is the time. The thermophysical properties of concrete were adopted from [162], while aluminium was considered as HCM [163]. As a result, a heat capacity ratio, $C_{ratio} = C_{HCM}/C_{concrete}$, of 0.8 was imposed. Besides, an initial homogeneous temperature $T_0 = 100\,°C$ was imposed in the entire ground domain.

The minimization of the energy in the ground domain at the desired discharge time t_f was selected as the objective function, while the maximum fraction of HCM was set at 0.1:

$$\begin{cases} min \;\; E\,(T(\boldsymbol{s}),\boldsymbol{s})|_{t_f} = \int_{\Omega_D} C(\boldsymbol{s})(\bar{T} - T_0)|_{t_f} \\ s.t. \int_{\Omega_D} \boldsymbol{s}\, dx - V^* \leq 0 \quad where\, V^* = 0.1 \\ 0 \leq \boldsymbol{s} \leq 1 \end{cases} \tag{3.17}$$

The SIMP penalization exponent, p, was fixed at 3.0 in this example, while the parameter t_f was varied to investigate the influence of the desired discharge time on the optimal design. Figure 3.9 presents the optimal design evolution considering three different desired discharge times. The optimal design for a short discharge time, $t_f = 0.01\ h$, is characterized by a large density of material close to the inner boundary. Short discharge times do not allow the heat to travel across the entire domain, and the heat transfer intensification through the HCM architecture is beneficial only in the proximity of the cooled boundary. Literature studies also exhibited that a further reduction of the desired discharged time could lead to designs with no branches but only a layer of HCM with a volume fraction equal to V^* [164].

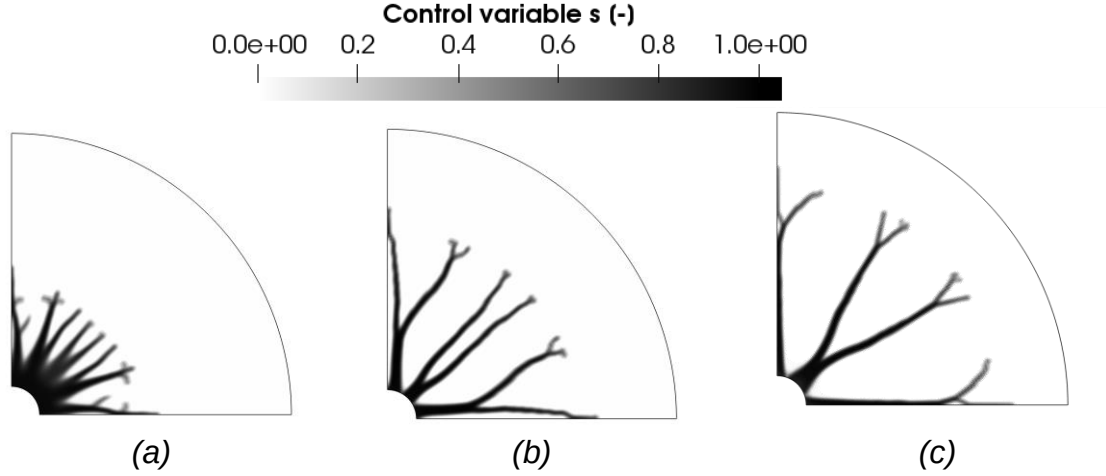

Figure 3.9. Effect of discharge time t_f on the optimal design: (a) t_f =0.01 h; (b) t_f =0.1 h; (c) t_f =1.0 h.

If larger desired discharge times are considered, e.g. $t_f = 0.1\ h$, the branches elongate further in the ground domain, Figure 3.9 (b), with optimal geometrical features similar to the ones found for the heat sink optimization case. For even larger desired discharge times, $t_f = 1\ h$, the number of HCM branches is reduced while the branches length is increased. In such a way, the heat transfer intensification becomes more effective in the storage material regions away from the cooled boundary, and a larger fraction of stored energy can be discharged in the desired discharge time.

Please also note that the ground domain adopted in both the numerical examples presented in this section could be further reduced by considering only one-eighth of the circular cross-section, which would reduce the computational burden of the optimization process. Nonetheless, preserving a line of symmetry in the ground domain allows for a qualitative assessment of the validity of the optimization history. In fact, in case of strong nonlinearities or ill-posed design problems, final asymmetrical designs might emerge, which should make the designer question the validity of the optimization parameters selected for the analysis.

3.3 Review of topology optimization for energy devices

This section provides an overview of the current state-of-the-art for topology optimization of energy devices. Given the multidisciplinarity of an energy system, the focus of this overview is not on a specific physics coupled with the optimization methodology but rather on the benefits that the optimization methodology can bring to an energy system compared to benchmark solutions. This can be considered a novel approach in the review of the state-of-art of topology optimization as a design tool. Several reviews have been published in the past; a survey for multidisciplinary continuum problems post-2000 was presented by Deaton

and Grandhi in 2013, highlighting the positive trend of publications on a wide range of physical problems. In 2020, Alexandersen and Andreasen [165] provided an overview of topology optimization of fluid-based problems. The authors suggested future advancements to focus on more complex problems, such as time-dependent analysis and turbulent regimes, with the aim of reducing the gap between the approximated physical problems and real applications. In the umbrella of fluid flow problems, two additional subgroups have also been reviewed: microfluidics [166] and thermo-fluidic [167,168].

For the review of the use of topology optimization for the performance enhancement of energy devices, the latter are clustered into three main groups, in agreement with the definitions provided by Orecchini [121]. The intent of each of the energy device group can be expressed as follows:

(i) **Energy intensification devices**: devices in which the energy type is not varied, but its state is varied;

(ii) **Energy conversion devices**: devices in which energy is transformed from one energy type to another;

(iii) **Energy storage devices**: devices in which energy is accumulated to be delivered in a second time;

The adopted energy device groups are summarized in Figure 3.10, along with the list of specific technologies addressed.

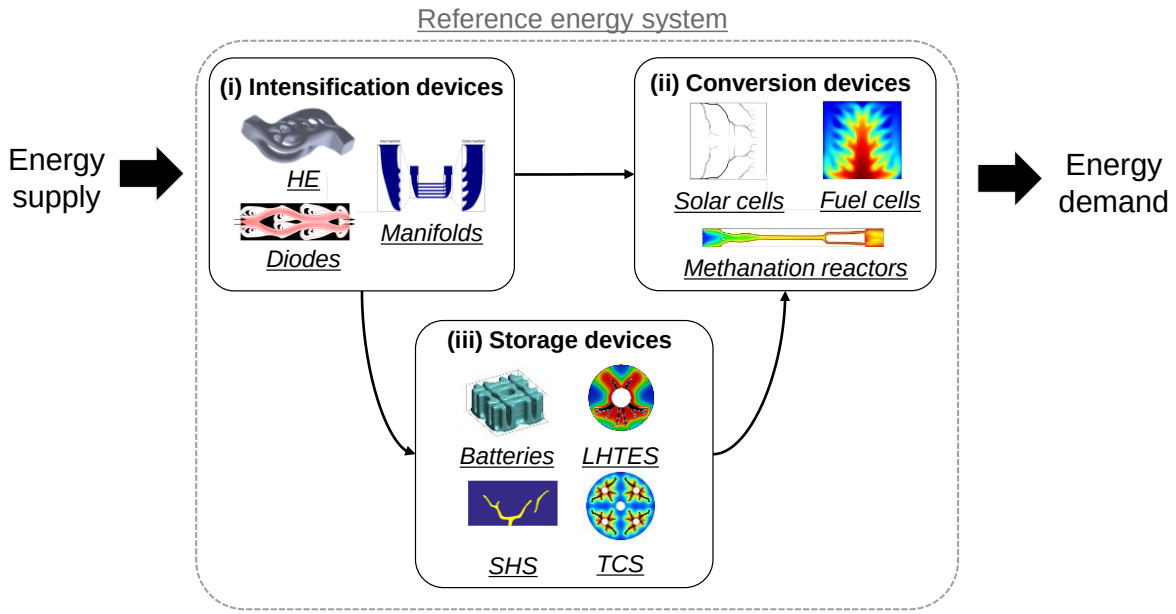

Figure 3.10 Classification adopted for the review of topology optimization for energy devices.

3.3.1 Energy intensification devices

In energy intensification devices, the energy state varies while the energy type remains unvaried. While many energy devices pertain to this category, the energy intensification devices for which application of the topology optimization algorithm is reported in the literature are heat exchangers, manifolds and fluidic diodes.

Concerning the application of TO for the performance enhancement of heat exchangers (HE), researchers aimed to find the optimal topology for the fluid-solid interfaces so that maximum heat transfer rates are achieved. Heat exchangers are devices whose task is to transfer heat from one medium to another, with each of these media in the gas, fluid or solid phase [169]. Such devices are present in various industrial applications such as chemical engineering, combustion engines, radiators, refrigerants and heat sinks [170]. Consequently, heat exchangers have a long technological history, having been used widely for industrial purposes since the beginning of the last century. Nonetheless, despite the extensive design

know-how gained through the years, applying TO for the performance enhancement of heat exchangers is a hot topic for research, with more than 30 papers published post-2010. In a way, such a high number of publications demonstrate the potential and interest in the study and application of topology optimization for the performance improvement of well-established technologies. In particular, the vast majority of these studies have been devoted to the optimal design of microchannel heat sinks for electronic components. In fact, given the large volumetric heat generation encountered in such components, the way heat is dissipated is crucial to avoid severe damage [171]. A heat sink usually consists of plate or pin fins attached to a metal substrate in contact with the heat source, as depicted in Figure 3.11. The design of heat sinks is a typical application of multi-physics topology optimization, where the distribution of a fluid and a solid is optimized by successfully solving the conjugate heat transfer and optimization problems.

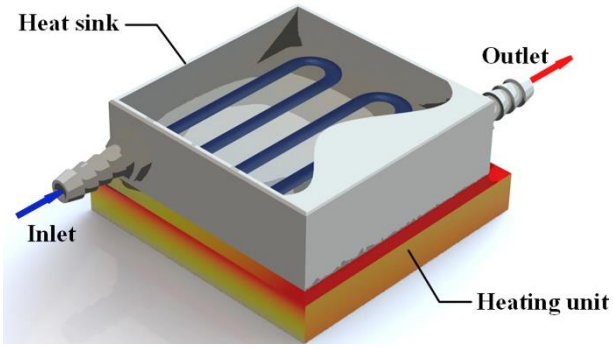

Figure 3.11 Schematic of a liquid-cooled heat sink [172]***. TO is typically adopted to determine the optimal geometry of the liquid cooling channels.***

While a high computational cost is required in the case of 3D ground domains [173], researchers demonstrated the analysis of 2D planar ground domains to enhance the devices' performance successfully. A common approach for the design of heat sinks cooled by forced convection is the use of Newton's law of cooling [174,175]. In this instance, no flow field

solution is required, and the computational cost is significantly reduced. However, single empirical convection constant is required, and, as observed by Alexandersen et al. [176], the influence of such convection constant value on the final design makes it hard to justify the use of Newton's law of cooling. As a result, modelling both solid and fluid phases becomes imperative for the performance maximization of heat sink devices.

Nevertheless, an absorption term is typically adopted in the momentum equation to limit the number of equations describing the physical system, as first presented by Borrvall and Petersson [177]. This term is a fictitious friction force representing the solid phase, leading to negligible local velocity values. Following this approach, Matsumori et al. [178] studied the optimal microchannel heat sink design subject to constant input power. The latter was expressed through an extra integral equation for the inlet pressure. Besides, both temperature-dependent and independent heat source terms were analysed. The optimal geometrical features were primarily influenced by the selected Reynolds number and heat source parameter, with more and more ramified channel networks in case of higher imposed pressure drops and heat source parameters. However, the authors found the validity of the optimized designs to be limited to relatively low Reynolds numbers.

Similarly, Zhou et al. [179] investigated the heat dissipation maximization, expressed as the thermal compliance minimisation, of an electric motor cover. A density-based approach was adopted coupled with a steady-state heat transfer model, with the convective heat transfer accounted for through the inclusion of design-dependent film coefficients, as initially suggested by Schousboue et al. [180]. The generated designs were compared with a literature benchmark using high-fidelity numerical models, and performance enhancements

up to +9% were evaluated. Haertel et al. [158] studied an air-cooled heat exchanger for power plant condensers. An approximation of the flow field was used to reduce the computational complexity to a 2D planar domain, and up to a +36% improvement in conductance was predicted compared to commercial designs. Similarly, Mo et al. [181] optimized the design of cooling channels for the thermal management of batteries. The optimal design trends were investigated for variable inlet temperature and mass flow rate. Besides, the cooling plates were manufactured by 3D printing with AlSi10Mg material. Compared to traditional designs, the experimental results showed a -47.9% pressure drop reduction and a -2.3°C in the maximum local temperature.

The trade-off between heat transfer maximization and reduced pressure losses was further investigated by Koga et al. [182]. Here, applications such as chemical reagent dosages and cooling devices in electronic components were targeted. A multi-objective function was adopted combining the pressure drop minimization inside the channels and the minimization of the mean temperature in the ground domain. Weighting factors were used to control the influence of both fluid flow and heat transfer cost functions, while the optimization problem was carried out assuming steady-state conditions for a planar 2D ground domain. Nonetheless, the derived optimal design was extruded and evaluated utilizing a full 3D numerical model, while prototype manufacturing studies were conducted to ensure the technical feasibility of the proposed design. The optimization results exhibited small channel ramifications when large heat transfer weighted problems were carried out, with these ramifications enhancing the heat distribution over the device. On the other hand,

such ramifications also penalize the pressure drop inside the channels and are not present in case of a large pressure drop weighting factor.

With a similar approach and finality, Subramaniam et al. [183] presented the Pareto-frontier for heat sink designs aiming at thermal performance enhancement and pressure drop reduction. Compared to a literature benchmark, the generated optimal designs were predicted to generate slightly superior thermal power outputs at the expense of a -50% lower pressure drop. Optimized designs based on the same approach were tested by Li et al. [184], as shown in Figure 3.12. Compared to a conventional parallel design, the TO design showed better heat transfer capability, with a maximum surface temperature reduction of -11.7%.

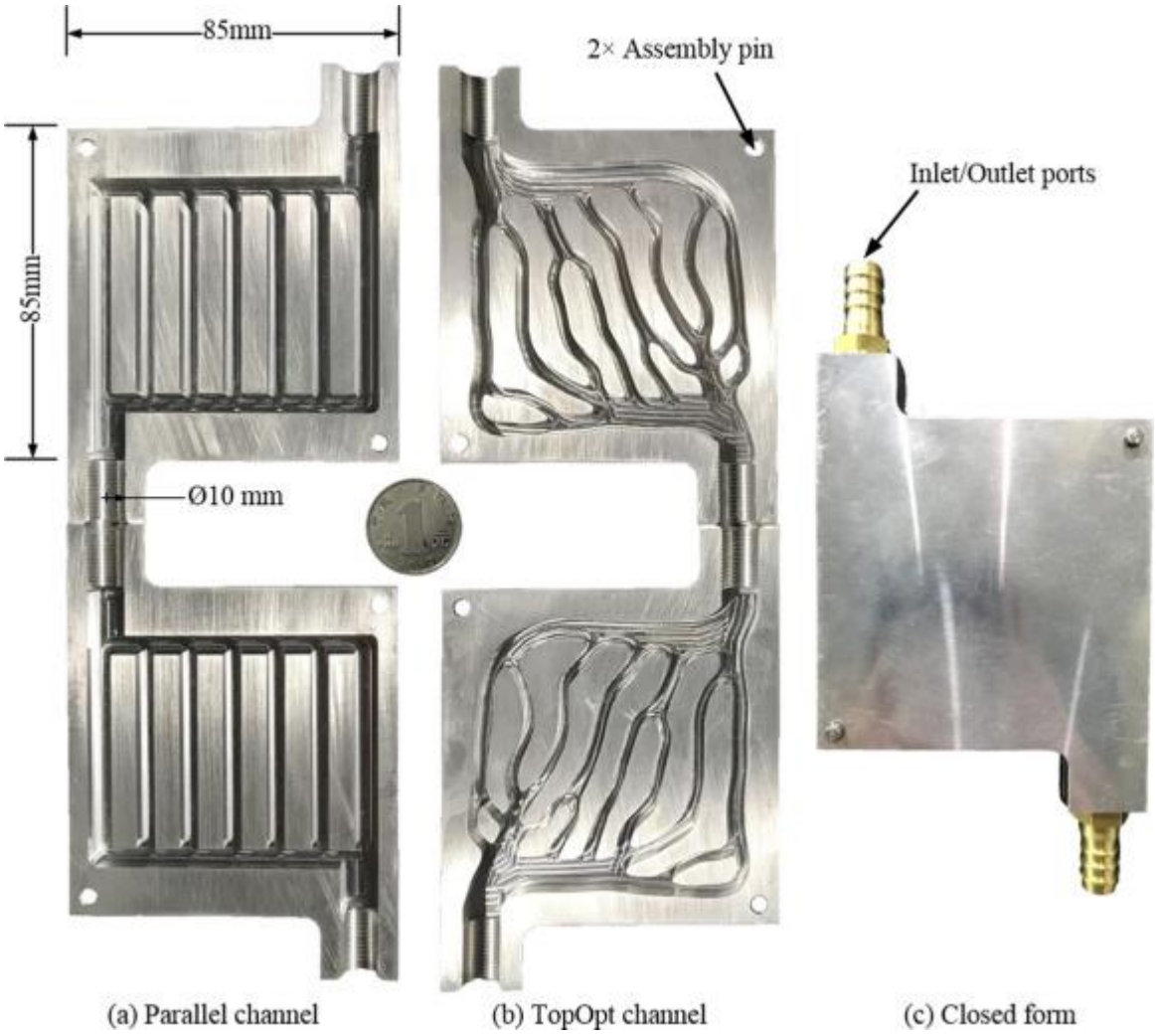

Figure 3.12 Comparison of the aluminium heat sinks prototypes tested by Li et al. [184]***.***

However, regarding the heat transfer process, recent studies demonstrated errors up to 50% and 24% if the volumetric heat flux is imposed evenly on the fluid and solid phases or solely on the solid phase, respectively [185]. As a consequence, particular attention has been made to the development of heat transfer models taking into account both the heat flux redistribution in the substrate and three-dimensional heat transfer effects. In this context, McConnell et al. [186] presented a two-layer model considering a solid substrate and a thermal-fluid layer. Such an approach was later on adopted by Haertel et al. [159] to derive a pseudo-3D thermos-fluidic model employing a design-dependent out-of-plane heat

transfer coefficient and to maximize the performance of a heat sink for electronics cooling. The optimal designs were predicted to achieve lower thermal resistance (-13.6%) compared to a size-optimized parallel fin heat sink. Compared to the typical cylindrical or rectangular pin fins shape, the optimized fins present a blade shape able to enhance heat transfer at the expense of a little pressure drop, in agreement with what was also observed by Ghasemi et al. [187]. Lazarov et al. [188] manufactured and tested optimized heat sinks promoting natural convection for the effective cooling of LED lights. The experimental results confirmed the superior performance compared to commercial benchmarks: the life expectancy was doubled, while the operational cost was cut by 50%. With the aim to approximate three-dimensional heat transfer effects, Yan et al. [189] presented a two-layer heat sink model comprising a fourth-order polynomial temperature profile of the heat sink thermal-fluid layer and a linear temperature profile in the substrate. The two-dimensional heat transfer governing equations of the two layers were thus coupled through an out-of-plane heat flux term. The so-obtained performance predictions agreed with a full 3D model for an extruded optimized design.

Nevertheless, one common limitation of the models described above is their use to laminar flows solely, which ultimately precludes their application for several energy devices. With the finality to optimize heat sinks with turbulent forced convection, Dilgen et al. [190] extended a previously developed fluid solver [191] to thermo-fluidic and 3D problems. The optimization problem sensitivities were obtained utilizing an automatic differentiation applied to the discrete system in such a way that no simplification assumptions were needed. As a result, the sensitivities were demonstrated to be exact to machine precision.

The comparison between optimized designs showed the benefits of full 3D optimization including turbulence modelling in the optimization process. However, the 3D optimized designs presented complex geometrical features that might prevent their use in commercial applications, as can be appreciated in Figure 3.13.

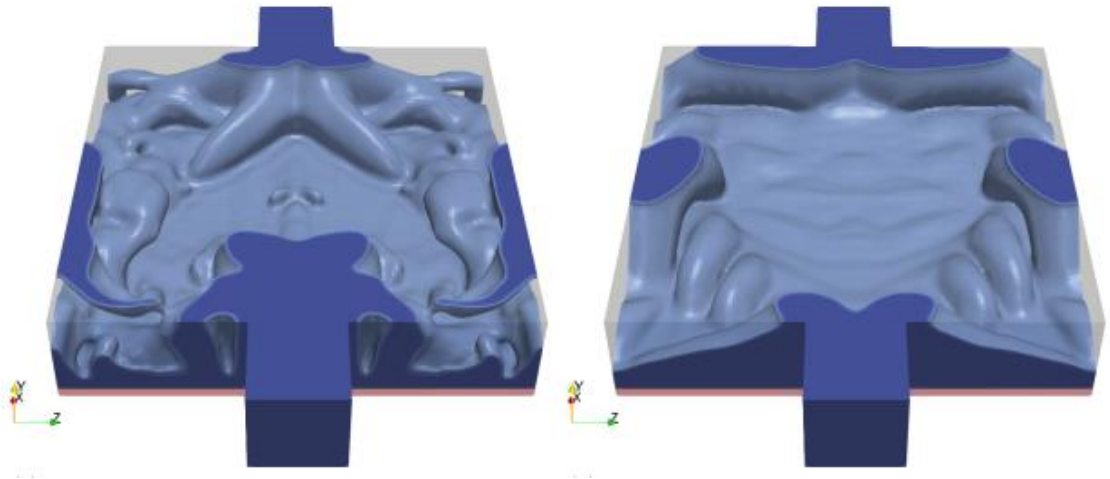

Figure 3.13 Examples of topology-optimized channels by Dilgen et al. [190]***. The TO process was conducted for turbulent flows in a 3D ground domain: left for Re=5000 and right for Re=50.***

When dealing with fluid-fluid heat exchangers, additional modelling challenges emerge. First, full three-dimensional problems are often necessary to gain satisfactory performance enhancements, leading to complex and expensive numerical problems. Second, non-mixing constraints are required between the two distinct fluids, particularly when a density-based approach is adopted. The latter challenge was first addressed in 2015 by Papazoglou [192], with his work then extended a few years later by Kobayashi et al. [193]. The representation model accounted for three states, two fluids and a solid wall in between fluids, described by a single control variable.

As a consequence, the mixing of the fluids was prevented without the need for any penalization scheme. Based on this approach, Saviers et al. [194] demonstrated the

application of TO for the design of fluid-to-fluid heat exchangers for aerospace applications. The optimization routine led to non-obvious organic geometries, which were additively built. Thus, the measured device performance was compared with a state-of-the-art counter-flow heat exchanger showing a -50% reduction in total pressure drop and a +10% heat transfer improvement. By combining several techniques from shape optimization and topology optimization employing the level-set approach, Feppon et al. [195] presented an innovative approach able to handle a wide variety of geometric constraints such as wall thickness and non-penetration constraints. In particular, the latter was enforced by prescribing a minimum distance between the two fluid phases. An example of an emerging design is depicted in Figure 3.14.

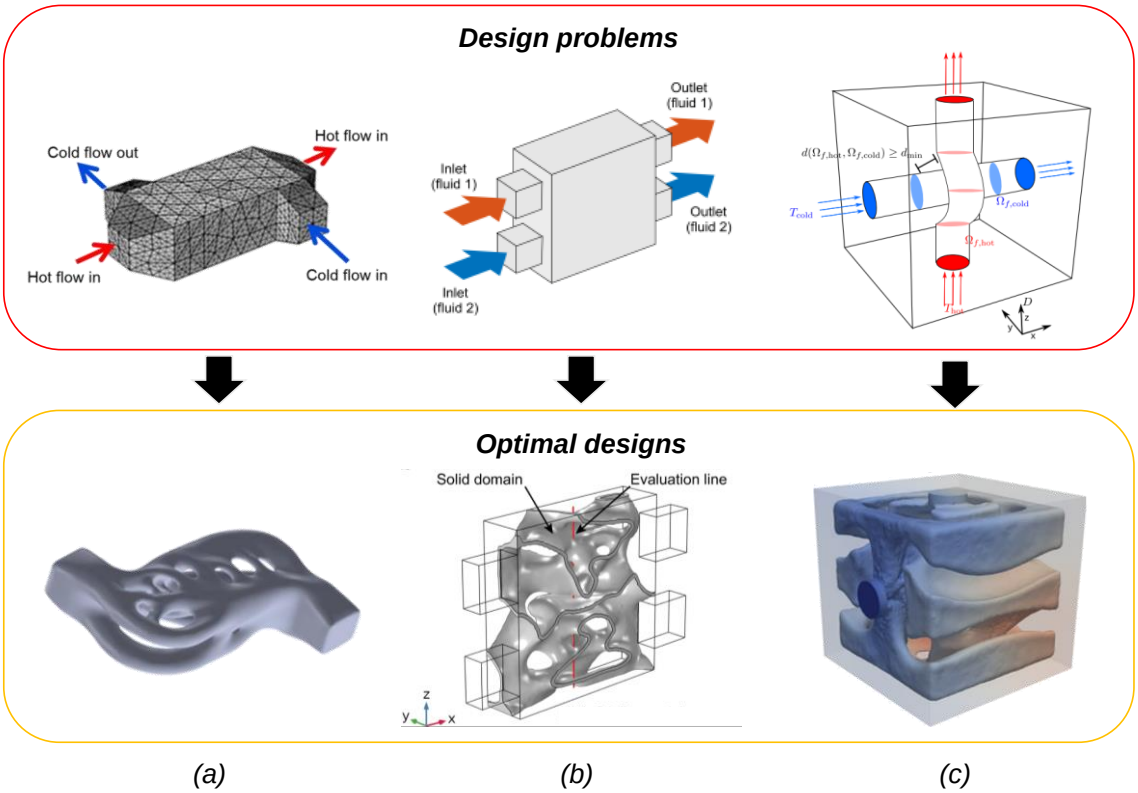

Figure 3.14 Example of design problems and TO-based designs for fluid-to-fluid heat exchangers: (a) Saviers et al. [194]***; Kobayashi et al.*** [193]***; Feppon et al.*** [195]***.***

The topological optimization of fluidic diodes has been studied by Lin et al. [196]. Fluidic diodes are a key safety component to guarantee lower flow resistance in the preferred direction than in the opposite one. The objective function considered was the maximization of the diodicity, defined as the ratio between the pressure drop in reverse over forward flow. A novel numerical strategy was adopted to consider that penalized regions become numerically desirable when maximizing diodicity. An objective function increase of up to +360% was predicted compared to a benchmark design. A few years later, the design of vortex-type passive fluidic diodes was optimized by Lim et al. [197] in the context of advanced nuclear reactors. The generated optimal design was manufactured and tested against commercial solutions. However, no benefits were measured for the generated design, with the lack of performance improvements attributed to significant pressure losses, which were neglected in the approximated 2D model. Intending to provide flow uniformity in a reactor manifold, Kubo et al. [198] optimized the geometry of the fluid channel for Z and U-shaped manifolds. The fluid total potential energy was adopted as an objective function, and an inequality constraint was imposed on the flow rate deviation.

Similarly, the optimal duct layout for HVAC systems was obtained by Manuel et al. [199]. Compared to state-of-the-art layouts, the TO-based design was predicted to lead to a 50% pressure drop reduction. However, a +75% increase in the ducted area was obtained during the design post-processing. Finally, Table 3.2 summarizes the latest research on the topology optimization of energy intensification devices reviewed in this section.

Table 3.2 Summary of the latest research (post-2009) on TO for energy intensification devices analysed in this section.

Device type	Application	Physical model	Ground domain	Objective function	Study state	Design model	Optimizer	Realization	Benefits to energy system	Model limitations	Ref.
Heat sink	Electric motor covers	Conjugate HT assuming Newton's law of cooling	3D	Min. of thermal compliance	Steady-state	Density-based	MMA	No	Average temperature reduction of -9% compared to commercial design	Fixed empirical convective coefficients are adopted	[179]
Heat sink	Electronic devices	Conjugate HT coupled with NS equations	Pseudo 3D	Min. of the maximum temperature in the solid substrate	Steady-state	Density-based	MMA	No	Not quantified	Model limited to laminar flows	[189]
Heat sink	Electronic devices	Conjugate HT coupled with NS equations	2D	Min. of average temperature and power dissipation	Steady-state	Density-based	SLP	Yes	Not quantified	Limited to laminar flows	[182]
Heat sink	Electronic devices	Conjugate HT coupled with NS equations	2D	Multi-objective function: min. of the dissipated power and max. of the	Steady-state	Density-based	MMA	no	2% increase in thermal power output and -50% pressure drop	Limited to laminar flows	[183]

				net thermal power							
Heat sink	Electronic devices	Conjugate HT coupled with NS equations	2D	Multi-objective function: max. of heat exchange and min. of the total pressure drop	Steady-state	Density-based	GCMMA	Yes	Maximum surface temperature is reduced by 11.7% compared to a parallel plate design	Limited to laminar flows	[184]
Heat sink	Electronic devices	Conjugate HT coupled with NS equations	Pseudo 3D	Min. of the heat sink thermal resistance	Steady-state	Density-based	MMA	No	13.6% reduction in thermal resistance compared to size-optimized parallel fin heat sink	Limited to laminar flows	[159]
Heat sink	Electronic devices	Conjugate HT coupled with NS equations	3D	Min. of the average temperature	Steady-state	Density-based	MMA	No	≈4K reduction in average temperature compared to optimal designs generated from laminar models	-	[190]
Heat sink	Batteries	Conjugate HT coupled with NS equations	2D	Min. of average temperature and power dissipation	Steady-state	Density-based	Not specified	Yes	The pressure drop and maximum temperature decrease by 47.9% and 2.3 °C	Model limited to Re<300	[181]

									compared to a traditional cooling plate		
Heat sink	LED lights	Conjugate HT coupled with NS equations	3D	Min. of the thermal compliance	Steady-state	Density-based	MMA	Yes	Doubled life expectancy and a 50% cut in operational cost	-	[188, 200]
Heat sink	Electronic devices	Pure heat conduction	3D	Max. of temperature variance	Steady-state	Density-based	MMA	Yes	The time to reach the extreme temperature is increased by +350% compared to commercial designs	The intrinsic time-dependent physics was approximated to a stationary case	[201]
Fluid-to-fluid HE	Power plant condenser	Conjugate HT coupled with NS equations	2D	Min. of thermal compliance	Steady-state	Density-based	GCMMA	No	36% increase in thermal conductance compared to a literature benchmark	Model limited to fully-developed laminar flows	[158]
Fluid-to-fluid HE	not specified	Conjugate HT coupled with NS equations	3D	Max. of e sum of the total HT in fluid 1 and fluid 2	Steady-state	Density-based	SLP	No	+407% HT rate compared to a reference design composed of straight flow channels	Limited to laminar flows	[193]

Fluid-to-fluid HE	Aerospace applications	Conjugate HT coupled with NS equations	3D	Max. of the heat exchange effectiveness	Steady-state	Density-based	GCMMA	Yes	50% pressure drop reduction and +10% HT rate	Limited to laminar flows	[194]
Fluid-to-fluid HE	Not specified	Conjugate HT coupled with NS equations	3D	Max. of the sum of the total HT in fluid 1 and fluid 2	Steady-state	Level-set	In-house optimizer	No	Not quantified	Limited to laminar flows	[195]
Fluidic diodes	Fixed geometry fluid diodes	NS equations	2D	Max. of diodicity	Steady-state	Density-based	MMA	Yes	Diodicity increased up to +360% compared to commercial solutions	Limited to Re<300	[196]
Fluidic diode	Nuclear reactors	NS equations	2D	Max. of diodicity	Steady-state	Density-based	MMA	Yes	The experimental testing did not demonstrate performance improvements compared to a commercial benchmark	Model limited to laminar flows and did not account for significant pressure loss terms	[197]
Manifold	Microchannel reactors	NS equations	2D	Max. of flow uniformity	Steady-state	Level-set	In-house optimizer	No	Not quantified	Model limited to Re<100	[198]

Manifold	HVAC	NS equations	2D	Min. of dissipated power	Steady-state	Density-based	MMA	No	50% pressure drop reduction compared to benchmark layouts	Significant duct area increase during the optimal design post-processing	[199]
Manifold	Electronics cooling, solar energy, fuel cells, etc.	NS equations	2D	Max. of flow distribution	Steady-state	Density-based	MMA	No	Similar flow distribution with a 21% pressure drop reduction	Less accurate than other optimization pathways examined	[202]

3.3.2 Energy conversion devices

In energy conversion devices, both energy state and energy type are varied. The energy conversion devices for which the application of the topology optimization algorithm is reported in the literature are fuel cells, solar cells and methane reactors.

Fuel Cells are electrochemical devices used to convert chemical energy into electricity. The operation of fuel cell devices strongly depends on how reactants, such as hydrogen and methane, are distributed to the active sites. The first efforts to apply topology optimization to the design of fuel cells were carried out by Kim and Sun [203]. Although valuable results were obtained, the work relied on a simplified electrochemical model that adopted a linear reaction rate in a single-component advection-diffusion equation. Moreover, the resulting geometries were characterized by a limited convergence to binary manufacturable designs. More recently, Behrou et al. [156] added essential features to the physics description of proton membrane fuel cells, reducing the gap between the analysis model and the real application. The reactants distribution flow field was thus obtained to maximize the power generation and the homogeneity of the current density distribution. In the instance of low-pressure drops (5 *Pa*), the Topology Optimization-based design yielded a +5.7% increase in average current density with respect to a literature benchmark with a parallel flow path and up to a +248.6% increase with respect to a serpentine flow, as summarized in Figure 3.15.

Furthermore, Onishi et al. [204] adopted a level-set approach to identify the optimal structure for the electrolyte-anode interface in solid oxide fuel cells. The objective function was formulated so that the total reaction current was maximized. The emerging design trends exhibited the optimal interface structure to present multiple branches at the top-side and complex sub-structures at the bottom side, with number and topology of such sub-

structures depending on the material properties. Improvements in the reaction current up to +22.2% were predicted compared to state-of-the-art designs.

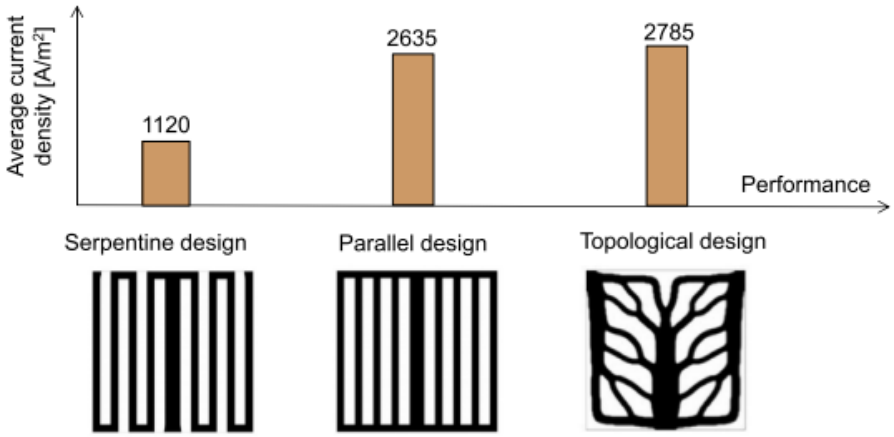

Figure 3.15 Performance comparison for commercial designs and the TO-based design from Behrou et al. [156]***.***

In recent years, topology optimization has been applied to the performance enhancement of solar devices. In a seminal paper, Wang et al. [205] optimized the light-trapping efficiency in solar cells. The optimization approach was aimed at achieving a low-cost thin film for PV panels with desired light-trapping performance. A density-based approach was adopted for the optimal distribution of air and dielectric materials. The absorption efficiency of the optimized design was predicted to overcome the so-called Yablonovitch limit (+300%), and the obtained broadband optimized pattern was successfully fabricated utilizing the electron beam lithography in a follow-up work [206].

A few years later, Gupta et al. [207] optimized the front electrode patterns. The metallic pattern topology aimed to reduce cell resistance to counterbalance the poor silicon conductivity, with the solar cell power output adopted as the objective function. However, the emerging design trends, depicted in Figure 3.16, were not predicted to outperform commercial solutions. The authors attributed this lack of performance to intermediate

materials which emerged during the optimization and concluded that more robust filtering techniques could generate clear black and white optimal design with superior performance. Finally, in the context of solar reactors, Jia et al. [208] adopted TO to optimise the thermal decomposition of methane reactions. A multi-objective problem was formulated to maximise heat transfer entropy generation and minimise viscous dissipation. The generated TO design was predicted to outperform a base case design, with a 7.7% increase in the conversion rate. However, the numerical problem complexity required a simplified reaction rate simplification, limiting the optimisation approach's accuracy. A summary of the reviewed studies is provided in Table 3.3.

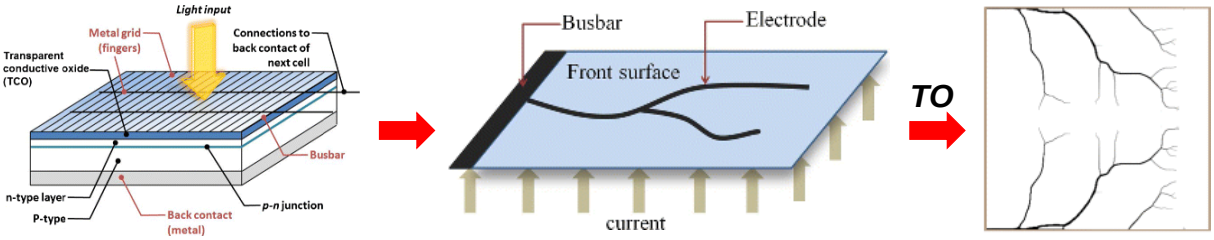

Figure 3.16 TO application to the performance enhancement of solar cells from Gutpa et al. [207]***: (a) schematic of a solar cell operation; (b) Description of the topological problem for the power output maximization of a solar cell; (c) Example of electrode patterns.***

Table 3.3 Summary of the latest research (post-2010) on TO for energy conversion devices analysed in this section.

Device type	Application	Physical model	Ground domain	Objective function	Study state	Design model	Optimizer	Realization	Benefits to energy system	Model limitations	Ref.
Solar cell	Light trapping in PV panels	Ohm's law	2D	Max. of the power output from the solar cell	Steady-state	Density-based	MMA	No	No enhancement was predicted compared to an optimized H-pattern design	advanced filtering methods were required to obtain more black and white designs	[207]
Solar cell	Light trapping in PV panels	Rigorous Coupled Wave Analysis (RCWA) method	2D	Max. of the broadband absorption efficiency	Steady-state	Density-based	GA	Yes	3-fold increase over the Yablonovitch Limit with the broadband absorption efficiency of 48.1%	-	[205, 206]
Methane reactor	Thermal decomposition of methane reaction	Conjugate heat transfer, NS equations, species transport and reaction kinetics equation	2D	Multi-objective: max. of heat transfer entropy generation and min. viscous dissipation	Steady-state	Density-based	GCMMA	No	+7.7% increase in conversion rate compared to a benchmark	A pseudo-homogeneous model was adopted for the reaction rate representation	[208]
Fuel cell	Fuel cells for the	Simplified electrochemic	2D	Max. of the reaction rate	Steady-state	Density-based	MMA	No	Not quantified	A simplified electrochemical	[203]

	automotive industry	al model with single advection-diffusion equation								model was adopted	
Fuel cell	Power generation	Species transport, NS equations and reaction kinetics equations	2D	Max. of power output and flow homogeneity	Steady-state	Density-based	GCMMA	No	+248.6% increase in average current density with respect to a serpentine design	-	[156]
Fuel cell	Power generation	Species transport and reaction kinetics equations	2D	Max. of the total reaction current in the anode	Steady-state	Level-set	In-house code	No	+22.2% increase in reaction current	-	[204]

3.3.3 Energy storage devices

Energy storage devices are defined here as devices in which energy is accumulated to be delivered a second time. The energy storage devices for which application of the topology optimization algorithm is reported in the literature are batteries, sensible thermal energy storage, latent heat thermal energy storage and thermochemical energy storage.

In the framework of batteries and micro-batteries design, Zadin et al. [209] adopted TO to configure the coating of current collectors. A level-set approach was considered to describe the distribution of active material, and the maximization of the electrochemical activity homogeneity was adopted as the objective function. The optimization results demonstrate a non-uniform active material distribution to lead to a cell performance improvement of up to 2.25 times more than conventional uniform coatings. Mitchell et al. [210] adopted TO for the 3D structuring of multifunctional silicon anodes for lithium-ion batteries. The key design challenges related to the silicon anode structure were addressed, specifically the induced mechanical degradation and the low electrical conductivity. To this extent, a multi-objective problem was considered including compliance minimization and electrical conduction maximization. The Pareto front for the multi-objective problem was derived, demonstrating a clear compromise between the competing design objectives, as can be appreciated in Figure 3.17. A rigid frame structure resulted as an efficient trade-off between the two criteria.

In the context of vanadium redox flow batteries, Yaji et al. [211] adopted topology optimization to configure flow fields for the effective distribution of the reactants. The optimization problem considered was the maximization of the generation rate of vanadium

species and was governed by a simplified electrochemical reaction model similar to previous works on microfluidic reactors [212].

Nonetheless, a key novelty of the work was the use of mass transfer coefficient terms as a function of the velocity field. In such a way, the mass transfer coefficients could be used to express the reaction conversion inside the porous medium domain. However, the authors also mentioned the need for higher prediction fidelity of the electrochemical reaction to better express the reaction phenomena in the flow field of VRFBs.

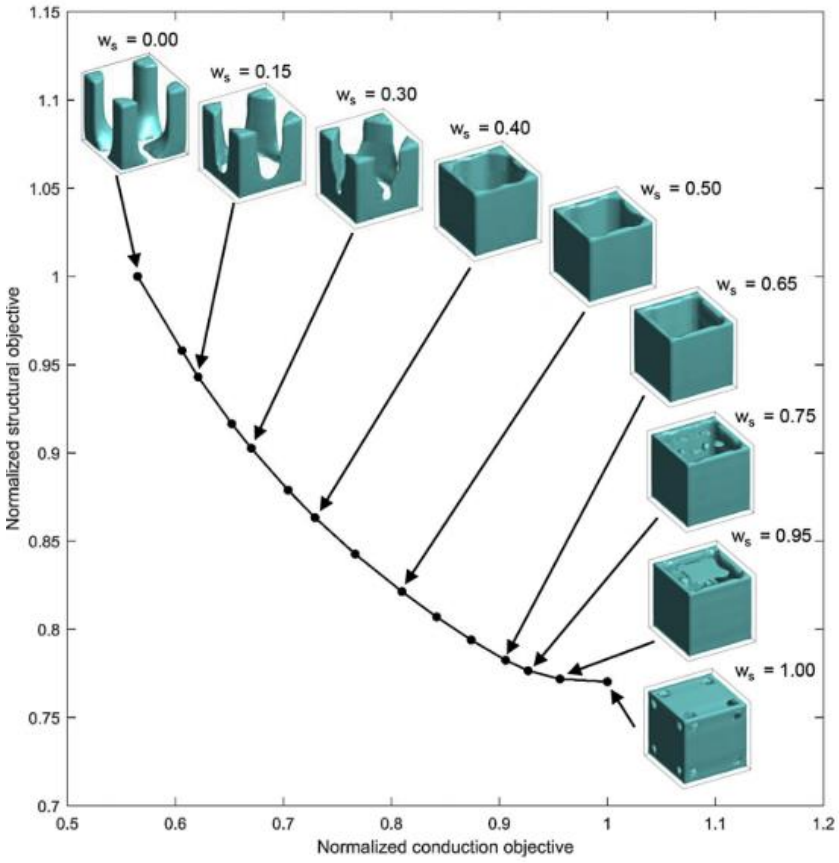

Figure 3.17 The Pareto front and corresponding optimal topologies for lithium-ion batteries from Mitchel et al. [210]***.***

Concerning TES technologies, only a single study has been reported in the literature on the performance maximization of sensible heat storage devices by Lundgaard et al. [161]. Packed bed configurations were analysed, with the distribution of sand and gravel in a 2D planar domain

considered as a design variable. The optimization problem was expressed as the maximization of the heat flux exiting the outlet boundary. The results exhibited a +46% increase in the objective value compared to a literature benchmark. However, the final design presents geometrical features with a problematic interpretation and manufacturability.

Compared to SHS devices, a larger number of publications have been devoted in the last years to the performance enhancement of LHTES devices. The seminal work in this field was published in 2017 by Pizzolato et al. [157]. Here, the optimal architecture of radial fins in a shell-and-tube configuration was analysed during the device discharge. Three optimization problems were formulated: (i) the maximization of the amount of energy discharged, (ii) the minimization of the discharging time and (iii) the thermal power output steadiness maximization. Interestingly, problems (i) and (ii) converged to the same Pareto front. A few years later, the work was extended to include natural convection in the analysis model [157]. The emerging design trends exhibited asymmetric fins geometries which could hardly be revealed with alternative design pathways. Compared to a reference design with a longitudinal fin, the optimized designs lead to superior performance, with 37 % and a 15 % faster charge and discharge, respectively.

The focus was then shifted to the design of multi-tube shell-and-tube devices and the influence of operating conditions and material properties in [213]. The results demonstrated designs obtained considering single pipes, i.e. based on periodicity assumptions, to lead to sub-optimal performance. Besides, the optimal design result was strictly connected to the operating process, making the use of fit-for-purpose design tools a necessity. Finally, a representative optimized design, reported in Figure 3.18, was manufactured and tested by Ge et al. [144]. Here, a 57.1% reduction in discharging time was measured compared to a literature benchmark.

An alternative route for the performance maximization of LHTES devices was taken by Yao et al. [214]. Here, the optimal design of fluid channels in a planar domain filled with a phase change material was investigated. A 32% reduction in charging time was measured compared to a

benchmark design. However, the generated and manufactured TO-based design presented sharp bends and surfaces which needed to be smoothed during the design process. Finally, in the instance of thermochemical energy storage reactors, Chen et al. [215] enhanced the charging process of a $Ca(OH)_2$ reactive bed. The optimal HCM distribution was targeted to maximise the reaction advancement at a fixed time. Multi-tube configurations were considered, and the number of pipes varied in the analysis. Heat conduction was observed as the driving heat transfer factor, with a negligible influence of the reactant transfer on the optimal fins architecture. A 43% charging time reduction was predicted compared to a literature benchmark with longitudinal fins. A summary of the reviewed studies is provided in Table 3.4.

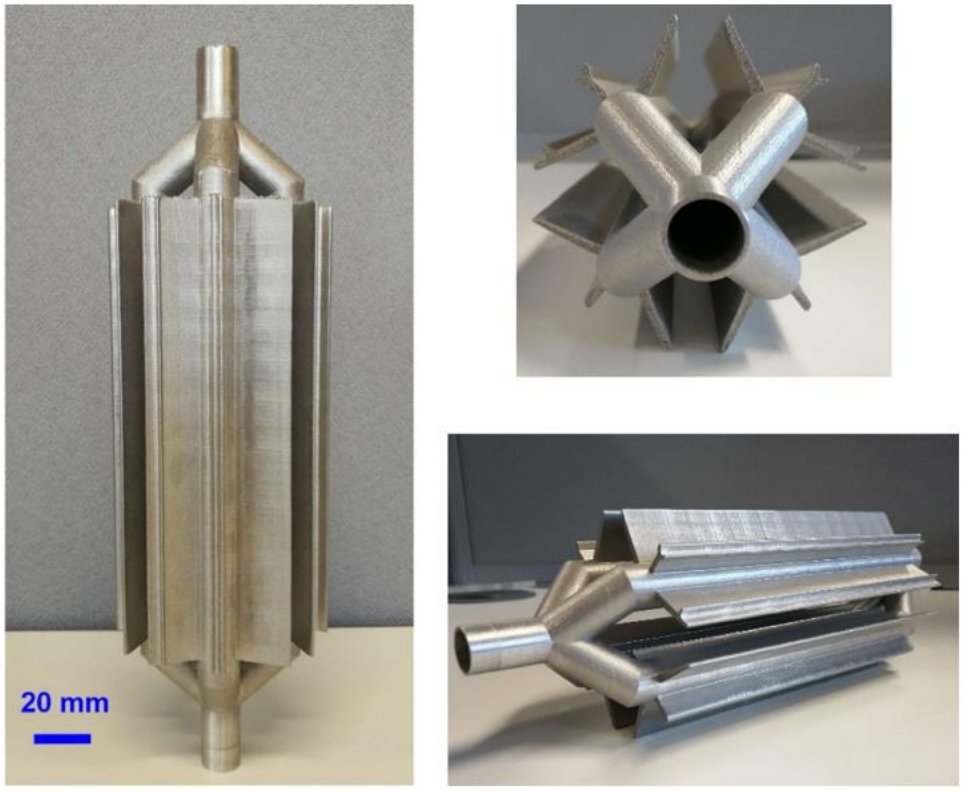

Figure 3.18 Manufactured topology-optimized device tested by Ge et al. [144]**.**

Table 3.4 Summary of the latest research (post-2010) on TO for energy storage devices analysed in this section.

Device type	Application	Physical model	Ground domain	Objective function	Study state	Design model	Optimizer	Realization	Benefits to energy system	Model limitations	Ref.
Battery	Power storage for portable devices	Species transport and reaction kinetics equations	3D	Homogeneity of current density	Steady-state	Level-set	In-house optimizer	No	225% increase in current density homogeneity	-	[209]
Lithium-ion battery	Power storage for portable devices	Elastic problem and Ohm law	3D	Compliance min. and the electrical conduction max.	Steady-state	Density-based	GCMMA	No	Not quantified	-	[210]
Redox flow battery	Large-scale energy storage	Simplified electrochemical reaction model	2D	Max. of the Vanadium generation rate	Steady-state	Density-based	SLP	No	Not quantified	Low prediction fidelity in the analysis model	[216]
SHS	Not specified	Conjugate HT coupled with NS equations	2D	Max. of the heat flux on the outlet boundary	Time-dependent	Density-based	In-house optimizer	No	46% increase in the heat flux at the outlet interface compared to benchmark	Final designs presented difficult interpretation and manufacturability	[161]
LHTES	industrial applications	Conjugate HT coupled with NS equations	2D	Min. of pressure drop and max. of thermal power output	Time-dependent	Density-based	MMA	Yes	Up to 32% reduction in charging time is	Smoothing of the generated channels	[214]

									measured compared to benchmark	was required	
LHTES	industrial applications	Conjugate HT coupled with NS equations	2D	Max. of the average temperature and min. of capacity dissipation	Time-dependent	Density-based	GCMMA	No	Melting and solidification time reduced by 93% and 80%, respectively	-	[217]
LHTES	domestic heating	Heat conduction	2D, 3D	Max. of discharged energy, min. of discharging time and max. of power output steadiness	Time-dependent	Density-based	MMA	Yes	Not quantified	Natural convection was not included	[157]
LHTES	domestic heating	Conjugate HT coupled with NS equations	2D	Min. of charging and discharging times	Time-dependent	Density-based	GCMMA	Yes	37 % and a 15 % faster charge and discharge, respectively	-	[218]
LHTES	domestic heating	Conjugate HT coupled with NS equations	2D	Min. of charging and discharging times	Time-dependent	Density-based	GCMMA	Yes	Not quantified	-	[213]
TCS	Industrial applications	Conjugate heat transfer, Darcy law and reaction kinetics	2D	Max. of reaction advancement	Time-dependent	Density-based	GCMMA	No	44% improvement in reaction advancement	Interfacial resistance was not accounted for	[215]

3.4 Conclusions

In this chapter, the concept and applications of topology optimization were presented. Particular emphasis was made on the use of this systematic tool to generate innovative designs with non-trivial geometrical features that can unlock energy devices' full potential. In such a context, the use of topology optimization as a design tool for the performance maximization of energy conversion, energy intensification, and energy storage devices was reviewed. In recent times, a positive trend has been observed even in well-established technologies such as heat exchanger devices, thus indicating the high potential and interest in the methodology. However, only a single study was published on the application of topology optimization for high-temperature TCS devices in the closed mode [215].

Furthermore, the chapter introduced the main parameters influencing the generation of optimal designs. The effect of these parameters was discussed by means of two numerical examples involving pure heat conduction physics. The algorithm presented in this chapter is used in chapters 5, 6 and 7 of this thesis in combination with advanced numerical tools for the performance enhancement of thermochemical energy storage reactors.

Chapter 4

Heat transfer enhancement in closed system reactors through surrogate models

As reviewed in chapter 2, the existing literature identifies heat transfer as the key limiting factor in TCS reactors operated in the closed mode [31]. While relevant progress has been made in developing new TCMs with tailored properties, poor efforts have been put into reconfiguring the TCS device architecture so that performance is maximized [7]. Besides, the vast majority of studies have addressed the use of HCM inserts exclusively with the primary purpose of augmenting heat transfer [219], but overlooking their impact on the mass transport aspects. That is, it is not clear from the literature how the design of HCM inserts has to be configured to be concurrently beneficial for heat as well as mass transport phenomena in closed-type TCS reactors. In order to clarify how the interplay between heat and mass transfer affects the optimal positioning of extended surfaces, this chapter analyses the optimal geometry of longitudinal fins in two different reactor configurations. The key distinction between the two configurations lies in the different preferential directions for the heat transfer and mass transfer mechanisms.

Furthermore, the bed properties are considered to vary with the TCM hydration level. In fact, while a reasonably efficient reactants transfer is observed in dehydrated TCMs, the

transfer efficiency reduces for fully hydrated materials. The intent of the analysis is thus also to evaluate how the mass transfer resistance increase along the hydration process can influence the optimal fin size and shape.

In order to achieve the goals mentioned above, surrogate models were adopted [220,221]. Surrogate models are approximations of more complex models and are used in this section to explore a selected design domain and to identify how the most efficient HCM architecture varies with the system desiderata. The use of surrogate models allows thus to study similar geometrical elements for different reactor configurations, with the goal of identifying how the heat and mass transfer interplay affect the optimal positioning of these geometrical elements.

The remainder of this chapter is organized as follows: section 4.1 presents the reactor configuration adopted, the rationale for their selection, and the TCM candidate selected for the investigation. In section 0, the design approach based on the use of the surrogate model is presented, and the FE numerical model for the reactor performance predictions is discussed. Section 4.3 deals with identified optimal designs and discusses the key differences between the optimal geometries for the two reactor configurations analyzed. In section 4.4, the main contributions from this chapter are presented.

4.1 Reactor configurations and material selection

Two types of closed system TCS reactor configurations with branched-fins (BF) are investigated: i) axial distribution systems (ADS) reactors and ii) radial distribution systems (RDS) reactors. These two configurations were selected as they present the different preferential directions for the heat transfer and mass transfer mechanisms, as detailed

further in this section. Figure 4.1 presents both configurations and the rationale leading to the representative geometries modelled in this chapter. For both storage module configurations, the whole TCS system was considered modular and constituted of multiple TCS reactors. Each reactor is positioned inside a shell supplied with vapour through an evaporator/condenser unit. The heat delivered to the TCM during the charging process is transferred by means of the branched-fins, resulting in faster water molecules desorption. In the same way, effective reactive bed cooling during the TCM hydration step leads to higher discharge rates.

The two TCS reactor configurations analysed present different vapour distribution systems, as shown in Figure 4.1. Concerning ADS-reactor, the vapour channels are distributed along the HTF pipeline direction, while the vapour channels are distributed along the shell radial direction for the RDS-reactor. Both distribution systems are widely adopted in the literature, e.g. in [20] and [222] for the ADS-reactor, while [118] and [53] for the RDS-reactor.

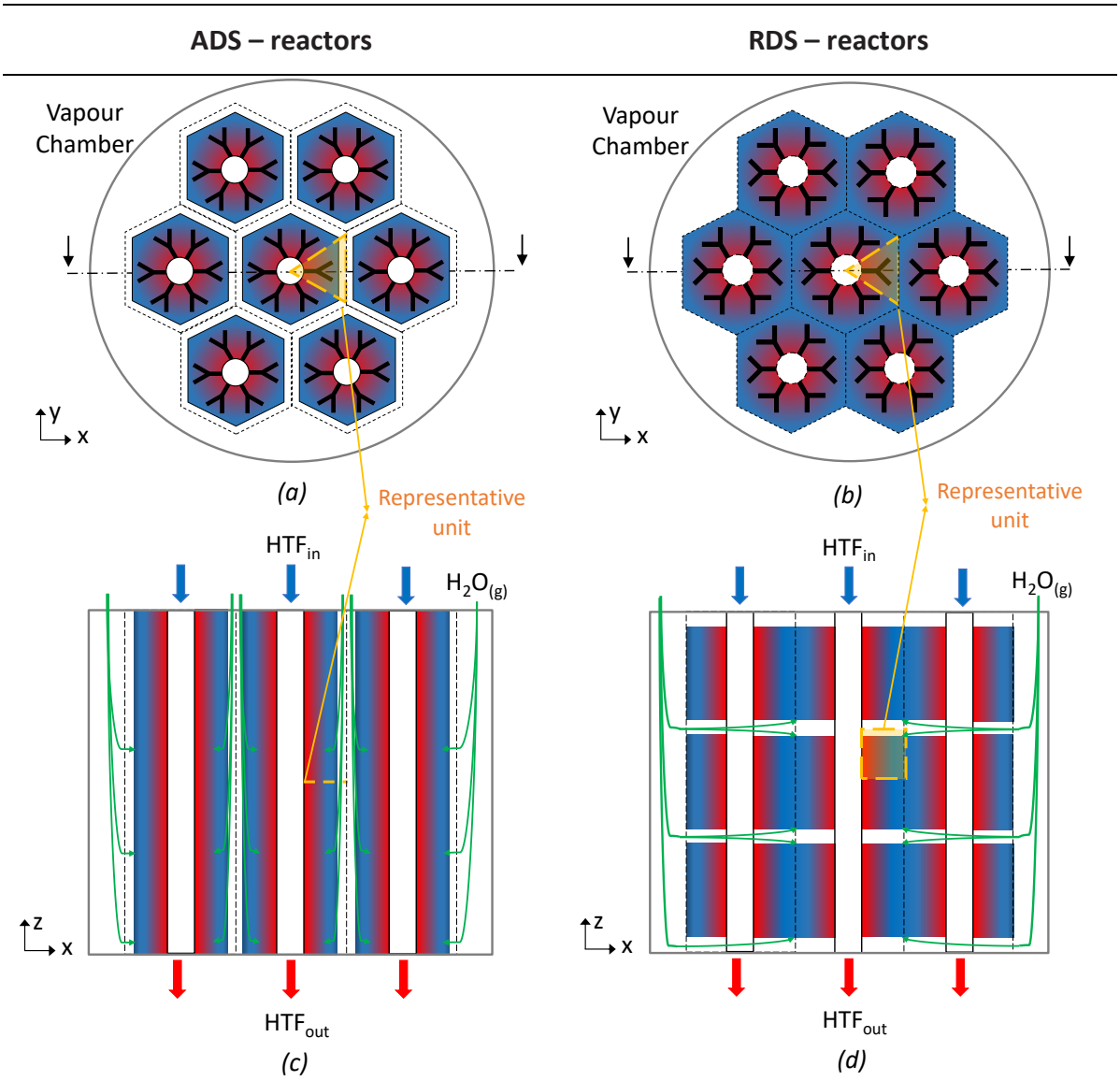

Figure 4.1 Schematic of the storage modules under investigation: (a) top view of the ADS-reactors; (b) top view of the RDS-reactors; (c) axial view of the ADS-reactors; (d) axial view of the RDS-reactors. The orange areas indicate the representative domains adopted for the heat transfer enhancement study.

The definition of the hexagonal cross-section derives from the staggered configuration assumed for the pipeline distribution in the shell and, assuming a fixed distance between pipes, allows for a ≈10% increase in storage material volume compared to circular cross-sections, i.e. cylindrical TCS reactors, as can be appreciated in Figure 4.2.

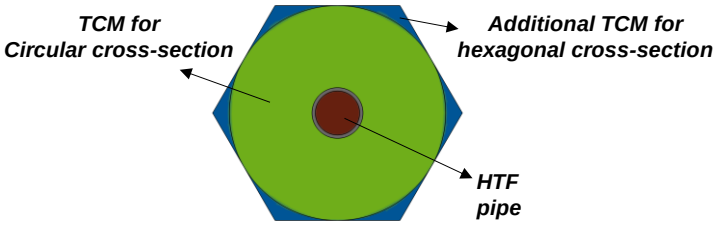

Figure 4.2 Additional TCM volume in hexagonal reactors compared to cylindrical reactors for staggered HTF pipes distribution.

4.1.1 Representative domains and geometrical parameters

Due to the different vapour distribution systems described above, different key preferential directions are observed in each configuration regarding the heat and mass transfer mechanisms, as shown in Figure 4.3. The transfer mechanisms are assumed to occur with a parallel preferential direction for the ADS-reactor [126], and, therefore, a 2D cross-section along the shell radial direction was assumed as a representative unit.

ADS – reactor	RDS – reactor

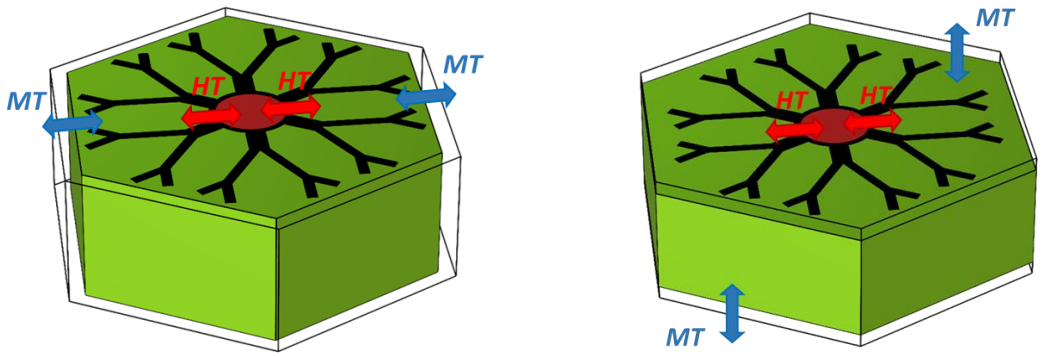

(a) *(b)*

Figure 4.3 Heat transfer (HT) and mass transfer (MT) preferential directions for the ADS- and RDS-reactor configurations.

Regarding RDS-reactors, heat transfer and mass transfer occur with orthogonal preferential directions. That is, the mass transfer phenomena along the axial direction (z-coordinate) are not negligible [110,223], and the thermodynamic behaviour of RDS-reactors must be

addressed by analyzing the heat and mass transfer occurring in the 3D representative unit [75,98,224], as depicted in Figure 4.4.

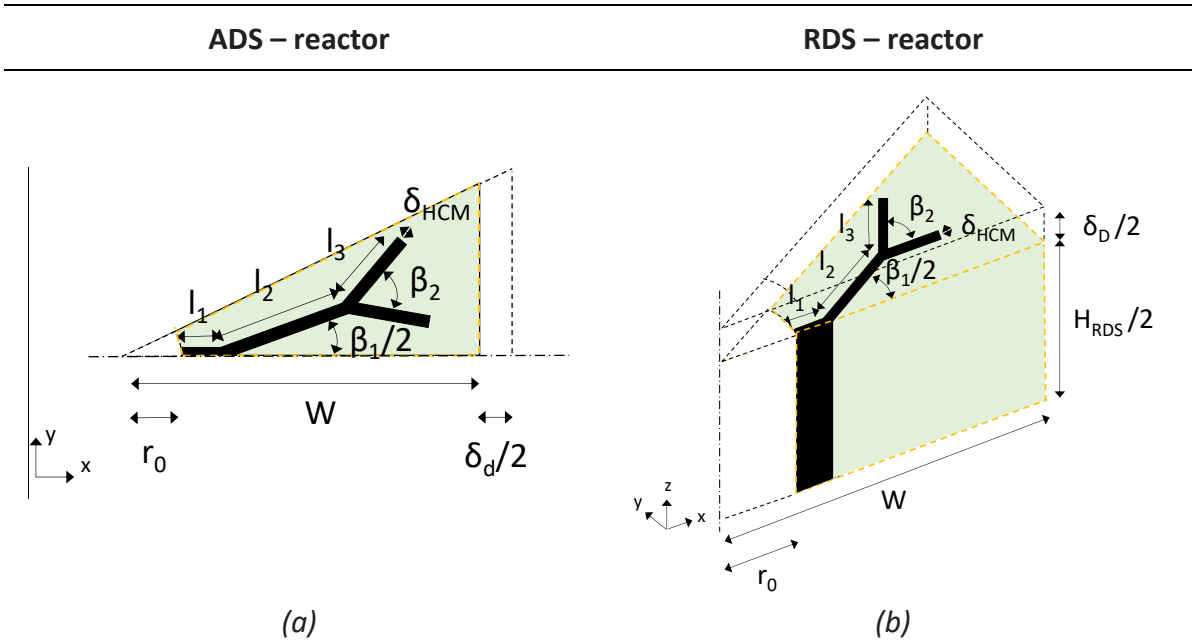

Figure 4.4 Parametrized geometrical parameters for the representative units of (a) ADS-reactor and (b) RDS-reactor, with the green area referring to the computational domains.

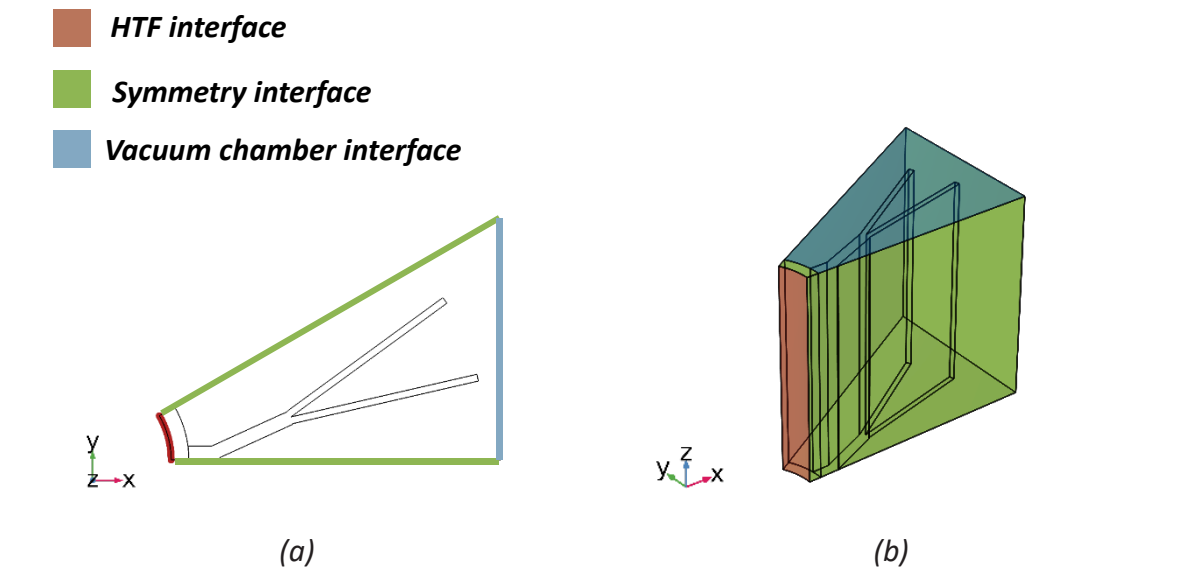

Figure 4.5 Computational domains for (a) ADS-reactor and (b) RDS-reactor, with a colour representation for the HCM/HTF interface (red boundaries), the symmetry faces (green boundaries), and the faces exposed to the vacuum chamber (blue boundaries).

Table 4.1 Dimensions for the RDS- and ADS-reactors' representative units.

Property	Units	ADS-reactor	RDS-reactor
r_o	*mm*	*12*	12
δ_{dif}	*mm*	6	6
δ_{HCM}	*mm*	0.8 - 1.6	0.8 - 1.6
W	*mm*	47	50
H	*mm*	-	70
l_1	*mm*	3.5	3.8
l_2	*mm*	9.5 - 25.3	10.3 - 27.5
l_3	*mm*	6.3 - 22.2	6.8 - 24.1
θ_1	°	30 - 60	30 - 60
θ_2	°	0 - 30	0 - 30
PF	*%*	*10*	10

The computational domains considered in the analysis are illustrated in Figures 4.5 (a) and (b), respectively, for the ADS-reactor and the RDS-reactor. The selected values for the geometrical parameters are listed in Table 4.1. Fixed dimensions are considered for the HTF pipes, r_0, and the vapour diffuser channels, δ_{dif}. The outer radius value of the heat transfer fluid pipes was selected considering the analogy between the investigated modular reactor design with staggered pipes distribution and shell-and-tube heat exchanger [225]. In such an application, small radius values are suggested to attain a larger heat transfer coefficient on the HTF side. However, minimum acceptable sizes must be considered to avoid cleaning

and vibration issues. In this work, a 12 mm outer radius was adopted according to [225] and in agreement with TCS reactor prototypes from the literature [30,226].

Small values are also desired for the diffuser channel size to maximize the amount of volume devoted to the storage material. Nevertheless, the vapour diffuser channel size must be sufficiently large to limit technical challenges during manufacturing and guarantee a homogeneous reactants distribution at the vapour chamber/TCM interface. Following what was reported by Maruran et al. [40] for a 60 kWh modular reactor, a vapour diffuser channel size of $6 \cdot 10^{-3}$ *m* was selected, in agreement also with the gas diffuser size adopted in other TCS reactor prototypes [58,104,227]. The distance between two adjacent HTF pipes was set at $1 \cdot 10^{-1}$ *m* [118], leading to a W value of 50 mm. The height of the RDS-reactor representative unit, H_{RDS}, was set as $2 \cdot (W - r_0 - \delta_{dif}/2)$ to ensure identical distance travelled by the vapour in the two reactor configurations.

The fins' branch lengths were represented by the parameters l_1, l_2, and l_3, while the first and second bifurcation angles were defined respectively by the parameters β_1 and β_2. When the parameter β_2 was set to 0°, radial fins with a single bifurcation are obtained. Besides, the following relationship was adopted between the fins length parameters l_2 and l_3 to ensure the fins length does not exceed the bed size:

$$l_3 = (W - \frac{\delta_{dif}}{2} - r_0 - l_1) - l_2 \qquad 4.1$$

Besides, the comparability between the designs was guaranteed by selecting a fixed packing factor value equal to 10%. The targeted PF value was ensured by tuning the fins thickness, δ_{HCM}.

4.1.2 Operating conditions and TCM selection

In order to better investigate the influence of the interplay between heat and mass transfer in closed system TCS reactors, the interest of this chapter is placed on TCS systems operating at relatively low-vapour pressure values. In particular, TCS systems for domestic heating applications were selected. In such a context, the adopted system thermodynamics constraints were derived considering the TCS charging process to be operated by a solar collector at 80°C [87] and the TCS discharging process to target a heating floor system with the desired temperature of 35°C [228]. During the charging process, an ambient temperature of 35°C was assumed, allowing for a saturation pressure in the condenser of 5.6 kPa, while an ambient temperature of 15 °C was considered during the unit discharge, with the latter leading to an evaporator pressure of 1.7 kPa during the TCS discharge process [40,229]. The resulting thermodynamics constraints fall within the operational range analysed by N'Tsoukpoe et al. in [35]. Here, the authors analysed a series of 125 candidates through a three-step screening approach. Disregarding the economic analysis, the study's conclusions identified three hygroscopic salts as suitable candidates and, given its largest material energy density, $SrBr_2 \cdot 6H_2O$/water was selected in this chapter as TCM:

$$SrBr_2 \cdot 1H_2O + 5H_2O \leftrightarrow SrBr_2 \cdot 6H_2O + \Delta H_r^0 \qquad 4.2$$

Where $SrBr_2 \cdot 1H_2O$ and $SrBr_2 \cdot 6H_2O$ are the monohydrate and hexahydrate salts, while the reactive gas is water. For the selected working pair, the reaction equilibrium pressure, p_{eq}, and the deliquescence pressure [230], p_{del}, are depicted along with the thermodynamics constraints in Figure 4.6. The analysis presented here solely deals with the reactor discharging process. In fact, discharge is the critical process since it delivers the stored energy to the end-user and ultimately determines the applicability of the TCS device.

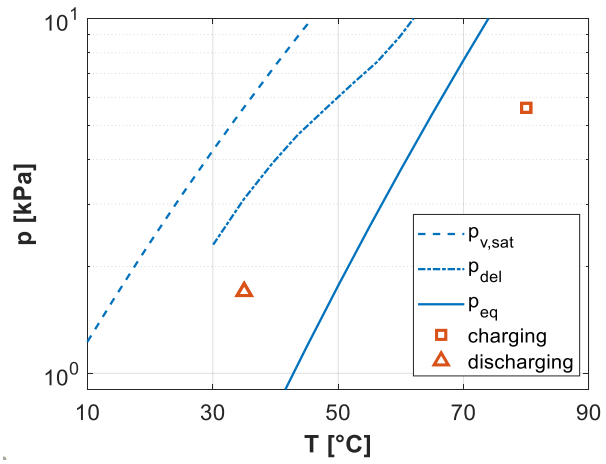

Figure 4.6 Thermodynamic constraints for a TCS system for domestic heating applications and equilibrium pressure curve for the working pair selected in this chapter ($SrBr_2 \cdot 6H_2O$/water).

The material properties for the selected salt hydrate are listed in Table 4.2, with subscript 0 referring to the monohydrate state and subscript 1 referring to the hexahydrate state. Water was used as the Heat Transfer Fluid (HTF), while aluminium was selected as the highly conductive material, with its thermophysical properties shown in Table 4.3.

Table 4.2. Thermophysical properties for the selected TCM: the subscript 0 refers to the monohydrate state, $SrBr_2 \cdot 1H_2O$, while the subscript 1 refers to the hexahydrate state, $SrBr_2 \cdot 6H_2O$ [87]***.***

Property	Value	Unit	Description
ΔH	$3.37 \cdot 10^5$	J/mol_{TCM}	Enthalpy of reaction
Δs	875	$J/mol_{TCM}/K$	Entropy of reaction
γ	5	-	Stoichiometric coefficient
λ_{TCM}	1	W/m/K	Thermal conductivity TCM
$\varepsilon_{TCM,0}$	0.64	-	Porosity monohydrate TCM
$\varepsilon_{TCM,1}$	0.38	-	Porosity hexahydrate TCM
$K_{TCM,0}$	$1.0 \cdot 10^{-10}$	m^2	Permeability monohydrate TCM
$K_{TCM,1}$	$5.0 \cdot 10^{-12}$	m^2	Permeability hexahydrate TCM
$M_{TCM,0}$	266	g/mol_{TCM}	Molar mass monohydrate TCM
$M_{TCM,1}$	356	g/mol_{TCM}	Molar mass hexahydrate TCM
$c_{p,TCM,0}$	456	J/kg/K	Specific heat monohydrate TCM
$c_{p,TCM,1}$	968	J/kg/K	Specific heat hexahydrate TCM
$\rho_{TCM,0}$	3481	kg/m^3	Density monohydrate TCM
$\rho_{TCM,1}$	2390	kg/m^3	Density hexahydrate TCM

Table 4.3. Thermos-physical properties for the selected HCM: aluminium [163]***.***

Property	Value	Unit	Description
λ_{HCM}	237	W/m/K	Thermal conductivity
$c_{p,HCM}$	900	J/kg/K	Specific heat
ρ_{HCM}	2700	kg/m^3	Density

4.2 Design approach and numerical methods

The flow diagram in Figure 4.7 represents the modelling and optimization strategy adopted in this chapter. First, the design problem was defined by the selection of 4 design variables describing the size and shape of the branched fins, namely l_2, l_3, β_1 *and* β_2, along with selecting the performance metrics to investigate the effect of the BF geometry on the reactor operation. Thus, a total of 54 FE simulations were carried out to explore the selected design domain. The derived data points were adopted to fit surrogate models in polynomial shapes. Surrogate models are approximation models that alleviate the FE simulations' computational burden but still allow exploring vast design domains with a large prediction accuracy [221]. The order of the polynomial functions was selected to satisfy an adjusted-R^2 value >0.99. Thus, an additional set of FE simulations was performed to verify the validity of the surrogate models' predictions. Finally, the meta-models were used to identify the optimal designs, with the Matlab optimization toolbox's interior-point (IP) algorithm adopted to search the functions' minimum.

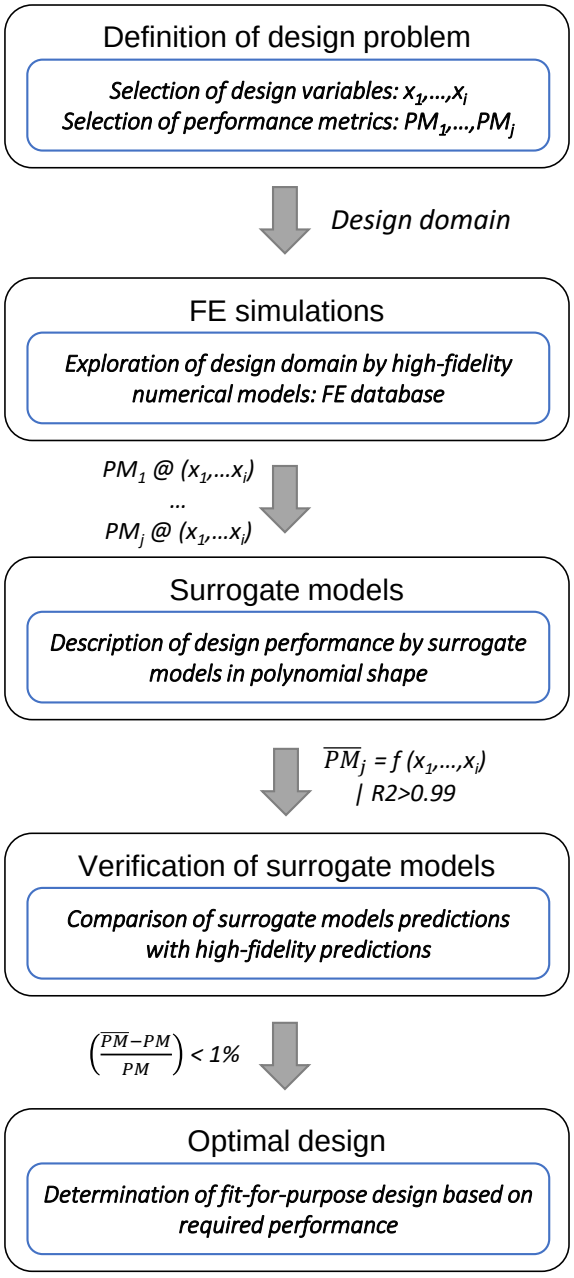

Figure 4.7 flow diagram for the design optimization approach adopted in this chapter.

4.2.1 Governing equations

A time-dependent FE model was developed to investigate the influence of the fins' geometry on the reactor performance. The model expressed the heat and mass transfer mechanisms

taking place in the reactive bed, with the vapour assumed as an ideal gas (temperature *<100°C* and relative pressure *<10 kPa*) [87]. The vapour mass conservation was written as:

$$\varepsilon \frac{\partial(c)}{\partial t} + \mathbf{u}\nabla c = \dot{c}(\dot{\alpha}) \tag{4.3}$$

Where c is the vapour molar concentration, ε is the bed macro-porosity, $\mathbf{u}$ is the velocity vector, $\dot{c}$ is the sink term accounting for the vapour consumed during the TCS discharge and $\dot{\alpha}$ is the time derivative of the reaction advancement. Null influence of the inertial effects on the velocity field was assumed [87]; hence the momentum balance in the porous media followed the Darcy Law:

$$\mathbf{u} = -\frac{K}{\mu}\nabla p_v \tag{4.4}$$

Where p_v is the vapour pressure, K is the permeability, and μ is the dynamic viscosity. Concerning the heat transfer in the reactive bed, three main assumptions were adopted: (i) radiation can be neglected due to the low-temperature values involved in the process, (ii) the reactive solid and the gas phase are in thermal equilibrium [231], as justified by the high solid/gas heat transfer rate usually measured in porous media with small grain size (<0.5 *mm*) [37] and (iii) the convective heat transfer can be neglected in the porous media due to the low vapour density [37]. Thus, the energy conservation was solved in the porous domain as:

$$(\rho c_p)_{eff} \frac{\partial \mathrm{T}}{\partial t} + \nabla \cdot \left(\lambda_{eff}\, \nabla T\right) = \dot{\mathrm{q}}(\dot{\alpha}) \tag{4.5}$$

Where T is the temperature and $\dot{\mathrm{q}}$ is the volumetric heat generation. The effective heat capacity, $(\rho c_p)_{eff}$, and the effective thermal conductivity, k_{eff}, were calculated as the volumetric average values between TCM and vapour:

$$(\rho c_p)_{eff} = (1-\varepsilon)\rho_{TCM} c_{p,TCM} + \varepsilon \rho_v c_{p,v} \quad 4.6$$

$$\lambda_{eff} = (1-\varepsilon)\lambda_{TCM} + \varepsilon \lambda_v \quad 4.7$$

According to [87], the reaction kinetics for the hydration of $SrBr_2 \cdot 6H_2O$ can be described with a 1st order model:

$$\dot{\alpha} = k_{cin}(1-\alpha)\, h(p) \quad 4.8$$

Where $k_{cin} = 1.3\, E-4\, s^{-1}$ is the reaction kinetic constant [30], α is the reaction advancement of the hydration process and $h(p) = (1 - {}^{p_{eq}(T)}/_{p_v})$ is the pressure term, with equilibrium pressure, $p_{eq}(T)$, expressed according to the Clausius-Clapeyron relation:

$$\ln(p_{eq}/p_0) = -\frac{\Delta H}{\gamma R T_{eq}} + \frac{\Delta s}{\gamma R_{gas}} \quad 4.9$$

Concerning the reaction advancement term, this was defined as the ratio between the moles of hydrated TCM at time *t* and the total number of TCM moles in the reactive bed [37]:

$$\alpha\,(t) = \frac{c_{TCM,1}\,(t)}{c_{TCM,bed}} \quad 4.10$$

Therefore, null reaction advancement values correspond to monohydrate salt ($SrBr_2 \cdot 1H_2O$), while a unitary reaction advancement value describes a hexahydrate salt ($SrBr_2 \cdot 6H_2O$). Finally, the volumetric heat generation, $\dot{q}$, and the molar sink term, $\dot{c}$, were expressed as a function of $\dot{\alpha}$ according to equations 4.11 and 4.12:

$$\dot{q}(\dot{\alpha}) = \frac{(1-\varepsilon_0)}{M_{s,0}\,\rho_{s,0}}\,\dot{\alpha}\,\Delta H \quad 4.11$$

$$\dot{c}(\dot{\alpha}) = \frac{(1-\varepsilon_0)}{M_{s,0}\,\rho_{s,0}} M_v\,\dot{\alpha} \quad 4.12$$

The material properties were interpolated between the monohydrate and hexahydrate salt as a linear function of the reaction advancement [37], except for the material permeability,

K, for which a 1/α behaviour was assumed according to [87]. The normalized material properties trend with the reaction advancement is reported in Figure 4.8. While the effective thermal conductivity and the heat capacity values increase hydration levels, an opposite trend characterizes the bed permeability and macro-porosity, ultimately leading to a larger mass transfer resistance in hydrated beds than in dehydrated ones.

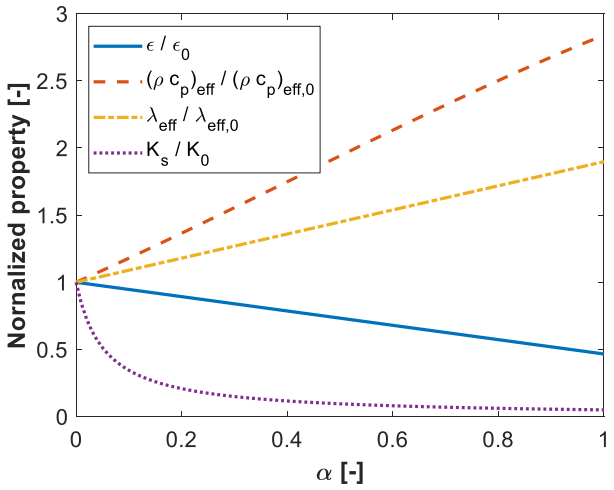

Figure 4.8 Normalized material properties evolution with the reaction advancement.

Concerning the bulk porosity, ε_{TCM}, this is typically provided for the dehydrated state, $\varepsilon_{TCM,0}$; thus, the porosity of the bulk in the hydrated phase was determined as:

$$\varepsilon_{TCM,1} = 1 + (\varepsilon_{TCM,0} - 1) \cdot \frac{M_{TCM,1}\, \rho_{TCM,0}}{M_{TCM,0}\, \rho_{TCM,1}} \qquad 4.13$$

The heat transfer fluid boundary depicted in Figure 4.5 was assumed to be cooled by a convective flux at a constant temperature, T_{HTF}:

$$n \cdot q = h_{HTF}(T_{HTF} - T) \qquad 4.14$$

With a fixed value of *1000 W/m²/K* assumed for the convective heat transfer coefficient, h_{HTF}, in agreement with [169]. Null heat flux conditions were instead considered for the other walls. Concerning the mass conservation equation, a constant vapour pressure value,

$p_{v,in}$, was prescribed for the boundary facing the vacuum chamber, while no-flow conditions were imposed on the other boundaries. The time-dependent study was solved utilizing a 2nd order BDF scheme, with a time-step adaptation scheme considering a maximum time-step of *120 s* [231]. Besides, given the significant pressure disequilibrium at the initial stages of the discharging process, an initial time-step of 10^{-4} *s* was enforced, and the inlet vapour pressure was ramped up from the initial equilibrium value to the selected inlet vapour pressure in a 120 s time range.

Unstructured triangular meshes were adopted, and a swept meshing technique was utilized for the RDS-reactor. Two reference meshes are reported in Figure 4.9, considering each representative unit under investigation and for which identical fins design was considered. Furthermore, the results from the mesh convergence study are reported in Table 4.4. A conservative number of 5500 elements was selected for the ADS-reactors, while a number of elements of 33400 was used for the RDS-reactors.

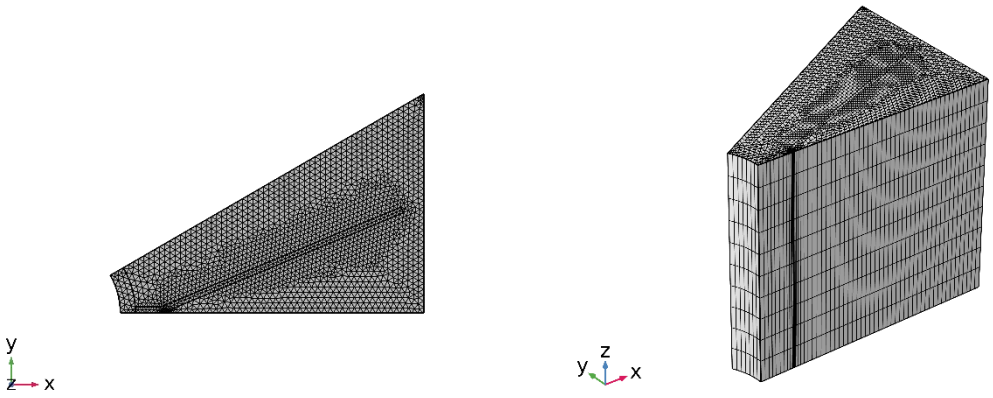

(a) *(b)*

Figure 4.9. Computational meshes adopted in the study for (a) ADS-reactor and (b) RDS-reactor.

Table 4.4 Mesh independence study for the two reactor configurations under investigation.

	ADS-reactor				RDS-reactor			
Number of elements [-]	1800	3800	5500	7300	8200	18200	30400	39400
T_{TCM} (900 s) [°C]	44.39	44.42	44.43	44.43	44.80	44.73	44.74	44.74

The adopted numerical model was validated against the experimental data reported by Lahmidi et al. [49]. Here, the authors measured the local temperatures time evolution in an $SrBr_2 \cdot 6H_2O$ cylindrical bed with a $24 \cdot 10^{-3}$ *m* diameter and $15 \cdot 10^{-2}$ *m* length. The temperature measurements were taken at two radial distances from the HE interface: T_{top} at $1 \cdot 10^{-2}$ *m* and T_b in contact with the heat exchanger surface. The measurements were performed for consecutive charging and discharging processes, and the quantitative comparison of the measured local temperatures with the numerical model predictions is reported in Figure 4.10. A good agreement can be observed, with a maximum discrepancy of 3.9%, indicating a good fidelity for the adopted numerical framework.

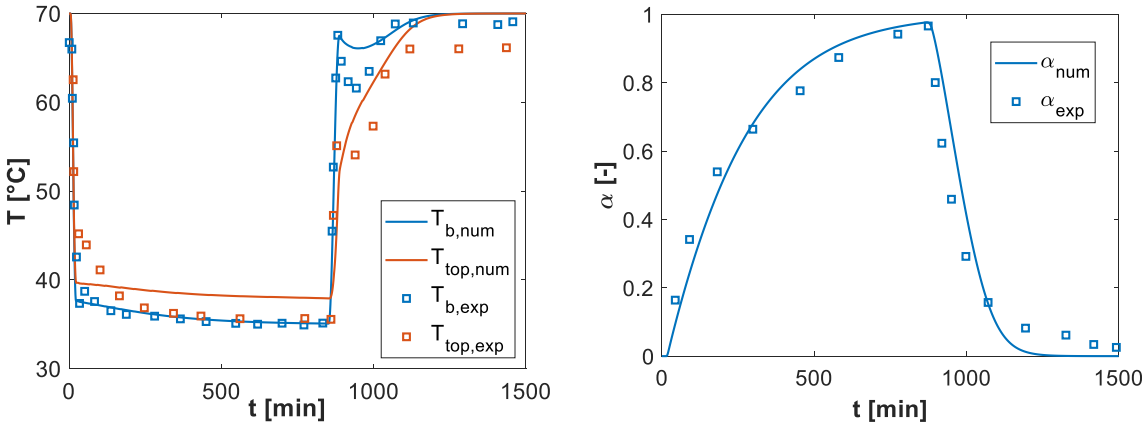

(a) *(b)*

Figure 4.10 Model validation against the data presented by Lahmidi et al. [47]: (a) temperature evolution in time with T_b referring to the temperature measured at the HE surface and T_{top} referring to the temperature measured at a $1 \cdot 10^{-2}$ m distance from the HE interface; (b) reaction advancement in time.

4.2.2 Performance metrics

The following performance metrics were considered to investigate the influence of the fins' geometry on the reactor operation:

1) The reaction advancement:

$$\alpha\ (t^*) = \int_{\Omega_{TCM}} \frac{\alpha\ (\boldsymbol{x}, t^*) d\Omega_{TCM}}{1\ d\Omega_{TCM}} \qquad 4.15$$

The average reaction advancement over the TCM domain, Ω_{TCM}, was adopted to indicate the state of discharge of the storage material at the desired discharge time, t^*. Given the relationship expressed in equation 4.11 and the imposed boundary conditions, the average reaction advancement represents the fraction of stored energy transferred from the storage material to the HTF. Hence, the maximization of the reaction advancement at a time t^* implies the maximization of the discharged energy from the reactor. The desired discharge times were set to 10 h and 20 h.

2) The peak power output:

$$P_{peak} = max(P(t)) \qquad 4.16$$

The peak of specific power is defined as the maximum specific power in time, with the specific power calculated as:

$$P(t) = \frac{1}{m_{TCM}} \int_{\Gamma_{HTF}} \frac{h_{HTF}\left(T_{TCM,j}(t) - T_{HTF}\right) d\Gamma_{HTF}}{1\ d\Gamma_{HTF}} \qquad 4.17$$

Where m_{TCM} is the TCM mass in the reactive bed, h_{HTF} is the convective heat transfer coefficient at the solid/HTF interface, Γ_{HTF}, and $T_{TCM,j}$ is the TCM temperature at the interface and Γ_{HTF} represents the HTF boundary.

4.2.3 Surrogate models

Surrogate models were created from a FE database derived from a series of 27 FE simulations for each reactor configuration under investigation. The design variables were varied in the parameters range reported in Table 4.1. The derived results were adopted as individual observations to explore the sensitivity of the selected performance metrics to the fins geometry. The aim of the surrogate models is to approximate the simulations results and to explicitly track the influence of the design variables on the selected performance metric:

$$PM_j = f_j\ (\beta_1, \beta_2, l_2\ , l_3) \tag{4.18}$$

Thus, the generation of surrogate models consists of defining a function f_j that suitably approximates the FE outcomes. In this chapter, surrogate models in polynomial shapes were considered. Polynomial functions are widely used in the literature due to their ease of implementation, assessment, and integration in optimization strategies [232,233]. The general form of an order *n* multivariate polynomial was written as [220]:

$$f_j = b_0 + \sum_{i=1}^{m} b_i\, x_i + \sum_{i=1}^{m}\sum_{j>i}^{m} b_{ii}\, x_i\, x_j + \sum_{i=1}^{m} b_{ii} x_i^2 + \sum_{i=1}^{m}\sum_{j>i}^{m}\sum_{p>j}^{m} b_{ijp}\, x_i\, x_j\, x_p + \cdots + \sum_{i=1}^{m} b_{ii\ldots i}\, x_i^n \tag{4.19}$$

Where $b_1, \ldots, b_m$ are the polynomial coefficients and $x_1, \ldots, x_m$ represents the design variables, specifically $\beta_1, \beta_2 \text{ and } l_2$ in this analysis. As a result of the relationship in equation 4.1, the design variable l_3 did not appear explicitly in the derived surrogate models, leading to *m*=3. The polynomial coefficients were fit to best approximate the FE predictions using an ordinary least square fitting. The order of the polynomial function, *n*, was instead selected

by an exhaustive search process for the lowest polynomial order leading to an adjusted-R^2>0.99. The resulting order of each generated polynomial function and respective adjusted-R2-values are reported in Table 4.5, while the list of polynomial coefficients is reported in the Appendix. Furthermore, the accuracy of the surrogate models was assessed through the definition of random verification points within the investigated design space. The surrogate model estimates, and the FE results, are depicted in the instance of *α (20h)* considering both ADS-reactor, Figure 4.11 (a), and RDS-reactor, Figure 4.12 (b). The red points refer to the FE dataset adopted for creating the meta-models, while the blue points refer to the verification points. The maximum discrepancy between surrogate model prediction and verification points was below 1.0%, thus indicating high fidelity for the meta-model estimates [221].

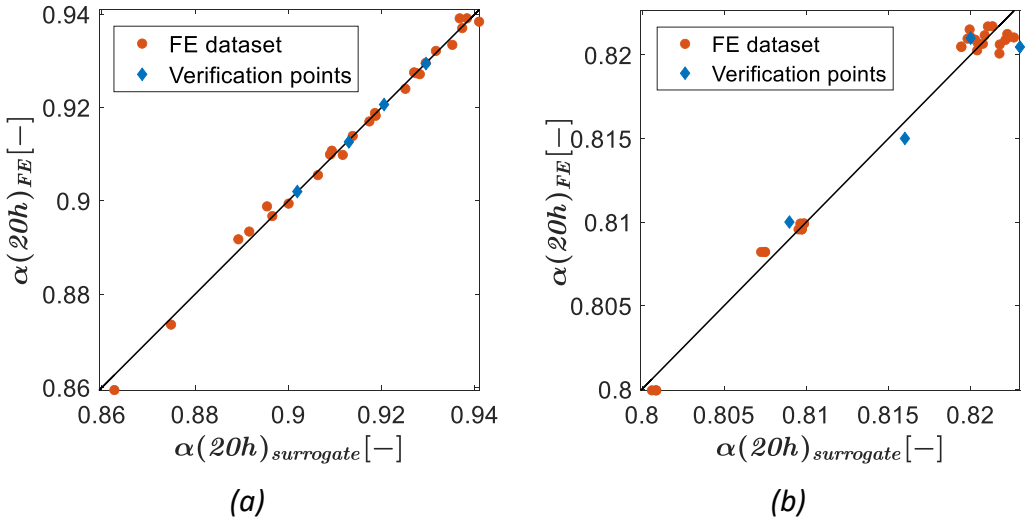

(a) *(b)*

Figure 4.11 Verification of surrogate models accuracy. FE results considering α(20 h) versus surrogate model estimates for (a) ADS-reactor; (b) RDS-reactor.

Table 4.5 Order of the polynomial functions and adjusted-R^2 parameter for the regression models.

	ADS-reactor			RDS-reactor		
	P_{peak}	α (10h)	α (20h)	P_{peak}	α (10h)	α (20h)
n	3	3	2	3	2	2
Adjusted-R^2	0.996	0.997	0.994	0.996	0.997	0.994

4.3 Results

The typical global performance histories in closed system TCS reactors are discussed in the instance of a fixed branched fins geometry for an ADS-rector configuration. Figure 4.12 presents the average temperature and pressure evolutions in time, along with the equilibrium and operating conditions. The difference between the average TCM temperature, T_{TCM}, and the equilibrium temperature, T_{HTF}, represents the temperature driver for the heat transfer from the porous bed to the heat transfer fluid. Such temperature driver varies depending on the HCM architecture, as more efficient extended surface geometries can boost the bed cooling and ultimately reduce the bed temperature. On the other hand, the difference between the bed temperature and the equilibrium temperature, T_{eq}, represents the disequilibrium driver for the reaction kinetics; the larger this difference, the larger the reaction rate. Efficient cooling of the reactive bed benefits the reaction rate, leading to larger $\Delta T_{reaction}$.

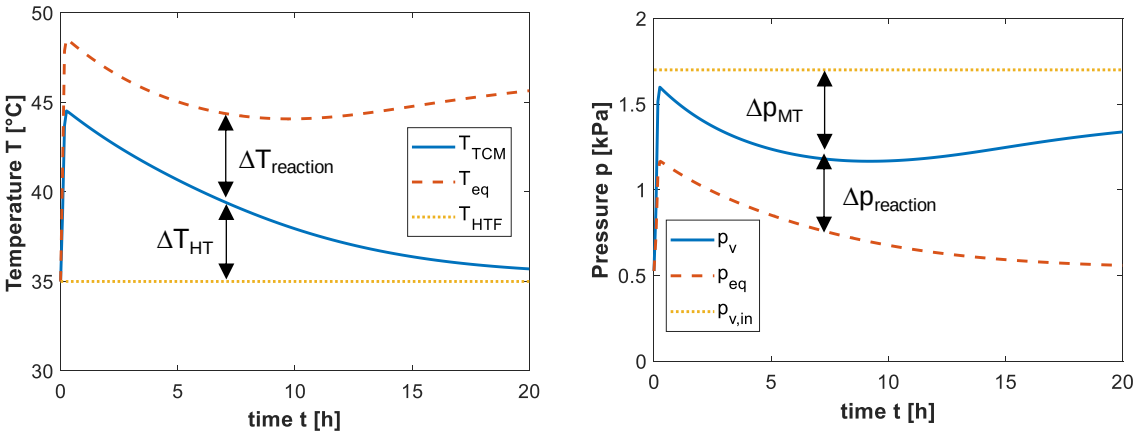

(a) *(b)*

Figure 4.12 Global histories for the ADS-1 design: (a) average temperatures; (b) average vapour pressures.

Concerning the pressure histories, Figure 4.12 (b), the disequilibrium driving the reaction rate, $\Delta p_{reaction}$, is expressed as the difference between the average vapour pressure in the bed and the equilibrium pressure, with the latter derived from equation 4.9, and thus dictated by the bed temperature. The pressure driver for the vapour transfer in the reactive bed is expressed instead by the difference between the average water vapour in the reactive bed and the vacuum chamber conditions. A low Δp_{MT} term is desired, which indicates good mass transfer efficiency for the reactive bed. Nevertheless, as discussed in the following sections, branched fins geometries inserted in the reactive bed can penalize the mass transfer, leading to lower Δp_{MT}.

4.3.1 ADS-reactor

The optimal branched fins geometries obtained employing surrogate models are presented in this section in the instance of the ADS-reactor configurations. For the entire design domain, power output peak was predicted during the initial stages of the hydration process for times below 900 s and low average reaction advancement, below 0.1. The optimal configurations emerging from the structured optimization approach are listed in Table 4.6.

Table 4.6 Optimal design parameters for branched fins in ADS-reactor and comparison with the literature benchmark [110]***. The geometrical parameters definition is reported in Figure 4.4.***

	P_{peak}	α (10 h)	α (20 h)	Benchmark
	ADS-1	*ADS-2*	*ADS-3*	*ADS-b*
l_1 *[mm]*	3.5	3.5	3.5	31.6
l_2 *[mm]*	9.5	9.5	31.6	-
l_3 *[mm]*	22.2	22.2	-	-
β_1 *[°]*	43.7	42.5	30	0
β_2 *[°]*	25	16.4	0	0

The geometrical features characterizing such designs differ depending on the selected performance metric and considered desired discharge time. For systems requiring large peaks of power outputs, branched fins with double bifurcations and large bifurcation angles are favourable, as indicated by the ADS-1 design. This result is in good agreement with the design guidelines for the performance enhancement of pure heat conduction problems derived from constructal theory [92] and topology optimization algorithm [218], thus highlighting a negligible influence of mass transfer during the initial stages of the discharging process. In fact, as described in section 4.2.1, a relatively small mass transfer resistance characterizes the poorly hydrated reactive bed.

Designs adopting double bifurcations remain the preferred geometrical solution for maximising the discharged energy considering a 10 h desired discharge time, i.e. design ADS-2 in Table 4.6. However, a reduction in the optimal β_2 value is predicted compared to ADS-1. This trend is caused by the conflict between heat transfer and mass transfer in the reactive domain. The fins' bifurcations hamper the vapour transfer in the reactive bed, ultimately

reducing the amount of reactants in the regions away from the vacuum chamber interface. Such vapour transfer penalization caused by fins bifurcations is amplified for larger salt hydration states, which entails lower bulk permeability values. As a result, branched fins with single bifurcation, i.e. $\beta_2 = 0°$, emerge as the optimal design when larger desired discharge times, and thus deeper discharge states, are considered.

The impact of the bifurcation angles on each performance metric is shown in Figure 4.13, considering fixed branch lengths. Concerning the maximization of the peak of power output, Figure 4.13 (a), if large secondary fin angles are adopted, e.g. β_2 =25°, performance enhancements up to +7.0% is obtained compared to single bifurcation designs. That is, a significant performance benefit is achieved by employing an HCM architecture evenly distributed in the reactive domain and through which heat can be effectively transferred to the heat transfer fluid wall. The effect of such HCM architecture on the vapour transfer has a negligible impact on the considered figure of merit due to the large bed permeability in the monohydrate salt. On the other hand, when the maximization of the reaction advancement for a *10 h* desired discharge time is considered, Figure 4.13 (b), the optimal β_2 angle is almost halved compared to the previous case, while the optimal β_1 results to be slightly increased, +1.2°.

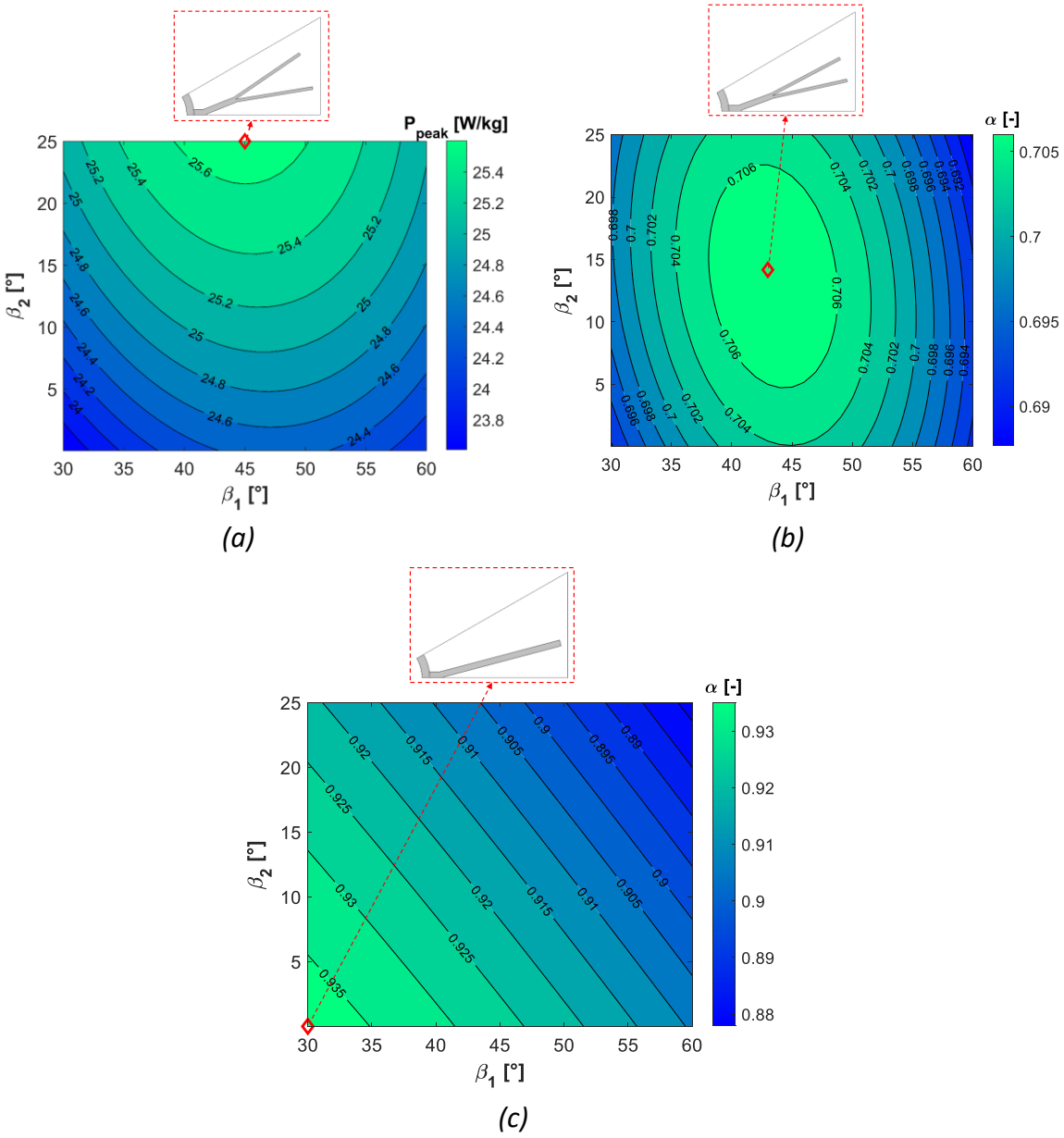

Figure 4.13 Response surface maps versus bifurcation angles in ADS-reactors for (a) peak of power output; (b) reaction advancement after 10 h discharge time; (c) reaction advancement after 20 h discharge time.

Furthermore, it is interesting to notice how only a small performance variation, ≈1.1%, is predicted for the depicted design domain. That is, only a mild performance enhancement is achieved using secondary bifurcations compared to single bifurcations. Such limited improvement is caused by the relatively low permeability value dictated by the reaction advancement values reached at the considered discharge time, reduced to ≈ 7E-12 m^2 for

reaction advancement values of 0.7. Given the poor bed permeability, the heat transfer benefits led by the secondary bifurcation are counter-balanced by its mass transfer penalization effect.

Finally, when a deep discharge state is targeted, as in the case of a *20 h* discharge time depicted in Figure 4.13 (c), a null β_2 angle is preferred. That is, the optimal branched fin geometry does not present a secondary bifurcation. Furthermore, if tree-shaped fins with wide bifurcation angles are selected, a reaction advancement reduction of up to *-8.1%* is predicted compared to the optimal point. This outcome derives again from the significant mass transfer resistance in the porous medium. The fins' geometry does not have to obstruct the vapour transfer in the domain, thus allowing the reaction to occur in the regions away from the vacuum chamber interface.

The influence of the second bifurcation geometry on the reactor performance is further detailed in Figure 4.14. Here, the vertical axis expresses the normalized performance metrics value:

$$\widetilde{f_j}(l_2, \beta_1, \beta_2) = \frac{f_j(l_2, \beta_1, \beta_2)}{\max(f_j(l_2, \beta_1, \beta_2))} \quad 4.20$$

While the horizontal axis refers to the secondary bifurcation angle, β_2.

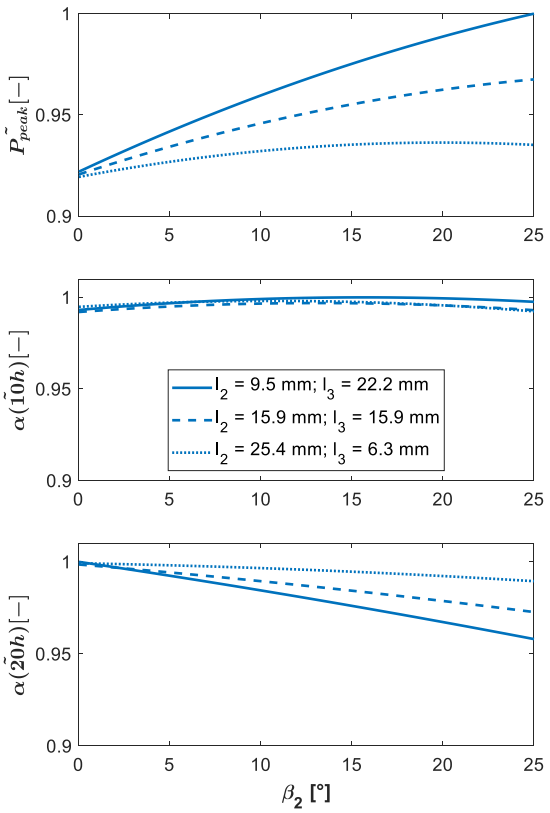

Figure 4.14 Influence of secondary bifurcation on the normalized performance metrics for ADS-reactors: top for the peak of power output; centre for the reaction advancement after 10 h discharge time; bottom for the reaction advancement after 20 h discharge time.

Moreover, the performance metrics value is shown for multiple branches' length, with l_3 dictated by the relationship 4.1. Long secondary branches are favourable for the peak of power output maximization, with a performance increase of up to +7.6% compared to fins with a single bifurcation. On the other hand, this trend flattens when the reaction advancement after a *10 h* discharge time is considered. Here, the size of the second bifurcation mildly impacts the reactor performance maximization, $\Delta\alpha \approx 0.5$. Nevertheless, long secondary branches penalise the reaction advancement after a *20 h* discharging time, with discrepancies between designs' performance up to *4.1%*.

The conflict between heat and mass transfer in ADS-reactors can be appreciated in the contour plots depicted in Figure 4.15. Here, the temperature, vapour pressure, and reaction advancement maps at a fixed time, *10 h*, are compared for a single, $\beta_2 = 0°$, and double bifurcation, $\beta_2 = 25°$, design. For the selected time-step, similar average reaction advancement values are predicted: 0.69 and 0.7, respectively, for the single and double bifurcation design. However, significantly different α-distributions are observed in Figure 4.14 (a) and (b). Homogeneous distribution is predicted for neither investigated design, as higher local reaction advancement is reached in the regions between two fins' branches. In such regions, the fin bifurcations convey vapour, as observed from the vapour pressure contours depicted in Figure 4.15 (c) and (d). On the other hand, secondary bifurcations also limit the reactants' concentration in the regions away from the vacuum chamber interface, with *≈100 Pa* difference in the minimum local vapour pressure compared to the single bifurcation design. As a result, lower local reaction advancement is predicted near the HTF interface in the case of HCM architectures with multiple branches.

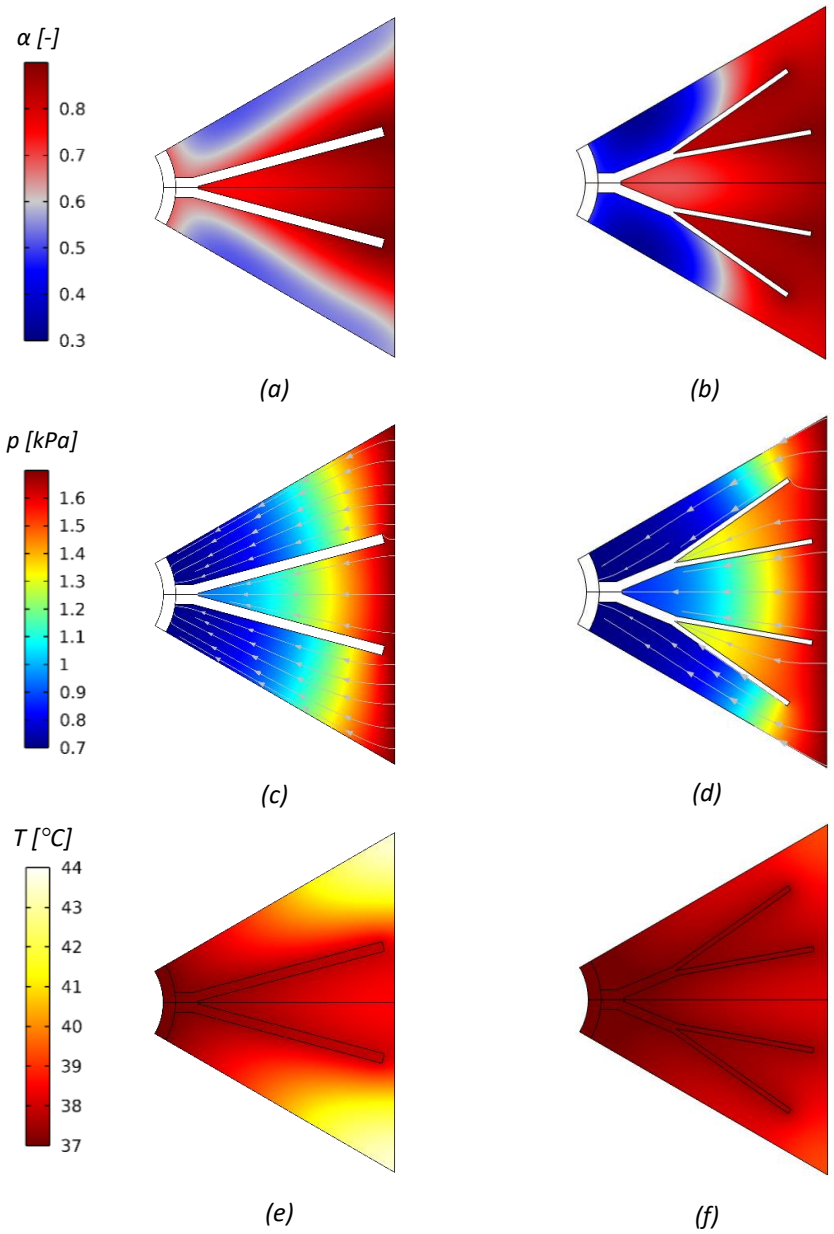

Figure 4.15 Temperature, pressure, and reaction advancement contours in ADS-reactors at a fixed time of 10 h considering a design with single bifurcation, left, and a design with double bifurcation, right.

Nonetheless, HCM architecture with multiple branches effectively cools the reactive material, as indicated by the more homogeneous temperature distribution observed in Figure 4.15 (e) compared to Figure 4.15 (f). Notably, a considerable temperature reduction, -3.8 °C, at the top and bottom corners of the computational domain is predicted for the

double bifurcation design compared to single bifurcation, leading to a ≈28% discrepancy in the local reaction advancement.

4.3.2 RDS-reactor

The best performing branched fins geometries are obtained in this section by optimising surrogate models for the RDS-reactor configuration. The optimal designs are reported in Table 4.7.

Table 4.7 Optimal design parameters for branched fins in RDS-reactor and comparison with the literature benchmark [110]**.**

	P_{peak}	α (10 h)	α (20 h)	Benchmark
	RDS-1	*RDS-2*	*RDS-3*	*RDS-b*
l_1 [mm]	3.8	3.8	3.8	38.2
l_2 [mm]	9.5	9.5	9.5	-
l_3 [mm]	22.2	22.2	22.2	-
β_1 [°]	49.1	46.5	44.9	0
β_2 [°]	23.2	19.4	17.8	0

In contrast to what was observed for ADS-reactors, the results indicated branched fins with large bifurcation angles and long branches as optimal designs for all the performance metrics and desired discharge time adopted in the investigation. No variation is found in the optimal branches lengths for the three design cases, while a slight variation between the optimal bifurcation angles is predicted, with the optimal β_1 and β_2 in the range from *44.9°* to *49.1°* and from *17.8°* to *23.2°*, respectively. Therefore, designers should consider these ranges for configuring RDS-reactors with superior thermal performance. The optimal angles' values

slightly decrease for a larger final discharge time. This trend is dictated by the optimal cooling of the reactive bed, with the optimized branch structure stretching towards the furthest regions from the HTF interface. Overall, the optimal HCM architectures agree with the typical design guidelines for pure heat conduction problems [92,218], thus indicating a negligible influence of mass transfer in selecting efficient fins geometries in RDS-reactors. That is, for reactor configurations where the heat transfer and mass transfer take place in orthogonal preferential directions, a negligible impact of mass transfer is found in the selection of optimal extended surface structures to maximize the reactor thermal performance.

The effect of bifurcation angles, β_1 and β_2, on the performance metrics is presented utilizing response surface maps in Figure 4.16. For all the investigated design cases, performance enhancements are achieved by the use of secondary branches, in particular when sizeable secondary bifurcation angles, β_2 >10°, are employed. Nonetheless, the performance improvement led by optimized bifurcated fins decreases with the considered discharge time. While a *+ 3%* improvement is predicted for the reaction advancement after a *10 h* desired discharge time, Figure 4.16 (b), such improvement reduces to only *+1.6%* when the discharge time is doubled, Figure 4.16 (c). Furthermore, the RDS-reactor operated with the optimized BF design only presents an average final reaction advancement of ≈82%, thus still far from a complete discharge state. This result indicates that heat transfer is not the only limiting factor for the complete discharge of the RDS-reactor.

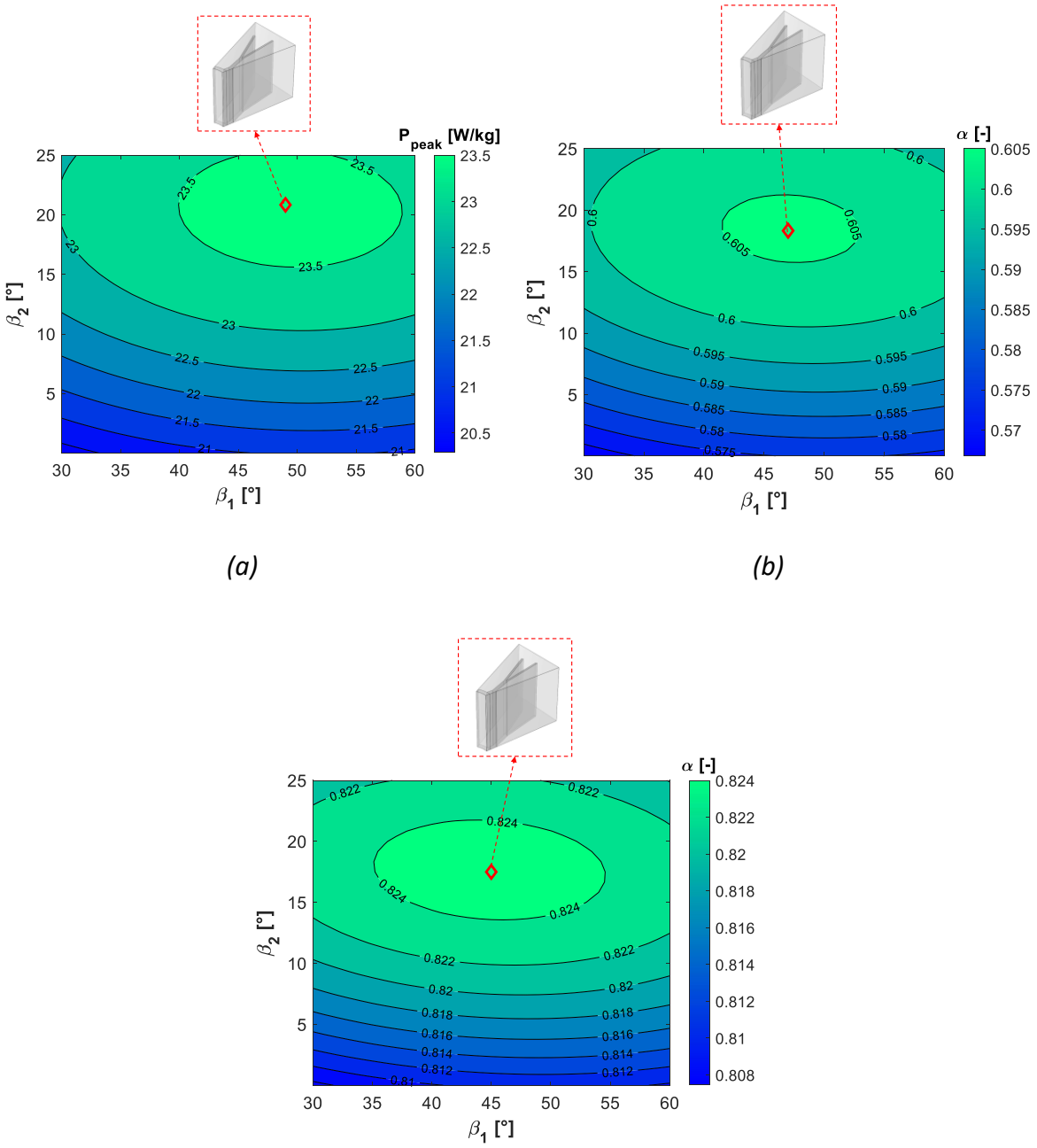

Figure 4.16 Response surface maps versus bifurcation angles in RDS-reactors for (a) peak of power output; (b) reaction advancement after 10 h discharge time; (c) reaction advancement after 20 h discharge time.

Figure 4.17 shows the effect of the secondary branches' geometry on the performance metrics. Again, a considerable performance variation concerns the peak of power output,

with performance enhancements up to +14% achieved by selecting suitable bifurcation geometries.

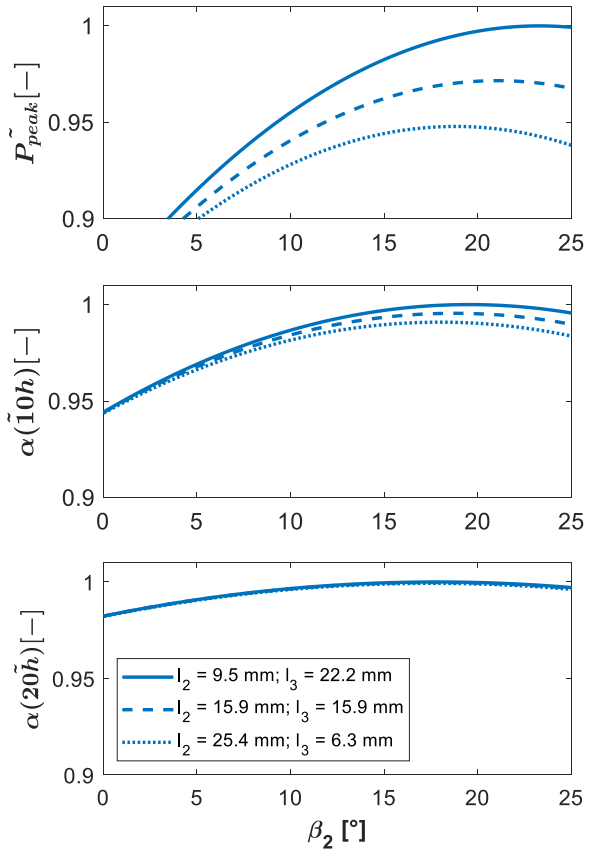

Figure 4.17 Influence of secondary bifurcation on the normalized performance metrics for RDS-reactors: top for the peak of power output; centre for the reaction advancement after 10 h discharge time; bottom for the reaction advancement after 20 h discharge time.

Besides, the optimal β_2 value increases when longer secondary branches are considered, i.e. larger l_3 values. Consequently, an HCM architecture evenly distributed in the reactive domain is particularly advised for designing high-power density RDS-reactors. However, the performance improvements led by secondary bifurcations are milder concerning the reaction advancement metric. In particular, an almost negligible variation is predicted for a 20 h desired discharge time, Figure 4.17 (c). Here, only a *+1.5%* enhancement in the discharged energy is achieved for β_2 values from 0° to 18°, while almost no performance

enhancement, < +0.1%, is predicted by the variation of the branches length. In other words, the reactor performance is almost insensitive to the secondary branch geometry in case of reaction advancements above *80%*.

The effects of double bifurcated fins on the performance of RDS-reactors are further detailed in the contour plots depicted in Figure 4.18. Here, the reaction advancement, vapour pressure and temperature distributions are depicted for a discharge time of *10 h*. Similarly to section 4.3.1, the contours for branched fins designs with single and double bifurcations are compared. Two different planes are examined for the representation of the 3D domain. A *zy* plane is considered at $x = (W - r_0)/2$, while a *xy* plane is considered at $z = H/4$, as can be observed at the top of Figure 4.18.

In contrast to what was observed for ADS-reactors, the reaction front in the shell radial direction, i.e. *xy* plane, is predicted to propagate from the TCM/HCM interface with no preferential directions, as can be observed in Figure 4.18 (a) and (b). Consequently, the under-utilized regions in the *xy* cross-section are those away from the HCM structure. Furthermore, given the improved HCM architecture for the double bifurcation design, a more uniform α distribution is predicted in Figure 4.18 (a). However, the higher reaction advancement values achieved using the double bifurcation design imply lower local bed permeability values, which hinders the reactants' transfer in the lower layers of the reactive bed. This effect can be appreciated by observing the reaction advancement distribution along the axial direction (*zy* plane). Here, lower reaction advancement values are predicted for the bottom layers of the reactive bed in the instance of double bifurcation design, Figure 4.18 (a), compared to single bifurcation fins, Figure 4.18 (b). In particular, the reactive regions away from the HCM/TCM interface create preferential paths for the vapour transfer,

ultimately allowing for a larger reactant concentration in the bottom layers of the reactive bed in case of poorer heat transfer. The lower cooling efficiency provided by the single bifurcation design allows for a more efficient vapour transfer in the regions away from the vacuum chamber. Nonetheless, such an effect has a limited impact on the overall reactor thermal performance, as highlighted by the optimal geometrical features in Table 4.7.

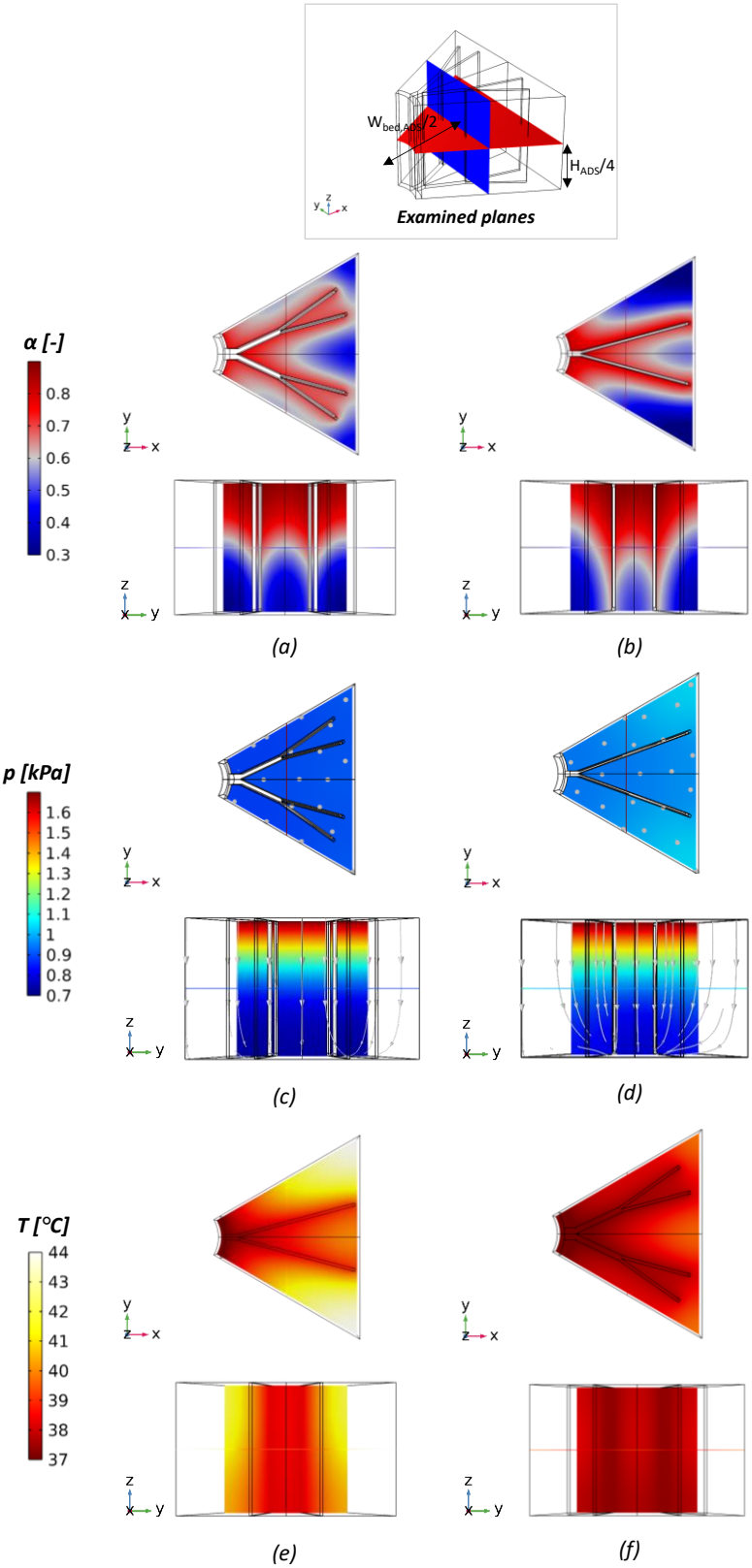

Figure 4.18 Temperature, pressure, and reaction advancement contours in RDS-reactors at a fixed time of 10 h considering a design with single bifurcation, left, and a design with double bifurcation, right.

4.3.3 Performance comparisons

The performance histories for the optimized branched fins designs and literature benchmarks are compared in this section. Three optimal geometries are considered concerning the ADS-reactor configuration, with each optimal geometry maximizing one of the performance metrics selected in section 4.2.2. Regarding RDS-reactors instead, given the similar geometrical features identified in section 4.3.2, only the performance for the branched fin design maximizing the reaction advancement for a 10 h desired discharge time is reported.

The comparison of the time evolution of the average reaction advancement, Figure 4.19 (a), shows noticeable different trends. In ADS-reactors, branched fin designs with secondary bifurcation, such as ADS-1 and ADS-2, are predicted to increase the reaction advancement up to +9.1% compared to the benchmark design, ADS-b. Nonetheless, for desired discharge times above 12.5 h, corresponding to $\alpha \approx 78$-80%, larger reaction advancement is achieved by single bifurcation designs, such as ADS-3. Hence, branched fins with secondary bifurcation in ADS-reactors should be considered only in the case of targeted final reaction advancement $\alpha < 80\%$. Concerning the RDS-reactors, BF with secondary bifurcations outperforms the literature benchmark design, RDS-b, during the whole discharge history, with a performance enhancement of up to ≈+4.8%. Hence, branched fins with multiple branches in RDS-reactors should be considered regardless of the targeted final reaction advancement.

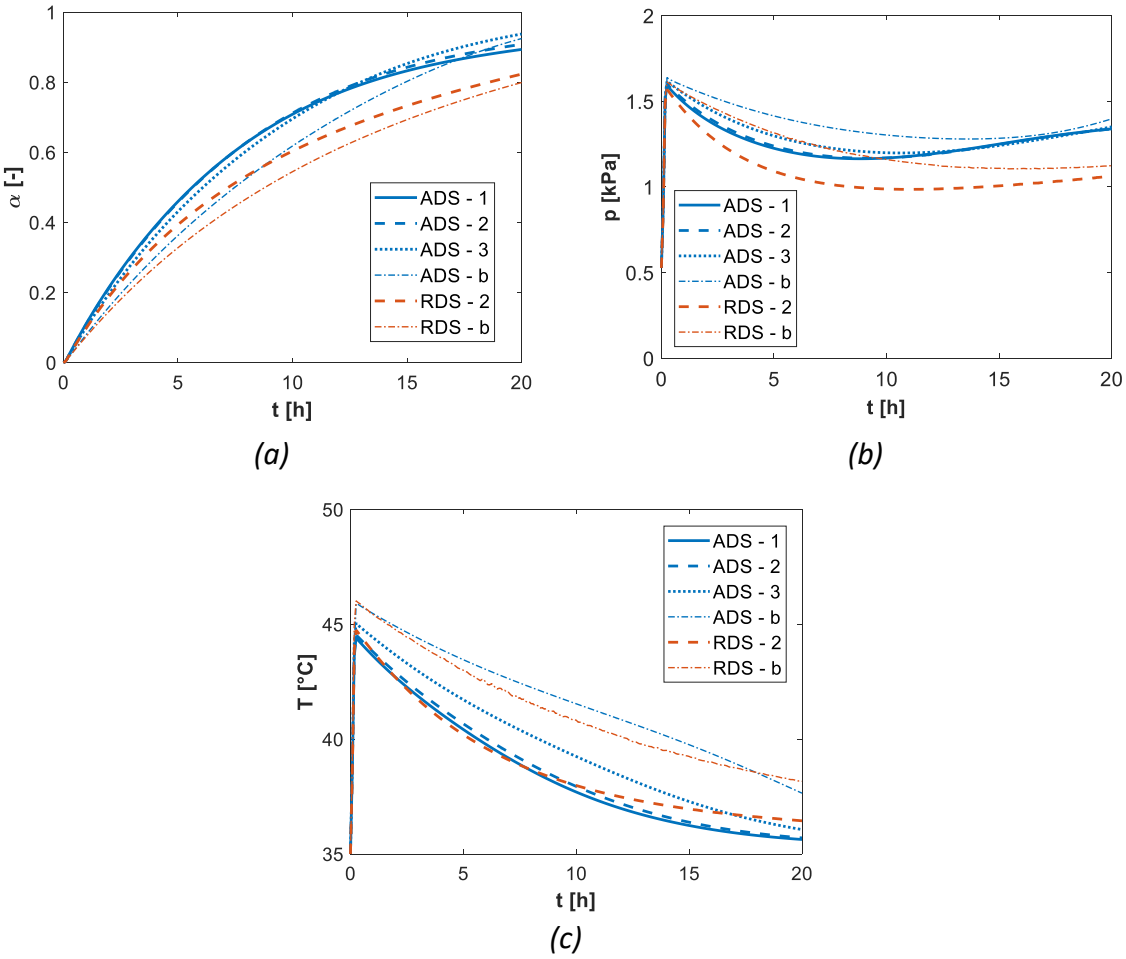

Figure 4.19 Comparison of the global performance histories for the optimized and benchmark designs: (a) average reaction advancement; (b) average vapour pressure in the reactive bed; (c) average TCM temperature.

Despite the optimized HCM architectures, a significant discrepancy between ADS- and RDS-reactors is observed, up to Δα≈9.4%. Such discrepancy is attributed to the lower reactant concentration observed in RDS-reactors, as shown in Figure 4.19 (b). Here, for similar branched fins designs, such as for ADS-2 and RDS-2, a significantly lower average vapour pressure is predicted in the case of radial distribution systems. Such vapour pressure reduction is dictated by the geometrical configuration of the reactive bed. In fact, despite the equal maximum distance travelled by the reactants in the two reactor configurations, a larger fraction of the reactive material is located *'away'* from the vapour chamber interface

in the case of RDS-reactors. As a result, the poor vapour concentration observed in the regions away from the vapour chamber affects a larger material volume fraction in the case of RDS-reactor compared to ADS-reactor configurations, ultimately penalizing the RDS-reactor thermal performance. For example, concerning a 10 h discharge process, a *+17%* of the reactive domain volume is predicted to have a poor local vapour pressure, set at $p<0.8$ kPa, for RDS-reactors compared to ADS-reactors.

The average TCM temperature evolution with time is shown in Figure 4.19 (c). For each reactor configuration, lower temperatures are predicted for the optimized designs than the literature benchmarks, highlighting a more efficient reactive domain cooling provided by fins architecture. Furthermore, branched fins geometries with secondary branches and large bifurcation angles, such as ADS-1, present the lowest temperature along the whole discharge process. That is, the lowest bed temperatures are obtained through fins elongating and evenly distributing in the reactive domain, regardless of the reaction advancement level in the reactive bed. Furthermore, despite the final larger material utilization after a *20 h* discharge time, the ADS-3 design is characterized by a relatively high TCM temperature for most of the discharge time. In other words, when a deep discharge is targeted, the optimal discharge is obtained through the trade-off between efficient cooling and reduced mass transfer penalization.

4.4 Conclusions

This chapter studied the optimal geometry of branched-fins in closed system TCS reactors using surrogate models. Two reactor configurations were investigated: (i) TCS reactors with an axial distribution of vapour, namely ADS-reactors, and (ii) TCS reactors with a radial

distribution of vapour, namely RDS-reactors. Due to the selected distribution systems, different preferential directions for the heat transfer and mass transfer mechanisms characterized each reactor configuration.

The results demonstrated branched fins to enhance the performance of both reactor configurations, with energy discharged increasing up to +9.1% compared to a literature design. However, distinct optimal fins designs were obtained when different objective functions were considered, indicating the need for advanced and accurate design tools for the fit-for-purpose configuration of TCS reactors:

- In ADS-reactors, the optimal extended surface architecture was significantly affected by the interplay between heat transfer and mass transfer. In fact, the fins bifurcations hamper the vapour transfer in the reactive bed and can cause a degradation in reactor thermal performance, with this effect being particularly pronounced during the latest stages of the hydration process due to high salt hydration level, and thus to the reduced bed permeability. Consequently, double bifurcations were favourable only for shallow to medium discharge depths, meaning final reaction advancements of approximately 80%.
- Concerning RDS-reactors, using multiple branches with large bifurcation angles maximizes the performance across all the metrics considered, with negligible variations in the optimal value of length and direction of the branches. This design trend implies that the optimality of branched fins in RDS-reactors is mainly unaffected by the coupling between the heat and mass transfer, but predominantly dictated by heat transfer only. Nevertheless, despite the mass transfer penalization

caused by extended surface inserts in ADS-reactors, this type of reactor outperformed RDS-reactors, with reaction advancement discrepancies of up to 9.4%.

Overall, the results presented in this chapter demonstrate how the interplay between heat and mass transfer can influence the optimal extended surface geometry in TCS reactive beds where heat transfer and mass transfer occur in parallel preferential directions, as in the instance of ADS-reactors, which past works on design optimization largely overlooked. In particular, the designs and associated guidelines presented in this work depart from pure heat conduction-based designs reported in the literature, especially in the case of large discharge time and, thus, poor bed permeability. On the other hand, when orthogonal preferential directions are considered for heat transfer and mass transfer, such as for RDS-reactors, the optimality of HCM inserts is unaffected by their interplay. As a consequence, the typical heat transfer maximization design guidelines can be adopted. Nonetheless, the results indicated the only heat transfer intensification to be inadequate to achieve the complete material hydration in the desired discharge time, also emphasizing the need for mass transfer enhancement to attain superior reactor performance, as addressed in chapter 7 of this dissertation.

The design domain explored in this chapter, i.e. range of geometrical parameters describing the branched fins' size and shape, was heuristically defined based on literature guidelines. However, despite significant performance improvements, the constraints dictated by this heuristic choice might prevent the full exploitation of the storage material potential. To break this barrier, in the next chapters, the topology optimization algorithm is adopted to ultimately maximize the TCS reactor thermal performance and capture non-intuitive design trends.

Chapter 5

Heat transfer enhancement in closed system reactors through topology optimization

This chapter addresses the need for heat transfer enhancement in closed system TCS reactors through the optimal configuration of extended surfaces made of HCM. Compared to the results presented in chapter 4, topology optimisation is adopted here to generate the optimal HCM geometries with enhanced design freedom. Topology optimization allows the discovery of non-intuitive fins architectures that primarily benefit the TCS system. The performance enhancement limitation deriving from the consideration of a limited and heuristically defined design space is broken by the use of the topology optimization algorithm. Besides the large performance improvements predicted for the generated designs compared to literature benchmarks, TO is used to capture how key design parameters affect the optimal extended surface geometry. In particular, this chapter explores the effect of the desired discharge time, the bed size and the bed macro-porosity on the optimal design. The uniqueness of the results presented rests in the use of a systematic design tool with matchless design freedom to capture design trends.

Furthermore, two optimization problems are formulated and investigated: material utilization maximization (MUM) and energy output maximization (EOM). The former refers

to the performance maximization for a fixed amount of storage material, while the latter refers to the performance maximization for a fixed volume of space. In particular, the EOM problem formulation allows for the use of a design tool concurrently leading to the optimal geometrical design and packing factor value, thus answering two key design questions at the same time.

The outline of the chapter is as follows: section 5.1 presents the reactor configuration adopted for the investigation along with the reference TCM selected. In section 5.2, the rationale for the design approach used for the optimal fins design generation is presented, and the analysis model for the reactor performance predictions is discussed. Section 5.3 deals with the topology optimization parameters and choices necessary for the algorithm coupling with the targeted physical systems. Besides, the selected objective functions are presented. In section 5.4, the post-processing steps adopted in this dissertation for the interpretation of the topology optimization results are presented and discussed for a specific optimal fin design. Section 5.5 presents the emerging design trends and quantifies the performance benefits against a literature benchmark. Finally, section 0 summarizes the main achievements from this chapter.

5.1 Reactor configuration and material selection

The optimal distribution of HCM is derived in this chapter for the axial distribution system (ADS) reactor configuration. Figure 5.1 depicts the reference TCS system employing a TO-based fins design. Similarly to chapter 4, the TCS storage modules are positioned inside a shell served with vapour through an evaporator/condenser component, and each reactor was considered to have a hexagonal cross-section with an HTF pipeline positioned at the

centre of the reactor. Each TCS reactor is thus assumed to operate identically within the whole storage module [31] in such a way that the same representative unit adopted in chapter 4 can be used to maximize the TCS system performance.

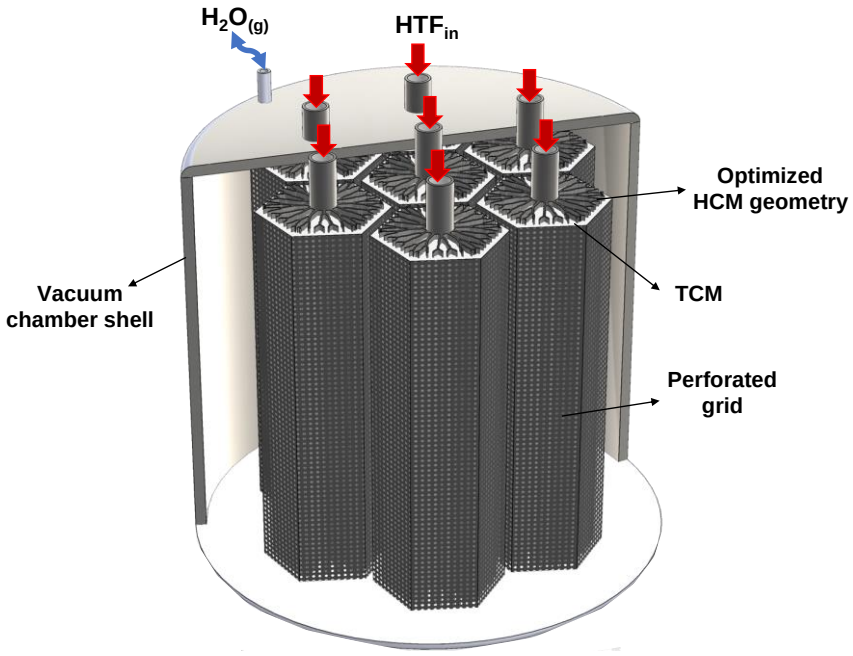

Figure 5.1 Schematic of the TCS system configuration considered in this chapter.

The focus in this chapter is shifted to medium-temperature TCS systems, while low-temperature systems are considered in chapters 6 and 7. In the context of medium-temperature TCS systems, Richter et al. [234] systematically screened 308 different inorganic salt candidates for reversible reactions in the temperature range of 150-300 °C. The hydration and dehydration of strontium bromide from/to monohydrate state was identified as the only candidate to meet all the imposed requirements and was thus recommended as the most suitable TCM:

$$SrBr_2 + 1H_2O \leftrightarrow SrBr_2 \cdot 1H_2O + \Delta H_r^0 \qquad 5.1$$

The thermophysical properties of the anhydrous and monohydrate strontium bromide are reported in Table 5.1. Aluminium is considered as HCM for the investigation, in agreement with literature studies [31,144].

Table 5.1 Thermophysical properties for $SrBr_2$ in anhydrous, subscript 0, and monohydrate, subscript 1, forms [235]***; no variation of the reactive bed permeability with the salt hydration level was assumed*** [235]**.**

Property	**Value**	**Unit**
ΔH	71.98	kJ/mol_{TCM}
Δs	143.9	$J/mol_{TCM}/K$
γ	1	-
k_{TCM}	1	W/m/K
$\varepsilon_{TCM,0}$	0.64	-
$\varepsilon_{TCM,0}$	0.71	
K_{TCM}	1E-10	m^2
$M_{TCM,0}$	247	g/mol_{TCM}
$M_{TCM,1}$	265	g/mol_{TCM}
$c_{p,TCM,0}$	305	J/kg/K
$c_{p,TCM,1}$	456	J/kg/K
$\rho_{TCM,0}$	4216	kg/m^3
$\rho_{TCM,1}$	3911	kg/m^3

5.2 Design approach and numerical methods

The design approach proposed in this chapter is summarized in Figure 5.2. For the identified design problem, the optimal distribution of HCM in the reactive bed was subsequently obtained by means of the topology optimization procedure. As described in section 3.1.1,

the adopted density-based approach uses a continuous scalar indicator function for the switching between material phases, with the density-property relations represented through differentiable artificial laws (section 5.3.2). Consequently, no explicit material interface is present if a density-based approach is adopted, thus preventing the representation of interfacial phenomena. In the context of the analysed physical system, this limitation precluded the modelling of the interfacial thermal resistance between HCM and TCM, which in turn was observed to influence the reactor performance in recent studies from the literature [20,40]. Nevertheless, the generated TO designs were reconstructed and re-evaluated to account for the effect of the interfacial thermal resistance. The design reconstruction step consisted of interpreting the optimized material distribution so that CAD designs could be generated. Finally, the predicted optimized design performance was compared with a literature benchmark to assess the performance benefits led by the proposed methodology.

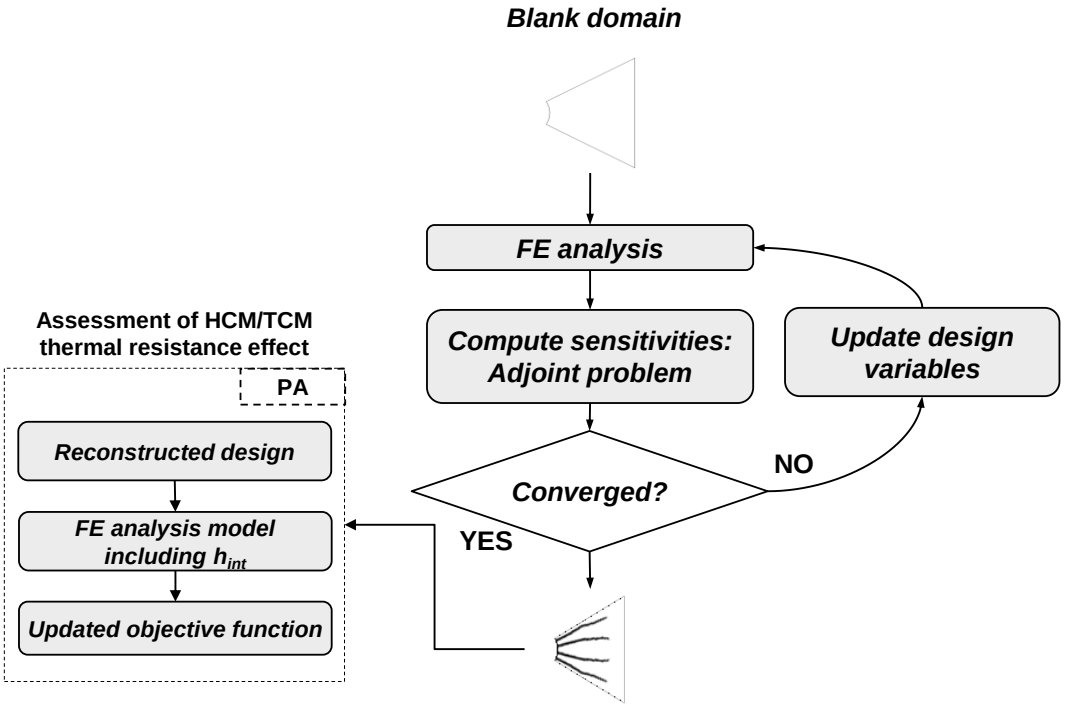

Figure 5.2 Design approach adopted for the topology optimization of closed system TCS reactors.

5.2.1 Governing equations

The governing equations presented in chapter 4 are modified in this section to allow for the design-dependent terms necessary to use the topology optimization algorithm. The schematic of the ground domain considered for the performance maximization of the ADS-reactor is depicted in Figure 5.3. One-sixth of the hexagonal representative unit was investigated. A further symmetric line is present along the horizontal direction (x-axis). Such symmetry line was preserved in the investigated ground domain, and symmetrical optimal designs were expected [128]. If asymmetric designs were generated by the optimization tool, the numerical accuracy of the tool must be increased. The parameter *W* was selected as 50 *mm*, while the outer pipe radius, r_0, was selected as 12 *mm*. While the parameter r_0 was kept constant throughout the analysis, the effect of the reactive bed size, *W*, on the optimal HCM architecture is investigated in section 5.5.3.

At the internal boundary, Γ_{in}, the interface with the HTF was modelled by means of a Robin boundary condition accounting for the heat transfer coefficient, h_{conv}; while no transport flux was assumed for the solution of the mass transfer problem. At the outer boundary, Γ_{out}, thermal insulation was considered, and prescribed vapour pressure was used to model the interface with the vacuum chamber. Regarding the boundaries Γ_{s_1} and Γ_{s_2}, symmetry boundary conditions were assumed to account for the ground domain periodicity.

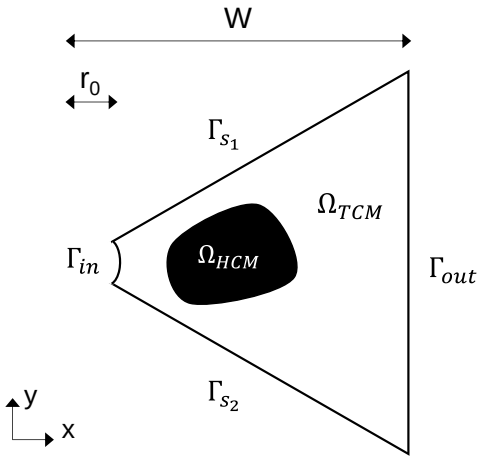

Figure 5.3 Schematic of the ground domain considered.

Thus, the vapour mass balance was written in the following form:

$$\varepsilon\,(\boldsymbol{s})\frac{\partial(c)}{\partial t} + \mathbf{u}\nabla c = \dot{c}(\boldsymbol{s}) \qquad 5.2$$

Where $\boldsymbol{s}$ indicates the material distribution and $\varepsilon(\boldsymbol{s})$ and $\dot{c}(\boldsymbol{s})$ become the design-dependent porosity and sink terms, respectively. Inertial effects in the porous medium were neglected [30,87] in such a way that the velocity field, $\mathbf{u}$, was assumed to follow the Darcy law:

$$\mathbf{u} = -\frac{K(\boldsymbol{s})}{\mu}\nabla p \qquad 5.3$$

With the term $K(\boldsymbol{s})$ indicating the design-dependent bed permeability and *p* representing the vapour pressure. Solid and gas phases were considered in thermal equilibrium [37,231], and given the low vapour density in the porous medium [37], the convective heat transfer was neglected. Thus, energy conservation was written as follows:

$$\mathrm{C}(\boldsymbol{s})\frac{\partial \mathrm{T}}{\partial t} + \nabla \cdot (\lambda(\boldsymbol{s})\nabla T) = \dot{\mathrm{q}}(\boldsymbol{s}) \qquad 5.4$$

Where $\mathrm{C}(\boldsymbol{s})$ and $\lambda(\boldsymbol{s})$ refer to the design-dependent heat capacity and thermal conductivity, respectively. Finally, the reaction kinetics was written in the general form [236]:

$$\dot{\alpha} = k_{cin}\, f(\alpha)\, h(p)\, g(\boldsymbol{s}) \qquad 5.5$$

Where the first three terms are the reaction kinetics constant, k_{cin}, the kinetics differential form, $f(\alpha)$, and the pressure term, $h(p)$, respectively. For the considered working pair, these terms were adopted from the empirical correlations derived by Stengler et al. [66] and are reported in Table 5.2. The fourth term of equation 5.5 is a design-dependent switch for the kinetics equation to activate only in the TCM regions.

Table 5.2 Kinetics model coefficients for the investigated TCMs [66]***.***

	k_{cin} [s^{-1}]	$f(\alpha)$ [-]	h(p) [-]
Hydr.	$3.04 \cdot 10^{-5}$	α	$\left(T_{eq,hydr}(p)[K] - T\,[K]\right)^{1.79}$
Dehydr.	$1.38\ 10^{6} \exp\left\{\frac{-75{,}7\left[\frac{kJ}{mol}\right]}{R_{gas}T}\right\}$	$(1-\alpha)$	$\left(1 - \frac{p}{p_{eq,dehyd}}\right)^{0.25}$

The coefficients reported in Table 5.2 were derived from an experimental set of around 100 hydration/dehydration cycles and validated for the ranges 0-97 kPa and 150 – 210 °C. Furthermore, in conflict with what is typically observed for salt hydrates in the low-temperature ranges [62], the equilibrium conditions for the solid-gas reaction departs from

the ones predicted by the Clausius-Clapeyron relation. Thus, empirical equilibrium correlations were derived for the dehydration, equation 5.6, and hydration, equation 5.7, processes [66]:

$$log_{10}\left(p_{eq,dehyd}\ [kPa]\right) = 14.69 - \frac{6.41 * \ 10^3}{T\ [K]} \tag{5.6}$$

$$log_{10}\left(p_{eq,hyd}\ [kPa]\right) = 8.18 - \frac{3.19 * \ 10^3}{T\ [K]} \tag{5.7}$$

The volumetric heat generation, $\dot{q}(\boldsymbol{s})$, and molar sink term, $\dot{c}(\boldsymbol{s})$, were calculated as a function of $\dot{\alpha}$ according to equations 5.8 and 5.9 :

$$\dot{q}(\boldsymbol{s}) = \frac{(1-\varepsilon_0)}{M_{s,0}\ \rho_{s,0}} \Delta H\ \dot{\alpha}(\boldsymbol{s})\ g(\boldsymbol{s}) \tag{5.8}$$

$$\dot{c}(\boldsymbol{s}) = \frac{(1-\varepsilon_0)}{M_{s,0}\ \rho_{s,0}} M_v\ \dot{\alpha}(\boldsymbol{s}) g(\boldsymbol{s}) \tag{5.9}$$

The material interpolation strategy, detailed in section 5.3.2, was formulated in such a way to recover the material properties in Ω_{HCM} and Ω_{TCM} according to:

$$\varepsilon(\boldsymbol{s}) = \begin{cases} \varepsilon_{HCM}\ in\ \Omega_{HCM} \\ \varepsilon_{TCM,\ \alpha=0.5}\ in\ \Omega_{TCM} \end{cases} \tag{5.10}$$

$$K(\boldsymbol{s}) = \begin{cases} K_{HCM}\ in\ \Omega_{HCM} \\ K_{TCM,\ \alpha=0.5}\ in\ \Omega_{TCM} \end{cases} \tag{5.11}$$

$$C(\boldsymbol{s}) = \begin{cases} \left(\rho c_p\right)_{HCM}\ in\ \Omega_{HCM} \\ \left(\rho c_p\right)_{eff,\alpha=0.5}\ in\ \Omega_{TCM} \end{cases} \tag{5.12}$$

$$\lambda(\boldsymbol{s}) = \begin{cases} \lambda_{HCM}\ in\ \Omega_{HCM} \\ \lambda_{eff,\alpha=0.5}\ in\ \Omega_{TCM} \end{cases} \tag{5.13}$$

$$g(\boldsymbol{s}) = \begin{cases} 0\ in\ \Omega_{HCM} \\ 1\ in\ \Omega_{TCM} \end{cases} \tag{5.14}$$

Furthermore, the following equation was adopted to formally define the packing factor in the TCS reactor:

$$PF = \frac{\int_{\Omega_{HCM}} 1 \, dxdy}{\int_{\Omega_d} 1 \, dxdy} \qquad 5.15$$

Concerning the TO framework, the packing factor value coincides with the spatial integral of the design variable, i.e. $PF = \int_{\Omega_D} \boldsymbol{s} \, d\boldsymbol{x}$, as the term s indicates the amount of HCM in the ground domain. The packing factor value was slightly varied when reconstructed designs were instead considered, as discussed in section 5.4.1.

A quadrilateral mesh was adopted to generate the TO-based designs, with element size, h_{el}, equal to W/70, as presented in Figure 5.4. Concerning the material porosity and permeability in the HCM regions, ideally, null values should be adopted to represent the null reactants transfer in Ω_{HCM}. However, the use of null material properties would lead to numerical instabilities in those regions. Thus, artificial porosity and permeability values were adopted in the HCM regions. The operating conditions were assumed to agree with the ones adopted in [31] and are reported in Table 5.3.

Table 5.3 Operating conditions adopted for the analysis.

Property	Value	Unit
$p_{v,\,in}$	67	kPa
T_{HTF}	207.6	°C

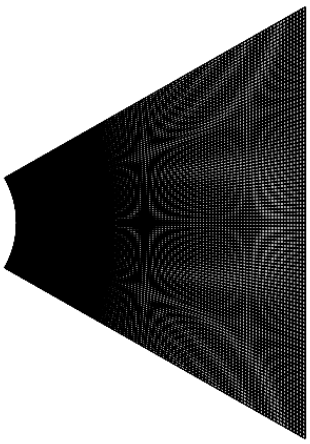

Figure 5.4 Quadrilateral mesh adopted for the generation of TO-based designs.

The design model adopted in this dissertation does not allow for the explicit tracking of the material interfaces along with the optimization iterations and, thus, precludes the use of interfacial thermal resistances in the FE analysis model. Nevertheless, the effect of such interfacial thermal resistance was evaluated in this work on the reconstructed optimal designs. When applied to a reconstructed design, the presented FE analysis model remains valid, although the design-dependent terms are lifted given the use of explicit materials boundaries. Thus, the local heat flux at the HCM and TCM interface was modelled as follows:

$$q = h_{int}(T_i - T_j) \tag{5.16}$$

Where T_i and T_j represent the local domain temperatures at the materials interface, while h_{int} represents the thermal resistance coefficient. Figure 5.5 depicts the boundary Γ_{int} for which equation 5.16 was imposed in the instance of a reconstructed TO design.

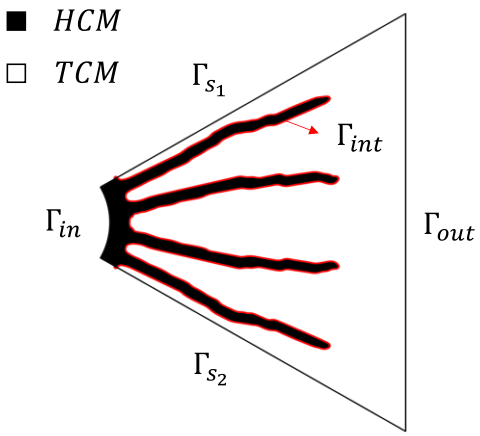

Figure 5.5 Schematic of the domain and boundaries for a reconstructed optimal design.

The developed numerical frameworks were validated in the instance of the hydration process of $SrBr_2 \cdot 1H_2O$ against the data presented by Stengler et al. [75], with the tested design shown in Figure 5.6 (a).

A correlation for the thermal resistance at the TCM/HCM interface was imposed. Such a correlation was expressed as a function of the reaction advancement and adopted according to the results presented in [75]:

$$h_{int} = 30 + 15\ \alpha \tag{5.17}$$

The comparison between numerical predictions and experimental data is reported in Figure 5.6 (a) concerning the reaction advancement histories. An excellent agreement with the experimental data was observed when the thermal resistance coefficient, h_{int}, was considered. On the other hand, a larger reaction advancement rate was predicted in the TO framework due to its inability to capture interfacial phenomena, which in turn leads to an overestimation of the bed cooling. Figure 5.6 (b) depicts the local temperature evolution in time for the thermocouple-B location, which was placed at a $1.2 \cdot 10^{-2}\ m$ distance from the HTF pipe [75]. While the FE models well reproduce the qualitative temperature progression

in the reactive bulk, an overestimation of the maximum temperature values was observed. Nevertheless, the numerical framework accounting for the interfacial thermal resistance adopted in this work resulted in excellent agreement with the predictions from the numerical model developed by the authors [75]. This allowed concluding that the adopted numerical framework well replicates the state-of-the-art for the modelling of the targeted physical system.

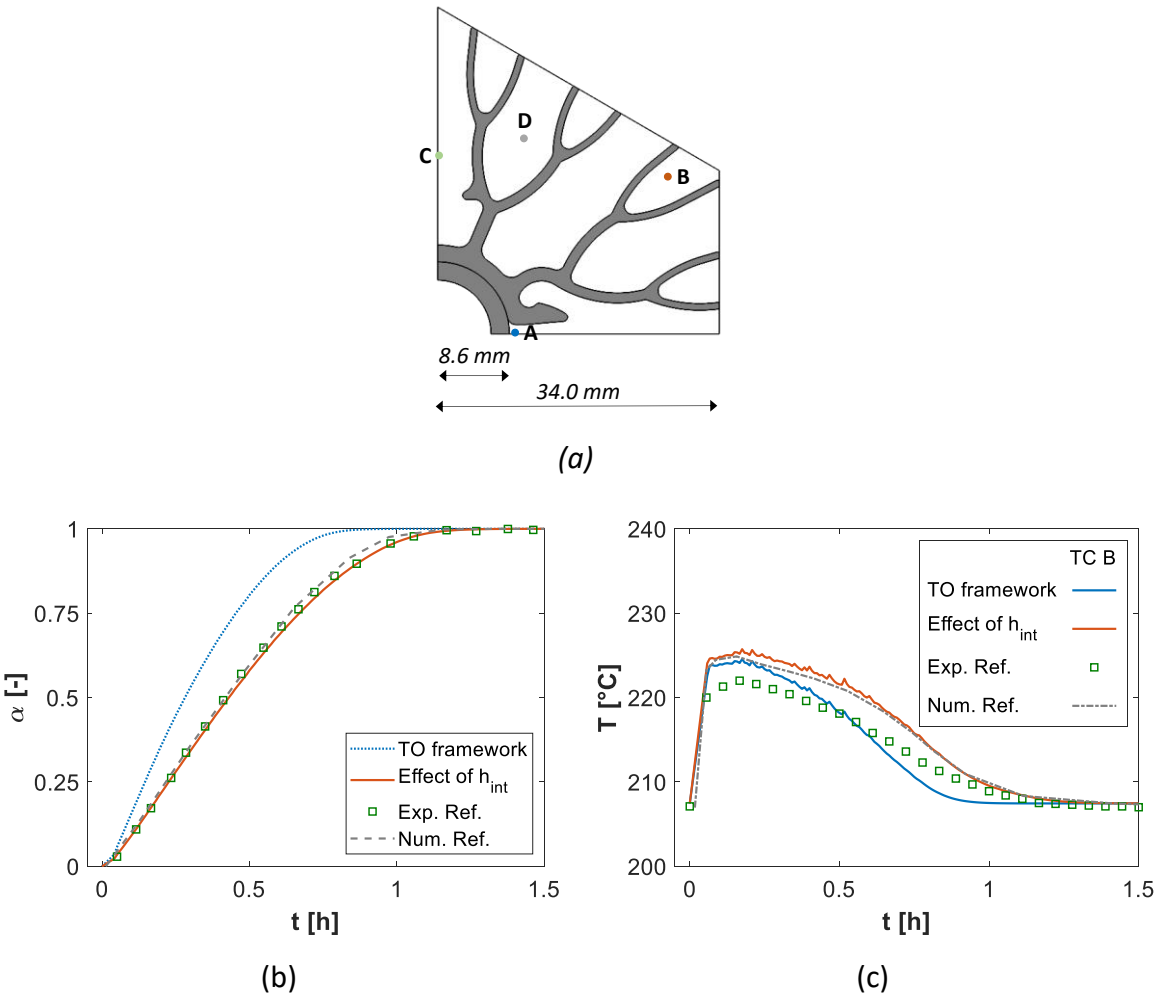

Figure 5.6 Numerical model validation against experimental data from [75]***: (a) design adopted for the experimental measurements and thermocouple locations; (b) reaction advancement histories; (c) local temperature evolution in time for thermocouple B. The validation case considers a discharge/hydration process at T_{HTF} = 207.6 °C and $p_{v,in}$ = 67 kPa***

5.3 Topology Optimization

5.3.1 Optimization problems formulation

Effective TCS reactor architectures are required to discharge the maximum amount of energy in a fixed discharge time, or viceversa, to discharge a fixed amount of energy in the least time. Previous studies demonstrated such optimization problems to be equivalent [218], with the same optimal design emerging regardless of the considered objective function. Consequently, this dissertation only considers the maximization of the discharged energy in a fixed time. Hence, the following optimization problems were formulated:

1) The material utilization maximization (**MUM**) problem:

$$\begin{cases} max \quad \alpha_{t^*} = \int_{\Omega_D} \alpha\,(\boldsymbol{s})\; dxdy \text{ at t}=t^* \\ \boldsymbol{s}.t. \int_{\Omega_D} \boldsymbol{s}\; d\boldsymbol{x} - V^* \leq 0 \\ 0 \leq \boldsymbol{s} \leq 1 \end{cases} \tag{5.18}$$

The MUM problem represents the maximization of the reaction advancement at the desired discharge time, *t**, for a maximum amount of enhancer material, *V**. Given the linear relationship between the amount of generated energy and the reaction advancement expressed in equation 5.4, the maximization of α_{t^*} is equivalent to the maximization of the energy discharged from a given amount of storage material. Such energy is entirely transferred to the HTF, given the boundary conditions assumed in section 5.2.1. In other words, the fraction of stored energy discharged in the time *t** is expressed by the final reaction advancement level.

In the instance of the MUM problem, the maximum amount of HCM, V^*, must always be specified. In fact, the use of a constraints-free optimization problem would lead to the trivial solution of a ground domain filled only with HCM, as this does not

present any chemical energy content and thus 'minimize' the energy discharged at time t^*. The MUM problem was formulated in agreement with the typical optimization problems adopted in the literature [157,215,218].

2) The energy output maximization (**EOM**) problem:

$$\begin{cases} max \quad E_{t^*} = \int_0^{t^*} \int_{\Omega_D} \frac{\dot{q}(\mathbf{s})}{V_{bed}} dxdy\, dt \\ 0 \leq \boldsymbol{s} \leq 1 \end{cases} \tag{5.19}$$

With E_{t^*} representing the amount of energy discharged after a time t^*. The EOM differs from the MUM since trivial optimal solutions cannot emerge. If no HCM is utilized, the discharged energy rate might be too slow to achieve optimal performance. On the other hand, if no TCM is used, no net energy output is achieved. As a result, the optimal solution is found between these two extreme cases, and the optimization problem formulation does not require any additional constraints. In other words, the EOM problem allows for a design tool providing simultaneously optimal enhancer topology and optimal enhancer volume fraction. While, formally, no volume constraints are needed for the EOM problem, the *V** was set to 0.4 to avoid generating optimal designs with poor practical use.

A qualitative representation of the discharged energy and packing factor histories along the optimization iterations for both MUM and EOM problems is depicted in Figure 5.7. The maximum packing factor value, *V**, adopted for the specific optimization problem is also reported. The maximum E_{t^*} represents the amount of chemical energy stored in the reactive bed and is thus linked to the reactor packing factor. While this value is fixed for the MUM problem, the packing factor value changes during the EOM problem iterations, and so does

the maximum E_{t^*}. When convergence is reached, i.e. when no significant objective function variations are predicted, the optimal packing factor value is identified.

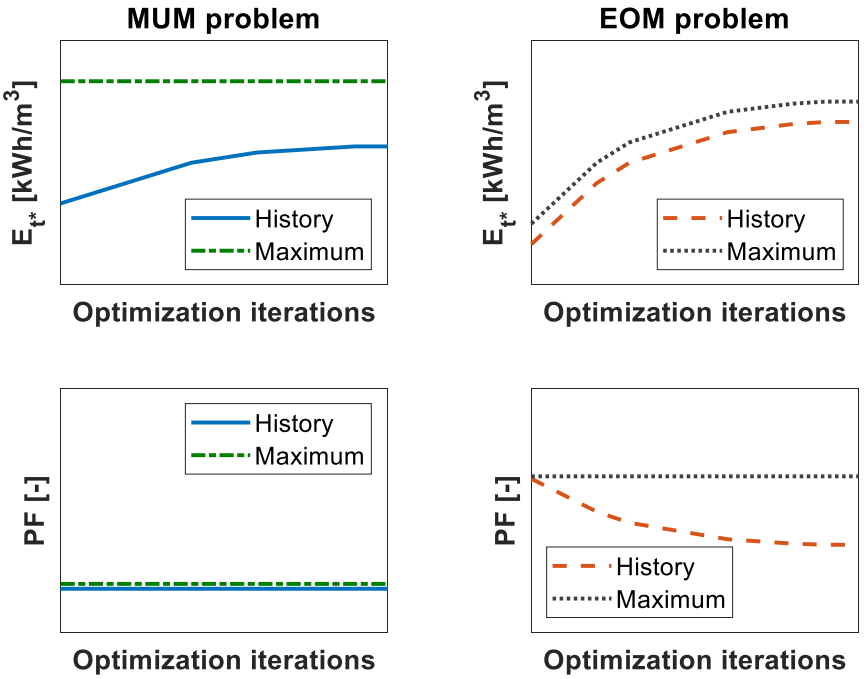

Figure 5.7 Qualitative representation of the discharged energy and packing factor histories for the material utilization maximization (MUM) problem and energy output maximization (EOM) problem.

As typically advised for the topology optimization problem definition [124], the maximization problems reported above are implemented as minimization problems by considering the opposite of the objective function.

5.3.2 Material interpolation

In this chapter, the conventional SIMP scheme was used to interpolate the thermal conductivity, $\lambda(\mathbf{s})$, and the heat capacity, $\mathrm{C}(\mathbf{s})$:

$$\lambda(\boldsymbol{s}) = \lambda_{TCM} + (\lambda_{HCM} - \lambda_{TCM})\boldsymbol{s}^{p_{SIMP}} \quad 5.20$$

$$\mathrm{C}(\mathbf{s}) = \mathrm{C}_{TCM} + (C_{HCM} - C_{TCM})\boldsymbol{s}^{p_{SIMP}} \quad 5.21$$

The power-law exponent, p_{SIMP}, was ramped-up during the optimization iteration steps. Such a gradual increase implied a more convex optimization problem during the initial optimization iterations, allowing for fairly homogeneous material distribution in the entire ground domain [124]. As the power-law exponent was ramped-up, the intermediate densities were further penalized, leading to crisp boundaries for the final design.

The use of the SIMP interpolation scheme on the design-dependent permeability, $K(\mathbf{s})$, was observed to lead to poor reactant transfer penalization in Ω_{HCM}. Such poor penalization derived from the relatively high permeability values for non-binary designs and was dictated by the large ratio between the materials' permeability. To overcome this issue, a TANH interpolation scheme was selected, with the ε_{TANH} coefficient set equal to 0.5. That is, the material properties switch was operated at $\boldsymbol{s} = 0.5$, while the regions with $\boldsymbol{s} > 0.5$ were characterized by a fictitious HCM permeability, K_{HCM}. As a result, the optimizer might allocate 'grey' material but with 'black' material properties, which is an undesired feature for the optimization strategy. However, combining a TANH approach with a SIMP interpolation allows for the complete material properties to be described only by large $\boldsymbol{s}$ values, i.e. near unitary values, ultimately still penalizing intermediate control variable values. In fact, the de-coupling of the material properties transitions preclude regions with intermediate properties for both permeability and e.g. thermal conductivity, as reported in Figure 5.8 considering normalized properties.

Linear interpolation was instead adopted for the design-dependent switch $g(\mathbf{s})$, and the bed porosity, $\varepsilon(\mathbf{s})$. The selection of the fictitious permeability and macro-porosity adopted in the HCM domain was carried out through a series of numerical tests and values of 10^{-20} m^2 and 10^{-10} were identified, respectively for K_{HCM} and ε_{HCM}.

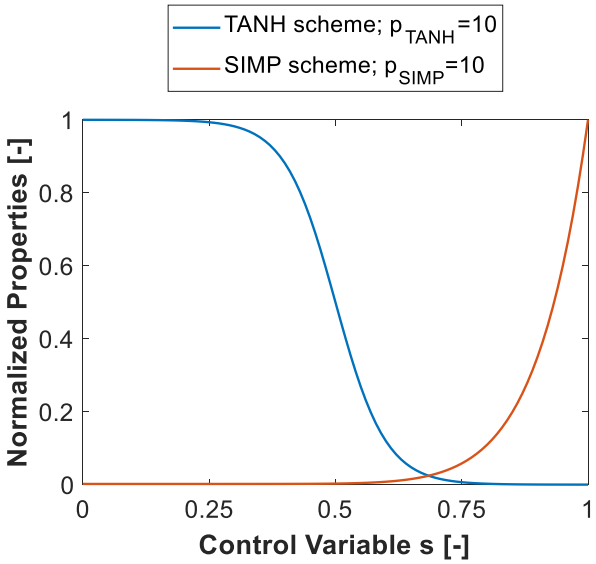

Figure 5.8 Normalized properties interpolation for TANH scheme and SIMP scheme. The material properties transition region is de-coupled.

5.3.3 Filtering and regularization

A filtering technique was adopted to ensure the results mesh independence and avoid checkerboard effects [139]. The linear filter presented in equation 3.10 was used, and the smoothing of the design variable gradients caused by the filtering techniques was adjusted by the hyperbolic tangent projection operator presented in equation 3.12. The filtering and projection parameters adopted in this chapter are reported in Table 5.5, while the continuation scheme adopted for the projection parameter, the SIMP penalization exponent, and the TANH penalization coefficient are reported in Table 5.4. Because no clear guidelines are defined in the literature for the selection of such parameters, the adopted values were identified after a series of preliminary numerical tests. Nevertheless, such values agree with typical choices from the literature [128,167,237]. The GCMMA was adopted as optimization routine to update the material density after each optimization iteration, and the optimization process was terminated after 150 iterations [135].

Table 5.4 Continuation scheme for the projection parameter, β, for the SIMP penalization exponent, p_{SIMP}, and the TANH scheme penalization coefficient, p_{TANH}.

	1-30	31-60	61-90	91-120	121-150
β	1.0	2.0	2.0	4.0	8.0
p_{SIMP}	1.0	2.0	4.0	6.0	10.0
p_{TANH}	1.0	2.0	3.0	6.0	10.0

Table 5.5 Filtering and projection threshold values adopted in this chapter.

Description	*Symbol*	*Value*
Filter radius	r_f	h_{el}*1.1
Projection Threshold	η	0.5

5.4 Post-processing of the topology optimization results

This section presents the steps adopted for generating CAD designs from the topology optimization results. First, the TO results were filtered by the formulation of a dataset for $s < s^*$, where s^* represents the material density cut-off parameter. A free-triangular mesh was then generated based on the visualization of the formulated dataset [238]. The mesh was refined or coarsened using an adaptation scheme considering an absolute element size, h_{el}. Figure 5.9 exhibits the adopted post-processing steps and shows three different routes characterized by an increasing refinement of the generated meshes. Besides, a zoom of a fins' secondary branch is depicted to assess the ability of the generated mesh to capture the optimal geometrical features.

The b-spline method was then used to connect the mesh boundary elements and generate explicit material interfaces. Using finer meshes, i.e. route 3 shown in Figure 5.9, accurately reproduces the initial filtered database. However, the generation of a large number of

boundary elements also leads to wavy boundaries, which can affect the manufacturability of the reconstructed designs. On the other hand, using too coarse meshes, such as in route 1 in Figure 5.9, led to poor accuracy in the filtered database representation and modification of the optimal geometrical features. The compromise between accurate geometrical description and boundary smoothing is found in the 'medium mesh' route, i.e. route 2 shown in Figure 5.9. Thus, unless otherwise stated, the reconstructed designs presented in this chapter adopt an absolute element size for the reconstructed mesh generation of $W/35$.

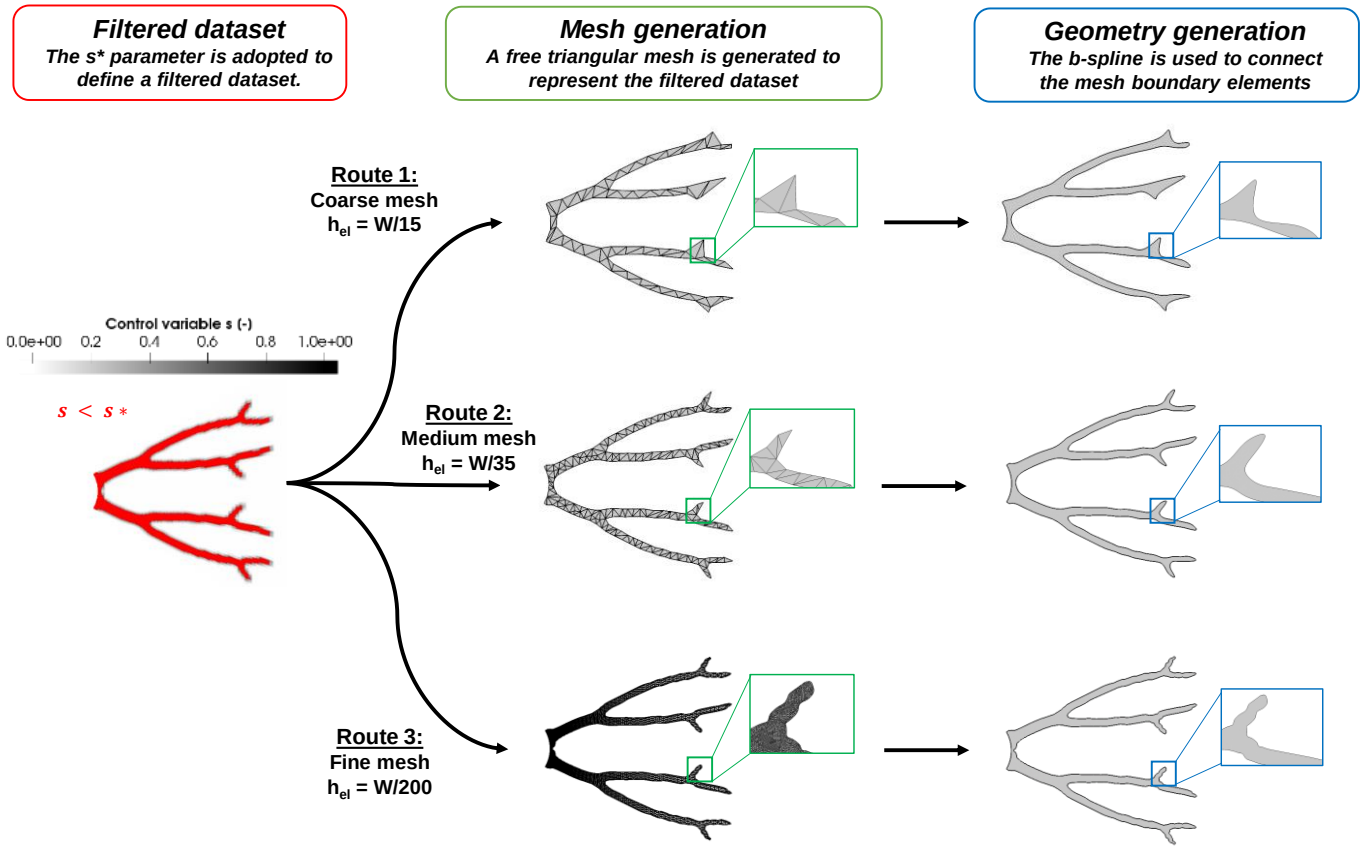

Figure 5.9 Steps for the TO results interpretation and the generation of CAD designs.

First, a filtered dataset was created considering a material density cut-off parameter, s^*. Thus, a free triangular mesh was generated based on the visualization of the formulated filter region. Three possible routes were considered, characterized by an increasing mesh refinement level. In the geometry generation step, the b-spline method was adopted to connect the mesh boundary elements and construct the fins' geometry. The generated geometries show the 'medium mesh' route to accurately reproduce the initial filtered domain and produce smoothed surfaces with good manufacturability.

5.4.1 Effect of the cut-off parameter

The material density cut-off parameter, s^*, was adopted to generate the filtered dataset for constructing the TO-based optimal designs. Figure 5.10 shows the effect of the s^* parameter on the reconstructed geometry for a MUM design considering a maximum volume fraction of 19.2%. In the case of a nearly un-filtered dataset, i.e. $s^* = 0.01$, the reconstructed geometry presents a large fin thickness, up to 2.9 mm, which reduces to only 1 mm for increased cut-off parameters, $s^* = 0.75$. The optimal geometrical features deriving from the TO framework are preserved in the reconstructed geometry for s^* values up to 0.5. If larger cut-off parameter values are adopted, part of these features is lost, such as primary and secondary branches. Consequently, it is advised to consider s^* values of 0.5 to capture the emerging design trends fully.

On the other hand, analysing the reconstructed geometries for $s^*>0.5$ can lead to relevant insights into the key geometrical features for the reactor performance enhancement. In the design case presented in Figure 5.10, the reconstructed geometry with $s* = 0.75$ highlights the performance benefits led by the four main branches elongating from the HTF wall. In contrast, a lower role in the performance enhancement can be attributed to the primary and secondary bifurcations, as such bifurcations are not visible in the case of larger cut-off parameter values. Hence, if highly manufacturable designs are targeted, e.g. by considering only straight fins, the TO results can be used to provide indications on the fins' directions.

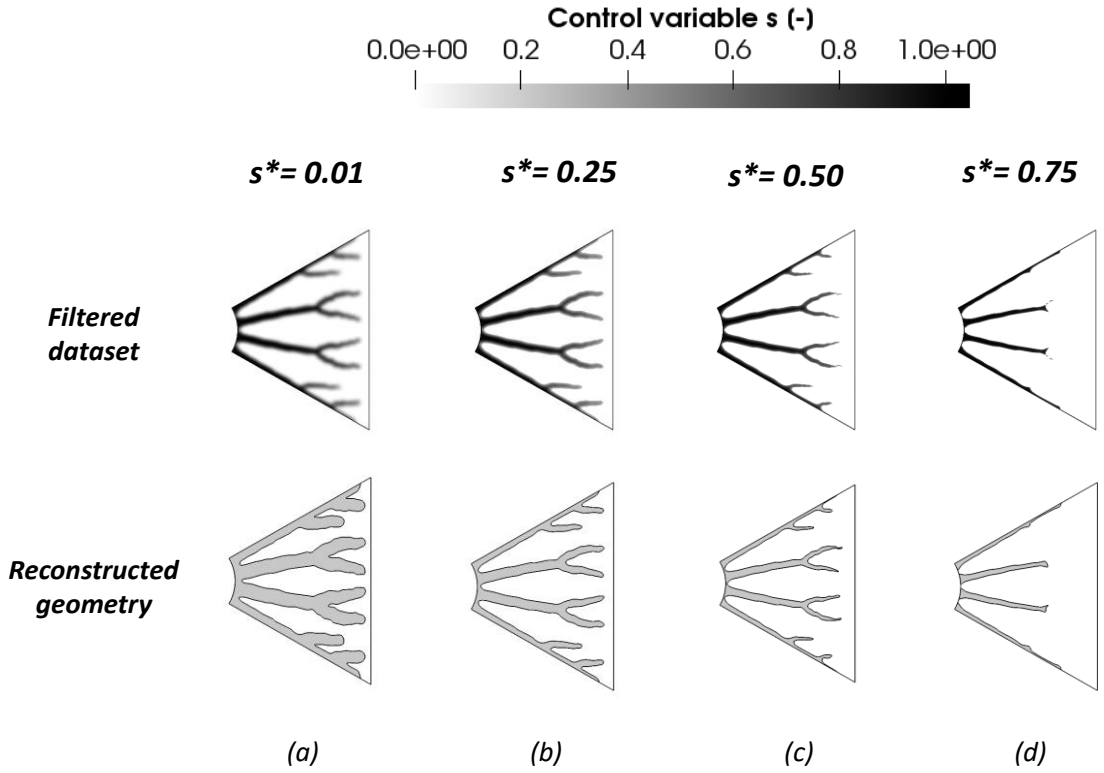

Figure 5.10 Influence of the material density cut-off parameter, s*, on the reconstructed geometry.

The various CAD designs depicted in Figure 5.10 were assessed to estimate the effect of the s^* parameter on the reactor performance metrics. The effect of the cut-off parameter on the packing factor, PF, final reaction advancement, α_{t^*}, and amount of energy discharged, E_{t^*}, is presented in Figure 5.11. As expected, for increasing *s**, lower packing factors are obtained. Similarly, lower final reaction advancements are predicted in the case of large values of the cut-off parameter. The α_{t^*} values reduction with s* is justified by (i) the more complex HCM architecture, (ii) the thicker HCM branches and (iii) the reduced amount of TCM in the ground domain. However, while a significant PF reduction is obtained for the *s** increase, e.g. -29.0% for s* from 0.01 to 0.5, a milder α_{t^*} variation is predicted, $\approx 23.0\%$.

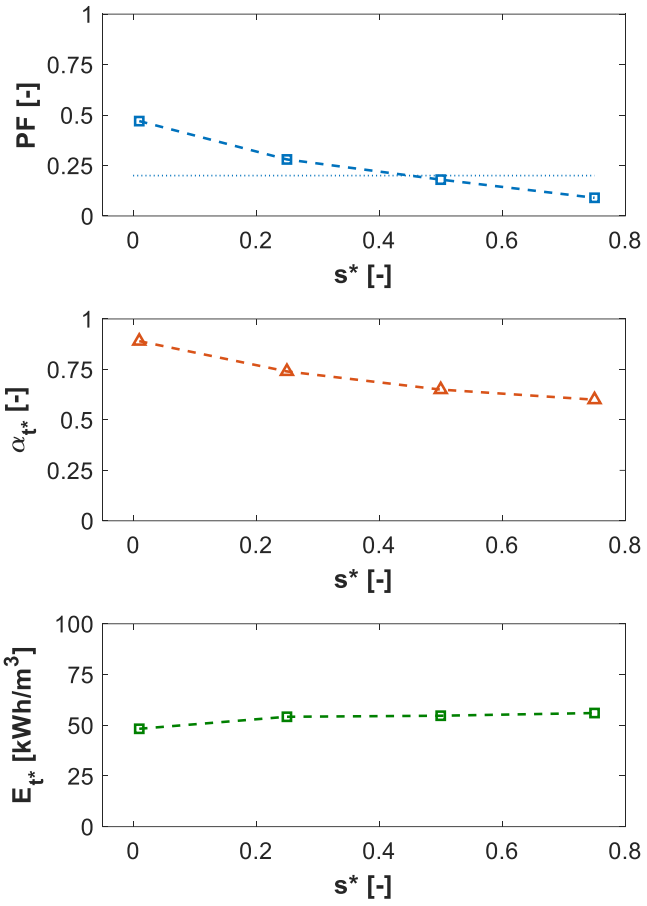

Figure 5.11 Effect of the material density cut-off parameter, s*, on the packing factor, PF, final reaction advancement, α_{t^*}, and discharged energy, E_{t^*}.

Consequently, a larger final discharged energy is also predicted in case of higher cut-off parameters. This is not a banal result and ultimately highlights the significant role in the performance benefits led by the control variables with nearly unitary values. Nonetheless, the use of s*=0.5 also leads to a negligible difference between the reconstructed geometry packing factor, 18%, and the adopted volume constraint for the optimization problem, 19.2%. To summarize, two main features emerged from the analysis carried out in this section: (i) the selection of $s^* = 0.5$ preserve all the optimal geometrical features emerging in the TO framework and leads to negligible packing factor discrepancy between the TO

framework and the CAD designs; (ii) the analysis of the reconstructed designs for $s^* > 0.75$ can be adopted to derive the key geometrical features for high-performing reactors with simplified HCM architecture.

5.5 Results

The typical global performance histories for the selected TCS system are analysed in this section. Figure 5.12 exhibits the temperature and pressure histories, defined as the average values in the reactive bed and considering the reactor design adopted for the model validation [75]. These average values are compared with the equilibrium and operating conditions. Overall, the depicted temperature histories resemble those presented in chapter 4 for the hexahydrate strontium bromide. The bed temperature peaks during the initial stages of the discharge process due to the high reaction rate in fully dehydrated TCMs.

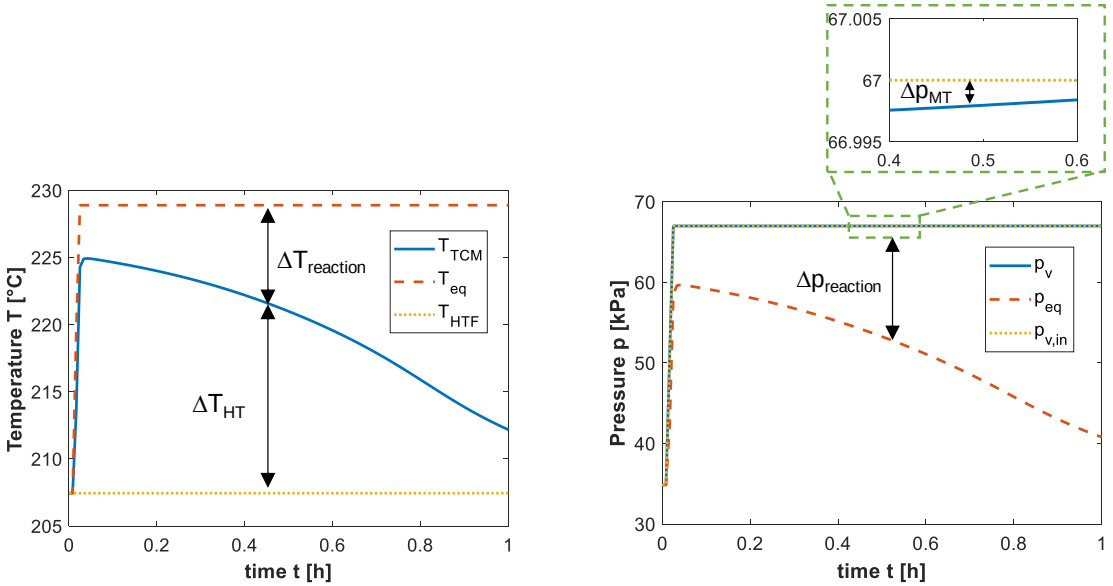

Figure 5.12 Global histories for the validation design [75]***: (a) average temperatures; (b) average vapour pressures.***

However, the equilibrium temperature, derived from equation 5.7 and thus dictated by the vapour pressure in the reactive bed, exhibits a flat behaviour in time. Such behaviour is justified by the vapour pressure trend in time, for which a negligible difference (<100 Pa) with the vacuum chamber is predicted. That is, a negligible influence of the vapour pressure distribution on the local and global performance of the reactor characterizes the investigated medium-temperature TCS reactor employing monohydrate strontium bromide, in agreement with the predictions by Stengler et al. [75].

5.5.1 Comparison with literature benchmark

In this section, the presented structured optimization approach is adopted to generate optimal reactor designs and to assess the performance benefits achieved compared to literature benchmarks. A desired discharge time, t^*, of 1 h is selected for the analysis. Figure 5.13 shows the design evolution along the optimization iterations for the EOM problem.

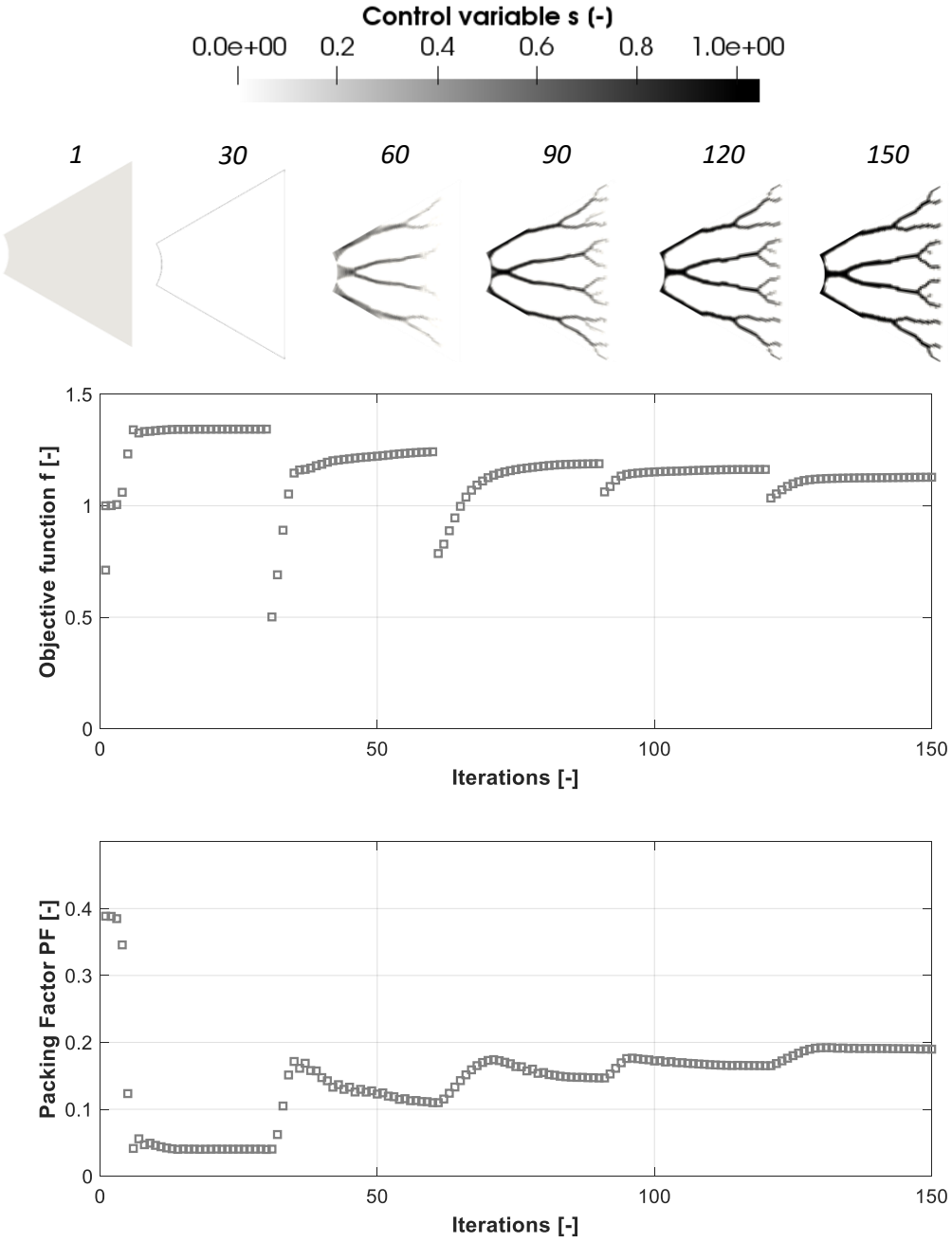

Figure 5.13 Objective function and packing factor histories versus optimization iterations and design evolution before each continuation scheme step.

In agreement with the selected colour bar, the white areas refer to the TCM regions, while the black areas refer to the HCM regions. The initial design corresponds to a homogeneous material distribution equal to the selected V^*. Thus, given the limited interpolation

penalization imposed in the initial steps of the continuation scheme, a significant amount of enhancer material is removed from the ground domain, with the packing factor value reduced to ≈0.05. At iteration 30, the adopted continuation scheme dictates a variation in the optimization parameters, which leads to a sharp increase in both the objective function and packing factor values. Thus, more crisp design features emerge at iteration 60, where the primary and secondary branches can already be distinguished. The remaining optimization history does not present significant design changes, with the packing factor value reaching the final optimal value of 0.18. The final design, i.e. iteration 150, presents a clear material transition contour with limited use of grey material.

Similarly, a MUM design is generated for a maximum volume constraint $V^* = 0.1$. The performance of both MUM and EOM designs is evaluated considering the HCM/TCM thermal resistance and compared against the benchmark design proposed by Ranjha et al. [110]. The benchmark design consists of a highly manufacturable solution where 6 straight fins were located in the reactive bed. The thickness of each fin is selected to ensure a 0.1 packing factor, and Figure 5.14 shows the three designs considered, obtained by exploiting the symmetry conditions. The MUM design presents 20 thin fins elongating from the HTF walls towards the vacuum chamber. No bifurcations are present, although a change in the fins' direction is observed. Bifurcations are instead present in the EOM design. Here, thicker fins are obtained as no strict volume constraint is imposed in the optimization problem. Such thicker fins allow for more effective heat transport in the regions away from the HTF wall and, thus, for a larger utilization of the storage material in such regions.

EOM design	*MUM design*	*Benchmark design*
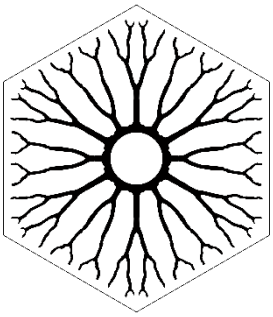	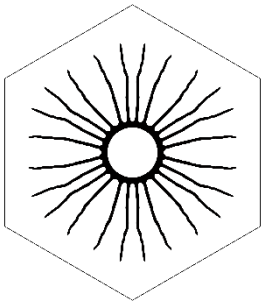	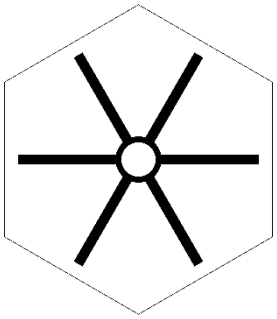
(a)	*(b)*	*(c)*

Figure 5.14 Comparison of the optimization design and benchmark design: (a) EOM design; (b) MUM design; (c) benchmark design from Ranjha et al. [110]***.***

The global performance histories for each of the three designs are depicted in Figure 5.15. The EOM design achieves more considerable material utilisation. This result might seem counterintuitive, as the maximization of the reaction advancement was adopted as the objective function for the MUM problem. Nevertheless, the achievement of a larger α_{t^*} is dictated by the larger final packing factor, 0.18, compared to the imposed volume constraint in the MUM problem. The use of a larger packing factor entails a lower storage material content in the reactive bed, which leads to an unfair comparison for the reaction advancement metric. Nevertheless, the MUM design, which ultimately entails similar storage material volume compared to the benchmark design, is predicted to lead to a $\Delta\alpha_{t^*}$ = 0.27.

The amount of discharged energy is compared based on the bed volume, which is calculated by accounting for the volume devoted to the storage material and the volume devoted to the HCM. In such a way, a fair comparison of the estimated performance can be made for all three designs. In Figure 5.15 (b), a larger amount of energy is discharged from the EOM

design, highlighting the importance of the proper packing factor selection to maximize the amount of energy retrieved from a fixed volume of space. A nearly threefold E_{t^*} is predicted for the EOM design compared to the benchmark design (+286%). Furthermore, a +44% increase is also estimated compared to the MUM design, concluding that the proposed optimization problem can be adopted to generate designs leading to superior final energy densities compared to conventional optimization problems adopted for TES devices.

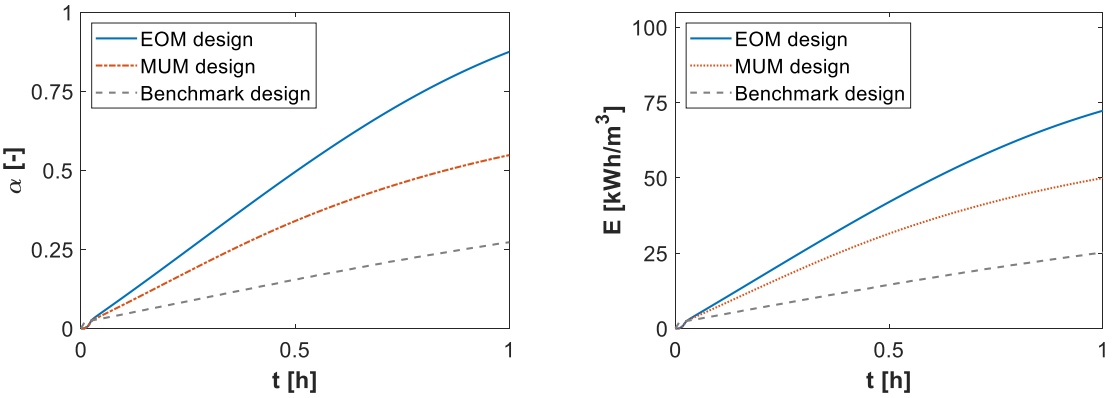

Figure 5.15 Comparison of the reaction advancement and discharged energy histories for the optimal designs and literature benchmarks.

The performance improvements led by using the TO algorithms can be further appreciated in the reaction advancement contours depicted in Figure 5.16. Here, a sharp reaction front is predicted to progress in time from the HCM and HTF walls, providing heat transfer as the main phenomenon limiting the hydration reaction. Poor reaction advancements are predicted for the benchmark design, given the large distance between the extended surface walls and the reaction sites. On the other hand, almost no unreacted TCM regions are observed in the EOM design. Given the imposed packing factor, the MUM design maximizes

the reaction advancement only for the regions near the HTF wall, while a fraction of unutilized storage material is predicted in the regions near the vacuum chamber boundary.

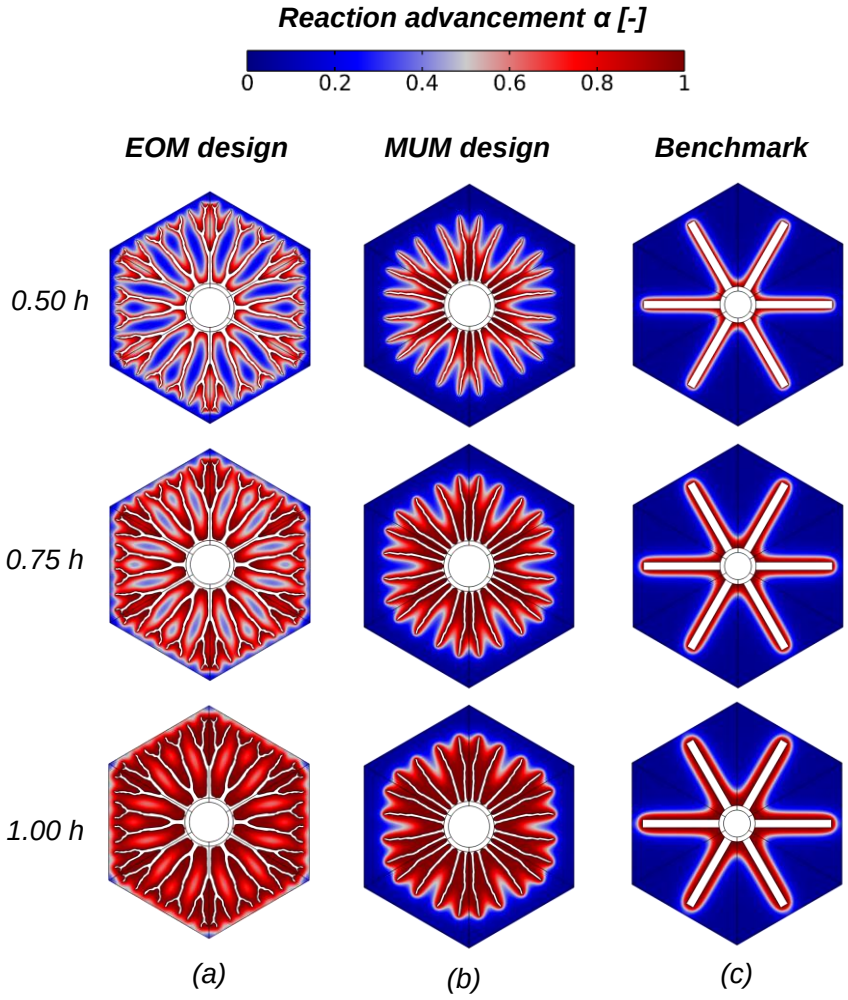

Figure 5.16 Reaction advancement contours evolution in time for: (a) EOM design; (b) MUM design (c) benchmark design from Ranjha et al. [110]***.***

5.5.2 Influence of the desired discharge time

This section analyzes the influence of the desired discharge time, *t*,* on the optimal design of HCM structures. The optimal designs are compared in Figure 5.17, considering both the MUM and EOM optimization problems and increasing *t** values. The majority of the optimal designs present main branches elongating along the diagonal of the hexagonal cross-section.

This is an interesting result from the optimization algorithm: for design cases characterized by the variable distance between the HTF interface and the adiabatic boundaries, HCM branches need to be placed where the distance is maximum. Additional main branches emerge in the central part of the ground domain, with the number of fins differing depending on the adopted optimization problem.

Regarding the MUM designs, the fins tend to stretch further in the ground domain for increasing t^* values. In other words, denser HCM distributions near the HTF wall are derived in case of shorter discharging times, as the energy can be mainly retrieved from these regions. Nevertheless, relatively poor material utilization is achieved in short discharge times. When the EOM problem is considered, a different trend is observed. Here, a large fraction of the ground domain is dedicated to the enhancer material, up to 38%, in the case of short discharging times. The emerging optimal design is complex, characterized by several fin bifurcations and wavy profiles. Besides, isolated TCM regions emerge in the final design for time $t^* = 0.2\ h$. In fact, despite the adopted mass transfer penalization strategy, vapour is still predicted to be transferred in these regions in the TO framework. Consequently, the storage material contained in the isolated regions is predicted to contribute to the enhancement of the amount of energy discharged from the ground domain. However, the storage material in these regions cannot be exploited in the real system, as no vapour could be provided. As a result, the energy density of the reconstructed design is penalized. A lower optimal packing factor for increasing t^* values is derived from the EOM problem (down to 0.18). Finally, in the instance of $t^* = 2.0\ h$, the HCM is mainly distributed in the proximity of the vacuum chamber interface to favour the heat transfer away from the HTF interface.

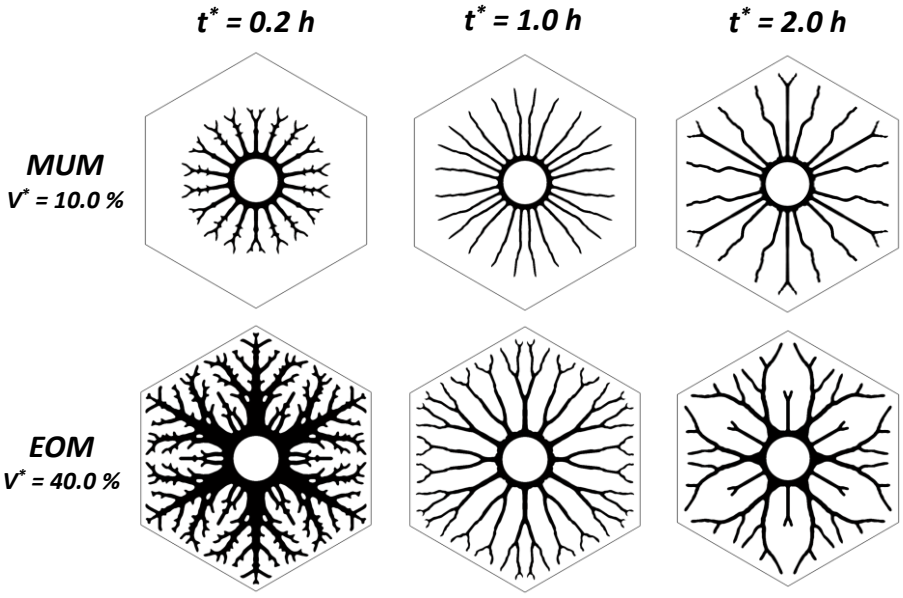

Figure 5.17 Optimal designs for the material utilization maximization, MUM, and the energy output maximization, EOM, problems for increasing values of the desired discharging time, t*.

The objective function values versus the desired discharge time are depicted in Figure 5.18, considering both the TO framework and the performance assessment conducted considering interfacial thermal resistance. Higher final reaction advancements are predicted for the EOM designs due to the larger packing factor, i.e. lower TCM content in the ground domain. The most significant performance discrepancy is observed for t^* =1 h, with the EOM design predicted to deliver +47% energy compared to the MUM design, as discussed in the previous section. However, when large desired discharge times are considered, e.g. t^* = 2 h, the EOM problem is inaccurate. Higher discharged energy is achieved here by means of the MUM design, especially in the TO framework. The authors believe this result to be caused by the large reaction advancement achieved in the physical model, $\alpha_{t^*} \approx 1.0$, which ultimately makes local minimum appealing for the optimizer routine. Nevertheless, in the instances of α_{t^*}<0.96, the objective function values reported in Figure 5.18 highlight the

design generated in the TO framework to remain the best performing design in the performance assessment step where the interfacial thermal resistance was considered. That is, the methodology presented in this chapter is reliable for generating fit-for-purpose designs. For a more straightforward representation of the results, the design performance presented hereafter solely refers to the numerical predictions accounting for the HCM/TCM thermal resistance.

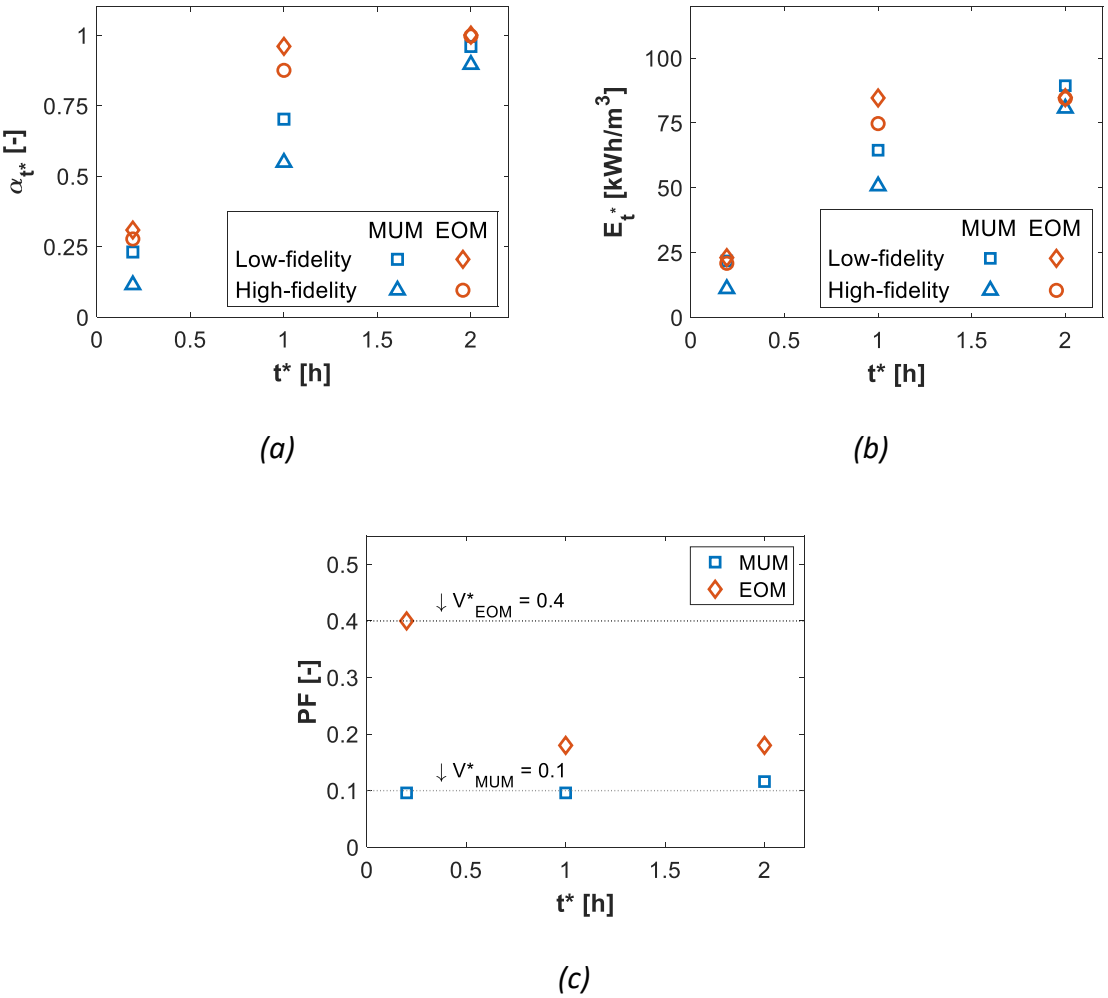

Figure 5.18 Performance metrics comparison for the optimized designs: (a) final reaction advancement, α_{t^*}; (b) Discharged energy, E_{t^*}; (c) Packing factor for the reconstructed designs, PF.

5.5.3 Effect of the bed size on the optimal design

This section analyses the design trends for the optimal HCM distribution for variable bed sizes. Specifically, compared to the design cases presented in the previous sections, the reactive bed length, *W*, is increased to *75 mm* and *100 mm*. The analysis is carried out considering a fixed discharging time of *2 h*.

Figure 5.19 shows the optimized designs. Concerning the MUM problem, the optimal number of branches varies depending on the value of *W*. In particular, instead of four main branches elongating from the HTF interface, the optimal design for 100 *mm* and 75 *mm* presents only two main branches with primary and secondary bifurcations.

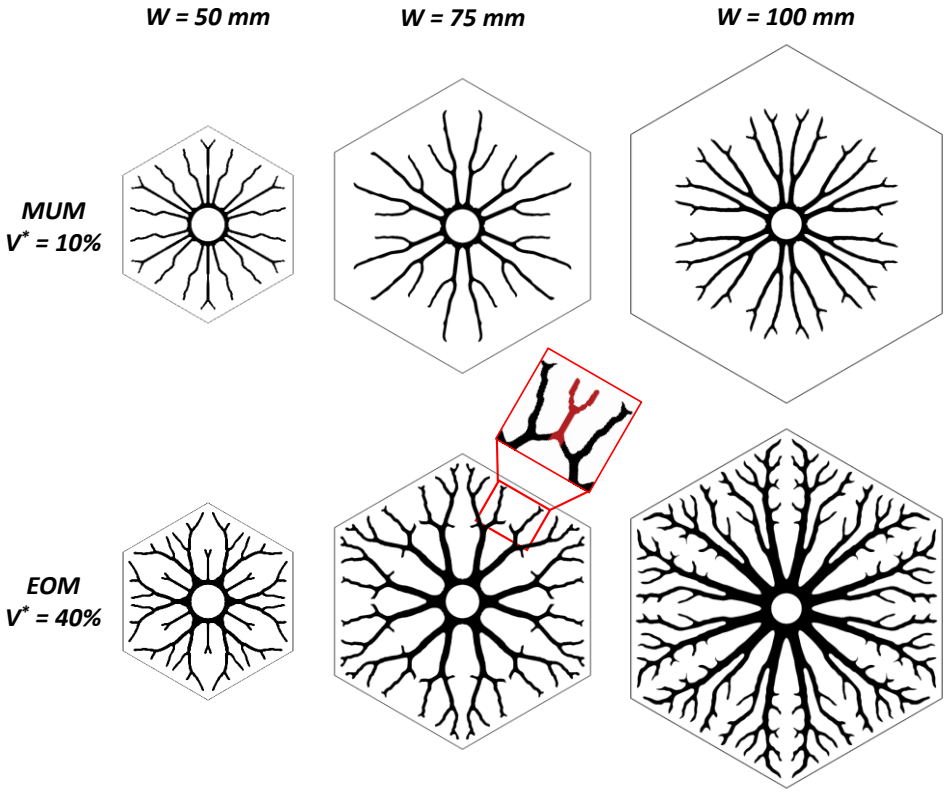

Figure 5.19 Optimal HCM distribution derived from the material utilization maximization, MUM, and the energy output maximization, EOM, problems for increasing bed size, W. The red box refers to the HCM feature that was manually removed during the design post-processing.

Interestingly, the MUM design does not present main branches elongating along the ground domain diagonal but rather two consecutive fins with a relatively small pitch. As a consequence, a small fraction of TCM is located along with the ground domain diagonal. Such TCM region is predicted to hydrate in relatively short times, with the TCM hydration boosted by the large cooling effect provided by the fins. Furthermore, given the longer distance travelled by the heat in the case of *100 mm* bed size, thicker fins are obtained, with a maximum thickness increasing from *1.1 mm* to *3.1 mm*, respectively, for the *50 mm* and *100 mm* designs. Consequently, the optimal design does not distribute in the regions near the vacuum chamber in case of larger bed sizes, with the fins elongating for a maximum distance from the HTF pipe centre of *0.76*W* versus *0.95*W*.

Compared to the MUM designs, more complex HCM architectures can be observed in the EOM designs. The fins present at least primary and secondary bifurcations, while the enhancer volume fraction adopted by the optimizer increases with the reactive bed size. A final HCM volume fraction of 0.18 was adopted in the case of medium size reactive bed, *50 mm*, while such fraction increases to 0.3 for a bed size of *100 mm*. Isolated TCM regions emerged in the instance of the EOM problem for *75 mm*. While these regions are predicted to react in the TO framework, they lead to an unused fraction of storage material in the reconstructed design. To overcome this limitation, the portion of HCM depicted in red was manually removed from the CAD model.

Figure 5.20 exhibits the performance metrics values. Large final reaction advancements (> *80%*) are achieved through the EOM problem regardless of the bed size, while a significant

α_{t^*} reduction is observed for the MUM problem for increasing W. That is, for design problems characterized by relatively large bed sizes, a 10% packing factor is not sufficient to obtain large material utilization factors. Similarly, the amount of energy discharged from the reactive bed is observed to reduce with the bed size, although relatively mild E_{t^*} value reductions are predicted for the EOM designs.

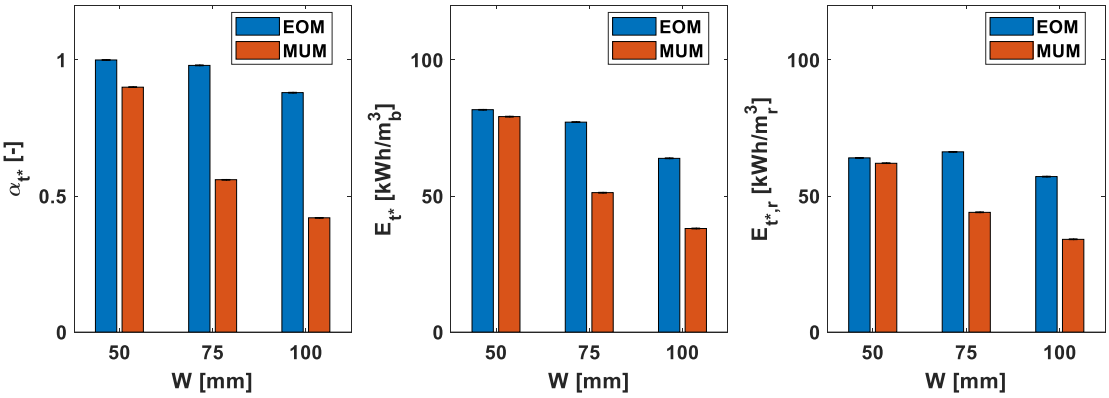

Figure 5.20 Performance metrics comparison for the optimized designs at different bed sizes: (a) final reaction advancement, α_{t^*}; (b) discharge energy over bed volume, E_{t^*}; (c) discharged energy over reactor volume, $E_{t^*,r}$.

As an additional performance metric, the reactor energy density is also evaluated. The reactor energy density was defined as the amount of energy discharged from the reactive bed over the reactor volume:

$$E_{t^*,r} = E_{t^*} \frac{V_{bed}}{V_{reactor}} \qquad 5.22$$

Where $V_{reactor}$ is the reactor volume, calculated as the sum of the bed volume, the volume devoted to the HTF pipes and the volume devoted to the vapour diffuser channels, for which a 6 *mm* size was assumed [40,239]. The size of the HTF pipes and the vapour diffuser

channels were assumed constant with the bed size, *W*. Consequently, larger bed over reactor volume ratios are obtained for increasing *W* values.

Interestingly, the predicted reactor energy density, Figure 5.20 (c), shows maximum values in the instance of the EOM problem at relatively high *W* values and a packing factor of 0.21. Thus, the best performing reactor configuration is obtained by employing relatively large packing factor values and a large distance between the HTF pipes. Table 5.6 reports the optimal packing factor values resulting from the EOM problem. The optimal packing factor does not linearly scale with the bed size. A relatively small increase is observed between the 50 *mm* and 75 *mm* cases, ultimately contributing to the larger reactor energy density obtained for the latter. On the other hand, a more significant increase is observed for $W = 100\ mm$, denoting the need for a large amount of enhancer material when a large distance between HTF pipes is selected.

Table 5.6 Packing factor values for the optimal designs from the EOM and MUM problems for different bed sizes.

	EOM			***MUM***		
W [mm]	50	75	100	50	75	100
PF [-]	0.18	0.21	0.28	0.12	0.1	0.1

5.5.4 Effect of the bed porosity on the optimal design

The influence of the bed properties on the optimal HCM architecture is explored in this section by varying the reactive bed porosity value, ε. The influence of the bed permeability, K, is disregarded in the analysis. As observed indeed in the global performance analysis and confirmed by Stengler et al. [128], given the high pressure adopted for the discharge process

of medium-temperature TCS reactors, mass transfer in the reactive bed does not influence the reactor performance. The bed porosity is considered constant with the TCM hydration level and is varied in the range of 0.30 to 0.69.

Figure 5.21 presents the optimal HCM architecture for increasing bed porosity values. Concerning the MUM problem, the optimal fins stretch towards the outer boundary in case of higher bed porosity, while a denser HCM distribution in the proximity of the HTF wall is derived in the case of highly-packed TCM. Besides, thinner fins are obtained in the instance of large porosity. These trends are due to the energy content variation in the ground domain dictated by the porosity variation. Reduced porosity entails higher maximum energy densities and, thus, a larger amount of energy potentially discharged in the discharge time t^*. On the other hand, a more packed TCM also guarantees higher effective thermal conductivity, as $\lambda_{TCM} > \lambda_{vapor}$. As a result, while a significantly higher energy can be discharged from the ground domain in the case of ε = 0.30 compared to ε = 0.69 (Figure 5.22), mild variations are predicted in terms of reaction advancement, i.e. fraction of stored energy discharged in the time t*. Concerning the EOM designs, thicker fins are obtained for highly packed reactors, with the fins' thickness reduced for increasing porosity. The number of primary branches does not vary with the bed porosity, although a larger number of ramifications is obtained for $\varepsilon = 0.3$ compared to higher values. This is due to the larger energy content in the reactive bed, which leads to a more ramified HCM architecture to retrieve the stored energy effectively.

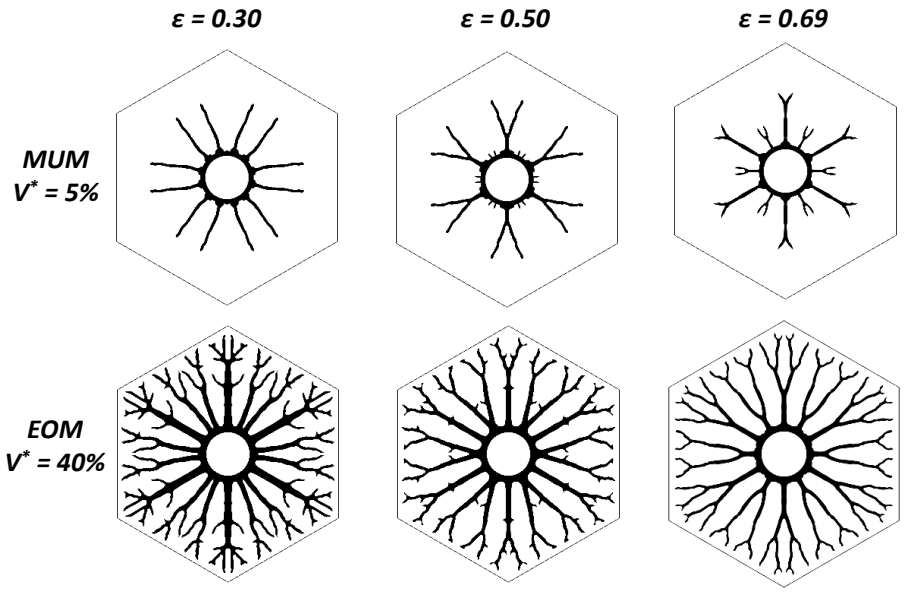

Figure 5.21 Optimal designs for the material utilization maximization, MUM, and the energy output maximization, EOM, problems for increasing values of the bed porosity, ε.

The generated EOM designs are predicted to outperform the MUM designs regardless of the performance metric adopted, as shown in Figure 5.22. Opposite trends are observed for the two performance metrics for increasing bed porosity: while the final reaction advancement increases with the bed porosity, the reactive bed energy density decreases. Larger material utilization can be achieved by selecting a less packed reactive bed, leading to a larger retrieved energy per mass of storage material.

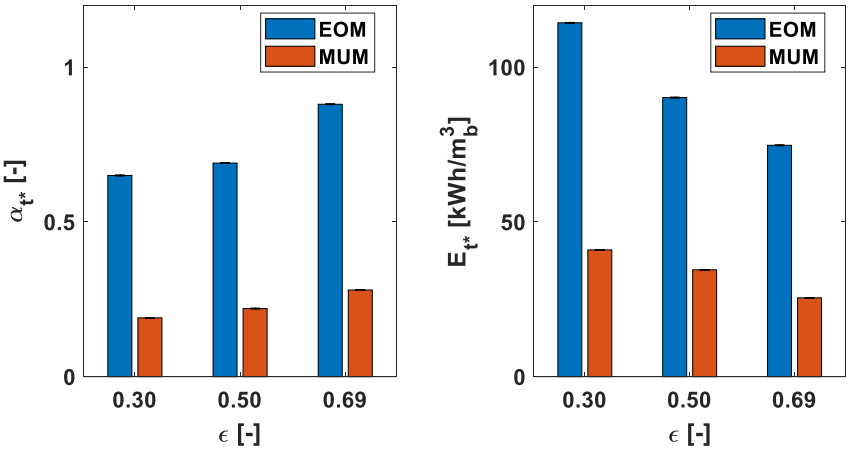

Figure 5.22 Performance metrics comparison for the optimized designs for different porosity values: (a) final reaction advancement, α_{t^*}; (b) discharged energy over bed volume, E_{t^*}.

On the other hand, a more packed reactive bed increases the amount of energy discharged in the selected desired discharge time. The selection of highly packed bed reactors, $\varepsilon = 0.3$, leads to a discharged energy increase up to +57.0 kWh/m^3 compared to beds presenting high void fractions, $\varepsilon = 0.7$. Such a larger bed energy density is obtained despite an increase in optimal packing factor (+0.09), as shown in Table 5.7. This is an interesting result, demonstrating how maximal performance can be obtained by highly packed reactors adopting relatively large packing factor values.

Table 5.7 Packing factor values for the optimal designs from the EOM and MUM problems for different bed porosity values.

	EOM			***MUM***		
ε [-]	0.30	0.50	0.69	0.30	0.50	0.69
PF [-]	0.27	0.21	0.18	0.05	0.05	0.05

5.6 Considerations on the manufacturing of the optimal designs

This section provides recommendations regarding the fabrication of the optimal designs. The non-intuitive geometrical features that emerged from the topology optimization algorithm were demonstrated in this work to provide significant performance enhancement; however, these geometrical features might raise questions regarding the manufacturability of the optimal design.

In these regards, two possible routes for the fabrication of the TO designs are envisioned:

(i) Direct fabrication via additive manufacturing;

(ii) Fabrication of TO-inspired designs with conventional manufacturing techniques;

In contrast with conventional manufacturing methods, additive manufacturing offers increased flexibility which enables the fabrication of complex geometrical features made of copper, aluminium, ferrous materials, etc. [240]. Additive manufacturing is, thus, an enabling technology that allows designers to overcome the current manufacturing limitation that inhibits the adoption of topology optimization. In recent years, additive manufacturing of topologically optimized thermal devices has been growing rapidly [241], as several successful examples have been reported in the literature. For example, Lazarov et al. [188] manufactured and tested TO-based designs for LED light cooling, for which a 50% decrease in operational cost was measured compared to conventional designs. Furthermore, in one of our previous works, we demonstrated the use of selective laser melting additive manufacturing as a manufacturing route for directly fabricating a TO-based design of a multi-tube shell-and-tube latent heat thermal energy storage device [144]. Stengler et al. [5] tested complex branched fins geometries in the context of closed system TCS reactors, thus

in close proximity with the study presented in this work. The operation of a small-scale (1 kW) reactor was demonstrated in a vast range of operating conditions (1 to 560 kPa). Nonetheless, the design considered for the study was adapted from a different thermal device [242] and thus was not specifically designed to maximize the behaviour of the TCS reactor.

However, while additive manufacturing cost is foreseen to reduce in time [243], this route is still not a cost-effective solution in most cases. Fabrication route (ii) entails using the TO results as design guidelines for generating highly manufacturable final designs. The TO designs can be interpreted by the designers and recreated by adopting highly manufacturable geometrical features. For example, Pizzolato et al. [157] presented the skeletonization of optimized fins in a latent heat energy storage device. A discharge time increase of 5% was predicted for the highly manufacturable design compared to the topological design. While these post-processing steps were performed manually in Pizzolato's work, numerical strategies have already been presented in the literature for systematic design post-processing to ensure manufacturability [244,245].

To limit the manufacturing cost, we envision manufacturing route (ii) as the preferred one. Nonetheless, it is crucial to stress that the proposed optimization approach is necessary to systematically identify the key geometrical features which greatly benefit performance. At the same time, post-processing techniques can be adopted to ensure the feasibility of these geometrical features and to ultimately manufacture high-performing reactors.

5.7 Conclusions

This chapter demonstrated topology optimization as a powerful design tool for the systematic generation of optimal extended surface geometries in closed system TCS reactors. The optimal designs were generated for ADS-reactors for multiple desired discharge times, bed sizes, and bed properties. From the results presented in this chapter, the following conclusions are derived:

- Topology optimization can be adopted to generate TCS designs with superior performance compared to state-of-the-art solutions [110]. For a fixed desired discharge time and fixed packing factor value, a final reaction advancement enhancement up to +27.0 % was predicted;
- The application of a novel optimization problem formulation, referred to as the energy output maximization problem, allowed for generating optimal designs without the need for a prescribed packing factor. For a fixed desired discharge time, the energy output maximization problem led to an increase of discharged energy up to +47.0% compared to conventional optimization problems adopted for the topology optimization of TES devices;
- The emerging design trends show that the investigated design parameters largely influence the optimal HCM architecture and packing factor value. The optimal packing factor value significantly reduces with time and increases with the bed size. Nevertheless, the maximum reactor energy density is obtained through a relatively high packing factor value of 21% and a large bed size of 75 mm. This solution was

found to effectively mitigate the influence of dead volumes, i.e. volume devoted to HTF pipes and reactants distribution channels, on the overall reactor energy density;

- Thicker fins are favourable in low porosity beds, with the number of fins varying only when a relatively small packing factor constraint is imposed. The maximum amount of retrieved energy from the TCS reactor was predicted for highly packed bed reactors employing a relatively high packing factor value, with enhancements up to +57 kWh/m^3 compared to less packed beds utilizing optimized fins.

The results presented in this chapter ultimately contribute to the generation of design guidelines for the correct positioning of extended surfaces and provide fundamental insights for advancing TCS technology maturity. The results also prove that advances at the component scale, i.e. reactor scale, are crucial to enhance the performance of TCS systems. The next chapter adopts topology optimisation as a design tool for generating non-intuitive flow channel designs in open system TCS reactors.

Chapter 6

Mass transfer intensification in open system reactors through topology optimization

The literature studies reviewed in chapter 2 highlighted the performance of TCS reactors operated in open mode to be limited by the effective gas reactants' transport to the active sites. However, limited and partial attempts have been reported in the literature to identify geometrical features that can benefit the gas reactants distribution in the reactive bed. Besides, these studies adopted design approaches based on the heuristic selection of geometrical parameters, which ultimately constrained the final design to the ones reviewed in chapter 2.

In this chapter, topology optimization was adopted to break the limitation posed by selecting a constrained design space and to generate non-heuristic flow channel geometries which enhance mass transfer in open system TCS reactors. Two reactor configurations were analysed, namely, sieve reactors and cylindrical reactors, and the performance of the generated designs were compared with literature benchmarks. A multi-step design approach was adopted, similar to what was initially proposed by Yaji et al. [246]. Such a design approach was tested by Yaji et al. in the instances of redox flow batteries [21] and

heat sinks involving turbulent regimes [22], demonstrating large performance benefits compared to state-of-the-art designs for both technological contexts.

The approach aims at indirectly solving complex topology optimization problems. The original problem was indeed addressed by defining the topological design optimization of a pseudo problem and a consecutive performance assessment. The pseudo problem optimization was based on a simplified numerical model and aimed at defining a series of TO-based flow channel geometries that effectively distribute gas reactants to reactive sites. Thus, a full numerical model was used to assess the generated design candidates and to quantify the performance enhancement obtained compared to literature designs. In such a way, a tailored and highly replicable design strategy was proposed to generate high-performing TCS reactors. Overall, the adopted design approach alleviates the topology optimization problem from the complexity of the full physical problem description but still allows for generating design guidelines for real-world devices.

Uniquely to this work, topology optimization is adopted for the non-heuristic design of flow channel geometries which enhances mass transfer. That is, unlike previous studies on the effective design of open system TCS reactors, the optimal geometries were obtained in this work with matchless design freedom. Furthermore, a comprehensive analysis of the emerging design trends was carried out to identify which geometrical features lead to TCS reactors with superior performance.

This chapter is organized as follows: section 6.1 presents the open system reactor configurations under investigation, the rationale for the selection of the representative units, and the adopted TCM. In section 6.2, the topology optimization approach proposed in

this chapter is presented, and the pseudo model used for the generation of multiple TO-design candidates is discussed. Section 6.3 defines the topology optimization parameters and objective function, while section 6.4 presents the performance metrics adopted for the performance assessment of the generated TO-design candidates. In section 6.5, the emerging design trends are analyzed for each reactor configuration considered. Finally, section 6.6 summarizes the contributions of the chapter.

6.1 Reactor configurations and material selection

Two open system TCS reactor configurations were investigated: sieve and cylindrical reactors. Both configurations are depicted in Figure 6.1 employing heuristic flow channel geometries from the literature. Modular storage units were considered where a series of identical TCS reactors were placed in parallel [95]. The reactor operated at ambient pressure, and the sorbate, H_2O, was transported by an airflow. This airflow was circulated utilizing a fan into the storage unit and crossed the porous TCM [37]. In such a way, the airflow concurrently constituted the reactants carrier and the heat transfer fluid. Identical operating conditions were assumed for each TCS reactor module in the storage unit, and thus the study of a single module was performed in order to enhance the whole system's performance [37,247].

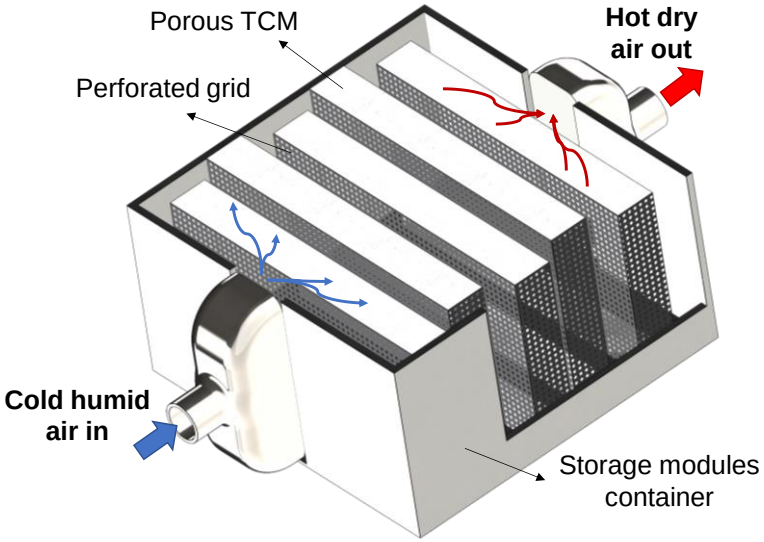

(a)

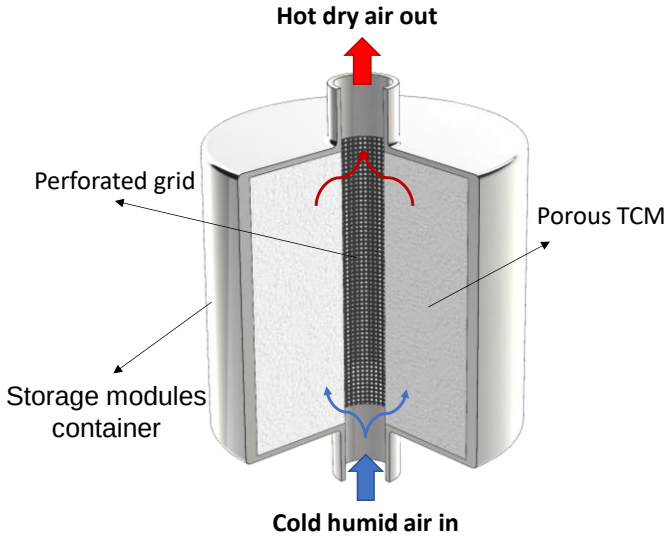

(b)

Figure 6.1 Schematic of the TCS reactor configurations under investigation: (a) sieve reactor adapted from Chen et al. [95]***, (b) cylindrical reactor adapted from Aydin et al. [61].***

Concerning sieve reactors, the reactor configuration proposed by Chen et al. [18] was considered a benchmark design. A serpentine flow channel geometry was employed to distribute moist air in six rectangular TCM domains. Three-dimensional effects can be

neglected, and heat and mass transfer was assumed to occur in the horizontal plane [95]. Following this assumption, a 2D planar ground domain was adopted for the analysis of the performance maximization of the TCS reactor in section 6.2. Similarly, an axisymmetric assumption was made for the cylindrical reactor [84], which ultimately alleviates the analysis from the need for 3D simulations. As a benchmark design, the reactor configuration proposed by Aydin et al. [61] was considered, with a straight inner diffuser distributing the airflow in the TCM region.

The investigation was carried out in the context of domestic heating applications, and $SrBr_2 \cdot 6H_2O$ was selected as reference TCM [33,35]. The monohydrate and hexahydrate salt thermo-physical properties are reported in Table 4.2. The analysis solely focuses on the TCM hydration as this controls the discharging process and ultimately governs the amount of heat retrieved from the TCS system [62]. The discharge process was assumed to be driven by an airflow temperature of 25 °C with a partial vapour pressure of 998 Pa [37].

6.2 Optimization approach and numerical methods

6.2.1 Optimization approach

The optimization approach adopted for the performance maximization of open system TCS reactors is reported in Figure 6.2. First, a representative unit was identified for each one of the investigated reactor configurations. Thus, the design problem for the efficient configuration of flow channels was divided into two subproblems: topological design optimization and performance assessment.

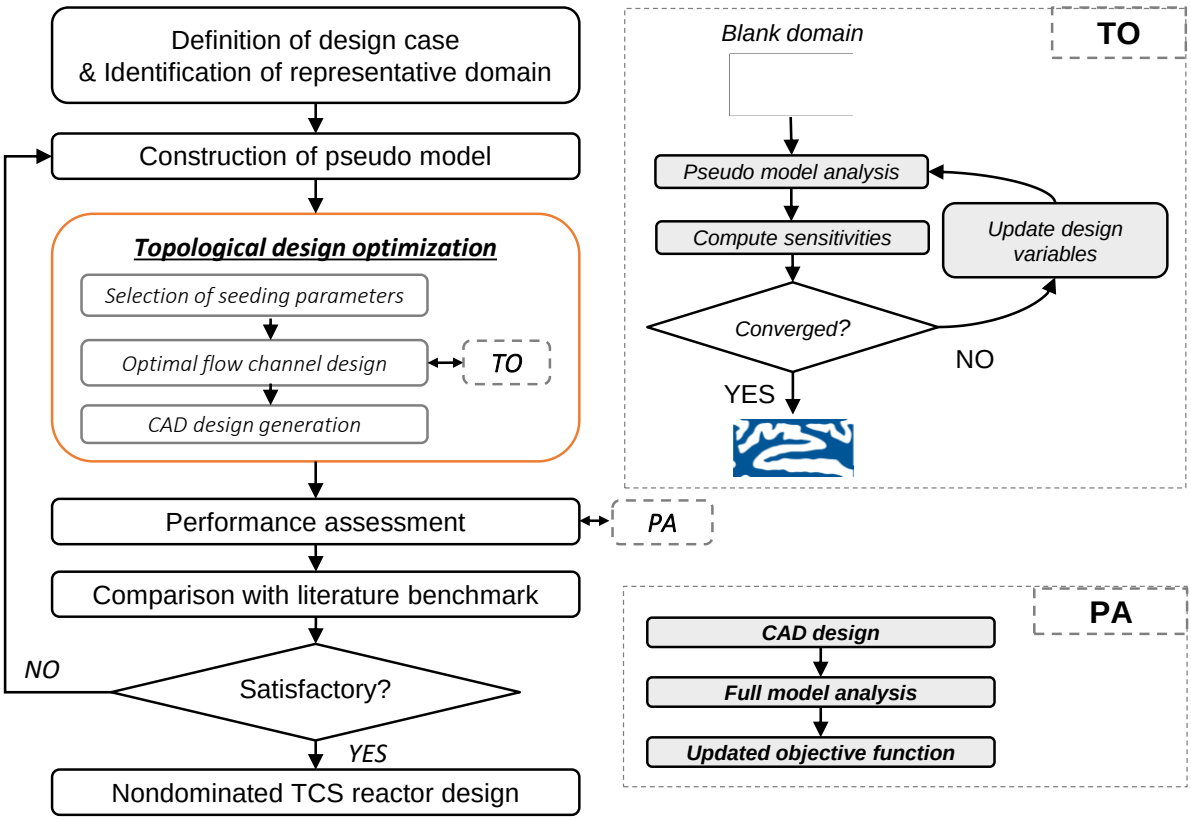

Figure 6.2 Optimization approach adopted for the mass transfer intensification in open system TCS reactors.

The topological design optimization makes use of a highly solvable numerical model, referred to as pseudo model, which decreases the nonlinearities of the original problem and can be thus easily coupled to the topology optimization algorithm. Besides, artificial design parameters, namely the seeding parameters, were incorporated into the pseudo problem optimization in such a way that various topology-optimized candidates were generated. The selection of proper seeding parameters is crucial to generating various design patterns. In this work, the seeding parameters were selected to represent physical parameters of the targeted problem in order to guarantee meaningful results interpretation and to guide the selection of the seeding parameter values. The multiple topology-optimized candidates were thus reconstructed to generate CAD designs whose performance was then evaluated

using a validated numerical model, referred to as the full model. Finally, the benefits led by the proposed optimization framework were quantified by comparison with the selected literature benchmarks [95].

6.2.2 Pseudo model

The aim of the flow channel design is to effectively distribute reactants in the porous region in such a way that TCM hydration can occur. To such an extent, the pseudo model was constructed by describing an isothermal reactor in steady-state conditions [248]. Besides, the governing equations were expressed to allow for a density-based description of the distributed materials, as typically done in fluid-based problems [165,249].

In the framework of the pseudo model, a convective diffusive equation was adopted to predict the reactants concentration distribution, while the Darcy law was used to describe the momentum conservation:

$$\nabla \cdot \mathbf{u} = 0 \tag{6.1}$$

$$\mathbf{u} = -\frac{1}{\alpha_b(\mathbf{s})} \nabla \cdot p \tag{6.2}$$

$$\mathbf{u}\nabla c = D\nabla^2 c - \dot{c}(\mathbf{s}) \left(\frac{p_v - p_{eq}\,(T_0)}{p_{v,in}} \right) \tag{6.3}$$

Where ***u*** is the velocity field, *c* is the vapour molar concentration, *p* is the airflow pressure, p_v is the relative vapour pressure, and p_{eq} is the equilibrium pressure for the TCM hydration. The terms $\alpha_b(\mathbf{s})$ and $\dot{c}(\mathbf{s})$ are the design-dependent inverse permeability and molar sink terms, respectively. The material interpolation strategies were formulated in such a way to recover the material properties in the TCM domain, Ω_{TCM}, and in the flow channel domain, Ω_{FC}, in the following way:

$$\mathbf{s} = \begin{cases} 0 \; in \; \Omega_{TCM} \\ 1 \; in \; \Omega_{FC} \end{cases} \quad 6.4$$

The ground domain, $\Omega_d = \Omega_{TCM} \cup \Omega_{FC}$, adopted for the generation of TO-based candidates is depicted in Figure 6.3. The same key geometrical dimensions were adopted for both the reactor configurations under investigation. The distinction between the two cases was made by the use of cylindrical coordinates in the instance of cylindrical reactor configuration [84].

The parameter *L* was fixed as 5 cm in the study and a quadrilateral mesh was adopted in the pseudo model framework, with an element size, h_{el}, equal to L/5. Ambient pressure was prescribed at the outlet interface, Γ_{out}, while a 1000 *Pa* pressure difference was imposed between the inlet and outlet interfaces. The inlet partial vapour pressure, $p_{v,in}$, was imposed at the inlet interface Γ_{in}. Null flux was instead prescribed at the wall and symmetry interfaces, Γ_w and Γ_s.

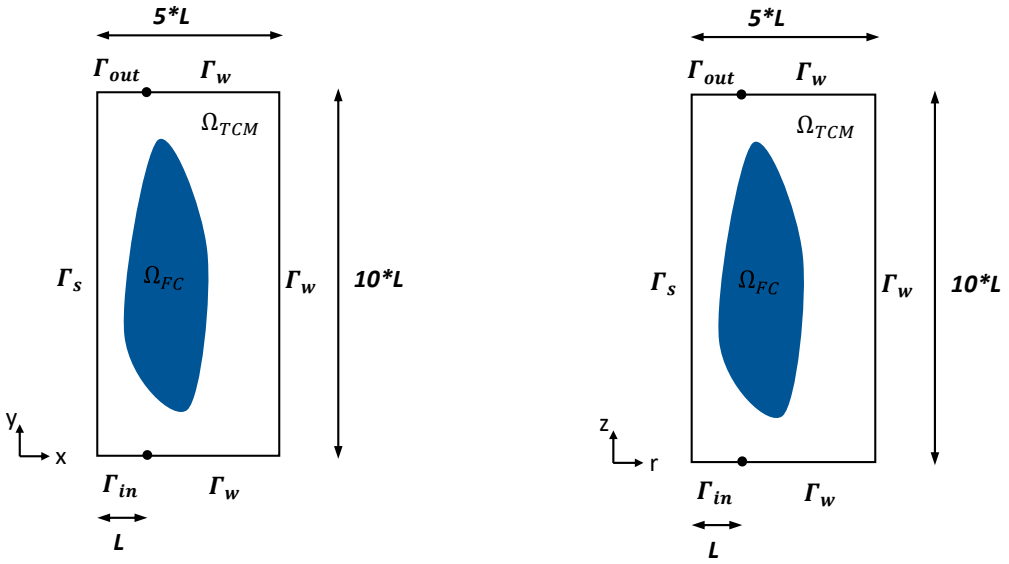

Figure 6.3 Ground domains for the topology optimization problems: (a) sieve reactor configuration; (b) cylindrical reactor configuration.

6.2.3 Full model

The full numerical model was implemented to accurately describe the heat and mass transfer mechanisms in the reactive bed and flow channels. The mass conservation for the vapour content in the porous TCM domain was described as follows:

$$\varepsilon \frac{\partial \mathrm{c}}{\partial t} + \boldsymbol{u}\nabla c + D\nabla^2 c = -\gamma \mathrm{n}_s \dot{\alpha} \qquad 6.5$$

Where ε represents the bed porosity, γ is the stoichiometric coefficient, n_s is the TCM molar density and $\dot{\alpha}$ represents the rate of the reaction advancement. Equation 6.5 was also adopted to describe the mass conservation in the flow channels domain, although here, a null molar sink term, $-\gamma \mathrm{n}_s \dot{\alpha} = 0$, was imposed, and an unitary porosity was considered [247]. The Darcy law described the momentum conservation in the porous domain [37,87]:

$$\mathbf{u} = -\frac{K}{\mu}\nabla p \qquad 6.6$$

Where *K* indicates the permeability, μ the dynamic viscosity and p the airflow pressure. An artificial $K_{air} = 1.0 \cdot 10^{-8}$ m^2 was adopted in the FC domain to represent the nearly negligible mass transfer resistance compared to the porous TCM [37]. The energy conservation was written within the porous TCM domain as follows:

$$(\rho c_p)_{eff}\frac{\partial \mathrm{T}}{\partial t} + \rho c_p \boldsymbol{u} \cdot \nabla T + \nabla \cdot (\lambda_{eff}\nabla T) = n_s \dot{\alpha} \Delta H \qquad 6.7$$

Where ρ is the density, c_p the specific heat, T the temperature, λ is the thermal conductivity, and ΔH is the enthalpy of the reaction. The subscript eff refers instead to the effective values, which were calculated according to:

$$(\rho c_p)_{eff} = (1-\varepsilon)\rho_{TCM} c_{p,TCM} + \varepsilon \rho_{air} c_{p,air} \qquad 6.8$$

$$\lambda_{eff} = (1-\varepsilon)\lambda_{TCM} + \varepsilon \lambda_{air} \qquad 6.9$$

The energy equation was instead written in the flow channels as:

$$(\rho c_p)_{air}\frac{\partial \mathrm{T}}{\partial t} + (\rho c_p)_{air}\, \boldsymbol{u} \cdot \nabla T + \nabla \cdot (\lambda_{air}\nabla T) = 0 \qquad 6.10$$

Finally, a 1st order reaction kinetics was adopted [30]:

$$\dot{\alpha} = k_{cin}\,(1-\alpha)\,(1 - \frac{p_{eq}(T)}{p_v}) \qquad 6.11$$

Where $k_{cin} = 8 \cdot 10^{-6}\, s^{-1}$ is the reaction kinetics constant [29] and $p_{eq}(T)$ is the equilibrium pressure, which was assumed to follow the Clausius-Clapeyron relationship [29]:

$$\ln(p_{eq}/p_0) = -\frac{\Delta H}{\gamma R T_{eq}} + \frac{\Delta \mathrm{s}}{\gamma R_{gas}} \qquad 6.12$$

The partial vapour pressure can be directly calculated from the molar concentration, assuming vapour as an ideal gas, $p_v = cR_{gas}T$ [87]. The material properties were

interpolated between monohydrate and hexahydrate state properties as a linear function of the reaction advancement [37], except for the material permeability, K_{TCM}, for which a $1/\alpha$ behaviour was assumed [87].

A constant temperature, T_{in} = 25 °C, and constant partial vapour pressure, $p_{v,in}$ = 998 *Pa*, were imposed at the inlet interface [29]. Besides, a reference pressure drop of 1000 Pa was adopted between the inlet and outlet interfaces, with the outlet interface considered at ambient pressure. In all the other boundaries, no flux conditions were imposed. The reactive bed was considered in thermal equilibrium with the inlet airflow at the initial time. That is, the initial temperature, T_0, was set equal to the inlet airflow temperature. The initial partial vapour pressure, $p_{v,0}$, was thus derived from equation 6.12 for the imposed initial temperature value.

The time-dependent study was solved in COMSOL Multiphysics environment [142] by adopting a backward differentiation formula with a time-adaptation scheme. Besides, an initial time step of 0.5 *min* and a maximum time step of *15 min* were imposed. The inlet vapour pressure was ramped up from the initial equilibrium pressure to the selected inlet vapour pressure in a *30 min* time range to smoothen the disequilibrium conditions during the initial stages of the hydration process [239]. Unstructured triangular meshes were adopted for the evaluation of each of the reconstructed designs, as depicted in Figure 6.5. The minimum element size was set at $1.0 \cdot 10^{-4}$, while the maximum element size was selected as $8.0 \cdot 10^{-3}$ through a mesh convergence study, as depicted in Figure 6.4.

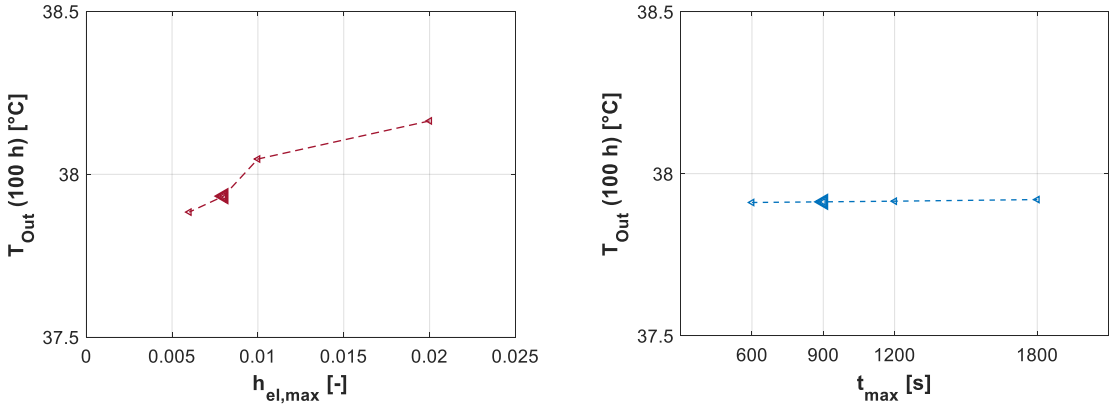

Figure 6.4 Convergence studies: (a) influence of the mesh maximum element size; (b) influence of the maximum time-step.

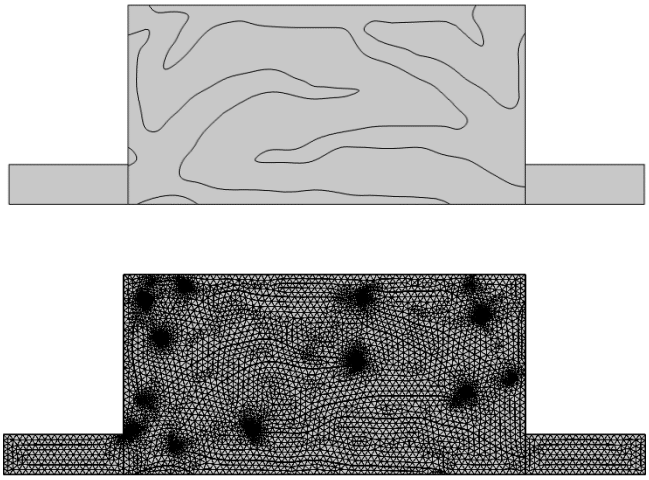

Figure 6.5 Unstructured triangular mesh adopted for a typical TO-based design in the instance of sieve reactor configuration: top for selected TO-based design and bottom for the generated mesh

The full model was validated against the experimental data presented by Michel et al. [29]. Here, the authors investigated consecutive hydration/dehydration cycles for a rectangular open TCS reactor with a 0.7x0.65 m^2 cross-section area and a 0.075 m thickness. The unit was tested for an inlet temperature of 25 °C and partial vapour pressure of 1 kPa, assumed

to represent mid-season operating conditions. Figure 6.6 shows the reaction advancement histories for the numerical and experimental data for three hydration cycles. A maximum mismatch below 3% was achieved, demonstrating good reliability for the model predictions.

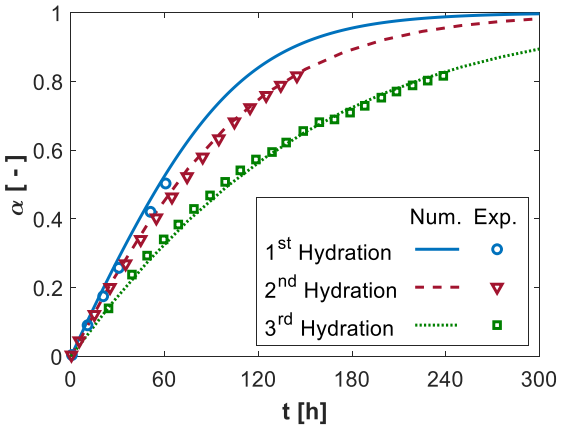

Figure 6.6 Model validation against the data presented by Michel et al. [29].

6.3 Topology optimization

The topology optimization algorithm was coupled with the pseudo model to generate multiple design candidates. The optimization problem considered in the analysis was the maximization of the reaction rate. The following objective function was, therefore, introduced:

$$\begin{cases} max \quad \int_{\Omega_d} \dot{m}(\mathbf{s}) \left(\dfrac{p_v - p_{eq}(T_0)}{p_{v,in}} \right) \\ 0 \leq \mathbf{s} \leq 1 \end{cases} \tag{6.13}$$

No volume constraints were necessary for the generation of optimal designs. In fact, while the generation of designs filled with TCM would lead to poor mass transfer performance, the use of solely FC material in the design domain would entail a null reaction rate. The packing factor value, PF, was estimated for each of the generated designs as follows:

$$PF = \frac{\int_{\Omega_{FC}} 1 \, dxdy}{\int_{\Omega_d} 1 \, dxdy} = \frac{\mathrm{V}_{FC}}{\mathrm{V}_{reactor}} \quad 6.14$$

The packing factor value thus represents the amount of volume devoted to the flow channels over the reactor volume. The adopted density-based approach required the definition of fictitious design-dependent material properties. The body force and reaction rate term were thus defined as a function of the design variable, ***s***, as follows:

$$\alpha_b(\boldsymbol{s}) = \alpha_{b,TCM} + (\alpha_{b,FC} - \alpha_{b,TCM}) \frac{\boldsymbol{s}(1+q)}{\mathbf{s}+q} \quad 6.15$$

$$\dot{m}(\mathbf{s}) = \dot{m}_{seeding} \, (1 - \boldsymbol{s}) \quad 6.16$$

With *q=0.1* representing the convexity of the interpolation scheme [250]. The body force terms for each of the distributed materials were defined as follows:

$$\alpha_{b,TCM} = \frac{K_{seeding}}{\mu} \quad 6.17$$

$$\alpha_{b,FC} = \frac{K_{air}}{\mu} \quad 6.18$$

Seeding parameters were incorporated in the pseudo model for the generation of multiple layouts. The seeding parameters were selected to represent the physical properties of the targeted design case. Specifically, the terms $K_{seeding}$ and $\dot{m}_{seeding}$ were adopted. The former refers to the TCM permeability. Given the TCM permeability value variation with the salt hydration level, two different $K_{seeding}$ values were considered. Specifically, the monohydrate and hexahydrate salt permeability were selected. Concerning the $\dot{c}_{seeding}$ parameter, this was thought of as the product of:

$$\dot{c}_{seeding} = \frac{k_{cin} \gamma \, \mathrm{n}_s}{\varepsilon} (1 - \alpha) \quad 6.19$$

In agreement with the molar sink term expressed in equation 6.5 for the full model. Thus, the term $\dot{c}_{seeding}$ represented the molar sink constant for the constructed pseudo model, and its numerical values were directly derived from physical parameters. Again, two values were used, accounting for different salt hydration levels. A first value was derived assuming $\alpha = 0$, while the second seeding parameter level was derived for $\alpha = 0.9$, as the assumption of a fully hydrated salt would result in null $\dot{c}_{seeding}$. Finally, the selected seeding parameter values are reported in Table 6.1. The optimal designs were generated by combining the selected values to obtain a total of four designs for each of the configurations under investigation.

Table 6.1 Values selected for the seeding parameters.

Seeding parameter	Units	Level 1	Level 2
$\dot{c}_{seeding}$	*[mol/m³/s]*	0.3	0.1
$K_{seeding}$	*[m²]*	$1.0 \cdot 10^{-10}$	$5.0 \cdot 10^{-12}$

Filtering and regularization techniques were adopted to ensure mesh independence and avoid the checkerboard effects in the emerging designs. The linear filter presented in [157] was considered, with a filtering radius equal to $h_{el} \cdot 1.1$ and a steepness projection parameter $\beta = 5.0$ [177]. The smoothing of the design variable was adjusted by the hyperbolic tangent projection operator, $\eta = 0.5$. The GCMMA was used as optimization routine to update the control variable [135], with a number of optimization iterations set at 200. Finally, the TO-based designs were reconstructed considering a cut-off parameter $s^* = 0.5$ [152].

6.4 Performance metrics

A series of performance metrics were defined and evaluated to assess the generated design candidates [46]:

1) The discharged energy, E_{t^*}:

$$E_{t^*} = \frac{\int_0^{t^*} \dot{m}_{air} c_{p.air} (T_{out} - T_{in})\, dt}{\mathrm{V}_{reactor}} \quad 6.20$$

The discharged energy was referred to the reactor volume and was calculated as the time integral of the thermal energy transferred to the HTF. The term $\dot{m}_{air}$ represents the air mass flow rate, while the terms T_{out} and T_{in} refer to the air temperature at the outlet and inlet interfaces, respectively. Finally, the term t^* represents the desired discharge time and was set equal to 200 *h* in the current investigation [29].

2) The discharged exergy, Ex_{out,t^*}:

$$\mathrm{Ex}_{out,t^*} = \frac{\int_0^{t^*} \dot{m}_{air} c_{p.air} \left(T_{out} - T_{in} - T_0 \ln\left(\frac{T_{out}}{T_{in}}\right)\right) dt}{\mathrm{V}_{reactor}} \quad 6.21$$

The discharged exergy was defined as the time integral of the rate of exergy recovered by the HTF [251,252]. Higher discharged exergy values are desired to achieve a higher quality of discharged energy [253].

3) The average temperature lift, ΔT_{t^*}:

$$\Delta T_{t^*} = \frac{\int_0^{t^*} T_{out} - T_{in}\ dt}{t^*} \quad 6.22$$

The temperature lift was defined as the temperature difference between the outlet and inlet interface temperatures averaged over the desired discharge time.

4) The peak of power output, P_{peak}:

$$P_{peak} = max\ (P) \tag{6.23}$$

The peak of power output was defined as the maximum thermal power output over the discharge history. The thermal power output, *P,* was defined as:

$$P = \frac{\dot{m}_{air} c_{p.air} (T_{out} - T_{in})}{\mathrm{V}_{reactor}} \tag{6.24}$$

6.5 Results

6.5.1 Sieve reactors

The topology-optimized candidates for the sieve reactor configuration obtained through the pseudo model described in section 6.2.2 are depicted in Figure 6.7. Interestingly, for most of the generated designs, no flow channels directly connecting inlet and outlet interfaces are obtained, but rather 'tentacular' configurations emerged. In such a way, the optimal flow channel design allows for effective transport of the moist air to TCM regions in the reactor, with the moist air crossing such regions prior to exiting the reactor. This is a unique result compared to the existing literature on the optimal FC designs of energy devices and derives from the relatively small mass transfer resistance characterizing the porous TCM regions. In fact, for design cases presenting stronger mass transfer resistance in the second distributed material, FC networks connecting inlet and outlet interfaces are typically obtained [156,211]. Thicker channels are obtained in case of increased pseudo-TCM permeability. This makes intuitive sense, as the larger permeability values entail lower mass transfer resistance, with the moist air able to cross thicker TCM regions in case of a fixed pressure drop. Besides, the FC thickness also increases in the case of larger reaction rate terms. In fact, larger $\dot{c}_{seeding}$

values entail higher rates at which water vapour is consumed, ultimately precluding the vapour transport in thick TCM regions. As a result, relatively small TCM content is obtained in e.g. design-D in Figure 6.7, while a large TCM over reactor volume ratio is achieved in the instance of design-A. Please note that volume constraints could be included in the TO algorithm for generating the sub-optimal designs in case targeted TCM over reactor volume ratios are required.

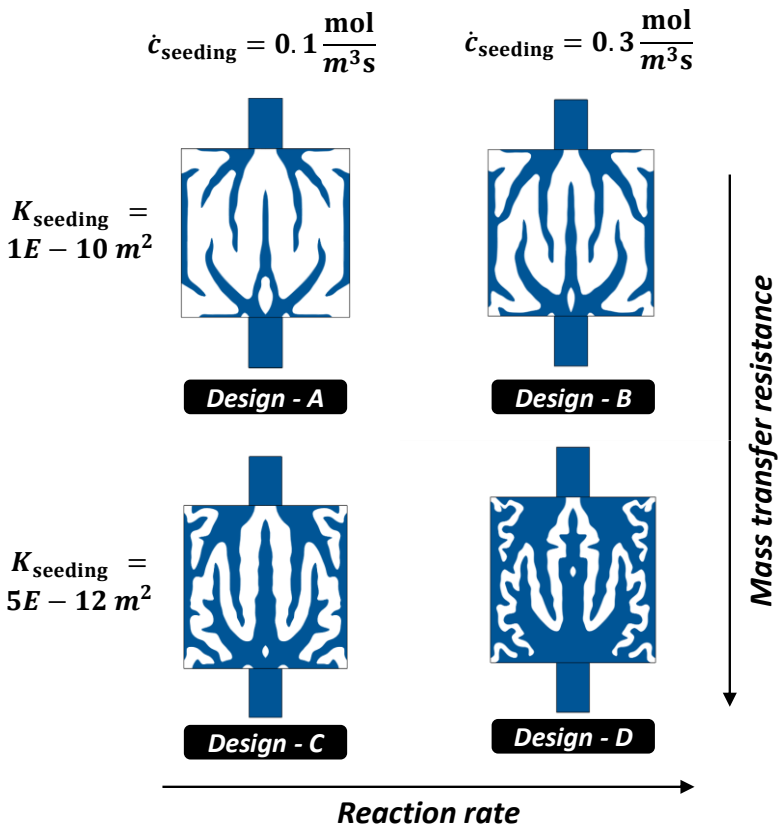

Figure 6.7 Topology optimization-based designs generated for the sieve reactor configuration. The blue domain refers to the FC geometry, while the white domain refers to the TCM.

The packing factor values for each generated design candidate and the selected benchmark are reported in Table 6.2. Overall, lower packing factor values are achieved for lower reaction rates and higher permeability.

Table 6.2 Packing factor for each generated design candidate and benchmark design [18].

	Design-A	***Design-B***	***Design-C***	***Design-D***	***Benchmark***
PF	0.28	0.40	0.53	0.68	0.43

6.5.1.1 Performance assessment

The performance of the generated designs is compared in this section with the selected literature benchmark. Firstly, the benefit led by the proposed design approach is evaluated by the comparison of the reactor energy density histories in Figure 6.8 (a). Concerning the energy discharged at the desired discharge time, *t**, all the proposed designs are predicted to outperform the selected benchmark. In particular, an increase in the amount of discharged energy up to +61% is obtained by the use of Design-B. The same design is also found as the best performing design for most of the simulated discharging time. However, if larger discharge times are considered, e.g. t = 300 h, Design-A is predicted as the most suitable design. This is due to the lower volume dedicated to the FC in the reactor, i.e. lower packing factor, which ultimately increases the amount of storage material. This result indicates that the best performing design depends on the selected discharge time, but also that the variation of the seeding parameters can be used to obtain suitable designs.

The discharged exergy histories are reported in Figure 6.8 (b). Differently from the discharged energy performance metrics, design-B is predicted here as the best performing design. This is an interesting result, demonstrating that the optimal geometrical features depend on the targeted performance metric. Thinner and shorter channels are the most efficient solution to maximize the discharged exergy. Besides, only a small discrepancy is predicted between the benchmark design and design-C and design-D. This result is dictated by the low mass transfer resistance for the two generated TO candidates and, thus, a larger

mass flow rate, which in turn entails a limited temperature lift, as shown in Figure 6.8 (c). The larger temperature lift is predicted for design-A, but only a mild enhancement is observed compared to the benchmark. The different mass flow rates predicted for each one of the designs are reported in Table 6.3.

Table 6.3 Mass flow rate for each generated design candidate and benchmark design [18].

	Design-A	***Design-B***	***Design-C***	***Design-D***	***Benchmark***
$\dot{m}$ *(t=0 s) [kg/s]*	0.046	0.068	0.083	0.099	0.009

Different trends are instead observed for the reactor power output histories, depicted in Figure 6.8 (d). A fairly steady history is predicted in the instance of the benchmark design, as was also suggested by the more linear energy discharge trend of Figure 6.8 (a). The topology-optimized candidates all present a pronounced peak of power output during the initial steps of the hydration process. Such behaviour derives from the large velocity field values characterizing all the generated designs compared to the benchmark, with up to a 10 times increase in the predicted outlet velocity. The largest peak of power output value pertains to design-B, which provides a performance enhancement of +216.0% compared to the literature benchmark. As a result, the proposed optimization approach can also be adopted to generate high-power density reactors. That is also, the tentacular geometrical features observed in Figure 6.7 are advised for such an aim. On the other hand, alternative design paths must be followed in design cases pursuing a high power output steadiness [218].

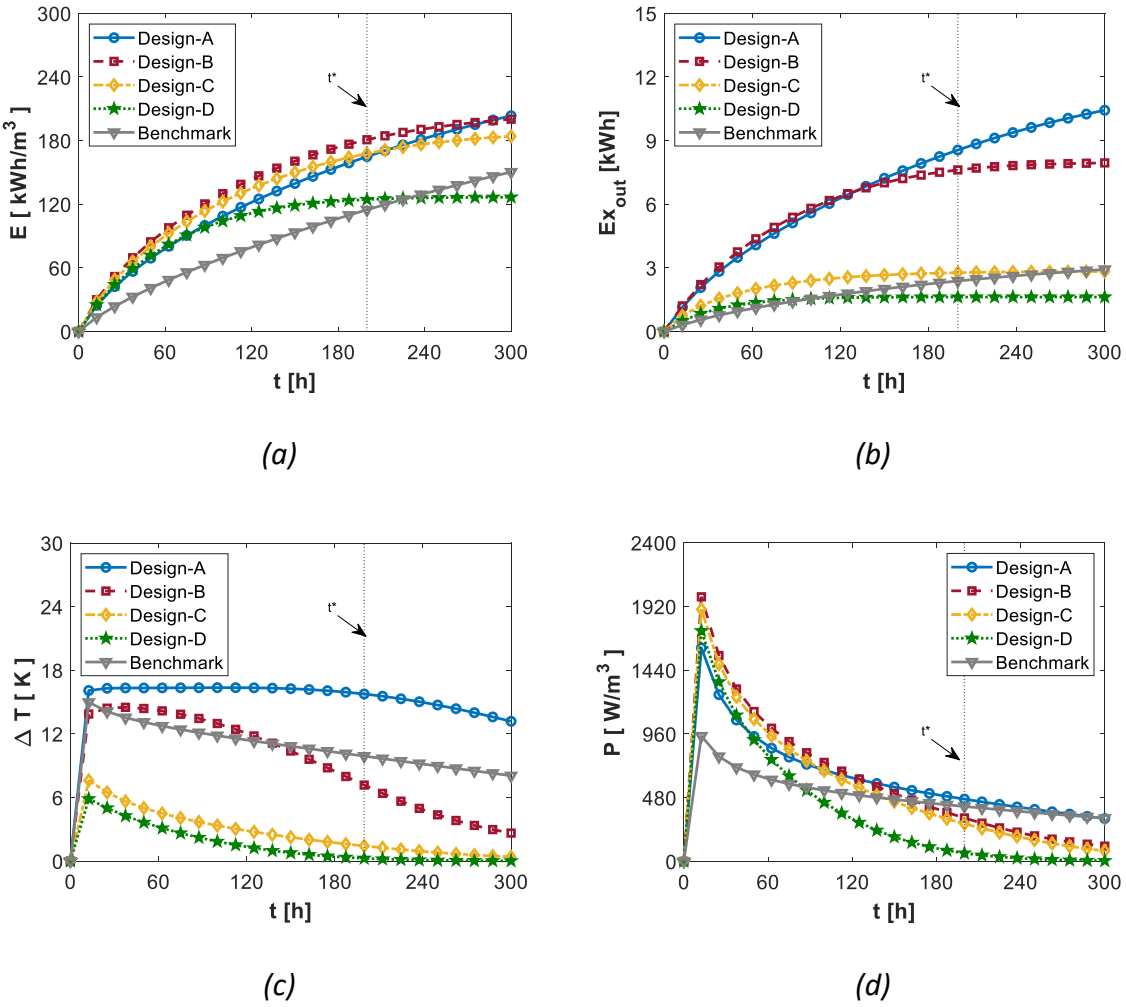

Figure 6.8 Performance metric histories comparison for the topology-optimized candidates in the sieve reactor configuration and benchmark design [18]: (a) Reactor energy density; (b) Exergy efficiency; (c) temperature lift; (c) Power output.

The performance metrics values for the selected desired discharge time, *t**, are summarized in Table 6.4. As mentioned, the most suitable design depends on the targeted performance metric. However, the use of tentacular flow channels characterizing design-A and design-B is always recommended to enhance the mass transfer in the reactive bed.

Table 6.4 Performance metrics values calculated considering a desired discharge time of 200 h.

PM	Design-A	Design-B	Design-C	Design-D	Benchmark
E_{t^*} *[kWh/m³]*	164.9	<u>180.8</u>	167.8	124.4	114.7
Ex_{out,t^*} *[kWh/m³]*	<u>8.6</u>	7.6	2.8	1.6	2.4
ΔT_{t^*} *[K]*	<u>16.1</u>	12.0	3.8	2.3	12.0
P_{peak} *[W/m³]*	1607.8	<u>1992.5</u>	1898.9	1736.2	944.2

Figure 6.9 shows the reaction advancement, temperature, airflow pressure and water vapour concentration contours at different time steps. The design-B and the benchmark design are compared. The TCM location in the benchmark design allows for good utilization of the first blocks of storage material, but a poor or null utilization is achieved for the blocks near the outlet interface due to the poor mass transfer in these regions. On the other hand, the generated FC geometry in design-B allows for a fairly homogeneous reaction advancement distribution, particularly in the proximity of the tentacular geometry elongating from the inlet interface. Relatively poor material utilization is still achieved for the TCM regions at the top of the reactor, which are thus found to react in longer times, $t > t^*$. Superior performance could likely be achieved by optimization approaches accounting for the complete physics interpretation and for time-dependent analysis.

Overall, no sharp transitions are predicted for the temperature distributions. The temperature in the TCM regions is higher than in the corresponding flow channels, as the reduced mass transfer resistance provides a more efficient cooling effect in the latter. A sharp transition is present in the airflow pressure contours and is dictated by the poor porous medium permeability of the hydrated salt. Limited influence from reaction rate is

predicted here, as the airflow pressure contours do not vary with time. Similarly to the reaction advancement, the water vapour concentration contours, Figure 6.9 (d), are predicted in design-B to propagate from the inlet flow channel boundaries towards the disconnected flow channel segments. A milder progression for the water vapour concentration distribution in the TCM regions is predicted for the benchmark design due to the poor mass flow rate crossing the porous medium.

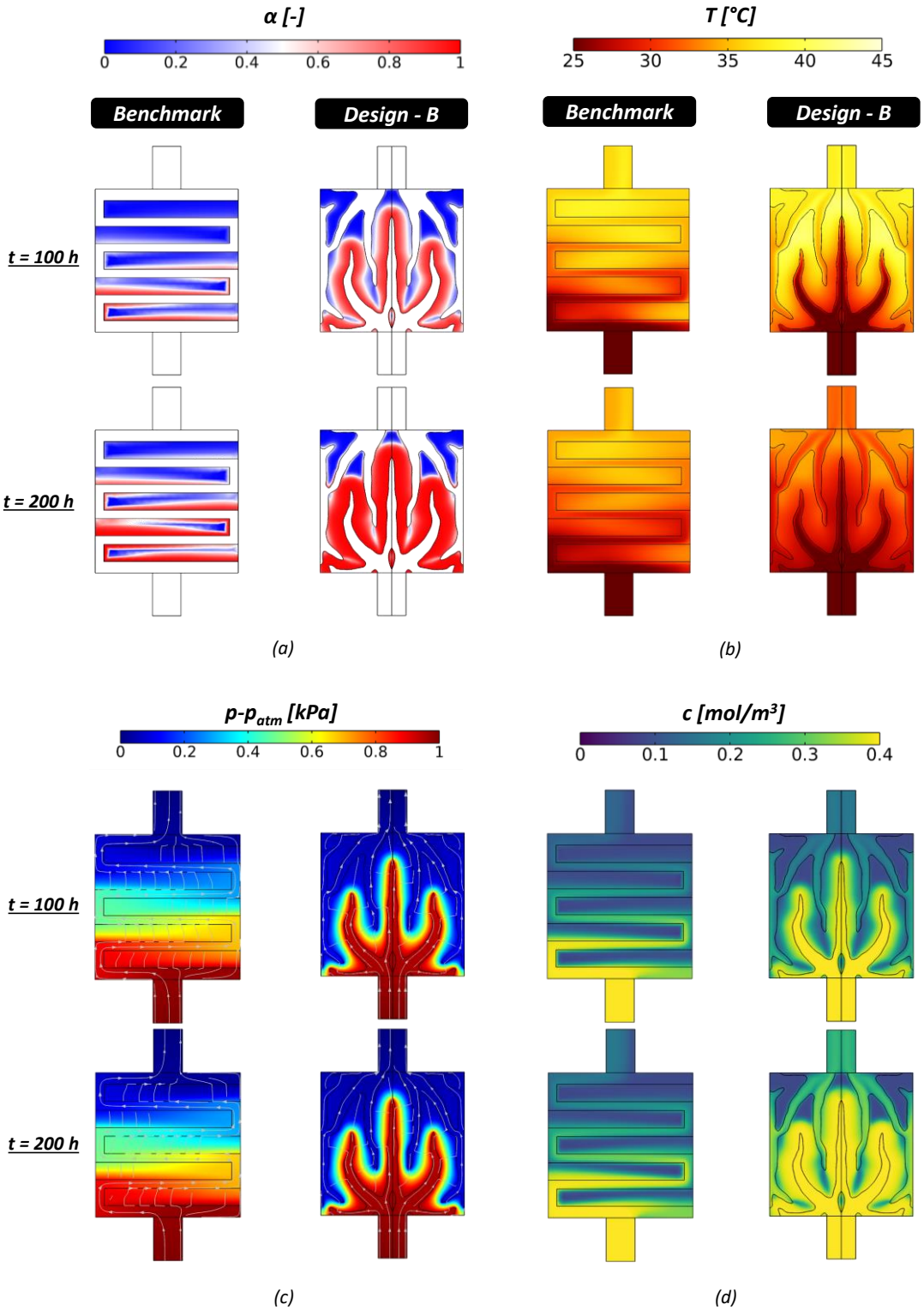

Figure 6.9 Contour plots for design-B and benchmark design [18] at different time-steps: (a) reaction advancement, (b) temperature, (c) relative pressure and (d) water concentration.

6.5.2 Cylindrical reactors

The TO-design candidates generated in the instance of cylindrical reactors are shown in Figure 6.10. The designs are depicted exploiting the axial symmetry, while three-quarters of the obtained geometry is reported to present the optimized flow channel geometries. Similarly to sieve reactors, the optimized flow channels do not directly connect inlet and outlet interfaces but aim to distribute reactants in various TCM regions. Also, the same effect of the seeding parameters value on the generated designs is observed, with thicker and longer channels obtained for increasing pseudo MT resistance and pseudo reaction rates. For some of the generated designs, e.g. design-2, flow channel segments disconnected from inlet and outlet interfaces emerged. These regions create preferential paths for the airflow directed to unreacted TCM before exiting the reactor, thus benefiting the mass transfer of the gas reactants. The manufacturability of these channel segments is beyond the scope of this work. Nevertheless, examples of topology optimization considering manufacturability constraints have been reported in the literature, e.g. [254]. Besides, a simple and practical approach is the manual removal of these segments to improve the design manufacturability.

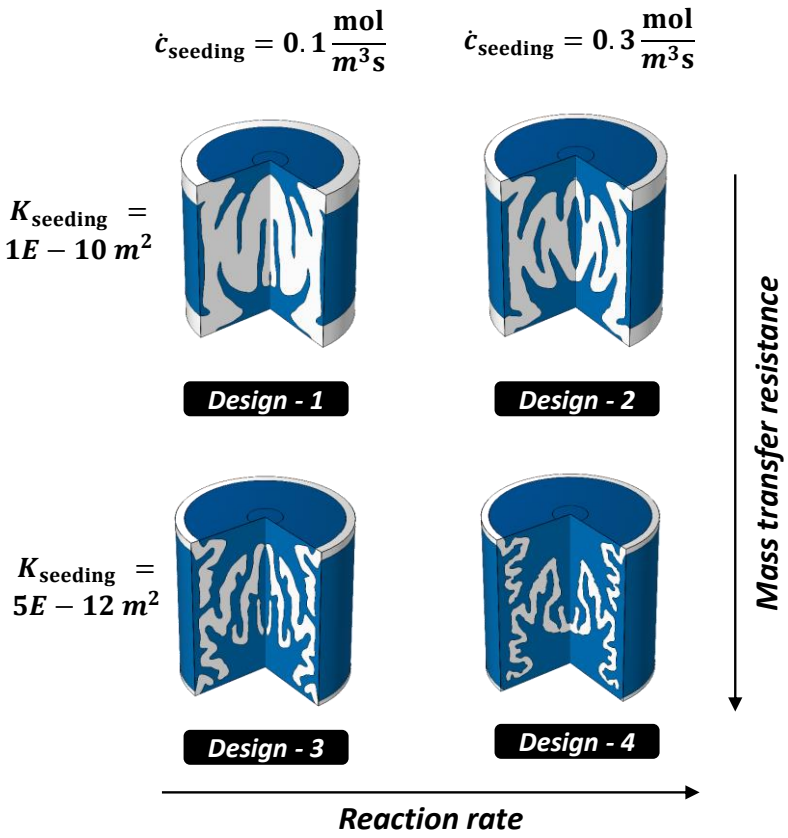

Figure 6.10 Topology optimization-based designs generated for the cylindrical reactor configuration. The blue domain refers to the FC geometry, while the white domain refers to the TCM.

Figure 6.11 compares the optimized flow channel designs for the sieve and cylindrical reactors for fixed values of seeding parameters. Specifically, the level 1 values from Table 6.1 was considered. A larger fraction of material was deposited by the optimizer near the inlet and outlet interfaces in the instance of the cylindrical reactor. On the other hand, a lower material amount is distributed near the outer shell. Both these features derive from using cylindrical coordinates for the cylindrical reactor.

Figure 6.11 Comparison of the optimized flow channel designs for sieve reactors, green colour, and cylindrical reactors, blue colour, for fixed values of seeding parameters, level 1.

The packing factor values for each generated design candidate and the selected benchmark are reported in Table 6.5. The TO designs all present a larger packing factor than the literature benchmark. This larger PF value derives from placing flow channels near the outer shell. The ability of these flow channels to retrieve more thermal energy from the reactive bed is assessed in the next section.

Table 6.5 Packing factor for each generated design candidate and benchmark design in the instance of cylindrical reactor configuration [61].

	Design-1	***Design-2***	***Design-3***	***Design-4***	***Benchmark***
PF	0.27	0.41	0.57	0.69	0.04

6.5.2.1 Performance assessment

The TO-design candidates reported in the previous section are assessed here by means of the full model presented in section 6.2.3.

Figure 6.12 shows the performance metric for the generated design candidates and the benchmark design. Concerning the amount of energy discharged, only a slight variation is

predicted among the four TO-design candidates. Again, the best performing design is observed to vary depending on the considered desired discharge time.

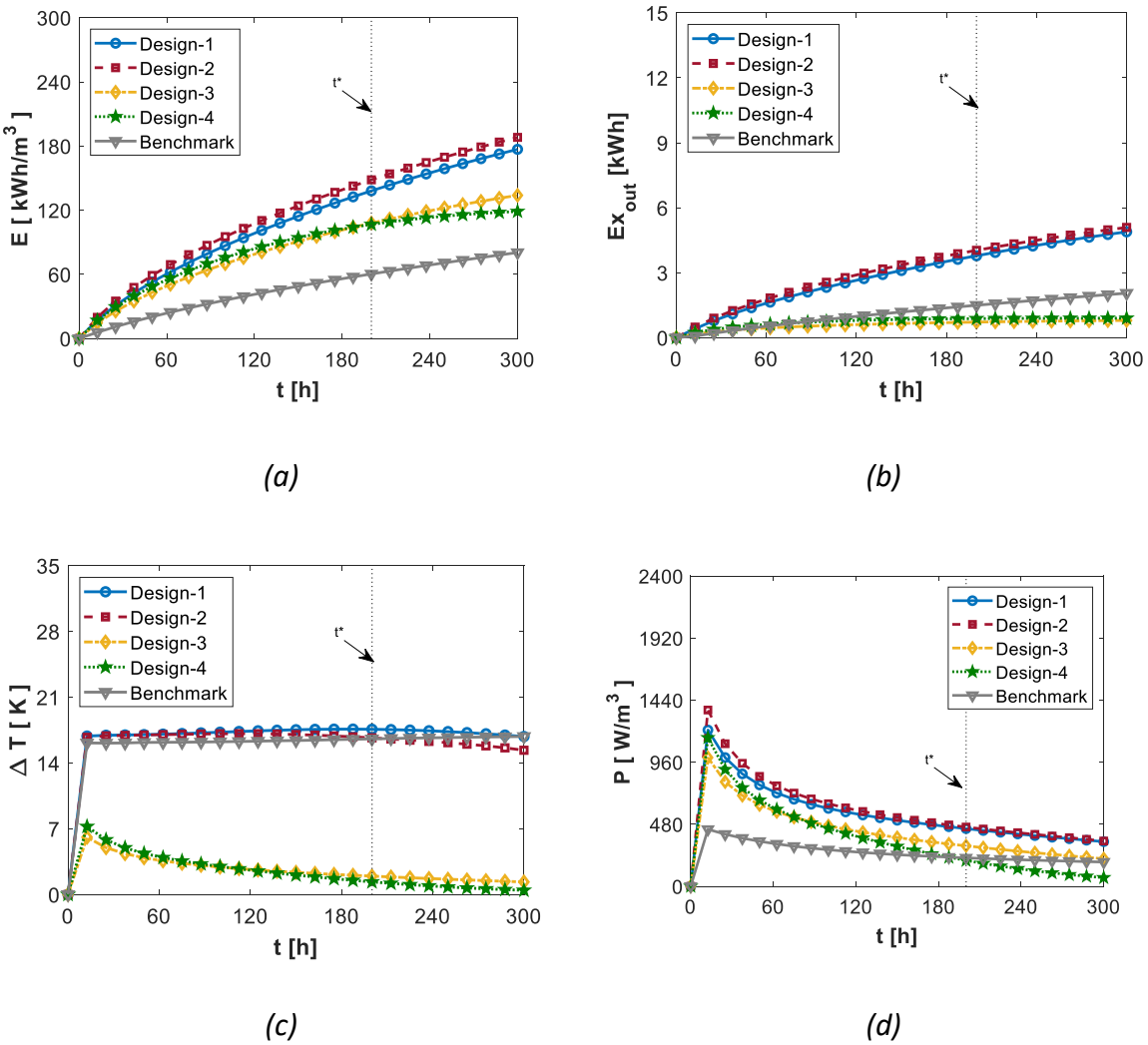

Figure 6.12 Performance metric histories comparison of topology-optimized candidates in the cylindrical reactor configuration and benchmark design [61]: (a) Reactor energy density; (b) Exergy efficiency; (c) temperature lift; (c) Power output.

In the instance of the selected *t**, design-2 is predicted as the best performing solution, with an increase in the amount of discharged energy up to $+245.7\%$ compared to the selected benchmark design. The best performing design, i.e. design-2, was generated by adopting the same seeding parameter values as for design-B. That is, large pseudo reaction values and

low pseudo MT resistance values appear as the most indicated seeding parameters to generate high-performing TCS devices.

Concerning the discharged exergy, Figure 6.12 (b), large performance discrepancies are obtained for the TO-design candidates. The designs presenting larger packing factors, i.e. design-3 and design-4, are predicted to lead to a low amount of discharged exergy. This result is dictated by the poor temperature lift, as shown in Figure 6.12 (c). In fact, thick and long flow channel geometries guarantee a large mass flow rate in the reactive bed and promote cooling. As a result, while fast hydration rates are achieved, a poor airflow temperature increase is obtained. Overall, these results highlight the importance of selecting a relatively low packing factor to achieve higher discharged exergy values.

Interestingly, after an initial spike, the temperature lift from design-1 is predicted to increase with the discharging time slightly. For example, the temperature lift increases by 0.38 $^{\circ}C$ from 100 h to 200 h. The geometrical features dictate this trend. The reaction front initially propagates from the diffuser channel connected to the inlet interface. When the reaction front intercepts different diffuser channel segments, the gas reactants are transferred to unreacted regions which are activated and thus begin to contribute to the airflow temperature increase. This trend was not observed in the design candidates for sieve reactors due to the smaller distance between channel segments. However, the results obtained in this chapter are insufficient to derive design guidelines on maximising the temperature lift steadiness in time, although they demonstrate that the flow channel design can significantly alter the temperature lift history from a TCS reactor.

Design-2 also results as a best performing solution in maximising the peak of power output. This result derives from the large temperature output and the larger mass flow rate compared to design-1. Interestingly, despite a poor temperature lift, design-4 is predicted to provide a large peak of thermal power output. This is due to the large packing factor adopted, which ultimately ensures a limited mass transfer resistance in the TCS device and, thus, a large mass flow rate.

The performance metrics values for the selected desired discharge time, t^*, are summarized in Table 6.6. Similarly to sieve reactors, the most suitable design varies with the targeted performance metric. Nevertheless, non-heuristic flow channels with low packing factors are recommended to enhance the mass transfer in the reactive bed. Overall, the predicted performance metrics values are lower than in sieve reactors. Considering the best performing solution from both investigated configurations, using sieve reactors ensures a +21.8% increase in the amount of discharged energy and +215.0% in discharged exergy.

Table 6.6 Performance metrics values calculated considering a desired discharge time, t^*, of 200 h.

PM	***Design-1***	***Design-2***	***Design-3***	***Design-4***	***Benchmark***
E_{t^*} [kWh/m^3]	138.1	<u>148.4</u>	107.9	106.7	60.4
Ex_{out,t^*} *[kWh/m^3]*	3.8	<u>4.0</u>	0.7	0.9	1.5
ΔT_{t^*} [K]	<u>17.1</u>	16.9	3.3	3.5	15.8
P_{peak} [W/m^3]	1209.1	<u>1363.5</u>	995.7	1149.4	440.8

Figure 6.13 depicts the reaction advancement, temperature, airflow pressure and water vapour concentration contours at different time steps. Design-2 and the benchmark design are compared here. In the latter, poor material utilization is predicted due to the poor mass

transfer achieved with the straight diffuser configuration. In fact, using a central pipe does not provide sufficient reactants distribution near the outer shell of the cylindrical reactor, ultimately preventing the discharge of a large fraction of the storage material. Concerning design-2, the reaction front propagates in time from the boundary of the flow channel connected to the inlet interface. Besides, after 200 h, the reaction front is predicted to propagate also from the disconnected flow channel segments. In fact, the presence of hydrated material between the inlet channel and these segments allows for gas reactants in the latter. As a result, regions of unreacted materials away from the inlet interface can be activated.

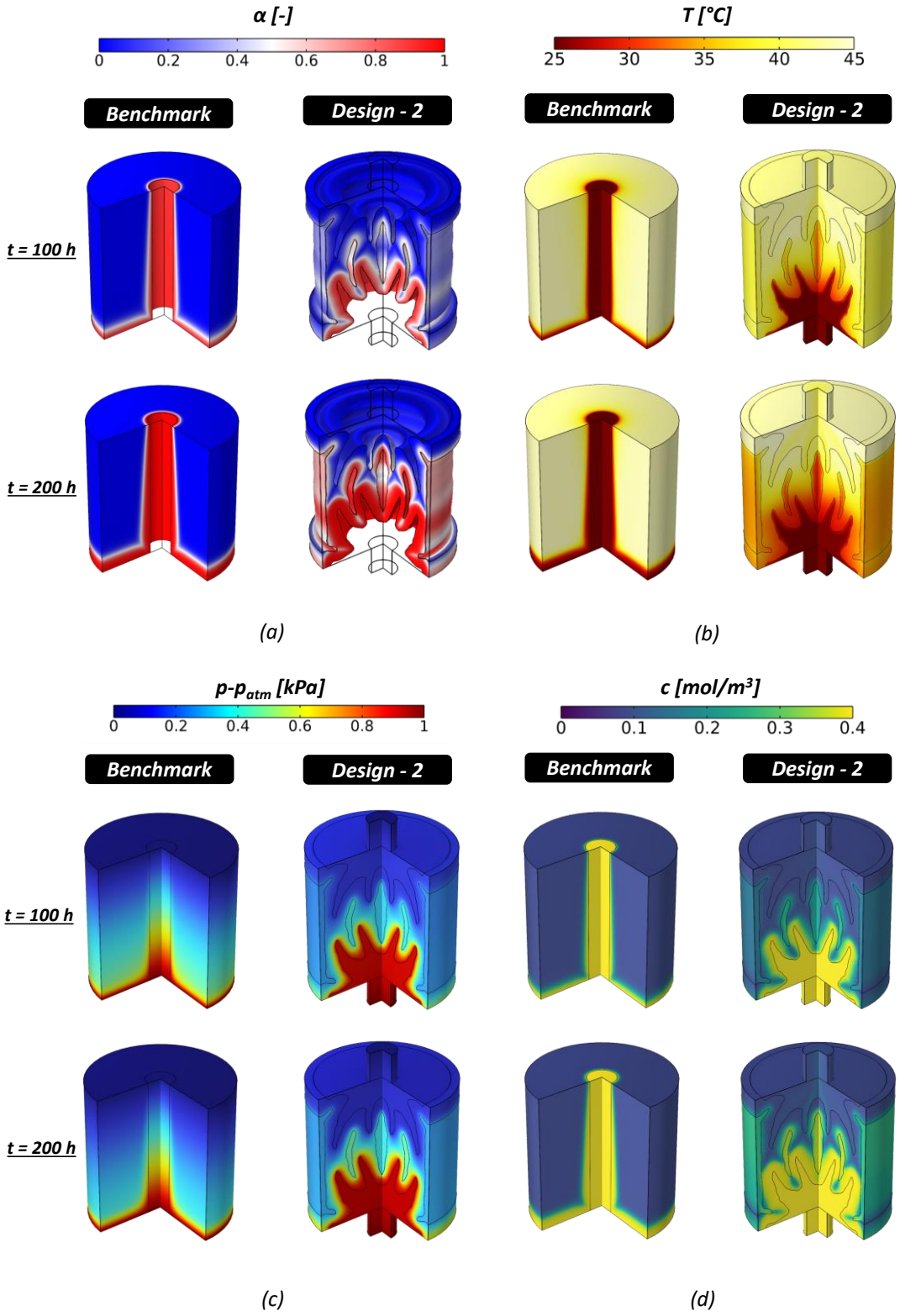

Figure 6.13 Contour plots for design-B and benchmark design [61] at different time-steps: (a) reaction advancement, (b) temperature, (c) relative pressure and (d) water concentration.

6.6 Considerations on the manufacturing of the optimal designs

This section discusses possible manufacturing routes for the optimal designs presented in this chapter. The complex geometrical emerging from the adopted optimization approach might indeed complicate the fabrication of the proposed reactors. Three-dimensional representations of two of the generated design candidates are depicted in Figure 6.14 . Concerning the sieve configuration, the design was obtained through the extrusion of the optimized flow channel geometries, while the cylindrical design was obtained through the revolution of the flow channel geometry around the central tube axis. The flow channel boundaries are made of a perforated metallic structure, which allows for the transfer of the carrier fluid (moist air) and, at the same time, ensures structural support for the storage material.

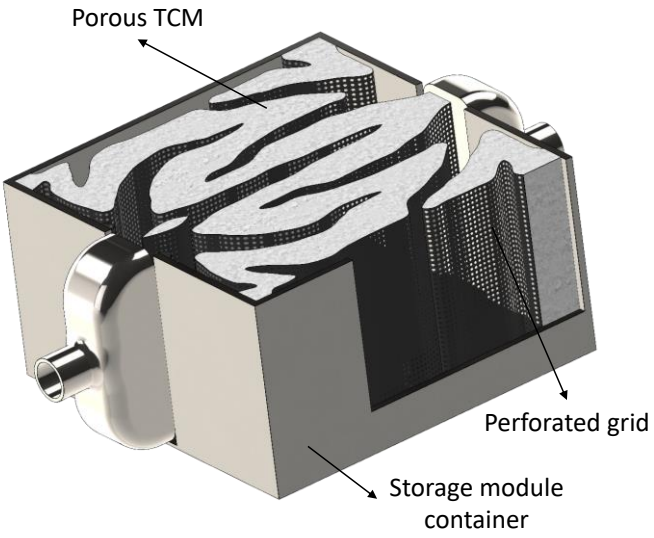

(a)

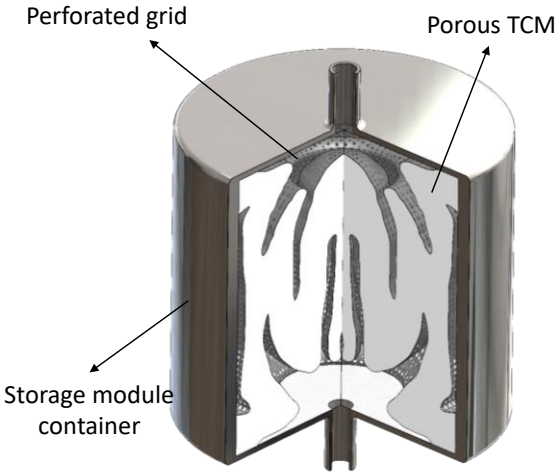

(b)

***Figure 6.14 3*D representation of two of the generated designs: (a) design-B and (b) design-1.**

Additive Manufacturing (AM) can be used to fabricate the flow channel designs. AM has many advantages over conventional manufacturing routes and has been increasingly used in a vast number of applications [245]. The flexibility of additive manufacturing to fabricate complex geometries from polymer and ferrous materials [240] presents unique opportunities for innovative design concepts. Additive manufacturing is, thus, an enabling

technology that allows designers to overcome the current manufacturing limitation that inhibits the adoption of topology optimization as a design tool. As reviewed in Chapter 2, additive manufacturing of topologically optimized energy devices has been growing rapidly [241,245], as several successful examples have been reported in the literature.

However, AM is still an emerging technique, while conventional manufacturing methods such as machining and injection molding/casting still dominate the manufacturing sector [149,243]. Consequently, as already mentioned in section 0, a second possible manufacturing route is envisioned based on the use of TO-inspired designs. The optimal geometrical features can be post-processed and simplified into *'conventional'* geometrical objects, such as straight channels. In this way, a trade-off between improved performance and manufacturability can be achieved.

6.7 Conclusions

This chapter addresses the need for mass transfer enhancement in open system TCS reactors. A topology optimization approach was proposed to generate and assess a series of non-heuristic flow channel designs. Such designs aim to effectively distribute a gas reactant in the reactive sites. From the results presented in this chapter, the following main conclusions can be derived:

- The proposed design methodology constitutes an affordable and thorough design approach for the non-heuristic configuration of open system TCS reactors. The performance of the generated designs was predicted to lead to an enhancement of

up to +245.7% in the amount of discharged energy compared to state-of-the-art solutions.

- The generated designs present tentacular flow channels which do not directly connect inlet and outlet interfaces. These flow channel geometries favour the transport of gas reactants in regions away from the inlet interface as well as the transport of the collected heat towards the outlet interface.
- The geometrical features for the most suitable design differ depending on the selected performance metrics. For example, thinner and shorter flow channels favour the maximization of the amount of exergy gained by the HTF compared to the amount of energy. Nevertheless, tentacular flow channel geometries are predicted to outperform benchmark designs regardless of the considered performance metric.
- Concerning the best performing solutions identified, sieve reactors outperform cylindrical reactors. An increased amount of discharged energy up to +21.8% is predicted. Thus, sieve reactors employing non-heuristic flow channel geometries are identified as the most-performing geometrical configuration for TCS devices.

Ultimately, the results and design framework presented in this chapter can largely impact the development of open system TCS devices. The evidence presented establishes new enhancement pathways in the context of open system TCS reactors.

In the next chapter, the generation of optimal flow channel designs is extended to closed system reactors and coupled with the generation of optimal fins geometries to enhance heat and mass transfer concurrently.

Chapter 7

Concurrent heat and mass transfer enhancement in closed system reactors through topology optimization

In this chapter, topology optimization is adopted to investigate the simultaneous heat transfer and mass transfer enhancement in closed system TCS reactors. The heat and mass transfer intensification techniques explored in chapters 5 and 6 are combined and extended here to generate reactive beds employing optimized flow channels and extended surface geometries. Three optimization routes were defined and investigated: (i) pure heat transfer intensification, (ii) pure mass transfer intensification, and (iii) concurrent heat and mass transfer intensification. While optimization routes (i) and (ii) have been extensively discussed in chapters 5 and 6, optimization route (iii) constitute a novel optimization pathway for the performance maximization of TCS reactors.

The concurrent heat and mass intensification was achieved through a multi-step topology optimization approach. First, the mass transfer in the reactive bed was enhanced by the generation of optimized flow channel geometries. That is, enhanced performance was achieved by removing TCM, ultimately leading to a lower investment cost for the storage

device. Thus, the reactive bed employing the generated flow channel design was adopted as the ground domain for the optimal distribution of HCM. In such a way, a final design presenting optimized flow channels and optimized extended surface architecture was obtained.

The three optimization routes were tested for the performance maximization of ADS-reactors and RDS-reactors employing $SrBr_2 \cdot 6H_2O$. Each route was investigated assuming a fixed amount of enhancer materials, in such a way that final devices utilizing the same amount of storage material were compared. Besides, the selection of the most suitable optimization pathway, i.e. optimization pathway leading to a design with superior performance, was elucidated through the off-design assessment of reference TO-based designs for variable operating conditions, bed properties and bed size.

The outline of this chapter is as follows: section 7.1 presents the closed system reactor configurations under investigation and the adopted TCM. In section 7.2, the governing equations for the physical problem and the approach for the design optimization of each of the reactor configurations under investigation are discussed. Thus, section 7.3 describes the objective function and material interpolation schemes adopted for the topology optimization problems. In section 7.4, the optimal designs are analyzed, as well as the design trends with respect to reactor configuration and TCM properties. Section 7.5 summarizes the achievements of the chapter.

7.1 Reactor configuration and material selection

The analysis focuses on the performance maximization of ADS-reactors and RDS-reactors. However, in addition to the design of extended surfaces discussed in chapters 4 and 5, flow

channel designs elongating from the vacuum chamber interface were considered, as depicted in Figure 7.1 in the instance of ADS-reactors. These flow channels aim to distribute the gas reactants in the reactive bed to enhance the mass transfer and elongate in the reactive bed from the vacuum chamber.

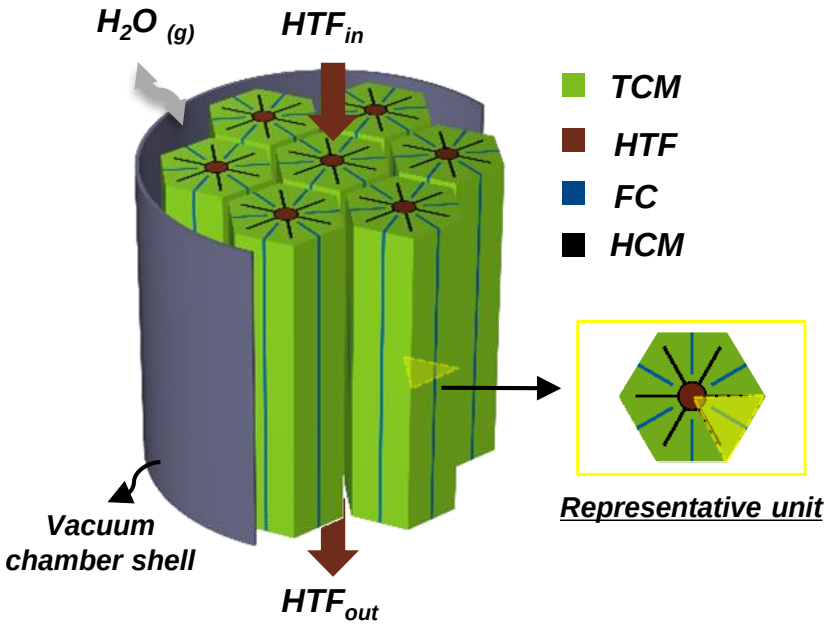

Figure 7.1 Schematic of the ADS-reactor concept employing radial fins for the heat transfer intensification and flow channels for the vapour distribution intensification.

Similarly to chapters 4 and 6, low-temperature TCS systems were considered and, in agreement with the results presented by N'Tsoukpoe et al. in [35], $SrBr_2 \cdot 6H_2O$ was selected as reference TCM. The hydration process was analysed, with the operating conditions and material properties adopted as per chapter 4. Nevertheless, two salt grain sizes were investigated to focus the analysis on the influence of the bed mass transfer properties on the optimal designs and most suitable optimization pathways. Specifically, a uniform 50 µm grain size was assumed for the small grain size, while a uniform 80 µm grain size was assumed for the large grain size. For the selected grain sizes, experimental values for the

bed permeability were derived by Michel et al. [81], as reported in Table 7.1. Instead, the bed porosity was assumed insensitive to the salt grain size [81]. As a result, only the dehydrated and hydrated salt permeability were influenced by the salt grain size selection and the remaining TCM thermophysical properties are reported in Table 4.2

Table 7.1 Influence of salt grain size on the TCM permeability [37,87]**.**

	large grain (LG)	***small grain (SG)***
	d_g = 80 µm	**d_g = 50 µm**
$K_{TCM,0}$ $[m^2]$	$1.0 \cdot 10^{-10}$	$0.2 \cdot 10^{-10}$
$K_{TCM,1}$ $[m^2]$	$5.0 \cdot 10^{-12}$	$0.8 \cdot 10^{-12}$

7.2 Design approach and numerical methods

Figure 7.2 presents the optimization routes explored in this chapter to obtain TCS reactor geometries with maximized thermal performance. For each optimisation pathway, the MUM problem was investigated (section 5.3.1). The final reaction advancement at the desired discharge time was thus maximized for a fixed amount of storage material.

Optimization route 1 (R1), i.e. heat transfer optimization pathway, has been extensively explored in chapter 5 and dealt with the definition of optimal HCM architectures to maximize the heat transfer in the reactive bed.

Optimization route 2 (R2) dealt with the mass transfer intensification in the reactive bed and was used to define flow channel layouts to distribute vapour to the reactive sites. This optimization route extends the results presented in chapter 6 to the instance of closed systems. Besides, compared to chapter 6, the TO algorithm was coupled with an analysis model capable of accurately predicting the reactor behaviour in such a way that no pseudo

models were necessary. Consequently, fit-for-purpose designs could be generated without the need for seeding parameters.

Optimization route 3 (R3) is a novel enhancement pathway combining both intensification approaches studied in this dissertation. In this optimization route, the heat transfer and mass transfer were concurrently intensified through a multi-step TO approach. First, the optimal flow channel design was generated; thus, the reactive bed utilizing the optimized flow channel design was adopted as the ground domain for the HT optimization problem. As a result, a final reactor employing optimized FC design and HCM architecture was obtained. The comparability between the designs was ensured by using fixed volume constraints for the FC and HCM distribution.

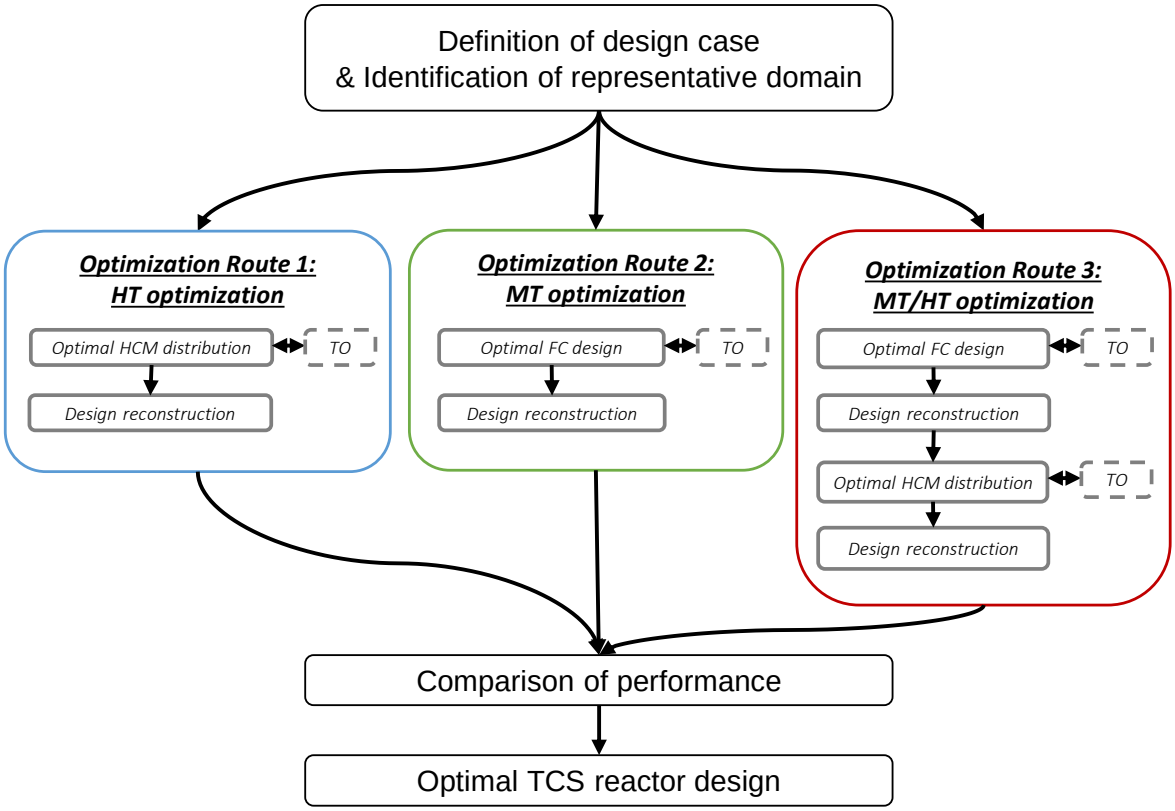

Figure 7.2 Optimization routes defined for the TCS reactor's performance maximization.

In ADS-reactors, such volume constraints were imposed as 10% for the HCM and FC material in optimization routes 1 and 2, respectively. Regarding optimization route 3, the volume requirement was respected by imposing a 5% constraint for the FC distribution and a 5% constraint for the HCM distribution. In the instance of RDS-reactors, the final packing factor value was instead reduced to 7.5%, as further detailed in section 7.2.2.

7.2.1 Governing equations

The governing equations were the ones presented in section 5.2.1, with the reaction kinetics modified to equation 4.8 in agreement with the selected TCM. Besides, the Darcy law was re-written to account for the material interpolation strategy adopted in chapter 6 to perform the MT optimization problem:

$$\mathbf{u} = -\frac{1}{\alpha_b(\boldsymbol{s})}\nabla \cdot p \tag{7.1}$$

In the context of ADS-reactors, the different ground domains adopted for the HT maximization, MT maximization and HT/MT maximization problems are reported in Figure 7.3. Similar to the previous chapters, in the internal boundary, Γ_{in}, a Robin boundary condition was prescribed, while no transport flux was imposed to solve the mass transfer problem. In the outer boundary, Γ_v, thermal insulation was considered and prescribed vapour pressure was used to model the interface with the vacuum chamber. Concerning the multi-step optimization, the optimal geometry obtained after the FC material distribution is removed from the ground domain and fixed vapour pressure was considered on the deriving boundary, as can be observed in Figure 7.3 (c). Symmetry boundary conditions, Γ_s, were assumed to account for the ground domain periodicity.

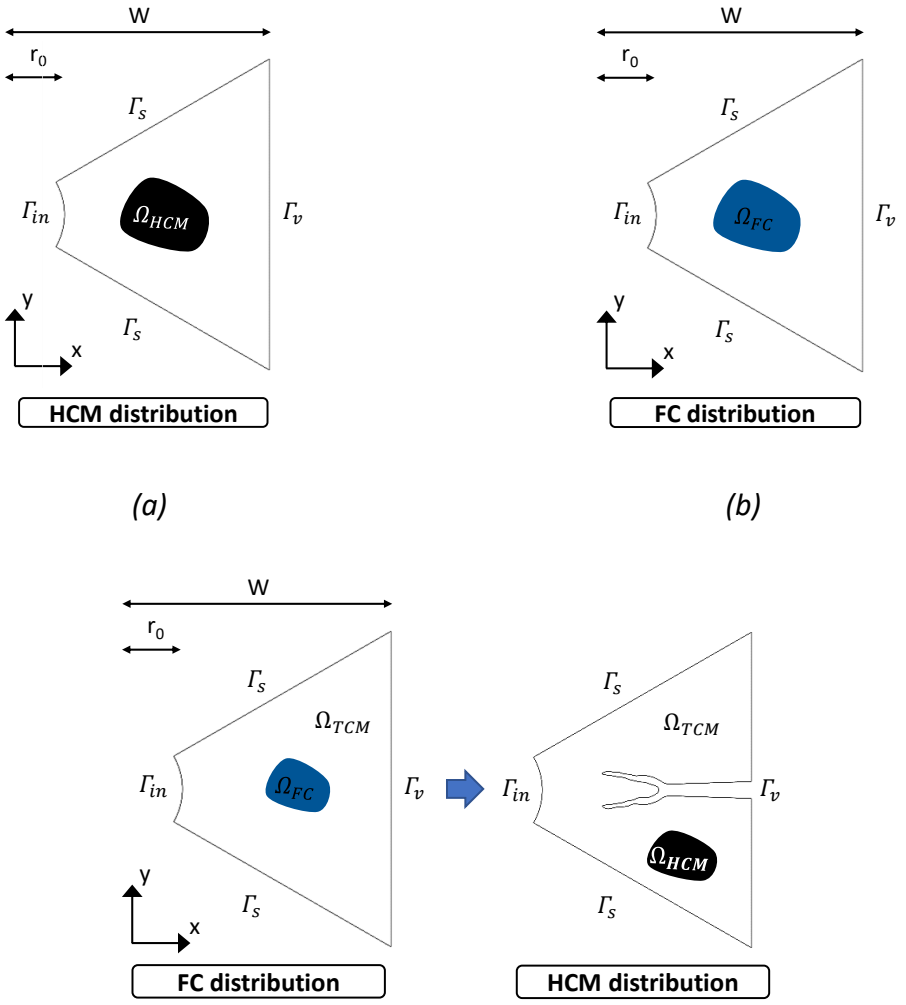

Figure 7.3 Ground domain for each of the three optimization routes: (a) optimization route 1; (b) optimization route 2; (c) optimization route 3.

The material interpolation strategy for the HCM distribution remained unvaried compared to section 5.2.1. Concerning the FC material distribution problem, the material interpolation schemes were formulated in such a way to recover the material properties in Ω_{FC} and Ω_{TCM} according to:

$$\varepsilon(\boldsymbol{s}) = \begin{cases} 1 \; in \; \Omega_{FC} \\ \varepsilon_{TCM,\ \alpha=0.5} \; in \; \Omega_{TCM} \end{cases} \qquad 7.2$$

$$\alpha_b(\boldsymbol{s}) = \begin{cases} \dfrac{K_{air}}{\mu} \; in \; \Omega_{FC} \\ \dfrac{K_{TCM,\alpha=0.5}}{\mu} \; in \; \Omega_{TCM} \end{cases} \quad 7.3$$

$$C(\boldsymbol{s}) = \begin{cases} \left(\rho c_p\right)_{air} \; in \; \Omega_{FC} \\ \left(\rho c_p\right)_{eff,\ \alpha=0.5} \; in \; \Omega_{TCM} \end{cases} \quad 7.4$$

$$\lambda(\boldsymbol{s}) = \begin{cases} \lambda_{air} \; in \; \Omega_{FC} \\ \lambda_{eff,\alpha=0.5} \; in \; \Omega_{TCM} \end{cases} \quad 7.5$$

$$g(\boldsymbol{s}) = \begin{cases} 0 \; in \; \Omega_{FC} \\ 1 \; in \; \Omega_{TCM} \end{cases} \quad 7.6$$

A fictitious air permeability, K_{air}, of $10^{-6} m^2$was set in the FC domain, Ω_{FC} [37]. Besides, the air thermo-physical properties were assumed to be constant with temperature. The operating conditions adopted for the optimal design generations are presented in section 4.1.2. For the optimal design generation, the parameter W was selected as 50 *mm*, while the outer pipe radius, r_0, was selected as 12 *mm*. Nevertheless, the influence of the operating conditions and reactive bed size on the most suitable optimization pathway is investigated in section 7.4.1.3.

A quadrilateral mesh was adopted for optimization routes 1, 2 and the first step of optimization route 3. The mesh element size, h_{el}, was set equal to $\frac{W}{50} = 10^{-3}\ m$. Concerning the second step of optimization route 3, a free triangular mesh with a maximum element size of $3.0 \cdot 10^{-4}\ m$. This maximum element size led to a large number of elements, as can be appreciated in Figure 7.4, with a consequent high computational time for the HCM distribution problem, $\approx 21\ h$. Nevertheless, a highly refined mesh was essential to ensure symmetrical designs between the top and bottom parts of the ground domain. Given the

adopted boundary conditions, asymmetrical geometrical features indicated a poorly accurate numerical problem.

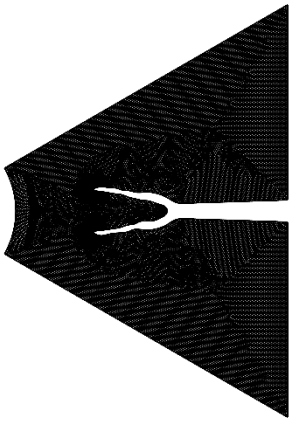

Figure 7.4 Free triangular mesh with 44573 elements adopted for the HCM distribution in optimization route 3.

7.2.2 Pseudo-3D optimization of RDS-reactors

This section presents the pseudo-3D design approach adopted for the concurrent heat and mass transfer enhancement via topology optimization of RDS-reactors. In RDS-reactors, the heat and mass transfer mechanisms pertain to orthogonal preferential directions. Hence, a pseudo-3D optimization strategy was proposed for concurrent heat and mass transfer intensification. Compared to a full 3D optimization, the proposed strategy allows for (i) reduced computational cost, (ii) higher numerical stability and (iii) more straightforward interpretation and manufacturing of the emerging design trends.

The pseudo-3D approach developed in this chapter is summarized in Figure 7.5. Two orthogonal planes were studied. A vertical plane, i.e. *zx*-plane, where the flow channel material was distributed. Here, the adopted coordinates were approximate to cylindrical ones for the solution of the analysis model. The upper boundary, referred to as Γ_v,

represented the interface with the vacuum chamber. The boundary Γ_{in} represented instead the interface with the HTF pipe, where a convective heat transfer boundary condition should typically be imposed. Nevertheless, the choice of such a boundary condition was observed to largely influence the optimal design and the selection of the most suitable boundary condition for Γ_{in} is discussed in the section 7.4.2.

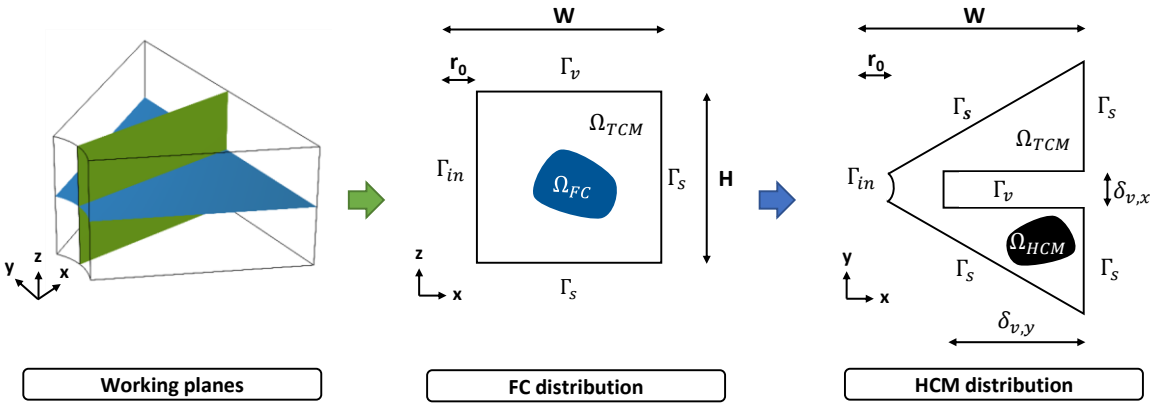

Figure 7.5 Schematic of the pseudo-3D approach adopted for the concurrent heat and mass intensification of RDS-reactors.

The obtained optimal geometry was extruded for a heuristically selected thickness, $\delta_{v,x}$, of 6 *mm*, with such a value selected in agreement with typical diffuser sizes from the literature [40]. A maximum volume fraction of 10% was chosen for FC design in the vertical plane. Nonetheless, given the extruded configuration, the volume fraction of the reactive bed dedicated to the flow channel geometry resulted in 2.5%. Thus, HCM was distributed on the horizontal plane, i.e. *yx* plane, to enhance the heat transfer. A maximum volume fraction of *5%* was selected for the HCM distribution. Furthermore, to avoid overlapping FC and HCM, the projected flow channel geometry was used in the HCM distribution problem. The length of the project FC geometry, $\delta_{v,y}$, was dictated by the optimal geometry emerging from the MT maximization step. The vacuum chamber pressure was imposed on the projected

geometry boundary to approximate the vapour transfer in the reactive bed for the heat transfer maximization problem.

In the framework of RDS-reactors, only optimization routes 1 and 3 were explored. For the solution of optimization route 1, solely the horizontal plane was considered in the absence of flow channels. In fact, in agreement with the conclusions reported in chapter 4 for RDS-reactors, the optimal distribution of HCM is insensitive to the gas reactants transfer. Thus, the vapour pressure in the whole reactive bed was assumed to be equal to the vacuum chamber pressure, and a pure heat conduction problem with a heat source term dictated by the reaction kinetics equation was coupled with the TO algorithm to derive the optimal extended surface architecture. The maximum volume fraction was selected in agreement with the packing factor from optimization route 3, $V^* = 7.5\%$. The parameter W was set at 50 *mm*, the outer pipe radius, r_0, was selected as 12 *mm*, and the bed height H was set at 38 *mm*, i.e. $W\text{-}r_0$.

7.3 Topology optimization

The desired discharging time was set at t^* = 10 h [47], and the MUM optimization problem was adopted. This choice was dictated by the need to ensure a fixed amount of storage material in each TO-based design to ensure fair comparability among the different optimization routes. For example, in the context of ADS-reactors, each optimized design presents a 10% packing factor. Such a packing factor value was achieved in optimization route 3 through a 5% volume fraction for the FC design and a 5% volume fraction for the extended surface design. The selection of these values was expected to influence the

emerging design and thermal performance. However, this dissertation does not investigate the influence of the packing factor selection on the final designs.

7.3.1 Material interpolation

The material interpolation strategies for the HCM distribution remain the ones described in section 5.3.2, with the interpolation scheme for the density-based permeability modified to a linear scheme to reduce nonlinearities. Concerning the FC design, a SIMP interpolation scheme was used for the thermal conductivity and heat capacity. Linear interpolation was adopted for the design-dependent switch $g(\boldsymbol{s})$, and the bed porosity, $\varepsilon\ (\boldsymbol{s})$. The body force term, $\alpha_b(\boldsymbol{s})$, was instead interpolated in agreement with the scheme introduced in equation 6.15.

Filtering and regularization schemes remained unvaried compared to section 5.3.3, as well as the adopted continuation scheme. The GCMMA was used as optimization routine to update the material density after each optimization iteration, and the optimization process was terminated after 150 iterations [135].

7.4 Results

7.4.1 ADS-reactor

Figure 7.6 depicts the design evolution along the optimization iterations for each optimization route under investigation in the instance of small grain, SG, size. The control variable is shown in agreement with the reported colour bar, although different materials are represented in the different optimization pathways.

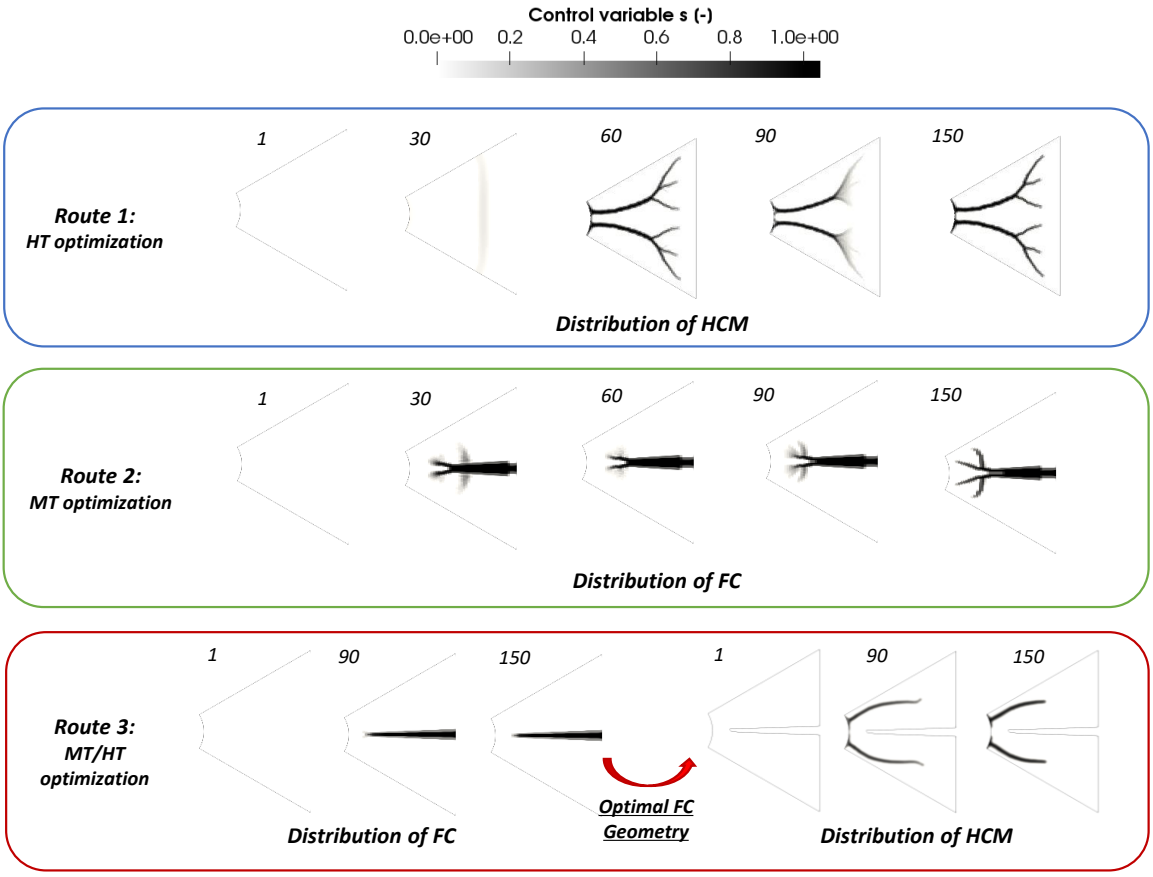

Figure 7.6 Material distribution evolution at selected optimization iteration steps for each of the investigated optimization routes in the instance of small grain size.

In the instance of the HT maximization problem, the white colour represents TCM, and the black colour represents HCM. After 30 iterations, the HCM is mainly distributed vertically at a specific distance from the vacuum chamber interface. This distance is dictated by the limited mass transfer properties of the reactive bed, which entails a short distance travelled by the vapour. After 60 iterations, two distinguished fins are visible, although with blurry secondary ramifications. With the progression of the optimization iterations, these ramifications become crisper, and no grey material is present in the final design at iteration 150.

Concerning the MT optimization route, white is used to represent TCM and black is used to represent the FC material. A clear flow channel geometry is already visible after only 30 iterations. The distributed material elongates from the vacuum chamber interface, i.e. right-hand side of the ground domain, towards the central HTF pipe, with bifurcations emerging near the central part of the ground domain. No significant design changes are present for the following iterations, although more crisp boundaries are achieved.

Finally, concerning the HMT maximization problem, the flow channel material is distributed in the first 150 iterations, while HCM is distributed in the following 150. The generation of the optimal flow channel design results to quickly converging to a horizontal straight channel. Irregular fins emerged from the second topology optimization problem. The length of these fins reduced with the optimization iterations, while their thickness increased. These geometry modifications are dictated by the imposed continuation scheme, through which unphysical materials, i.e. grey colours, are made progressively less attractive along the optimization history.

7.4.1.1 Influence of bed permeability on the optimal design

The generated designs are reported in Figure 7.7 for each investigated optimization route and salt grain size (Table 7.1). Concerning optimization route 1, i.e. the pure HT maximization, the optimal design significantly differs depending on the selected grain size. In particular, the geometrical features of the SG-R1 design appear to depart from the design guidelines derived in chapter 4, in which bifurcations were not recommended in case of poor bed MT properties. However, the poor bed permeability assumed for the small grain size entails limited vapour transfers in the reactive bed.

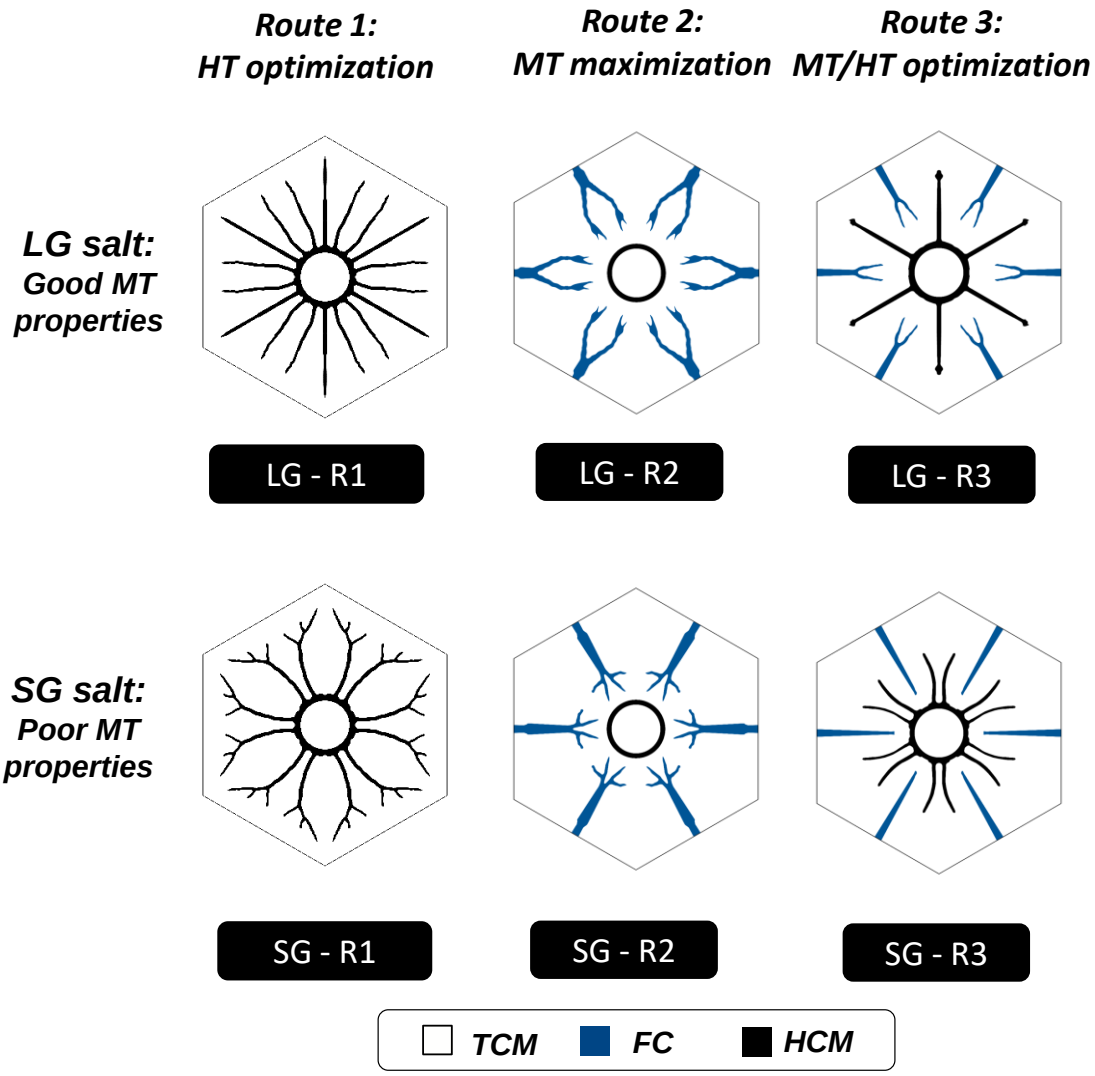

Figure 7.7 Optimal designs from the three explored optimization routes and salt grain size. LG refers to large grain size, and SG refers to small grain size.

Consequently, the HCM architecture obtained for optimization route 1 aims at the cooling of the reactive bed fraction where vapour transfer is effectively achieved. As a result, the optimal design stretches towards the outer boundary and presents a series of ramifications to intensify the heat transfer locally.

Concerning optimization route 2 in Figure 7.7, the flow channels always elongate from the midpoint of each of the sides of the hexagon, i.e. from the midpoint of the boundary facing

the vacuum chamber. That is, from the point with the lowest distance from the HTF wall. In this way, a lower amount of material needs to be distributed to transfer the gas reactants in the low temperature regions. A less ramified FC design emerged in the instance of SG size. This is due to the lower bed permeability, which entails the FC stretching further towards the HTF wall compared to the large grain salt designs. In fact, in the instance of the LG size, the superior mass transfer properties of the bed allow a more distributed FC geometry.

Concerning the FC designs in route 3, similar optimal geometrical features emerge compared to route 2. However, thinner channels are present due to the lower maximum volume fraction imposed. Besides, the poor bed mass transfer properties in the instance of SG size led to the use of a straight channel to allow vapour to distribute near the HTF wall. The HCM elongates instead from the HTF wall, and it is distributed to surround the FC. The distance between the flow channel and the HCM reduces for reduced permeability. This makes intuitive sense, as the gas reactants can travel shorter distances in the reactive bed for reduced mass transfer properties.

7.4.1.2 Performance comparison

Figure 7.8 presents the reaction advancement history comparison for the generated optimal designs. While the optimization problem was conducted for the desired discharge time $t^*=10h$, the design behaviours are reported until *20 h* for a more comprehensive analysis of the different optimization pathways' benefits.

Overall, larger final reaction advancements are achieved when large grain sizes are considered. This makes intuitive sense, as the only difference assumed in this chapter between the two considered salt grain sizes is their permeability, and larger permeability

was considered for LG size. A poor final reaction advancement is achieved if the MT maximization route is selected regardless of the considered bed properties. Reaction advancements below *0.21* are obtained at the desired discharge time.

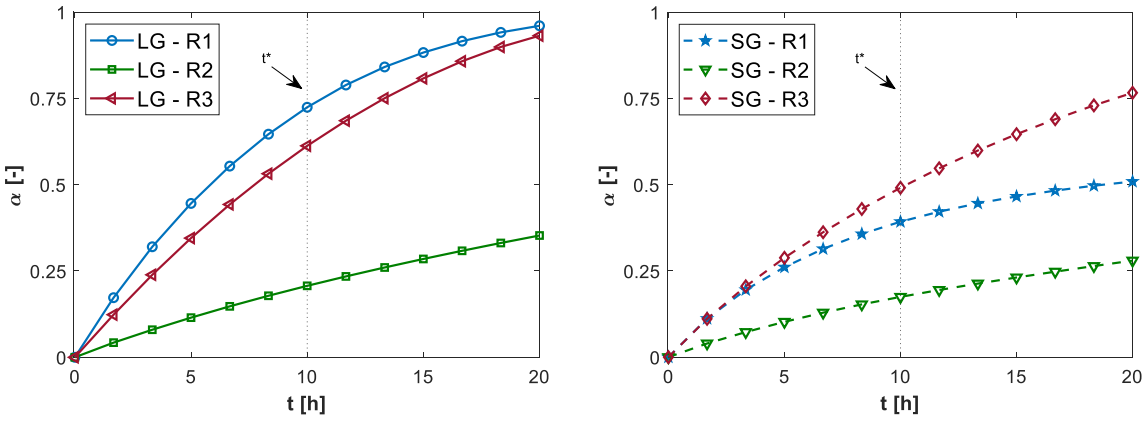

(a) *(b)*

Figure 7.8 Comparison of the reaction advancement histories: (a) large grain (LG) designs; (b) small grain (SM) designs.

A significantly larger performance enhancement is instead obtained through the optimization routes involving heat transfer intensification, as reported in Table 7.2. Maximum thermal performance is achieved in optimization route 1, i.e. the pure HT maximization pathway, and large grain size. For the same bed properties, poorer performance is obtained if a fraction of enhancer materials is dedicated to the use of flow channels. The opposite trend is predicted in the instance of small grain size, Figure 7.8 (b). Here, the design generated from optimization route 2 resulted in the best performing one due to the required intensification of both heat and mass transfer in case of poor bed MT properties.

Table 7.2 Final reaction advancement for the optimal design from each investigated optimization route.

	LG-R1	***LG-R2***	***LG-R3***	***SG-R1***	***SG-R2***	***SG-R3***
α_{t^*} ***[-]***	0.72	0.21	0.61	0.39	0.17	0.49

For each of the generated designs, the bed temperature and vapour pressure histories are depicted in Figure 7.9. Here, optimization route 1 provides more effective cooling of the reactive bed. Lower bed temperature is predicted for the *LG-R1* and *SG-R1* designs throughout the entire discharge history. The largest vapour pressure values are instead predicted for the designs generated to attain maximized mass transfer. The trade-off between these two extremes is achieved through the optimal designs deriving from the proposed multi-step approach. These designs, i.e. *LG-R3* and *SG-R3*, are characterized by efficient bed cooling and transfer of the gas reactants. Nevertheless, for design cases where null or partial MT limitations are present, the intensification trade-off obtained in route 3 does not lead to maximized storage material utilization.

LG size – *Good MT properties*	*SG size –* *Poor MT properties*

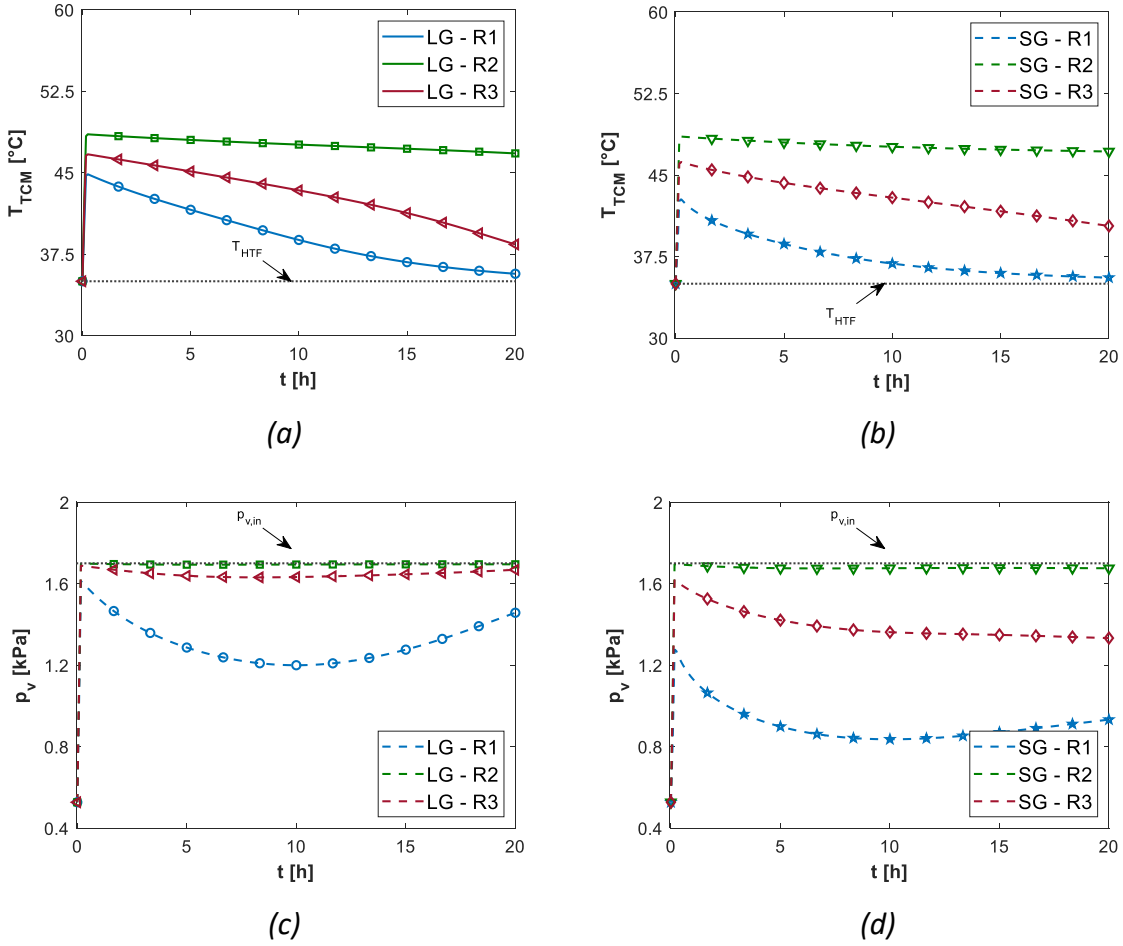

Figure 7.9 For the TO-based designs generated from each optimization route, comparison of (a) bed temperature for large grain size; (b) bed temperature for small grain size; (c) vapour pressure for large grain size; (d) vapour pressure for small grain size.

Figure 7.10 exhibits the contour plots for the reaction advancement evolution in time for the designs generated for small grain size. A relatively homogenous propagation is predicted for the *LG–R1* design. The storage material regions located near the HTF wall are the ones reacting at the lowest rate. This is due to the limited gas reactants transfer in those regions. Nevertheless, as already observed in chapter 4, this limitation does not preclude satisfactory thermal performance from the TCS device.

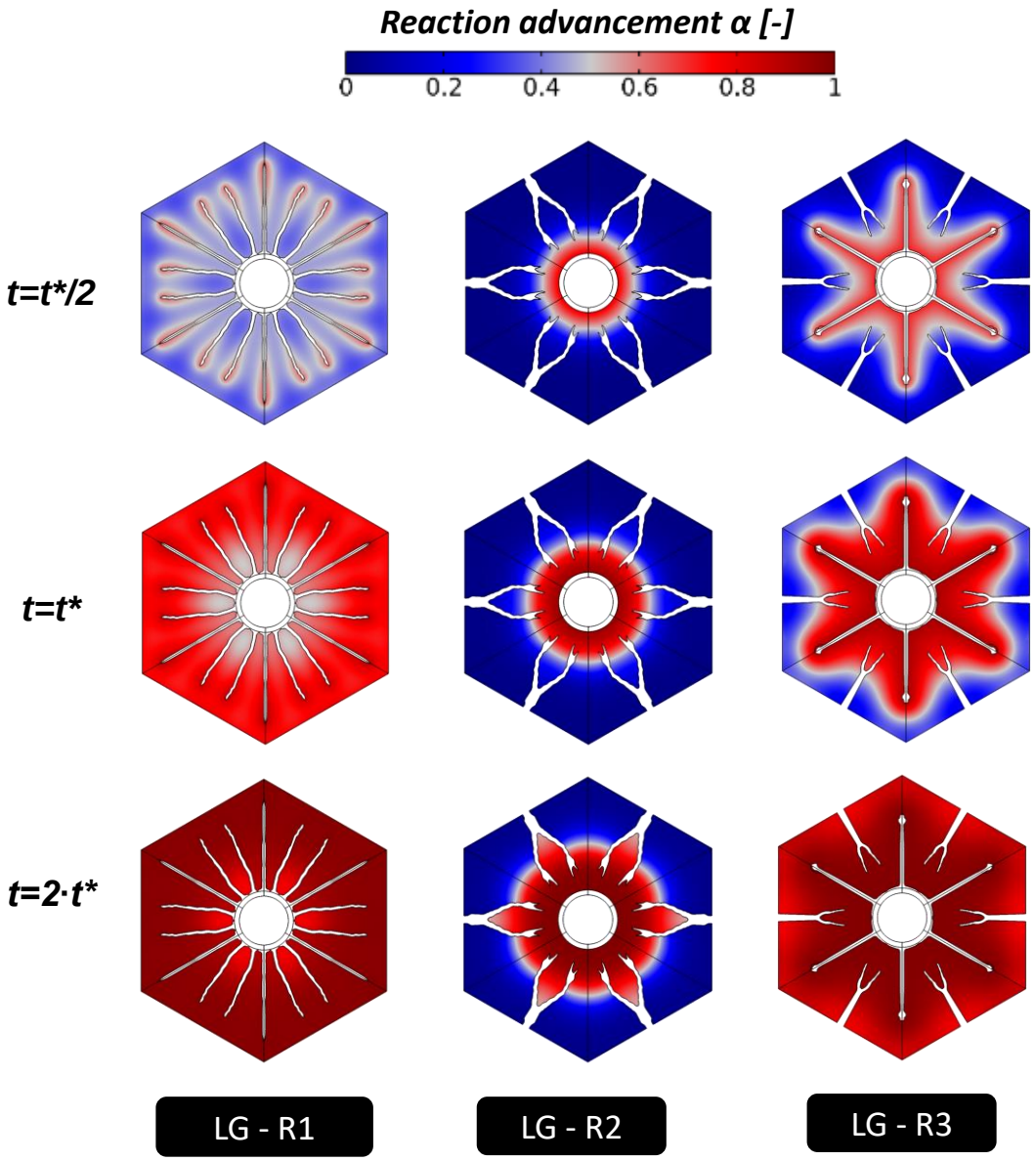

Figure 7.10 Contour plots for the reaction advancement at selected time-steps for the optimal designs generated in the instance of large grain, LG, size. The desired discharging time, t*, was set as 10h.

Concerning the *LG-R2* design, the reaction front propagates from the HTF wall, while a significant fraction of underutilized material is located near the vacuum chamber interface. This trend indicates that only mass transfer intensification is insufficient to maximize the thermal performance of the reactor. Finally, for design *LG-R3*, the reaction front propagates homogenously from the HCM/TCM interfaces, with no regions of storage material penalized

by limited mass transfer. Nevertheless, adopting a lower volume of HCM compared to *LG – R1* entails lower cooling performance and, thus, a lower final reaction advancement at time *t**.

Different trends are instead predicted for the designs generated in the instance of small grain size, as can be appreciated in Figure 7.11. Here, the pure HT intensification pathway results inefficient due to the large fraction of unreacted material for regions away from the vacuum chamber interface. Such regions are cooled by the HCM architecture but inaccessible by the gas reactants due to poor bed permeability. Furthermore, these regions remain unreacted also if larger discharge times are considered, e.g. *2·t*,* thus indicating the necessity of MT intensification to attain satisfactory material utilization.

Concerning the *SG-R2* design, the flow channel geometry effectively transfers gas reactants near the HTF wall, where large local reaction advancement is predicted. Nevertheless, the absence of heat transfer intensification techniques entails poor reaction rates, leading to poor material utilization at the desired discharge time. Finally, the concurrent heat and mass transfer intensification obtained through optimization route 3 achieves the requested trade-off between the two transfer mechanisms. The HCM architecture surrounds the straight flow channel, in such a way that efficient cooling and gas reactants distribution are achieved in the regions in between. A fairly homogeneous reaction advancement distribution is also predicted for larger discharge times than *t**.

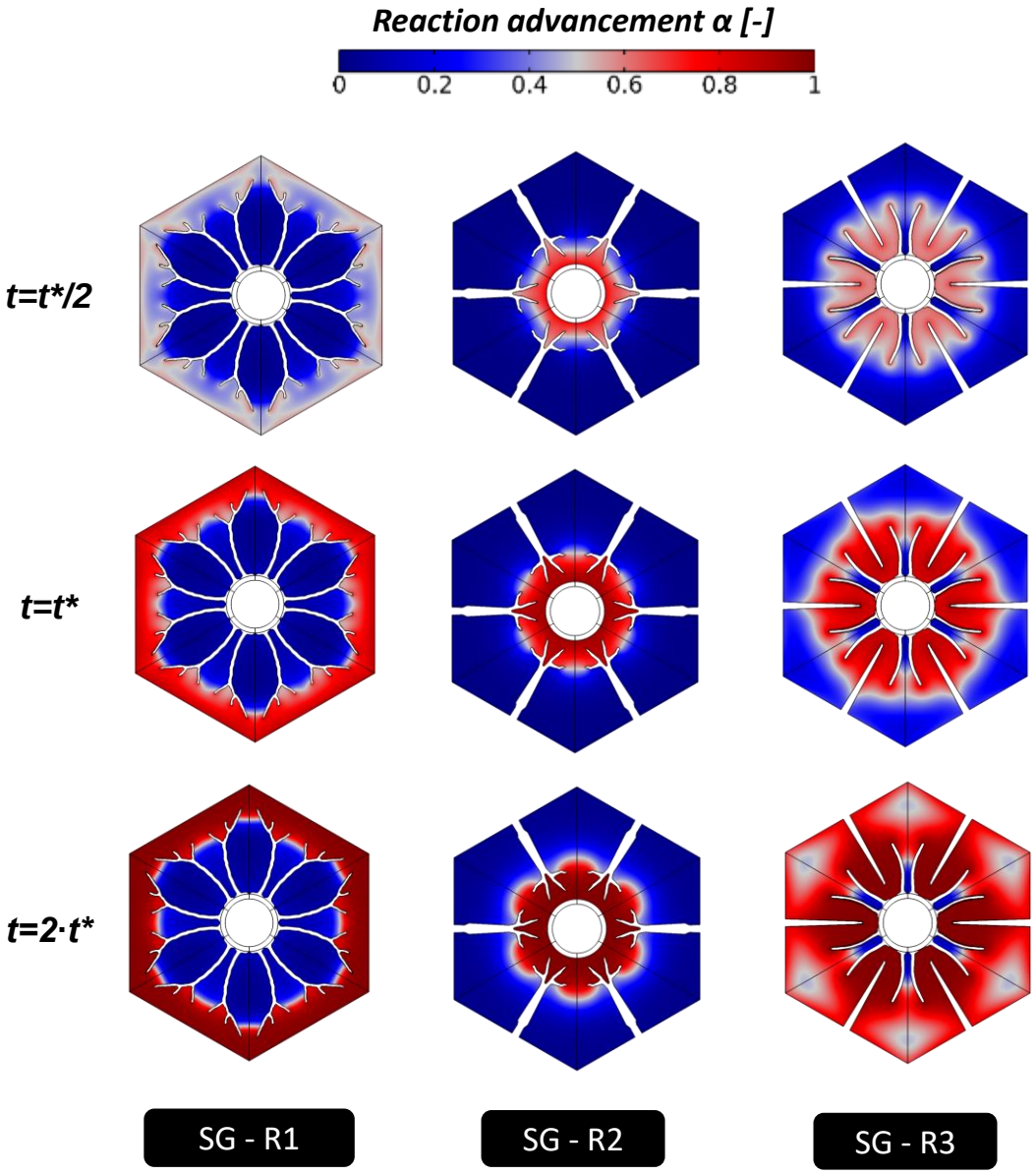

Figure 7.11 Contour plots for the reaction advancement at selected time-steps for the optimal designs generated in the instance of small grain, SG, size. The desired discharging time, t*, was set as 10h.

However, almost null reaction advancement is achieved between two consecutive fins. The presence of the HCM hampers the transfer of gas reactants in these regions. This particular geometrical feature emerged from the use of a fit-for-purpose optimization tool. That is, it represents the optimal geometrical solution for the selected desired discharge time. Overall,

for designs aimed at flexible operations, the use of fins elongating along the hexagon diagonal is recommended, thus similar to the design *LG–R3*.

A 3D representation of LG-R3 design is shown in Figure 7.12. The generated TO-design is extruded along the axial direction, with the flow channel walls characterized by perforated metallic grids. As already discussed in sections 5.6 and 6.6, this design can be fabricated by AM or simplified into TO-inspired designs with improved manufacturability.

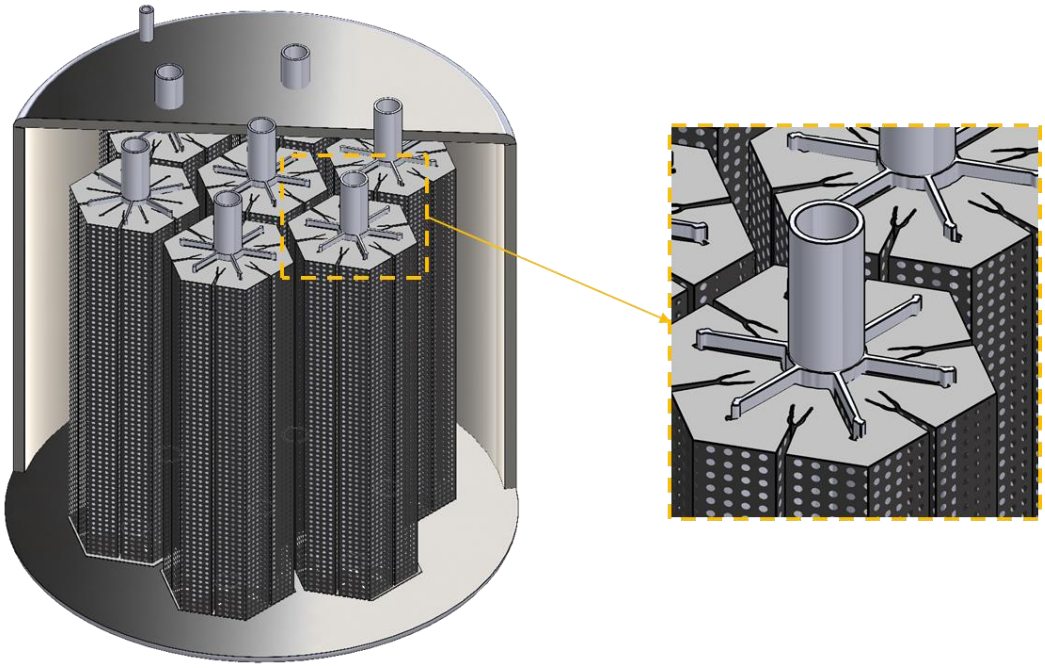

Figure 7.12 3D representation of the extruded LG-R3 design with a zoom on the optimal fin and flow channel geometry.

As a final note, it is worth noting that the design case labelled as *LG–R1* coincides with one of the design cases investigated in chapter 4 through surrogate models. The TO-based design is predicted to lead to a +3% final reaction advancement compared to the heuristic solution obtained in chapter 4, demonstrating the need for non-heuristic design tools to unlock the full storage material potential.

7.4.1.3 Off-design performance

LG-R1 and *LG-R3* designs are selected as reference designs for optimization routes 1 and 3, respectively. The off-design performance of these reference designs is studied in this section. The intent is to define for which design conditions the use of optimization pathways considering the concurrent heat and mass transfer intensification, i.e. route 3, can provide superior performance to conventional heat transfer intensification pathways. To this extent, the selected designs' performance is predicted for variable bed size and variable vacuum pressure. Besides, the two designs, which were generated for large grain size, are also assessed considering a salt filling with small grain size.

Small and large bed sizes, respectively *W=50 mm* and *W=100 mm*, are considered. The generation of the large bed size designs is obtained through the scale-up of the optimal designs by a factor of two. In such a way, also the HTF pipe size is doubled. Each design is thus tested considering low-pressure, medium-pressure and high-pressure conditions. Here, the terms low, medium and high refer to the pressure range typically adopted in low-temperature TCS devices. For the definition of the vacuum pressure values, first three HTF temperature levels are defined. Thus, the specific vacuum pressure values are calculated considering a fixed temperature difference, 15°C [37], between the selected HTF temperature level and the equilibrium temperature dictated by the Clausius-Clapeyron relation, equation 4.9, at the vacuum chamber pressure. That is, for each selected HTF temperature level, the following relationship is imposed to determine the vacuum chamber pressure:

$$T_{eq}(p_{v,in}) - T_{HTF} = 15°C \qquad 7.7$$

Table 7.3 reports the predicted final reaction advancement for each design condition reported above. The desired discharge time, t^*, is fixed at 10 h. The most-performing design between the two selected candidates is reported in green in such a way that for each design case, it is made clear which optimization pathway resulted in the most suitable one. Overall, the reference designs derived from the conventional heat transfer enhancement pathway are the most suitable for four design cases over six. The use of concurrent heat and mass transfer enhancement pathways appears to be the most indicated one in the context of low-pressure operation, for which mass transfer limitations play a crucial role. Interestingly, the *LG-R1* design remains dominant also for larger bed sizes, indicating only a mild influence of the distance travelled by the gas reactants on the reactor thermal performance in the instance of fixed properties and operating conditions.

Table 7.3 Off-design performance for the selected designs filled with LG size. The green and red colours indicate the best performing and least performing solutions for fixed operating conditions and bed size.

		LG-R1	***LG-R3***
Bed size	**Operating conditions**	**α_{t^*} [-]**	**α_{t^*} [-]**
Small bed size *W = 50 mm*	*Low-pressure* $p_{v,in}$ = 0.8 kPa ; T_{HTF} =25°C	*0.49*	*0.59*
	Medium-pressure $p_{v,in}$ = 1.7 kPa ; T_{HTF} = 35°C	*0.72*	*0.61*
	High-pressure $p_{v,in}$ = 5.4 kPa ; T_{HTF} =50°C	*0.83*	*0.63*
Large bed size *W = 100 mm*	*Low-pressure* $p_{v,in}$ = 0.8 kPa ; T_{HTF} =25°C	*0.24*	*0.26*
	Medium-pressure $p_{v,in}$ = 1.7 kPa ; T_{HTF} = 35°C	0.38	0.30
	High-pressure $p_{v,in}$ = 5.4 kPa ; T_{HTF} =50°C	0.52	0.32

In the same fashion, the final reaction advancement predictions are reported in Table 7.4 for the selected designs filled with small grain salt. Here, the highest performance is obtained with the route 3-design for four cases over six. In fact, in the instance of poor bed mass transfer properties, optimization route 3 becomes the most suitable pathway in the case of medium-pressure operating conditions. No variation in the recommended optimization route is instead observed for scale-up design. That is, regardless of the salt grain size, the bed size does not influence the selection of the most suitable enhancement pathway.

Table 7.4 Off-design performance for the selected designs filled with SG size. The green and red colours indicate the best performing and least performing solutions for fixed operating conditions and bed size.

		LG-R1	LG-R3
Bed size	**Operating conditions**	α_{t^*} [-]	α_{t^*} [-]
Small bed size $W = 50$ mm	*Low-pressure* $p_{v,in} = 0.8$ kPa ; $T_{HTF} = 25°C$	0.17	0.29
	Medium-pressure $p_{v,in} = 1.7$ kPa ; $T_{HTF} = 35°C$	0.32	0.46
	High-pressure $p_{v,in} = 5.4$ kPa ; $T_{HTF} = 50°C$	0.71	0.61
Large bed size $W = 100$ mm	*Low-pressure* $p_{v,in} = 0.8$ kPa ; $T_{HTF} = 25°C$	0.07	0.10
	Medium-pressure $p_{v,in} = 1.7$ kPa ; $T_{HTF} = 35°C$	0.13	0.16
	High-pressure $p_{v,in} = 5.4$ kPa ; $T_{HTF} = 50°C$	0.32	0.29

7.4.2 RDS-reactor

In the context of RDS-reactors, only optimization routes 1 and 3 are explored, with the optimal designs generated for small grain size. The flow channel optimal design derived in the first step of optimization route 3 in the considered vertical plane is depicted in Figure 7.13. Two possible problem implementations are analysed. The first solution, Figure 7.13 (a), refers to the FC design generated considering the left boundary cooled by a convective boundary condition. The emerging flow channel geometry transports the gas reactants towards the left boundary, where the reactive bed cooling occurs. Nevertheless, this solution is dictated by the absence of heat transfer enhancement techniques in the reactive

bed. As an alternative, the optimal FC geometry is generated for a thermally insulated domain. A constant temperature equal to the HTF temperature is considered in this case. In other words, the second problem implementation assumes a perfect cooling of the reactive domain, with the rate of reaction advancement purely dictated by the ability of the flow channel design to distribute gas reactants in the domain. In this case, the generated design presents an L-shaped geometry. The vapour is transferred through a vertical channel located near the outer boundary to the lower layers of the reactive bed. Here, the gas reactants are distributed horizontally to promote the reaction rate in the regions away from the vacuum chamber interface. The latter problem implementation was selected as the most suitable for the multi-step optimization of RDS-reactors.

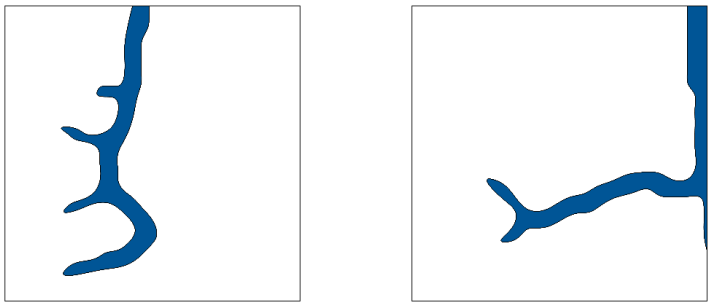

(a) (b)

Figure 7.13 Optimal FC design in the vertical plane for optimization route 3 considering: (a) convective boundary condition for the left boundary; (b) thermally insulated domain.

The HT maximization problem is thus conducted on the horizontal plane considering the thickness and length of the projected FC geometry. Specifically, a projected length, $\delta_{v,y}$, of *28 mm* was adopted. The TO-based extended surface design is depicted in Figure 7.14 (b). Similarly to what was observed for ADS-reactors, the optimal HCM architecture tends to surround the reactive bed boundaries assigned to the vapour inlet. Consequently, a single

bifurcation characterizes the optimized architecture. No bifurcations are instead present in the TO-based design derived from optimization route 1, Figure 7.14 (a). Two additional fins emerged compared to the multi-step optimization geometry, which allows for a stronger heat transfer intensification in the central part of the ground domain. Finally, the 3D designs deriving from both optimization routes are depicted in Figure 7.15.

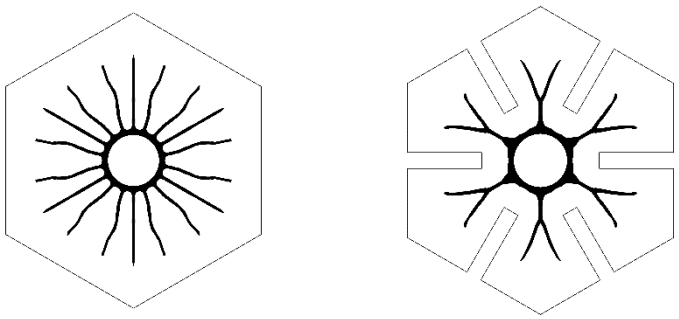

(a) (b)

Figure 7.14 Optimal HCM distribution in the horizontal plane for (a) optimization route 3 and (b) optimization route 1.

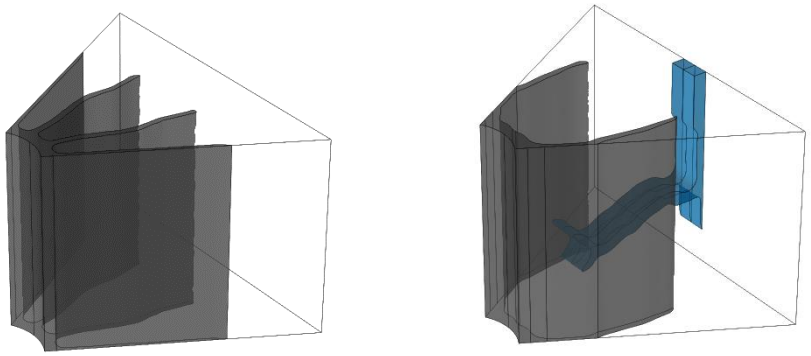

(a) (b)

Figure 7.15 Extruded TO-based designs deriving from: (a) optimization route 1; (b) optimization route 3.

7.4.2.1 Performance comparison

The performance of the optimal designs presented in the previous section is assessed here. While the designs were generated considering the thermos-physical properties for small grain size, the assessment is conducted for both small and large grain size. Figure 7.16 shows the reaction advancement histories. Concerning the desired discharge time, the concurrent enhancement of heat and mass transfer leads to greater reaction advancement regardless of the salt properties.

Interestingly, the most suitable optimization route varies in time in Figure 7.16 (a). In fact, during the initial stages of the discharge process, the relatively good mass transfer properties characterizing a poorly hydrated bed ensure a sufficient transfer of the gas reactants. Nonetheless, with the advancement of the discharge process, the bed permeability reduction causes a limited transfer of reactants in the lower layers of the reactive domain with a consequent underutilization of the storage material in the absence of mass transfer enhancement techniques. For the same reasons, the performance increase led by optimization route 3 compared to optimization route 1 increases with time. Even larger performance enhancement is predicted for small grain size, up to +17% at time t^*, as also reported in Table 7.5.

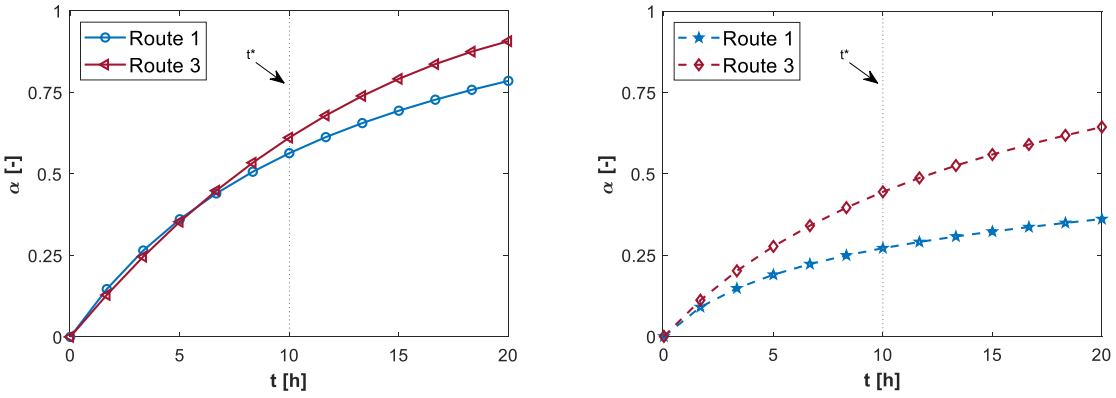

Figure 7.16 Comparison of the reaction advancement histories: (a) large grain size, (b) small grain size.

Table 7.5 Reaction advancement at the desired discharge time.

	Large grain size		Small grain size	
	Route 1	**Route 3**	**Route 1**	**Route 3**
α_{t^*}	0.56	<u>0.61</u>	0.27	<u>0.44</u>

The contour plots for the reaction advancement evolution in time are depicted in Figure 7.17. The horizontal and vertical planes adopted for the multi-step optimization approach are used to depict the contours. Concerning the TO-based design originating from optimization route 1, a nearly null reaction advancement is predicted on the horizontal plane. This is due to the distance between the vacuum chamber interface and the considered plane, which prevents the transfer of the gas reactants in case of poor MT bed properties. Larger reaction rates are instead predicted in the vertical plane in the regions near the HTF wall, although only the upper layers of the reactive bed are predicted to react due to MT limitations.

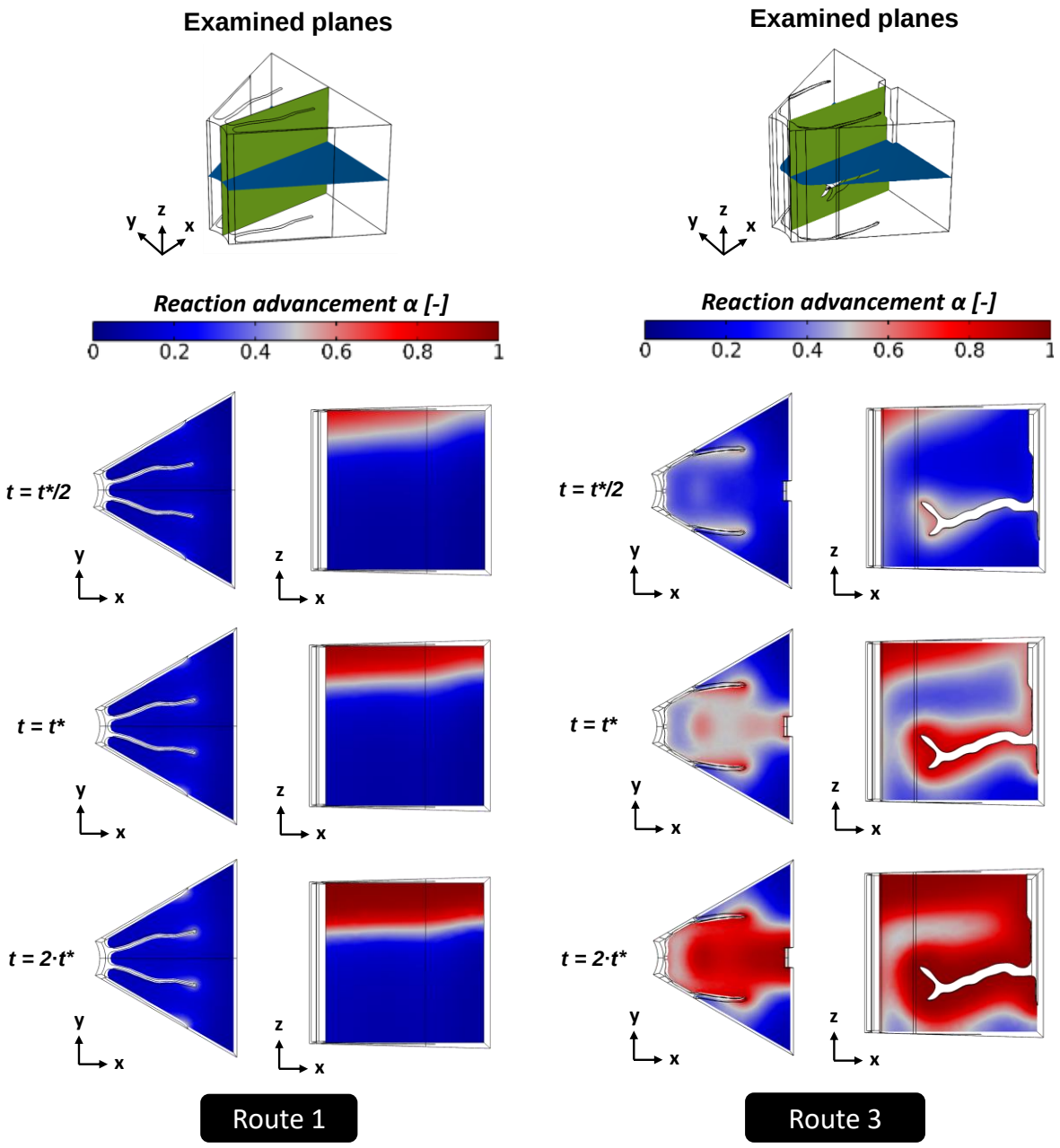

Figure 7.17 Contour plots for the reaction advancement at selected time-steps for the optimal designs and small grain, SG, size.

Larger reaction rates are predicted for the TO-based design generated from optimization route 3. Here, the reaction front is predicted to propagate in time from the central part of the examined horizontal plane. Heat and mass transfer are enhanced in these regions

through the adopted fins and flow channel geometries. For discharge times larger than the selected *t**, the reaction front is predicted to propagate homogeneously in the central part of the domain. However, almost null reaction advancement is predicted in the regions between the fins bifurcations due to the MT penalization provided by the metallic insertions. That is, similarly to what was observed for ADS-reactors, straight fins elongating along the ground domain diagonal are recommended for design cases operating with flexible discharge times.

The reaction advancement in the vertical plane propagates in time from both the vacuum chamber interface and the flow channels. Thanks to the optimized flow channel geometry, the gas reactants are transferred to the bottom layers of the reactive bed in such a way that the whole storage material volume can react. Furthermore, larger reaction advancement is predicted for the regions near the HTF wall due to the enhanced local bed cooling.

7.5 Conclusions

This chapter explored the concurrent heat transfer and mass transfer enhancement in closed system TCS reactors. A multi-step optimization approach was proposed, where topology optimization was first used to derive optimal flow channel geometries to distribute the gas reactants in the reactive bed. Thus, the generated flow channel configuration was adopted in a second topology optimization problem to distribute highly conductive material. As a result, final designs presenting optimized flow channels and extended surface geometries were derived.

The thermal performance of such optimal designs was compared to those of optimal designs derived from optimization problems for mass transfer and heat transfer intensification.

Furthermore, the optimization problems were conducted considering two different salt grain sizes, leading to different bed permeability values. From the results presented in this chapter, the following main conclusions can be derived:

- The systematic tool for the performance maximization of closed system TCS reactor is extended to consider the mass transfer enhancement. Nevertheless, for the considered design cases, the pure mass transfer enhancement was never predicted to lead to superior performance compared to design pathways involving heat transfer intensification;
- Innovative performance enhancement pathways consisting of the concurrent intensification of mass transfer and heat transfer are proposed and predicted to lead to superior performance in the instance of reactive bed presenting poor mass transfer properties. For ADS-reactors employing reactive bed with poor permeability, final reaction advancement increase up to +0.10 are achieved compared to a TO-based design optimized for heat transfer maximization solely.
- The most suitable optimization route depends on the bed properties and operating conditions, while a negligible effect of the reactive bed size was predicted. In particular, the pure heat transfer intensification pathway maximises performance in poor MT resistance beds and medium to high vacuum pressure values. The mass transfer and heat transfer intensification pathways are suitable in TCS reactors with large MT resistance and low to medium vacuum pressure values. That is, the optimal enhancement pathway must be carefully considered depending on the targeted design case;

- The multi-step optimization strategy was also tested in RDS-reactors through a pseudo-3D optimization strategy. Non-intuitive designs emerged, with L-shaped diffuser channels aiming at proving gas reactants into the lower reactive bed layers. Compared to a pure heat transfer maximization case, final reaction advancement enhancements up to +0.17 were predicted.

Overall, the results presented in this chapter constitute a unique solution for the concurrent heat and mass transfer enhancement of TCS reactive beds and elucidate in which context and how much this novel solution can improve the thermal performance of closed system TCS reactors. This solution is envisioned to greatly impact the design of highly packed reactors, for which large theoretical energy densities are achieved but for which challenges in the satisfactory provision of both heat and mass must be faced.

Chapter 8

Conclusions and perspectives

In this dissertation, the performance of TCS reactors was maximized through the optimal design of extended surfaces and flow channels. Such optimal designs were generated through systematic design frameworks based on surrogate models and topology optimization. Overall, the proposed methodologies were demonstrated to (i) lead to designs with markedly higher performance compared to traditional configurations; (ii) the topology optimization framework allowed to identify designs that are hardly achievable by heuristic approaches; (iii) the analysis of the optimized configurations provided significant understanding on the causal correlations between physical phenomena, geometrical features and performance, in such a way to unlock full technology potential. The four research questions formulated in chapter 1 have been addressed through the main contributions of this dissertation in the following way.

Q_1: *How does the interplay between heat transfer and mass transfer in TCS reactive beds influence the correct positioning of extended surfaces?*

This research question was addressed in chapter 4 through the investigation of the optimal geometry of branched fins through surrogate models. Two reactor configurations were investigated: (i) reactors with an axial distribution of gas reactants, namely ADS-reactors, and (ii) reactors with a radial distribution of gas reactants, namely RDS-reactors. The key difference between the two reactor configurations lies in the preferential directions for the heat and mass transfer mechanisms, which are parallel in ADS-reactors and orthogonal in RDS-reactors.

The adopted optimization strategy identified distinct optimal designs for different objective functions, thus proving the need for fit-for-purpose design tools to design TCS devices effectively. Furthermore, in the instance of fixed design case and objective function, distinct optimal designs were obtained for the investigated reactor configurations. In particular, for reactor configurations characterized by parallel preferential directions for the transfer mechanisms, the design guidelines for the correct positioning of extended surfaces depart from the typical ones for heat conduction maximization problems. Branched fins with large bifurcation angles were predicted to hamper the gas reactants' transfer, with this effect more pronounced during the latest stages of the hydration process due to the reduced bed permeability. That is, for TCS reactive beds characterized by parallel preferential directions for the transfer mechanisms, the heat and mass transfer interplay influence the correct positioning of extended surfaces. Concerning instead RDS-reactors, branched fins with large bifurcation angles were predicted as the optimal design solution for all the considered design cases, thus indicating a negligible influence of mass transfer on the effective extended surface positioning.

Q_2: *How and how much can the thermal performance of closed system TCS reactors be enhanced through the design of optimized extended surface geometries?*

This research question was addressed in chapter 5 through the use of topology optimization as a systematic tool for radial fins in TCS reactive beds. A novel optimization problem was introduced, from which optimal geometry and amount of enhancer materials were concurrently derived, thus allowing the answer to two crucial design questions simultaneously. The optimal designs were generated for ADS-reactors for multiple desired discharge times, bed sizes, and bed properties.

In the instance of a fixed amount of enhancer material, the TO-based design was predicted to lead to a final reaction advancement increase of +0.27 compared to a state-of-the-art design. The application of the proposed novel optimization problem allowed instead to generate optimal designs with an energy output increase of up to +47.0% compared to a design derived from the conventional optimization problem.

The emerging design trends showed the optimal extended surface geometry and amount of enhancer material to be largely influenced by the considered design case. The optimal amount of enhancer material reduces with increased discharge time and increases with the bed size. For typical operating conditions, the maximal amount of discharged energy was obtained through a relatively large amount of enhancer material, *21%*, and a large bed size, *75 mm*. This solution mitigated the influence of dead volumes on the overall reactor energy density. That is, higher effective energy storage density is achieved with a larger amount of highly conductive material, i.e. through a lower amount of thermochemical storage material.

Thicker fins were predicted to be favourable in low porosity beds, with the number of fins varying only when a relatively small amount of enhancer material was imposed. The maximum amount of retrieved energy from the TCS reactor was predicted in the instance of highly packed bed reactors employing a relatively high amount of highly conductive material, with enhancements up to +57 kWh/m^3 compared to less packed beds utilizing optimized fins.

Q_3: *How and how much can the thermal performance of open system TCS reactors be enhanced by the design of optimized flow channel geometries?*

This research question was addressed in chapter 6 through the use of the topology optimization algorithm. The intent was to generate flow channel geometry to effectively distribute gas reactants to the reactive sites. A simplified model was coupled with the topology optimization algorithm to generate non-intuitive design candidates. Each generated candidate was thus numerically tested in a validated numerical framework, and the thermal performance was compared to literature solutions.

In the context of cylindrical reactors, the best performing TO-based design was predicted to enhance the amount of discharged energy up to +245.7% compared to the selected benchmark. Tentacular flow channel designs which do not directly connect inlet and outlet interfaces greatly improved mass transfer. These flow channel geometries indeed favour the transport of gas reactants in regions away from the inlet interface as well as the transport of the collected heat towards the outlet interface.

The optimal geometrical features differ depending on the selected performance metrics. For example, thinner and shorter flow channels favour the maximization of the amount of exergy gained by the HTF compared to the amount of energy. Nevertheless, tentacular flow channel geometries were predicted to outperform benchmark designs regardless of the considered performance metric. Concerning the best performing solution for the two investigated reactor configurations, sieve reactors outperform cylindrical reactors. An increased amount of discharged energy up to +21.8% was predicted. Thus, sieve reactors employing non-heuristic flow channel geometries are identified as the most-performing geometrical configuration. Overall, these conclusions provide insight into what governs optimal performance in open system TCS reactors and establish new pathways for performance enhancement.

Q_4: *How and how much can we concurrently enhance heat and mass transfer in closed system TCS reactors by the design of optimized flow channels and extended surface geometries?*

Research question 4 was addressed in chapter 7 through the use of a unique multi-step topology optimization approach. Such an approach combined and extended the methodologies adopted in chapter 5 and chapter 6 and entailed the consecutive design optimization of flow channels and extended surfaces. The designs generated through the multi-step topology optimization approach were predicted to lead to superior performance in the instance of reactive bed presenting poor mass transfer properties.

For ADS-reactors employing reactive bed with poor permeability, performance increase up to +10% compared to a TO-based design optimized for heat transfer maximization solely. The most suitable optimization route depends on the bed properties and operating conditions, while a negligible effect of the reactive bed size was predicted. In particular, the pure heat transfer intensification pathway, i.e. use of extended surface in the absence of flow channels, led to superior performance in the instance of poor mass transfer resistance beds and medium to high vacuum pressure values. The concurrent heat and mass transfer intensification pathway was suitable in TCS reactors with large MT resistance and low to medium vacuum pressure values. That is, the optimal enhancement pathway must be carefully considered depending on the targeted design case.

8.1 Recommendations for future works

The work presented in this thesis can be improved and extended in numerous ways. Several of these ways with high potential impacts are discussed in the following paragraphs.

- Primary efforts need to be placed on the validation of the optimization results reported in this dissertation. Overall, the scientific community is still sceptical regarding the engineering outcomes of the topology optimization algorithm. To win this scepticism, experimental evidence is necessary to fully demonstrate the benefits led by non-heuristic design tools. In the experimental assessment of these devices, it is crucial to connect the analysis to conventional designs to quantify and discuss the advantages.

- The proposed systematic design can be employed to address topological problems in multiple geometrical configurations, thus allowing for a more comprehensive and exhaustive definition of practical design guidelines for the performance maximization of TCS devices. In particular, a high potential is envisioned for topological problems where HTF temperature gradients are present, e.g. axial temperature variations in shell-and-tube configurations [75]. Besides, the current framework could be extended to full 3D optimization problems. Recent studies demonstrated indeed that 3D topology optimization models further improve the device performance compared to approximated 2D models [173,218].
- The novel energy output maximization, EOM, problem formulated in chapter 5 is envisioned to have a large potential in the TES community. Its application can be easily extended to a large variety of topological problems and other TES devices and could enable to derive the optimal amount and geometry of enhancer materials for specific design cases. This would further reduce the number of heuristic choices in the design process of TES devices, resulting in more efficient use of the storage material.
- Efforts must be made to reduce the gap between the considered optimization constraints and real devices' operation. In this regard, a feature not explored in the dissertation is the use of dynamic boundary conditions for the design optimization. Using constant boundary conditions in time can often be a poor approximation of realistic operations. The modelling framework developed in this dissertation is

capable of capturing dynamic behaviours for the adopted boundary conditions and can thus be used to investigate design trends for realistic operations.

- The methodology adopted in chapter 6 for the multifidelity topology optimization [246] of open system TCS reactors can be easily extended to other energy devices. The use of topology optimization for the performance enhancement of energy devices is often hampered by the inability to couple a full physical description with the topology optimization algorithm.

  Nevertheless, insights on the performance enhancement of energy devices can be derived from the optimization of simplified cases re-evaluated through more accurate numerical models. This design pathway can rely on topology optimization problems which are well-established in the literature and already available from commercial software. That is, little efforts need to be made by research to couple the TO algorithm to the desired analysis model. Nevertheless, in the instance of well-approximated problems, the non-intuitive TO-based designs can enhance the performance of the existing devices and lead to technological advancements. This route is a rapid way to increase energy efficiency, which is key to achieving the decarbonisation goals set for future energy scenarios.

- In the framework of the concurrent heat and mass transfer enhancement of reactive beds presented in chapter 7, the multi-step approach is not capable of capturing the mutual influence of HCM and FC material distribution. A possible approach to overcome this limitation is multi-material topology optimization [255], through

which both enhancer materials can be iteratively distributed during the same optimization process.

References

[1] BEIS. Clean Growth - Transforming Heating: Overview of Current Evidence. 2018.

[2] IEA. Heat - Renewable 2018.

[3] IEA. World Energy Outlook 2021. IEA Publ 2021:15.

[4] Gibb D, Seitz A, Johnson M, Romani J, Gasia J, F. Cabeza L, et al. Applications of Thermal Energy Storage in the Energy Transition - Public Report of IEA ECES Annex 30. 2018.

[5] IRENA. Innovation outlook thermal energy storage. 2020.

[6] Sarbu I, Sebarchievici C. A comprehensive review of thermal energy storage. Sustainability 2018;10. https://doi.org/10.3390/su10010191.

[7] Precedence Research. Global Thermal Energy Storage Market Size Report: 2020-2027 2022.

[8] Li Q, Li C, Du Z, Jiang F, Ding Y. A review of performance investigation and enhancement of shell and tube thermal energy storage device containing molten salt based phase change materials for medium and high temperature applications. Appl Energy 2019;255:113806. https://doi.org/10.1016/j.apenergy.2019.113806.

[9] Humbert G, Roosendaal C, Swanepoel JK, Navarro HM, Le Roux WG, Sciacovelli A. Development of a latent heat thermal energy storage unit for the exhaust of a recuperated solar-dish Brayton cycle. Appl Therm Eng 2022:118994. https://doi.org/10.1016/J.APPLTHERMALENG.2022.118994.

[10] Palacios A, Navarro ME, Jiang Z, Avila A, Qiao G, Mura E, et al. High-temperature corrosion behaviour of metal alloys in commercial molten salts. Sol Energy 2020;201:437–52. https://doi.org/10.1016/j.solener.2020.03.010.

[11] Liu M, Saman W, Bruno F. Review on storage materials and thermal performance enhancement techniques for high temperature phase change thermal storage systems. Renew Sustain Energy Rev 2012;16:2118–32. https://doi.org/10.1016/j.rser.2012.01.020.

[12] Solé A, Martorell I, Cabeza LF. State of the art on gas–solid thermochemical energy storage systems and reactors for building applications. Renew Sustain Energy Rev 2015;47:386–98. https://doi.org/10.1016/J.RSER.2015.03.077.

[13] André L, Abanades S. Recent advances in thermochemical energy storage via solid–gas reversible reactions at high temperature. Energies 2020;13. https://doi.org/10.3390/en13225859.

[14] Nguyen T-T, Martin V, Malmquist A, Silva CAS. A review on technology maturity of small scale energy storage technologies. Renew Energy Environ Sustain 2017. https://doi.org/10.1051/rees/2017039.

[15] Palomba V, Frazzica A. Recent advancements in sorption technology for solar thermal energy storage applications. Sol Energy 2019;192:69–105. https://doi.org/10.1016/j.solener.2018.06.102.

[16] Tamme R, Laing D, Steinmann W-D, Bauer T. Thermal Energy Storage thermal energy storage. Encycl. Sustain. Sci. Technol., New York, NY: Springer New York; 2012, p. 10551–77. https://doi.org/10.1007/978-1-4419-0851-3_684.

[17] Banaei A, Zanj A, Banaei A;, Zanj AA, Lampasi A. A Review on the Challenges of Using Zeolite 13X as Heat Storage Systems for the Residential Sector. Energies 2021, Vol 14, Page 8062 2021;14:8062. https://doi.org/10.3390/EN14238062.

[18] Clark RJ, Mehrabadi A, Farid M. State of the art on salt hydrate thermochemical energy storage systems for use in building applications. J Energy Storage 2020;27:101145. https://doi.org/10.1016/j.est.2019.101145.

[19] Donkers PAJ, Sögütoglu LC, Huinink HP, Fischer HR, Adan OCG. A review of salt hydrates for seasonal heat storage in domestic applications. Appl Energy 2017;199:45–68. https://doi.org/10.1016/j.apenergy.2017.04.080.

[20] Stengler J, Weiss J, Linder M. Analysis of a lab-scale heat transformation demonstrator based on a gas–solid reaction. Energies 2019;12. https://doi.org/10.3390/en12122234.

[21] Scapino L, De Servi C, Zondag HA, Diriken J, Rindt CCM, Sciacovelli A. Techno-economic optimization of an energy system with sorption thermal energy storage in different

energy markets. Appl Energy 2020;258:114063. https://doi.org/10.1016/J.APENERGY.2019.114063.

[22] Belaïd F. Understanding the spectrum of domestic energy consumption: Empirical evidence from France. Energy Policy 2016;92:220–33. https://doi.org/10.1016/J.ENPOL.2016.02.015.

[23] Stitou D, Mazet N, Mauran S. Experimental investigation of a solid/gas thermochemical storage process for solar air-conditioning. Energy 2012;41:261–70. https://doi.org/10.1016/j.energy.2011.07.029.

[24] Srivastava NC, Eames IW. A review of adsorbents and adsorbates in solid–vapour adsorption heat pump systems. Appl Therm Eng 1998;18:707–14. https://doi.org/10.1016/S1359-4311(97)00106-3.

[25] Daguenet-Frick X, Gantenbein P, Müller J, Fumey B, Weber R. Seasonal thermochemical energy storage: Comparison of the experimental results with the modelling of the falling film tube bundle heat and mass exchanger unit. Renew Energy 2017;110:162–73. https://doi.org/10.1016/j.renene.2016.10.005.

[26] Scapino L, Zondag HA, Van Bael J, Diriken J, Rindt CCM. Sorption heat storage for long-term low-temperature applications: A review on the advancements at material and prototype scale. Appl Energy 2017;190:920–48. https://doi.org/10.1016/j.apenergy.2016.12.148.

[27] Freni A, Maggio G, Sapienza A, Frazzica A, Restuccia G, Vasta S. Comparative analysis of promising adsorbent/adsorbate pairs for adsorptive heat pumping, air conditioning and refrigeration. Appl Therm Eng 2016;104:85–95. https://doi.org/10.1016/j.applthermaleng.2016.05.036.

[28] Zbair M, Bennici S. Survey Summary on Salts Hydrates and Composites Used in Thermochemical Sorption Heat Storage: A Review. Energies 2021, Vol 14, Page 3105 2021;14:3105. https://doi.org/10.3390/EN14113105.

[29] Michel B, Mazet N, Neveu P. Experimental investigation of an innovative thermochemical process operating with a hydrate salt and moist air for thermal storage of solar energy: Global performance. Appl Energy 2014;129:177–86.

https://doi.org/10.1016/j.apenergy.2014.04.073.

[30] Fopah-Lele A, Rohde C, Neumann K, Tietjen T, Rönnebeck T, N'Tsoukpoe KE, et al. Lab-scale experiment of a closed thermochemical heat storage system including honeycomb heat exchanger. Energy 2016;114:225–38. https://doi.org/10.1016/j.energy.2016.08.009.

[31] Stengler J, Linder M. Thermal energy storage combined with a temperature boost: An underestimated feature of thermochemical systems. Appl Energy 2020;262:114530. https://doi.org/10.1016/j.apenergy.2020.114530.

[32] Ding B, Xu C, Liao Z, Ye F. Study on long-term thermochemical thermal storage performance based on SrBr2-expanded vermiculite composite materials. J Energy Storage 2021;42:103081. https://doi.org/10.1016/j.est.2021.103081.

[33] Fopah-Lele A, Tamba JG. A review on the use of SrBr2·6H2O as a potential material for low temperature energy storage systems and building applications. Sol Energy Mater Sol Cells 2017;164:175–87. https://doi.org/10.1016/j.solmat.2017.02.018.

[34] Cabeza LF, Solé A, Barreneche C. Review on sorption materials and technologies for heat pumps and thermal energy storage. Renew Energy 2017;110:3–39. https://doi.org/10.1016/j.renene.2016.09.059.

[35] N'Tsoukpoe KE, Schmidt T, Rammelberg HU, Watts BA, Ruck WKL. A systematic multi-step screening of numerous salt hydrates for low temperature thermochemical energy storage. Appl Energy 2014;124:1–16. https://doi.org/10.1016/j.apenergy.2014.02.053.

[36] Tanguy G, Marias F, Rouge S, Wyttenbach J, Papillon P. Parametric studies of thermochemical processes for seasonal storage peer-review under responsibility of PSE AG. Gwennyn Tanguy Al / Energy Procedia 2012;30:388–94. https://doi.org/10.1016/j.egypro.2012.11.046.

[37] Michel B, Neveu P, Mazet N. Comparison of closed and open thermochemical processes, for long-term thermal energy storage applications. Energy 2014;72:702–16. https://doi.org/10.1016/j.energy.2014.05.097.

[38] Aydin D, Casey SP, Riffat S. The latest advancements on thermochemical heat storage

systems. Renew Sustain Energy Rev 2015;41:356–67. https://doi.org/10.1016/j.rser.2014.08.054.

[39] Abedin AH, Rosen MA. Closed and open thermochemical energy storage: Energy- and exergy-based comparisons. Energy 2012;41:83–92. https://doi.org/10.1016/j.energy.2011.06.034.

[40] Mauran S, Lahmidi H, Goetz V. Solar heating and cooling by a thermochemical process. First experiments of a prototype storing 60 kW h by a solid/gas reaction. Sol Energy 2008;82:623–36. https://doi.org/10.1016/j.solener.2008.01.002.

[41] N'Tsoukpoe KE, Restuccia G, Schmidt T, Py X. The size of sorbents in low pressure sorption or thermochemical energy storage processes. Energy 2014;77:983–98. https://doi.org/10.1016/J.ENERGY.2014.10.013.

[42] Fumey B, Weber R, Baldini L. Sorption based long-term thermal energy storage – Process classification and analysis of performance limitations: A review. Renew Sustain Energy Rev 2019;111:57–74. https://doi.org/10.1016/J.RSER.2019.05.006.

[43] Bertsch F, Jaehnig D, Asenbeck S, Kerskes H, Drueck H, Wagner W, et al. Comparison of the Thermal Performance of a Solar Heating System with Open and Closed Solid Sorption Storage. Energy Procedia 2014;48:280–9. https://doi.org/10.1016/J.EGYPRO.2014.02.033.

[44] Kant K, Pitchumani R. Advances and opportunities in thermochemical heat storage systems for buildings applications. Appl Energy 2022;321:119299. https://doi.org/10.1016/J.APENERGY.2022.119299.

[45] HYBIUL. Innovative compact HYbrid electrical/thermal storage systems Innovative compact HYbrid electrical/thermal storage systems for low energy BUILDings - D1.3. 2020.

[46] Cabeza LF, Galindo E, Prieto C, Barreneche C, Inés Fernández A. Key performance indicators in thermal energy storage: Survey and assessment. Renew Energy 2015;83:820–7. https://doi.org/10.1016/j.renene.2015.05.019.

[47] Lahmidi H, Mauran S, Goetz V. Definition, test and simulation of a thermochemical storage process adapted to solar thermal systems. Sol Energy 2006;80:883–93.

https://doi.org/10.1016/j.solener.2005.01.014.

[48] Trambouze P, Euzen J-P. Chemical reactors : from design to operation. Editions Technip; 2004.

[49] Farcot L, Le Pierrès N, Fourmigué JF. Experimental investigation of a moving-bed heat storage thermochemical reactor with SrBr2/H2O couple. J Energy Storage 2019;26:101009. https://doi.org/10.1016/J.EST.2019.101009.

[50] Farcot L, Le Pierrès N, Michel B, Fourmigué JF, Papillon P. Numerical investigations of a continuous thermochemical heat storage reactor. J Energy Storage 2018;20:109–19. https://doi.org/10.1016/J.EST.2018.08.020.

[51] Chen CH, Ma SS, Wu PH, Chiang YC, Chen SL. Adsorption and desorption of silica gel circulating fluidized beds for air conditioning systems. Appl Energy 2015;155:708–18. https://doi.org/10.1016/J.APENERGY.2015.06.041.

[52] Hauer A. Adsorption systems for TES - Design and demonstration projects. Therm Energy Storage Sustain Energy Consum 2007:409–27. https://doi.org/10.1007/978-1-4020-5290-3_25.

[53] Jähnig D, Hausner R, Wagner W, Isaksson C. Thermo-chemical storage for solar space heating in a single-family house. AEE – INTEC (Austria), Ecostock Conf New Jersey; 31 May - 02 June 2006:1–7.

[54] Van Alebeek R, Scapino L, Beving MAJM, Gaeini M, Rindt CCM, Zondag HA. Investigation of a household-scale open sorption energy storage system based on the zeolite 13X/water reacting pair. Appl Therm Eng 2018;139:325–33. https://doi.org/10.1016/j.applthermaleng.2018.04.092.

[55] Gaeini M, Javed MR, Ouwerkerk H, Zondag HA, Rindt CCM. Realization of a 4kW thermochemical segmented reactor in household scale for seasonal heat storage. Energy Procedia 2017;135:105–14. https://doi.org/10.1016/j.egypro.2017.09.491.

[56] De Boer R, Smeding S, Zondag H, Krol G. Development of a prototype system for seasonal solar heat storage using an open sorption process. Eurotherm Semin. #99 Adv. Therm. Energy Storage, 2014.

[57] Johannes K, Kuznik F, Hubert JL, Durier F, Obrecht C. Design and characterisation of a

high powered energy dense zeolite thermal energy storage system for buildings. Appl Energy 2015;159:80–6. https://doi.org/10.1016/j.apenergy.2015.08.109.

[58] Bales C, Gantenbein Dagmar Jaenig Henner Kerskes P, Summer Martijn van Essen K, Robert Weber A. Laboratory Tests of Chemical Reactions and Prototype Sorption Storage Units - Task 32. 2008.

[59] Finck C, Henquet E, Van Soest C, Oversloot H, De Jong AJ, Cuypers R, et al. Experimental results of a 3 kWh thermochemical heat storage module for space heating application. Energy Procedia 2014;48:320–6. https://doi.org/10.1016/j.egypro.2014.02.037.

[60] Han X, Liu S, Zeng C, Yang L, Shukla A, Shen Y. Investigating the performance enhancement of copper fins on trapezoidal thermochemical reactor. Renew Energy 2020;150:1037–46. https://doi.org/10.1016/J.RENENE.2019.11.052.

[61] Aydin D, Casey SP, Chen X, Riffat S. Novel “open-sorption pipe” reactor for solar thermal energy storage. Energy Convers Manag 2016;121:321–34. https://doi.org/10.1016/j.enconman.2016.05.045.

[62] Fisher R, Ding Y, Sciacovelli A. Hydration kinetics of K2CO3, MgCl2 and vermiculite-based composites in view of low-temperature thermochemical energy storage. J Energy Storage 2021;38. https://doi.org/10.1016/j.est.2021.102561.

[63] Romaní J, Gasia J, Solé A, Takasu H, Kato Y, Cabeza LF. Evaluation of energy density as performance indicator for thermal energy storage at material and system levels. Appl Energy 2019;235:954–62. https://doi.org/10.1016/j.apenergy.2018.11.029.

[64] Liu H, Wang W, Zhang Y. Performance gap between thermochemical energy storage systems based on salt hydrates and materials. J Clean Prod 2021;313:127908. https://doi.org/10.1016/j.jclepro.2021.127908.

[65] Palacios A, Navarro ME, Barreneche C, Ding Y. Water sorption-based thermochemical storage materials: A review from material candidates to manufacturing routes. Front Therm Eng 2022;2. https://doi.org/10.3389/fther.2022.1003863.

[66] Stengler J, Bürger I, Linder M. Thermodynamic and kinetic investigations of the SrBr2 hydration and dehydration reactions for thermochemical energy storage and heat

transformation. Appl Energy 2020;277:115432. https://doi.org/10.1016/j.apenergy.2020.115432.

[67] Gilles D, Segato T, Courbon E, Degrez M, D'Ans P. Affordable Process for the Production of Strontium Bromide Used in Low Grade Heat Recovery Applications. Procedia CIRP 2018;69:383–8. https://doi.org/10.1016/j.procir.2017.11.056.

[68] De Jong AJ, Trausel F, Finck C, Van Vliet L, Cuypers R. Thermochemical heat storage - System design issues. Energy Procedia, vol. 48, Elsevier Ltd; 2014, p. 309–19. https://doi.org/10.1016/j.egypro.2014.02.036.

[69] Humbert G, Ding Y, Sciacovelli A. Performance maximization of closed-system thermochemical energy storage through reactor design and dynamic operating condition formulation. ECOS 2021 Proc., Curran Associates, Inc.; 2021, p. 916–27. https://doi.org/10.52202/062738-0082.

[70] Solé A, Miró L, Barreneche C, Martorell I, Cabeza LF. Corrosion Test of Salt Hydrates and Vessel Metals for Thermochemical Energy Storage. Energy Procedia 2014;48:431–5. https://doi.org/10.1016/J.EGYPRO.2014.02.050.

[71] Weber R, Asenbeck S, Kerskes H, Drück H. SolSpaces - Testing and Performance Analysis of a Segmented Sorption Store for Solar Thermal Space Heating. Energy Procedia 2016;91:250–8. https://doi.org/10.1016/j.egypro.2016.06.214.

[72] Bürger I, Linder M. Operation strategies for gas solid reactions in thermal energy storage systems. J Energy Storage 2021;40:102767. https://doi.org/10.1016/J.EST.2021.102767.

[73] Casey SP, Aydin D, Elvins J, Riffat S. Salt impregnated desiccant matrices for 'open' thermochemical energy conversion and storage – Improving energy density utilisation through hygrodynamic & thermodynamic reactor design. Energy Convers Manag 2017;142:426–40. https://doi.org/10.1016/j.enconman.2017.03.066.

[74] Zhao Q, Lin J, Huang H, Wu Q, Shen Y, Xiao Y. Energy & Buildings Optimization of thermochemical energy storage systems based on hydrated salts : A review. Energy Build 2021;244:111035. https://doi.org/10.1016/j.enbuild.2021.111035.

[75] Stengler J, Bürger I, Linder M. Performance analysis of a gas-solid thermochemical

energy storage using numerical and experimental methods. Int J Heat Mass Transf 2021;167:120797. https://doi.org/10.1016/j.ijheatmasstransfer.2020.120797.

[76] Hawwash AA, Mori S, Feky K El, Hassan H. Numerical Study for Open Reactor Design Using Salt Hydrate. IOP Conf Ser Earth Environ Sci 2019;322. https://doi.org/10.1088/1755-1315/322/1/012021.

[77] Mohammadzadeh Kowsari M, Niazmand H, Tokarev MM. Bed configuration effects on the finned flat-tube adsorption heat exchanger performance: Numerical modeling and experimental validation. Appl Energy 2018;213:540–54. https://doi.org/10.1016/j.apenergy.2017.11.019.

[78] Yang FS, Wang GX, Zhang ZX, Rudolph V. Investigation on the influences of heat transfer enhancement measures in a thermally driven metal hydride heat pump. Int J Hydrogen Energy 2010;35:9725–35. https://doi.org/10.1016/j.ijhydene.2010.06.110.

[79] Linder M, Roßkopf C, Schmidt M, Wörner A. Thermochemical energy storage in kW-scale based on CaO/Ca(OH)2. Energy Procedia, vol. 49, Elsevier Ltd; 2014, p. 888–97. https://doi.org/10.1016/j.egypro.2014.03.096.

[80] Gaeini M, Zondag HA, Rindt CCM. Effect of kinetics on the thermal performance of a sorption heat storage reactor. Appl Therm Eng 2016;102:520–31. https://doi.org/10.1016/j.applthermaleng.2016.03.055.

[81] Ferchaud CJ, Zondag HA, Rubino A, De Boer R. Seasonal sorption heat storage – Research on thermochemical materials and storage performance. Proc Heat Power Cycle 2012 2012:1–7.

[82] Vahedi N, Oztekin A. Split flow modified packed bed reactor for cobalt oxide based high-temperature TCES systems. ASME Int. Mech. Eng. Congr. Expo. Proc., vol. 6, American Society of Mechanical Engineers (ASME); 2019. https://doi.org/10.1115/IMECE2019-10740.

[83] Clark RJ, Farid M. Experimental investigation into the performance of novel SrCl2-based composite material for thermochemical energy storage. J Energy Storage 2021;36:102390. https://doi.org/10.1016/J.EST.2021.102390.

[84] Gaeini M, Wind R, Donkers PAJ, Zondag HA, Rindt CCM. Development of a validated

2D model for flow, moisture and heat transport in a packed bed reactor using MRI experiment and a lab-scale reactor setup. Int J Heat Mass Transf 2017;113:1116–29. https://doi.org/10.1016/j.ijheatmasstransfer.2017.06.034.

[85] Li W, Klemeš JJ, Wang Q, Zeng M. Numerical analysis on the improved thermo-chemical behaviour of hierarchical energy materials as a cascaded thermal accumulator. Energy 2021;232:120937. https://doi.org/10.1016/J.ENERGY.2021.120937.

[86] Dorai F, Rolland M, Wachs A, Marcoux M, Climent E. Packing Fixed Bed Reactors with Cylinders: Influence of Particle Length Distribution. Procedia Eng 2012;42:1335–45. https://doi.org/10.1016/J.PROENG.2012.07.525.

[87] Michel B, Mazet N, Mauran S, Stitou D, Xu J. Thermochemical process for seasonal storage of solar energy: Characterization and modeling of a high density reactive bed. Energy 2012;47:553–63. https://doi.org/10.1016/j.energy.2012.09.029.

[88] Hawwash AA, Hassan H, feky K El. Impact of reactor design on the thermal energy storage of thermochemical materials. Appl Therm Eng 2020;168:114776. https://doi.org/10.1016/J.APPLTHERMALENG.2019.114776.

[89] Krönauer A, Lävemann E, Brückner S, Hauer A. Mobile sorption heat storage in industrial waste heat recovery. Energy Procedia 2015;73:272–80. https://doi.org/10.1016/j.egypro.2015.07.688.

[90] McTigue JD, White AJ. A comparison of radial-flow and axial-flow packed beds for thermal energy storage. Appl Energy 2018;227:533–41. https://doi.org/10.1016/j.apenergy.2017.08.179.

[91] Malley-Ernewein A, Lorente S. Constructal design of thermochemical energy storage. Int J Heat Mass Transf 2019;130:1299–306. https://doi.org/10.1016/j.ijheatmasstransfer.2018.10.097.

[92] Bejan A. The constructal law of organization in nature: Tree-shaped flows and body size. J Exp Biol 2005;208:1677–86. https://doi.org/10.1242/jeb.01487.

[93] Mukherjee A, Majumdar R, Saha SK, Kumar L, Subramaniam C. Assessment of open thermochemical energy storage system performance for low temperature heating

applications. Appl Therm Eng 2019;156:453–70. https://doi.org/10.1016/J.APPLTHERMALENG.2019.04.096.

[94] Mette B, Kerskes H, Drück H. Experimental and Numerical Investigations of Different Reactor Concepts for Thermochemical Energy Storage. Energy Procedia 2014;57:2380–9. https://doi.org/10.1016/J.EGYPRO.2014.10.246.

[95] Chen W, Li W, Zhang Y. Analysis of thermal deposition of MgCl2·6H2O hydrated salt in the sieve-plate reactor for heat storage. Appl Therm Eng 2018;135:95–108. https://doi.org/10.1016/j.applthermaleng.2018.02.043.

[96] Li W, Guo H, Zeng M, Wang Q. Performance of SrBr2·6H2O based seasonal thermochemical heat storage in a novel multilayered sieve reactor. Energy Convers Manag 2019;198:111843. https://doi.org/10.1016/j.enconman.2019.111843.

[97] Liu H, Nagano K, Sugiyama D, Togawa J, Nakamura M. Honeycomb filters made from mesoporous composite material for an open sorption thermal energy storage system to store low-temperature industrial waste heat. Int J Heat Mass Transf 2013;65:471–80. https://doi.org/10.1016/J.IJHEATMASSTRANSFER.2013.06.021.

[98] Papakokkinos G, Castro J, López J, Oliva A. A generalized computational model for the simulation of adsorption packed bed reactors – Parametric study of five reactor geometries for cooling applications. Appl Energy 2019;235:409–27. https://doi.org/10.1016/j.apenergy.2018.10.081.

[99] Yu N, Wang RZ, Wang LW. Sorption thermal storage for solar energy. Prog Energy Combust Sci 2013;39:489–514. https://doi.org/10.1016/J.PECS.2013.05.004.

[100] Gluesenkamp KR, Frazzica A, Velte A, Metcalf S, Yang Z, Rouhani M, et al. Experimentally Measured Thermal Masses of Adsorption Heat Exchangers. Energies 2020, Vol 13, Page 1150 2020;13:1150. https://doi.org/10.3390/EN13051150.

[101] Mbaye M, Aidoun Z, Valkov V, Legault A. Analysis of chemical heat pumps (CHPs): Basic concepts and numerical model description. Appl Therm Eng 1998;18:131–46. https://doi.org/10.1016/S1359-4311(97)00027-6.

[102] Stitou D, Crozat G. Dimensioning nomograms for the design of fixed-bed solid-gas thermochemical reactors with various geometrical configurations. Chem Eng Process

Process Intensif 1997;36:45–58. https://doi.org/10.1016/S0255-2701(96)04172-4.

[103] Pons M, Dantzer P, Guilleminot JJ. A measurement technique and a new model for the wall heat transfer coefficient of a packed bed of (reactive) powder without gas flow. Int J Heat Mass Transf 1993;36:2635–46. https://doi.org/10.1016/S0017-9310(05)80200-5.

[104] Stitou D, Mazet N, Bonnissel M. Performance of a high temperature hydrate solid/gas sorption heat pump used as topping cycle for cascaded sorption chillers. Energy 2003;29:267–85. https://doi.org/10.1016/j.energy.2003.08.011.

[105] Neveu P, Tescari S, Aussel D, Mazet N. Combined constructal and exergy optimization of thermochemical reactors for high temperature heat storage. Energy Convers Manag 2013;71:186–98. https://doi.org/10.1016/j.enconman.2013.03.035.

[106] Mitra S, Muttakin M, Thu K, Saha BB. Study on the influence of adsorbent particle size and heat exchanger aspect ratio on dynamic adsorption characteristics. Appl Therm Eng 2018;133:764–73. https://doi.org/10.1016/j.applthermaleng.2018.01.015.

[107] Niazmand H, Talebian H, Mahdavikhah M. Effects of particle diameter on performance improvement of adsorption systems. Appl Therm Eng 2013;59:243–52. https://doi.org/10.1016/j.applthermaleng.2013.05.043.

[108] Niazmand H, Talebian H, Mahdavikhah M. Bed geometrical specifications effects on the performance of silica/water adsorption chillers. Int J Refrig 2012;35:2261–74. https://doi.org/10.1016/J.IJREFRIG.2012.08.017.

[109] Golparvar B, Niazmand H, Sharafian A, Ahmadian Hosseini A. Optimum fin spacing of finned tube adsorber bed heat exchangers in an exhaust gas-driven adsorption cooling system. Appl Energy 2018;232:504–16. https://doi.org/10.1016/j.apenergy.2018.10.002.

[110] Ranjha Q, Vahedi N, Oztekin A. High-temperature thermochemical energy storage – heat transfer enhancements within reaction bed. Appl Therm Eng 2019;163:114407. https://doi.org/10.1016/j.applthermaleng.2019.114407.

[111] Haertel J, Engelbrecht K, Lazarov B, Sigmund O. Topology Optimization of Thermal Heat Sinks. Proc COMSOL Conf 2015:6.

[112] Kant K, Pitchumani R. Analysis of a novel constructal fin tree embedded thermochemical energy storage for buildings applications. Energy Convers Manag 2022;258:115542. https://doi.org/10.1016/J.ENCONMAN.2022.115542.

[113] Fernandes MS, Brites GJVN, Costa JJ, Gaspar AR, Costa VAF. Modeling and parametric analysis of an adsorber unit for thermal energy storage. Energy 2016;102:83–94.

[114] Fernandes MS, Gaspar AR, Costa VAF, Costa JJ, Brites GJVN. Optimization of a thermal energy storage system provided with an adsorption module – A GenOpt application in a TRNSYS/MATLAB model. Energy Convers Manag 2018;162:90–7. https://doi.org/10.1016/J.ENCONMAN.2018.02.027.

[115] Chang WS, Wang CC, Shieh CC. Experimental study of a solid adsorption cooling system using flat-tube heat exchangers as adsorption bed. Appl Therm Eng 2007;27:2195–9. https://doi.org/10.1016/J.APPLTHERMALENG.2005.07.022.

[116] Liu YL, Wang RZ, Xia ZZ. Experimental study on a continuous adsorption water chiller with novel design. Int J Refrig 2005;28:218–30. https://doi.org/10.1016/J.IJREFRIG.2004.09.004.

[117] Wang B, Wang Z, Ma Y, Liang Y. Heat Transfer Enhancement of Indirect Heat Transfer Reactors for Ca(OH)2/CaO Thermochemical Energy Storage System. Process 2021, Vol 9, Page 1136 2021;9:1136. https://doi.org/10.3390/PR9071136.

[118] Kant K, Shukla A, Smeulders DMJ, Rindt CCM. Performance analysis of a K2CO3-based thermochemical energy storage system using a honeycomb structured heat exchanger. J Energy Storage 2021;38:102563. https://doi.org/10.1016/j.est.2021.102563.

[119] IEA. Market Report Series: Energy Efficiency. 2018.

[120] European Commision. 2030 climate & energy framework - Climate Action. 2020.

[121] Orecchini F. The era of energy vectors. Int J Hydrogen Energy 2006;31:1951–4. https://doi.org/10.1016/J.IJHYDENE.2006.01.015.

[122] Bendsøe MP, Kikuchi N. Generating optimal topologies in structural design using a homogenization method. Comput Methods Appl Mech Eng 1988;71:197–224. https://doi.org/10.1016/0045-7825(88)90086-2.

[123] Wang D, Zhang WH, Jiang JS. Combined shape and sizing optimization of truss structures. Comput Mech 2002;29:307–12. https://doi.org/10.1007/s00466-002-0343-x.

[124] Bendsoe M, Sigmund O. Topology optimization: theory, methods, and applications. 2004. https://doi.org/10.1007/ 978-3-662-05086-6.

[125] Sigmund O, Maute K. Topology optimization approaches: A comparative review. Struct Multidiscip Optim 2013;48:1031–55. https://doi.org/10.1007/s00158-013-0978-6.

[126] Deaton JD, Grandhi R V. A survey of structural and multidisciplinary continuum topology optimization: Post 2000. Struct Multidiscip Optim 2014;49:1–38. https://doi.org/10.1007/s00158-013-0956-z.

[127] The New Age of Highly Efficient Products Made with Generative Design 2020.

[128] Pizzolato A. Topology Optimization for Energy Problems - Ph.D. Thesis. Politecnico di Torino, 2018. https://doi.org/10.1039/B317095K.

[129] Bendsøe MP, Sigmund O. Material interpolation schemes in topology optimization. Arch Appl Mech 1999;69:635–54. https://doi.org/10.1007/s004190050248.

[130] Li P, Wu Y, Yvonnet J. A SIMP-phase field topology optimization framework to maximize quasi-brittle fracture resistance of 2D and 3D composites. Theor Appl Fract Mech 2021;114:102919. https://doi.org/10.1016/J.TAFMEC.2021.102919.

[131] Das S, Sutradhar A. Multi-physics topology optimization of functionally graded controllable porous structures: Application to heat dissipating problems. Mater Des 2020;193:108775. https://doi.org/10.1016/J.MATDES.2020.108775.

[132] Stolpe M, Svanberg K. An alternative interpolation scheme for minimum compliance topology optimization. Struct Multidiscip Optim 2001;22:116–24. https://doi.org/10.1007/s001580100129.

[133] Amigo RCR, Paiva DSPJL, Silva RWHECN. Topology optimisation of biphasic adsorbent beds for gas storage. Struct Multidiscip Optim 2018:2431–54. https://doi.org/10.1007/s00158-018-2117-x.

[134] Sigmund O. On the usefulness of non-gradient approaches in topology optimization

2011;43:589–96. https://doi.org/10.1007/s00158-011-0638-7.

[135] Svanberg K. MMA and GCMMA-two methods for nonlinear optimization 2007.

[136] Jameson S, Jameson A. Adjoint Formulations for Topology, Shape and Discrete Optimization. 45 th Aerosp. Sci. Meet. Exhib., 2007.

[137] Haftka RT, Gürdal Z. Elements of Structural Optimization. vol. 11. Dordrecht: Springer Netherlands; 1992. https://doi.org/10.1007/978-94-011-2550-5.

[138] Díaz A, Sigmund O. Checkerboard patterns in layout optimization. Struct Optim 1995;10:40–5. https://doi.org/10.1007/BF01743693.

[139] Sigmund O, Petersson J. Numerical instabilities in topology optimization: A survey on procedures dealing with checkerboards, mesh-dependencies and local minima. vol. 16. 1998. https://doi.org/10.1007/BF01214002.

[140] Wang F, Lazarov BS, Sigmund O. On projection methods, convergence and robust formulations in topology optimization. Struct Multidisc Optim 2010;43:767–84. https://doi.org/10.1007/s00158-010-0602-y.

[141] Jensen KE. Performing Topology Optimization with the Density Method n.d.

[142] COMSOL Multiphysics® Modeling Software 2020.

[143] MATLAB - MathWorks - MATLAB & Simulink 2020.

[144] Ge R, Humbert G, Martinez R, Attallah MM, Sciacovelli A. Additive manufacturing of a topology-optimised multi-tube energy storage device: Experimental tests and numerical analysis. Appl Therm Eng 2020;180:115878. https://doi.org/10.1016/j.applthermaleng.2020.115878.

[145] Yazdani MR, Laitinen A, Helaakoski V, Farnas LK, Kukko K, Saari K, et al. Efficient storage and recovery of waste heat by phase change material embedded within additively manufactured grid heat exchangers. Int J Heat Mass Transf 2021;181:121846. https://doi.org/10.1016/J.IJHEATMASSTRANSFER.2021.121846.

[146] Lei T, Alexandersen J, Lazarov BS, Wang F, Haertel JHK, De Angelis S, et al. Investment casting and experimental testing of heat sinks designed by topology optimization. Int J Heat Mass Transf 2018;127:396–412. https://doi.org/10.1016/j.ijheatmasstransfer.2018.07.060.

[147] Guest JK, Prévost JH, Belytschko T. Achieving minimum length scale in topology optimization using nodal design variables and projection functions. Int J Numer Methods Eng 2004;61:238–54. https://doi.org/10.1002/NME.1064.

[148] Guest JK. Topology optimization with multiple phase projection. Comput Methods Appl Mech Eng 2009;199:123–35. https://doi.org/10.1016/J.CMA.2009.09.023.

[149] Liu J, Ma Y. A survey of manufacturing oriented topology optimization methods. Adv Eng Softw 2016;100:161–75. https://doi.org/10.1016/j.advengsoft.2016.07.017.

[150] Bremicker M, Chirehdast M, Kikuchi N, Papalambros PY. Integrated Topology and Shape Optimization in Structural Design. Mech Struct Mach 2007;19:551–87. https://doi.org/10.1080/08905459108905156.

[151] Lin CY, Chao LS. Automated image interpretation for integrated topology and shape optimization. Struct Multidiscip Optim 2000;20:125–37. https://doi.org/10.1007/S001580050144.

[152] Maute K, Ramm E. Adaptive topology optimization. Struct Optim 1995 102 1995;10:100–12. https://doi.org/10.1007/BF01743537.

[153] Youn SK, Park SH. A study on the shape extraction process in the structural topology optimization using homogenized material. Comput Struct 1997;62:527–38. https://doi.org/10.1016/S0045-7949(96)00217-9.

[154] Chang KH, Tang PS. Integration of design and manufacturing for structural shape optimization. Adv Eng Softw 2001;32:555–67. https://doi.org/10.1016/S0965-9978(00)00103-4.

[155] Li B, Byon C. Experimental and numerical study on the heat sink with radial fins and a concentric ring subject to natural convection. Appl Therm Eng 2015;90:345–51. https://doi.org/10.1016/J.APPLTHERMALENG.2015.06.083.

[156] Behrou R, Pizzolato A, Forner-Cuenca A. Topology optimization as a powerful tool to design advanced PEMFCs flow fields. Int J Heat Mass Transf 2019;135:72–92. https://doi.org/10.1016/j.ijheatmasstransfer.2019.01.050.

[157] Pizzolato A, Sharma A, Maute K, Sciacovelli A, Verda V. Design of effective fins for fast PCM melting and solidification in shell-and-tube latent heat thermal energy storage

through topology optimization. Appl Energy 2017;208:1–18. https://doi.org/10.1016/j.apenergy.2017.10.050.

[158] Haertel JHK, Nellis GF. A fully developed flow thermofluid model for topology optimization of 3D-printed air-cooled heat exchangers. Appl Therm Eng 2018;119:10–24. https://doi.org/10.1016/j.applthermaleng.2017.03.030.

[159] Haertel JHK, Engelbrecht K, Lazarov BS, Sigmund O. Topology optimization of a pseudo 3D thermofluid heat sink model. Int J Heat Mass Transf 2018;121:1073–88. https://doi.org/10.1016/J.IJHEATMASSTRANSFER.2018.01.078.

[160] EnergyNest: Thermal Battery Company 2020.

[161] Lundgaard C, Engelbrecht K, Sigmund O. A density-based topology optimization methodology for thermal energy storage systems. Struct Multidiscip Optim 2019;60:2189–204. https://doi.org/10.1007/s00158-019-02375-8.

[162] Howlader MK, Rashid MH, Mallick D, Haque T. Effects of aggregate types on thermal properties of concrete. ARPN J Eng Appl Sci 2012;7:900–7.

[163] Valencia JJ, Quested PN. Thermophysical Properties. ASM Handb 2008;15:468–81. https://doi.org/10.1361/asmhba0005240.

[164] Wu S, Zhang Y, Liu S. Topology optimization for minimizing the maximum temperature of transient heat conduction structure. Struct Multidiscip Optim 2019;60:69–82. https://doi.org/10.1007/s00158-019-02196-9.

[165] Alexandersen J, Andreasen CS. A review of topology optimisation for fluid-based problems. Fluids 2020;5:1–33. https://doi.org/10.3390/fluids5010029.

[166] Chen X. Topology optimization of microfluidics - A review. Microchem J 2016;127:52–61. https://doi.org/10.1016/j.microc.2016.02.005.

[167] Dbouk T. A review about the engineering design of optimal heat transfer systems using topology optimization. Appl Therm Eng 2017;112:841–54. https://doi.org/10.1016/j.applthermaleng.2016.10.134.

[168] Fawaz A, Hua Y, Le Corre S, Fan Y, Luo L. Topology optimization of heat exchangers: A review. Energy 2022:124053. https://doi.org/10.1016/J.ENERGY.2022.124053.

[169] Incropera F P, DeWitt D P, Bergman T L, Lavine A S. Fundamentals of heat and mass

transfer. 6th ed. 2012.

[170] Feppon F. Shape and topology optimization applied to Compact Heat Exchangers. Hal-03207863 2021.

[171] Tuckerman DB, Pease RFW. High-Performance Heat Sinking for VLSI. IEEE Electron Device Lett 1981;EDL-2:126–9. https://doi.org/10.1109/EDL.1981.25367.

[172] Li H, Ding X, Jing D, Xiong M, Meng F. Experimental and numerical investigation of liquid-cooled heat sinks designed by topology optimization. Int J Therm Sci 2019;146:106065. https://doi.org/10.1016/J.IJTHERMALSCI.2019.106065.

[173] Alexandersen J, Sigmund O, Aage N. Large scale three-dimensional topology optimisation of heat sinks cooled by natural convection. Int J Heat Mass Transf 2016;100:876–91. https://doi.org/10.1016/J.IJHEATMASSTRANSFER.2016.05.013.

[174] Iga A, Nishiwaki S, Izui K, Yoshimura M. Topology optimization for thermal conductors considering design-dependent effects, including heat conduction and convection. Int J Heat Mass Transf 2009;52:2721–32. https://doi.org/10.1016/J.IJHEATMASSTRANSFER.2008.12.013.

[175] Coffin P, Maute K. Level set topology optimization of cooling and heating devices using a simplified convection model. Struct Multidiscip Optim 2015 535 2015;53:985–1003. https://doi.org/10.1007/S00158-015-1343-8.

[176] Alexandersen J, Aage N, Andreasen CS, Sigmund O. Topology optimisation for natural convection problems. Int J Numer Methods Fluids 2014;76:699–721. https://doi.org/10.1002/FLD.3954.

[177] Borrvall T, Petersson J. Topology optimization of fluids in Stokes flow. Int J Numer Methods Fluids 2003;41:77–107. https://doi.org/10.1002/fld.426.

[178] Matsumori T, Kondoh T, Kawamoto A, Nomura T. Topology optimization for fluid-thermal interaction problems under constant input power. Struct Multidiscip Optim 2013;47:571–81. https://doi.org/10.1007/s00158-013-0887-8.

[179] Zhou M, Alexandersen J, Sigmund O, Claus CB. Industrial application of topology optimization for combined conductive and convective heat transfer problems. Struct Multidiscip Optim 2016;54:1045–60. https://doi.org/10.1007/s00158-016-1433-2.

[180] Schousboe C, Alexandersen J, Aage N, Andreasen CS, Sigmund O. Topology optimisation of natural convection problems 2014. https://doi.org/10.1002/fld.

[181] Mo X, Zhi H, Xiao Y, Hua H, He L. Topology optimization of cooling plates for battery thermal management. Int J Heat Mass Transf 2021;178:121612. https://doi.org/10.1016/J.IJHEATMASSTRANSFER.2021.121612.

[182] Koga AA, Lopes ECC, Villa Nova HF, Lima CRD, Silva ECN. Development of heat sink device by using topology optimization. Int J Heat Mass Transf 2013;64:759–72. https://doi.org/10.1016/J.IJHEATMASSTRANSFER.2013.05.007.

[183] Subramaniam V, Dbouk T, Harion JL. Topology optimization of conjugate heat transfer systems: A competition between heat transfer enhancement and pressure drop reduction. Int J Heat Fluid Flow 2019;75:165–84. https://doi.org/10.1016/J.IJHEATFLUIDFLOW.2019.01.002.

[184] Li H, Ding X, Meng F, Jing D, Xiong M. Optimal design and thermal modelling for liquid-cooled heat sink based on multi-objective topology optimization: An experimental and numerical study. Int J Heat Mass Transf 2019;144:118638. https://doi.org/10.1016/J.IJHEATMASSTRANSFER.2019.118638.

[185] Fabbri G. Optimization of heat transfer through finned dissipators cooled by laminar flow. Int J Heat Fluid Flow 1998;19:644–54. https://doi.org/10.1016/S0142-727X(98)10036-X.

[186] McConnell C, Pingen G. Multi-Layer, Pseudo 3D Thermal Topology Optimization of Heat Sinks. ASME Int Mech Eng Congr Expo Proc 2013;7:2381–92. https://doi.org/10.1115/IMECE2012-93093.

[187] Ghasemi A, Elham A. Multi-objective topology optimization of pin-fin heat exchangers using spectral and finite-element methods. Struct Multidiscip Optim 2021;64:2075–95. https://doi.org/10.1007/S00158-021-02964-6/FIGURES/17.

[188] Lazarov BS, Sigmund O, Meyer KE, Alexandersen J. Experimental validation of additively manufactured optimized shapes for passive cooling. Appl Energy 2018;226:330–9. https://doi.org/10.1016/J.APENERGY.2018.05.106.

[189] Yan S, Wang F, Hong J, Sigmund O. Topology optimization of microchannel heat sinks

using a two-layer model. Int J Heat Mass Transf 2019;143:118462. https://doi.org/10.1016/j.ijheatmasstransfer.2019.118462.

[190] Dilgen SB, Dilgen CB, Fuhrman DR, Sigmund O, Lazarov BS. Density based topology optimization of turbulent flow heat transfer systems. Struct Multidiscip Optim 2018;57:1905–18. https://doi.org/10.1007/S00158-018-1967-6.

[191] Dilgen CB, Dilgen SB, Fuhrman DR, Sigmund O, Lazarov BS. Topology optimization of turbulent flows. Comput Methods Appl Mech Eng 2018;331:363–93. https://doi.org/10.1016/J.CMA.2017.11.029.

[192] Papazoglou P. Topology Optimization of Heat Exchangers. TU Delft, Master Thesis, 2015.

[193] Kobayashi H, Yaji K, Yamasaki S, Fujita K. Topology design of two-fluid heat exchange. Struct Multidiscip Optim 2021;821–834.

[194] Saviers KR, Ranjan R, Mahmoudi R. Design and validation of topology optimized heat exchangers. AIAA Scitech 2019 Forum 2019. https://doi.org/10.2514/6.2019-1465.

[195] Feppon F, Allaire G, Dapogny C, Jolivet P. Body-fitted topology optimization of 2D and 3D fluid-to-fluid heat exchangers. Comput Methods Appl Mech Eng 2021;376. https://doi.org/10.1016/J.CMA.2020.113638.

[196] Lin S, Zhao L, Guest JK, Weihs TP, Liu Z. Topology Optimization of Fixed-Geometry Fluid Diodes. J Mech Des Trans ASME 2015;137:1–9. https://doi.org/10.1115/1.4030297.

[197] Lim DK, Song MS, Chae H, Kim ES. Topology optimization on vortex-type passive fluidic diode for advanced nuclear reactors. Nucl Eng Technol 2019;51:1279–88. https://doi.org/10.1016/j.net.2019.03.018.

[198] Kubo S, Yaji K, Yamada T, Izui K, Nishiwaki S. A level set-based topology optimization method for optimal manifold designs with flow uniformity in plate-type microchannel reactors. Struct Multidiscip Optim 2017;55:1311–27. https://doi.org/10.1007/s00158-016-1577-0.

[199] Manuel MCE, Lin PT, Chang M. Optimal duct layout for HVAC using topology optimization. Sci Technol Built Environ 2018;24:212–9.

https://doi.org/10.1080/23744731.2017.1346444.

[200] Alexandersen J, Sigmund O, Meyer KE, Lazarov BS. Design of passive coolers for light-emitting diode lamps using topology optimisation. Int J Heat Mass Transf 2018;122:138–49. https://doi.org/10.1016/J.IJHEATMASSTRANSFER.2018.01.103.

[201] Iradukunda AC, Vargas A, Huitink D, Lohan D. Transient thermal performance using phase change material integrated topology optimized heat sinks. Appl Therm Eng 2020;179:115723.

[202] Zeng S, Lee PS. A Header Design Method for Target Flow Distribution among Parallel Channels Based on Topology Optimization. Proc 17th Intersoc Conf Therm Thermomechanical Phenom Electron Syst ITherm 2018 2018:156–63. https://doi.org/10.1109/ITHERM.2018.8419642.

[203] Kim J, Yim E, Jeon C, Jung C, Han B. Topology Optimization of a Gas Flow Channel Routes in an Automotive Fuel Cell. Int J … 2012;13:293–300. https://doi.org/10.1007/s12239.

[204] Onishi J, Shikazono N. Topology Optimization of Electrolyte-Anode Interfaces in Solid Oxide Fuel Cells. ECS Trans 2019;91:2127–35. https://doi.org/10.1149/09101.2127ecst.

[205] Wang C, Yu S, Chen W, Sun C. Highly efficient light-trapping structure design inspired by natural evolution. Sci Rep 2013;3. https://doi.org/10.1038/srep01025.

[206] Yu S, Wang C, Sun C, Chen W. Topology optimization for light-trapping structure in solar cells. Struct Multidiscip Optim 2014;50:367–82. https://doi.org/10.1007/s00158-014-1077-z.

[207] Gupta DK, Langelaar M, Barink M, van Keulen F. Topology optimization of front metallization patterns for solar cells. Struct Multidiscip Optim 2015;51:941–55. https://doi.org/10.1007/s00158-014-1185-9.

[208] Jia S, Cao X, Yuan X, Yu KT. Multi-objective topology optimization for the solar thermal decomposition of methane reactor enhancement. Chem Eng Sci 2021;231:116265. https://doi.org/10.1016/J.CES.2020.116265.

[209] Zadin V, Brandell D, Kasemägi H, Lellep J, Aabloo A. Designing the 3D-microbattery

geometry using the level-set method. J Power Sources 2013;244:417–28. https://doi.org/10.1016/j.jpowsour.2012.12.004.

[210] Mitchell SL, Ortiz M. Computational multiobjective topology optimization of silicon anode structures for lithium-ion batteries. J Power Sources 2016;326:242–51. https://doi.org/10.1016/j.jpowsour.2016.06.136.

[211] Yaji K, Yamasaki S, Tsushima S, Suzuki T, Fujita K. Topology optimization for the design of flow fields in a redox flow battery. Struct Multidiscip Optim 2018;57:535–46. https://doi.org/10.1007/s00158-017-1763-8.

[212] Wesseling P, Oñate E, Périaux J, Okkels F, Bruus H. Design of micro-fluidic bio-reactors using topology optimization. Eur. Conf. Comput. Fluid Dyn. ECCOMAS, 2006.

[213] Pizzolato A, Sharma A, Ge R, Maute K, Verda V. Maximization of performance in multi-tube latent heat storage – Optimization of fins topology, effect of materials selection and flow arrangements. Energy 2019. https://doi.org/10.1016/j.energy.2019.02.155.

[214] Yao QY, Zhao CY, Zhao Y, Wang H, Li W. Topology optimization for heat transfer enhancement in latent heat storage. Int J Therm Sci 2021;159. https://doi.org/10.1016/J.IJTHERMALSCI.2020.106578.

[215] Chen JT, Xia BQ, Zhao CY. Topology optimization for heat transfer enhancement in thermochemical heat storage. Int J Heat Mass Transf 2020;154. https://doi.org/10.1016/j.ijheatmasstransfer.2020.119785.

[216] Lin TY, Baker SE, Duoss EB, Beck VA. Topology optimization of 3D flow fields for flow batteries. J Electrochem Soc 2022;169.5. https://doi.org/10.48550/arXiv.2202.13032.

[217] Tian Y, Liu X, Xu Q, Luo Q, Zheng H, Song C, et al. Bionic topology optimization of fins for rapid latent heat thermal energy storage. Appl Therm Eng 2021;194:117104. https://doi.org/10.1016/J.APPLTHERMALENG.2021.117104.

[218] Pizzolato A, Sharma A, Maute K, Sciacovelli A, Verda V. Topology optimization for heat transfer enhancement in Latent Heat Thermal Energy Storage. Int J Heat Mass Transf 2017;113:875–88. https://doi.org/10.1016/j.ijheatmasstransfer.2017.05.098.

[219] Kant K, Shukla A, Smeulders DMJ, Rindt CCM. Analysis and optimization of the closed-adsorption heat storage bed performance. J Energy Storage 2020;32:101896.

https://doi.org/10.1016/j.est.2020.101896.

[220] Zhao D, Xue D. A multi-surrogate approximation method for metamodeling. Eng Comput 2011;27:139–53. https://doi.org/10.1007/S00366-009-0173-Y/TABLES/2.

[221] Rezaei E, Barbato M, Ortona A, Haussener S. Design and optimization of a high-temperature latent heat storage unit. Appl Energy 2020;261:114330. https://doi.org/10.1016/j.apenergy.2019.114330.

[222] Ma Z, Bao H, Roskilly AP. Seasonal solar thermal energy storage using thermochemical sorption in domestic dwellings in the UK. Energy 2019;166:213–22. https://doi.org/10.1016/j.energy.2018.10.066.

[223] Shi T, Xu H, Qi C, Lei B, Wu Y, Zhao C. Multi-physics modeling of thermochemical heat storage with enhance heat transfer. Appl Therm Eng 2021;198:117508. https://doi.org/10.1016/J.APPLTHERMALENG.2021.117508.

[224] Gediz Ilis G, Demir H, Mobedi M, Baran Saha B. A new adsorbent bed design: Optimization of geometric parameters and metal additive for the performance improvement. Appl Therm Eng 2019;162:114270. https://doi.org/10.1016/j.applthermaleng.2019.114270.

[225] Edwards JE. Design and Rating Shell and Tube Heat Exchangers. Chemistations - Technical Report; 2008.

[226] Köll R, van Helden W, Engel G, Wagner W, Dang B, Jänchen J, et al. An experimental investigation of a realistic-scale seasonal solar adsorption storage system for buildings. Sol Energy 2017;155:388–97. https://doi.org/10.1016/j.solener.2017.06.043.

[227] Zhao YJ, Wang RZ, Li TX, Nomura Y. Investigation of a 10 kWh sorption heat storage device for effective utilization of low-grade thermal energy. Energy 2016;113:739–47. https://doi.org/10.1016/j.energy.2016.07.100.

[228] Amirifard M, Kasaeian A, Amidpour M. Integration of a solar pond with a latent heat storage system. Renew Energy 2018;125:682–93. https://doi.org/10.1016/j.renene.2018.03.009.

[229] Palomba V, Vasta S, Freni A. Experimental testing of AQSOA FAM Z02 / water

adsorption system for heat and cold storage. Appl Therm Eng 2017;124:967–74. https://doi.org/10.1016/j.applthermaleng.2017.06.085.

[230] D'Ans P, Courbon E, Frère M, Descy G, Segato T, Degrez M. Severe corrosion of steel and copper by strontium bromide in thermochemical heat storage reactors. Corros Sci 2018;138:275–83. https://doi.org/10.1016/j.corsci.2018.04.020.

[231] Balasubramanian G, Ghommem M, Hajj MR, Wong WP, Tomlin JA, Puri IK. Modeling of thermochemical energy storage by salt hydrates. Int J Heat Mass Transf 2010;53:5700–6. https://doi.org/10.1016/j.ijheatmasstransfer.2010.08.012.

[232] Hussain MF, Barton RR, Joshi SB. Metamodeling: Radial basis functions, versus polynomials. Eur J Oper Res 2002;138:142–54. https://doi.org/10.1016/S0377-2217(01)00076-5.

[233] Box GEP, Behnken DW. Some New Three Level Designs for the Study of Quantitative Variables. Technometrics 1960;2:455–75. https://doi.org/10.1080/00401706.1960.10489912.

[234] Richter M, Habermann EM, Siebecke E, Linder M. A systematic screening of salt hydrates as materials for a thermochemical heat transformer. Thermochim Acta 2018;659:136–50. https://doi.org/10.1016/J.TCA.2017.06.011.

[235] Wagman DD, Evans WH, Parker VB, Schumm RH, Halow I. The NBS Tables of Chemical Thermodynamic Properties. J Res 1982. https://doi.org/10.6028/jres.125.007.

[236] Khawam A, Flanagan DR. Solid-State Kinetic Models: Basics and Mathematical Fundamentals. J Phys Chem B 2006;110:17315–28. https://doi.org/10.1021/JP062746A.

[237] Haertel JHK. Design of Thermal Systems Using Topology Optimization - Ph.D. Thesis. DTU, 2017.

[238] Gothäll H. How to Use Topology Optimization Results as Model Geometries | COMSOL Blog n.d.

[239] Humbert G, Ding Y, Sciacovelli A. Combined enhancement of thermal and chemical performance of closed thermochemical energy storage system by optimized tree-like heat exchanger structures. Appl Energy 2022;311:118633.

https://doi.org/10.1016/J.APENERGY.2022.118633.

[240] Pham T, Kwon P, Foster S. Additive manufacturing and topology optimization of magnetic materials for electrical machines—a review. Energies 2021;14:1–24. https://doi.org/10.3390/en14020283.

[241] McDonough JR. A perspective on the current and future roles of additive manufacturing in process engineering, with an emphasis on heat transfer. Therm Sci Eng Prog 2020;19:100594. https://doi.org/10.1016/j.tsep.2020.100594.

[242] Johnson M, Vogel J, Hempel M, Hachmann B, Dengel A. Design of high temperature thermal energy storage for high power levels. Sustain Cities Soc 2017;35:758–63. https://doi.org/10.1016/J.SCS.2017.09.007.

[243] Thomas D. Costs, benefits, and adoption of additive manufacturing: a supply chain perspective. Int J Adv Manuf Technol 2016;85:1857–76. https://doi.org/10.1007/s00170-015-7973-6.

[244] Nana A, Cuillière JC, Francois V. Automatic reconstruction of beam structures from 3D topology optimization results. Comput Struct 2017;189:62–82. https://doi.org/10.1016/j.compstruc.2017.04.018.

[245] Meng L, Zhang W, Quan D, Shi G, Tang L, Hou Y, et al. From Topology Optimization Design to Additive Manufacturing: Today's Success and Tomorrow's Roadmap. Arch Comput Methods Eng 2020;27:805–30. https://doi.org/10.1007/s11831-019-09331-1.

[246] Yaji K, Yamasaki S, Fujita K. Multifidelity design guided by topology optimization. Struct Multidiscip Optim 2019;61:1071–85. https://doi.org/10.1007/s00158-019-02406-4.

[247] Malley-Ernewein A, Lorente S. Analysis of thermochemical energy storage in an elemental configuration. Sci Rep 2019;9:15875. https://doi.org/10.1038/s41598-019-52249-8.

[248] Okkels F, Bruus H. Scaling behavior of optimally structured catalytic microfluidic reactors. Phys Rev E - Stat Nonlinear, Soft Matter Phys 2007;75:2–5. https://doi.org/10.1103/PhysRevE.75.016301.

[249] Gersborg-Hansen A, Sigmund O, Haber RB. Topology optimization of channel flow problems. Struct Multidiscip Optim 2005;30:181–92. https://doi.org/10.1007/s00158-004-0508-7.

[250] Yaji K, Yamasaki S, Fujita K. Data-driven multifidelity topology design using a deep generative model: Application to forced convection heat transfer problems. Comput Methods Appl Mech Eng 2022;388:114284. https://doi.org/10.1016/J.CMA.2021.114284.

[251] Moran MJ, Shapiro HN, Boettner DD, Bailey MB. Fundamentals Of Engineering Thermodynamics. 1987.

[252] Pahamli Y, Hosseini MJ, Ardahaie SS, Ranjbar AA. Improvement of a phase change heat storage system by Blossom-Shaped Fins: Energy analysis. Renew Energy 2022;182:192–215. https://doi.org/10.1016/J.RENENE.2021.09.128.

[253] Luu MT, Milani D, Nomvar M, Abbas A. A design protocol for enhanced discharge exergy in phase change material heat battery. Appl Energy 2020;265. https://doi.org/10.1016/J.APENERGY.2020.114801.

[254] Harzheim L, Graf G. A review of optimization of cast parts using topology optimization. Struct Multidiscip Optim 2006 315 2005;31:388–99. https://doi.org/10.1007/S00158-005-0554-9.

[255] Zuo W, Saitou K. Multi-material topology optimization using ordered SIMP interpolation. Struct Multidisc Optim 2016. https://doi.org/10.1007/s00158-016-1513-3.

Appendix

The polynomial coefficient resulting from the ordinary least square fitting described in section 4.2.3 are reported in Table 9.1.

Table 9.1 List of coefficients for the surrogate models in polynomial shape.

	$f(l_2, \beta_1, \beta_2)$					
	ADS-reactor			***RDS-reactor***		
	f_{Ppeak}	$f_{\alpha\ (10\ h)}$	$f_{\alpha\ (20\ h)}$	f_{Ppeak}	$f_{\alpha\ (10\ h)}$	$f_{\alpha\ (20\ h)}$
n	3	3	2	3	2	2
$b_{0,0,0}$	0.00E+00	0.00E+00	9.57E-01	0.00E+00	5.24E-01	7.90E-01
$b_{0,0,1}$	0.00E+00	0.00E+00	-1.24E-03	3.20E+00	-2.52E-05	2.24E-05
$b_{0,0,2}$	8.96E-04	1.17E-05	1.56E-05	-1.88E-01	-1.18E-06	-1.04E-06
$b_{0,0,3}$	4.25E-05	-1.28E-07	-	3.43E-03	-	-
$b_{0,1,0}$	0.00E+00	0.00E+00	-1.20E-03	0.00E+00	3.97E-03	1.85E-03
$b_{0,1,1}$	-1.26E-02	-1.88E-04	7.57E-05	-6.62E-03	-1.76E-05	-1.49E-06
$b_{0,1,2}$	3.51E-06	2.07E-06	-	-2.97E-06	-	-
$b_{0,2,0}$	2.73E-02	4.44E-04	-7.84E-06	4.15E-02	-8.91E-05	-4.61E-05
$b_{0,2,1}$	1.68E-04	2.26E-06	-	8.70E-05	-	-
$b_{0,3,0}$	-8.61E-04	-1.41E-05	-	-1.42E-03	-	-
$b_{1,0,0}$	1.60E+00	4.76E-02	1.05E-04	1.68E-01	2.07E-03	8.07E-04
$b_{1,0,1}$	-1.10E-03	4.77E-06	1.45E-05	-4.34E-04	9.87E-07	9.02E-08
$b_{1,0,2}$	-6.00E-05	-1.57E-07	-	7.35E-06	-	-
$b_{1,1,0}$	2.37E-03	-3.32E-05	-1.96E-05	1.51E-03	-7.19E-06	-4.39E-06
$b_{1,1,1}$	8.61E-05	9.77E-07	-	2.26E-05	-	-
$b_{1,2,1}$	-2.75E-05	-2.13E-07	-	6.36E-06	-	-
$b_{2,0,0}$	-3.40E-02	-1.04E-03	-1.45E-05	-1.45E-03	-2.07E-05	-8.15E-06
$b_{2,0,1}$	3.48E-05	-1.22E-08	-	2.15E-06	-	-
$b_{2,1,0}$	-4.23E-05	1.19E-07	-	-2.73E-05	-	-
$b_{3,0,0}$	2.31E-04	7.27E-06	-	-2.08E-06	-	-